Dissertation

Performance of the ATLAS Muon Spectrometer

ausgeführt zum Zwecke der Erlangung des akademischen Grades eines Doktors der technischen Wissenschaften unter der Leitung von

Ao. Univ. Prof. Dr. Christian W. Fabjan
Institut für Kernphysik der TU Wien (E142)

eingereicht an der Technischen Universität Wien

Technisch-Naturwissenschaftliche Fakultät

von

Dipl.-Ing. Martin Aleksa

Matrikelnummer 9028010
geboren am 9. Juli 1972 in Wien
Heiligenstädter Str. 107-109/35, A-1190 Wien

Genf, am 11. September 1999

Kurzfassung

ATLAS ist ein Universalexperiment für den geplanten Large Hadron Collider (LHC) am CERN. Das Myonspektrometer von ATLAS wird aus Präzisionskammern mit einer Gesamtfläche von $\sim 5500\,\mathrm{m}^2$ bestehen und Myonentrajektorien entlang eines 5 m bis 15 m langen Spektrometerarms in einem Magnetfeld von $\sim 0.5\,\mathrm{T}$ messen. Als Präzisionsdetektoren im Myonspektrometer werden 370.000 Hochdruckdriftrohre (MDTs), zusammengesetzt zu etwa 1200 Präzisionsdrahtkammern, verwendet werden. Um das vom LHC gebotene Entdeckungspotential für ,,neue Physik" voll ausschöpfen zu können, ist eine Impulsauflösung von $\sim 10\,\%$ für Myonen mit einem Transversalimpuls von $p_\mathrm{T} = 1\,\mathrm{TeV}/c$ nötig. Aufgrund einer ausführlichen technischen Optimierung der Magnetfeldstärke gegen die Drahtkammerauflösung entschied sich die ATLAS Kollaboration für ein Driftkammersystem mit hoher Ortsauflösung von $\bar{\sigma} < 80\,\mu\mathrm{m}$ pro Driftrohr.

Dieses ambitionierte Ziel wurde noch nie in einem Detektor dieser Größenordnung erreicht, geschweige denn in einem Hochratenumfeld, das dem des LHCs entspricht. Simulationen der Untergrundzählraten des Myonspektrometers ergaben, dass die oben erwähnte Ortsauflösung von $\bar{\sigma} < 80\,\mu\mathrm{m}$ selbst bei Zählraten bis zu 1500 Hz pro cm Drahtlänge erreicht werden muss.

Diese Arbeit beschreibt die Suche nach einem geeigneten Driftgas für die Präzisionskammern. Durch Messungen und Simulationen einiger Driftgase konnte ein geeignetes Gas für das MDT System gefunden werden, welches alle Anforderungen selbst bei höchsten Untergrundzählraten erfüllt ($\mathrm{Ar/CO_2}$ 93/7).

Messungen in einem ATLAS-ähnlichen Hochratenumfeld ermöglichten ein lückenloses Verständnis der einzelnen Hochratenffekte, die zu einer Ortsauflösungsverschlechterung beitragen. Vier Effekte wurden gefunden und genau quantifiziert: Zwei Elektronikeffekte, die von der Zählrate pro Rohr abhängen (Grundlinienverschiebung und Grundlinienfluktuationen), und zwei Raumladungseffekte, die von der lokalen Zählrate abhängen (Gasverstärkungsabfall und Driftfeldfluktuationen). Das genaue Wissen um diese Effekte hatte großen Einfluss auf die Driftgas- und Elektronikauswahl.

Die starke Abhängigkeit der Driftgeschwindigkeit vom Driftfeld ist der wesentliche Nachteil von $\mathrm{Ar/CO_2}$ 93/7. In dieser Arbeit werden alle Effekte, die zu systematischen Fehlern der Myonenspurenpositionsmessung in einem Driftrohr führen (z.B. Untergrundzählratenvariationen), unter realistischen LHC-Bedingungen untersucht und quantifiziert. Für die größten Effekte konnten analytische Korrekturen gefunden werden.

Schließlich wurde in dieser Arbeit die Auflösung des gesamten Myonsystems untersucht und eine Kalibrationsmethode für die absolute Massenskala entwickelt. Anhand von Simulationen wurde gezeigt, dass der Energieverlust und das Magnetfeld gleichzeitig mit einer Genauigkeit von 10^{-3} unter Verwendung von $\mathrm{Z} \rightarrow \mu^+\mu^-$ Ereignissen kalibriert werden können und dass eine Kalibration der absoluten Massenskala in der Größenordnung von 10^{-4} möglich ist.

Abstract

ATLAS is a general-purpose experiment for the future Large Hadron Collider (LHC) at CERN. Its Muon Spectrometer will require $\sim 5500\,\mathrm{m}^2$ of precision tracking chambers to measure the muon tracks along a spectrometer arm of 5 m to 15 m length, embedded in a magnetic field of $\sim 0.5\,\mathrm{T}$. The precision tracking devices in the Muon System will be high pressure drift tubes (MDTs). Approximately 370,000 MDTs will be assembled into ~ 1200 drift chambers. The LHC physics discovery range indicates the need for a momentum resolution of $\sim 10\,\%$ for muons with a transverse momentum of $p_\mathrm{T} = 1\,\mathrm{TeV}/c$. Following a detailed engineering optimisation of the magnetic-field strength versus the chamber resolution, the ATLAS collaboration opted for a drift-chamber system with very high spatial resolution, $\bar{\sigma} < 80\,\mu\mathrm{m}$ for a single-tube measurement.

This performance goal has never been achieved in a large-scale experiment, let alone in the high-rate background of the LHC. Simulations of the background in the ATLAS hall show that the MDTs have to meet the requirement of a resolution $\bar{\sigma} < 80\,\mu\mathrm{m}$ in the presence of a background rate of up to 1500 Hz per cm wire length.

This work deals with the search for a suitable drift gas for the precision drift chambers. Measurements and simulations done for several gas mixtures allowed us to establish a new baseline gas for the MDT system which satisfies all requirements even for the highest background rates (Ar/CO_2 93/7).

Measurements performed in a high-background environment – similar to the ATLAS operational environment – gave us a complete understanding of the individual effects which deteriorate the spatial resolution at high rates. Four effects responsible for a resolution deterioration have been identified: two electronics effects which depend on the count rate of a tube (baseline shift and baseline fluctuations), and two space-charge effects that depend on the local count rate (gain drop and field fluctuations). The understanding of these effects had a major impact on the choice of the drift gas and the front-end electronics.

The strong dependence of the drift velocity on the drift field is one major disadvantage of the baseline gas. In this work the full set of effects which lead to systematic errors to the track-position measurement in one tube (e.g. variations of the background rate) was investigated and quantified for realistic LHC operating conditions. For the biggest effects analytical corrections are presented.

Finally, the Muon-System performance was investigated and a calibration method for the absolute mass scale developed. By means of simulation it was shown that the energy loss of the muons and the magnetic field can be calibrated at the 10^{-3} level by reconstructing $\mathrm{Z} \rightarrow \mu^+\mu^-$ events and that a calibration of the absolute mass scale at the 10^{-4} level is possible.

Acknowledgement

I am most grateful not only for the continuous support and competent guidance I received from Chris Fabjan but also for his incredible ability to motivate. Sometimes, when I found myself unsure about the importance of my investigations, five minutes with him (and his apple) were enough to convince me for a while that the success of ATLAS depended crucially on my results. I also greatly enjoyed the skiing days together!
From Werner Riegler I learned a large part of everything I know about drift chambers. Besides that, he introduced me to the night life of St. Genis and helped me to settle down here. I remember, when we inspected together my little apartment, he was not sure whether to encourage me to take it, or to rent it himself!
Thanks to him, Nigel Hessey, Mario Deile ("…I will never write *daß* with *ss*!"), Konrad Bussmann, Volker Paschhoff, Jim Shank, Vladimir Gapienko, Vadim Gratchev and Valeri Tcherniatine I had a highly successful and interesting time during the test-beam periods. I learned from them not to panic even if the MDT chamber almost fell apart or nothing worked until three days before the end of our beam time. I cordially thank Nigel for his invaluable technical help and all the critical discussions, which triggered many additional investigations trying to understand the MDT behaviour down to the last microns. Due to his, Mario's and Arnold Staude's critical reconsiderations I have been prevented from being fooled by my own simulations. Thanks a lot to all of them!
I also want to express my gratitude to Frank Linde who was always open for questions even between hundreds of phone calls, which – since I was sharing a desk with him – continuously kept me informed of the latest end-plug design. Thanks also to Walter Blum, Rob Veenhof, Michael Treichel, Robert Richter, Uwe Bratzler and Jörg Wotschack for their support and help. I am most grateful to Giorgos Stavropoulos, Theodora Papadopoulou, Aleandro Nisati, Claude Guyot, Jean-François Laporte and Laurent Chevalier for getting me started with DICE and MUONBOX and for inaugurating me into the field of detector simulation. I very much appreciated the warm atmosphere in our collaboration thanks to the numerous social events organised with a great spirit by the ATLAS secretariat.
Thanks to Edda I could share all the tiny but motivating results immediately and was frequently consoled with a cup of coffee on dispiriting days. I also really looked forward to our coffee breaks with Hemma, Adrian "oh my darling", Helmut and Nigel. I will always remember the wonderful time I had with Thomas singing in the choir and afterwards the far reaching discussions beer in hand. I found many friends in our "Mittach"-group consisting of Edda, Uli, Regina, Barbara, Thomas, Karsten, Peter, Parvez, the "theory" Adrian, Volker and all who joined us from time to time like Cathi, Sandra, Ingrid, Hemma, Lali, Michael, Alex "…g'rad' sitzen!", Günther, Marko and Adrian. During lunch time hundreds of parties and barbecues were organised, which made my time here so enjoyable. Also the wonderful, but unfortunately short moments with my friends from Vienna – Axl, Hannes, Wolfram, Markus, Norbert, … – contributed a lot to my well being. Many thanks to all of them!
A big "Thank You" to my family for all their unconditional support, their continuous interest in my work and for encouraging me to go abroad and take advantage of this great opportunity to work at CERN. I am of course most grateful to Sophie for being by my side, making me feel at home wherever she is and letting me forget the ups and downs of work in the glance of her eyes.

Contents

Chapter 1

A New Generation of Research Facilities

1.1 Introduction

The next generation of high-energy physics research facilities has to operate in the TeV range in order to address important new issues of elementary particle physics (see Section 1.3). This chapter gives an introduction to the **L**arge **H**adron **C**ollider (LHC). This accelerator will allow to explore particle physics up to energies that dominated the universe just 10^{-12} s after the "Big Bang" when the temperature was about 10^{16} K. We will discuss the physics potential of the collider and focus afterwards on its impact on the design of the ATLAS experiment and – in greater detail – its Muon System.

1.2 The Large Hadron Collider

1.2.1 Design Parameters of the LHC

Already in the beginning of the 1980's, people at CERN started to think about testing the standard model beyond LEP energies. The LEP machine (e^+-e^-) has worked around the Z resonance ($M_Z = 91.187\,\mathrm{GeV}/c^2$) and is presently upgraded to LEP2 with a maximum centre-of-mass energy $\sqrt{s}$ of $\geq 200\,\mathrm{GeV}$. This value of $\sqrt{s}$ is the practical limit achievable with a circular electron accelerator in the 27 km circumference LEP tunnel due to the rapid increase of synchrotron radiation loss with energy. The large mass of hadrons with respect to electrons has the advantage that less energy is lost due to this effect. The main disadvantage of a hadron collider is the compositeness of the hadron. This means that the available energy of the hadron is distributed over the individual constituents (quarks and gluons).

Considering the above arguments and given that a new collider at CERN has to match the existing LEP tunnel, the LHC was designed. It is planned to be operational in the year 2005. The LHC will be a p-p collider with a centre-of-mass energy $\sqrt{s}$ of $2 \times 7 = 14\,\text{TeV}$ and a design luminosity of $\mathcal{L} = 10^{34}\,\text{cm}^{-2}\text{s}^{-1}$. Apart from accelerating protons, it will be possible to use the LHC with Pb-Pb ions at a centre-of-mass energy in the PeV range. The LHC will consist of two separate beam lines (with counter-rotating beams) which will be installed in the existing LEP tunnel and will be filled with 0.45 TeV protons delivered from the **S**uper **P**roton **S**ynchrotron (SPS) and its pre-accelerators (see Figure 1.1).

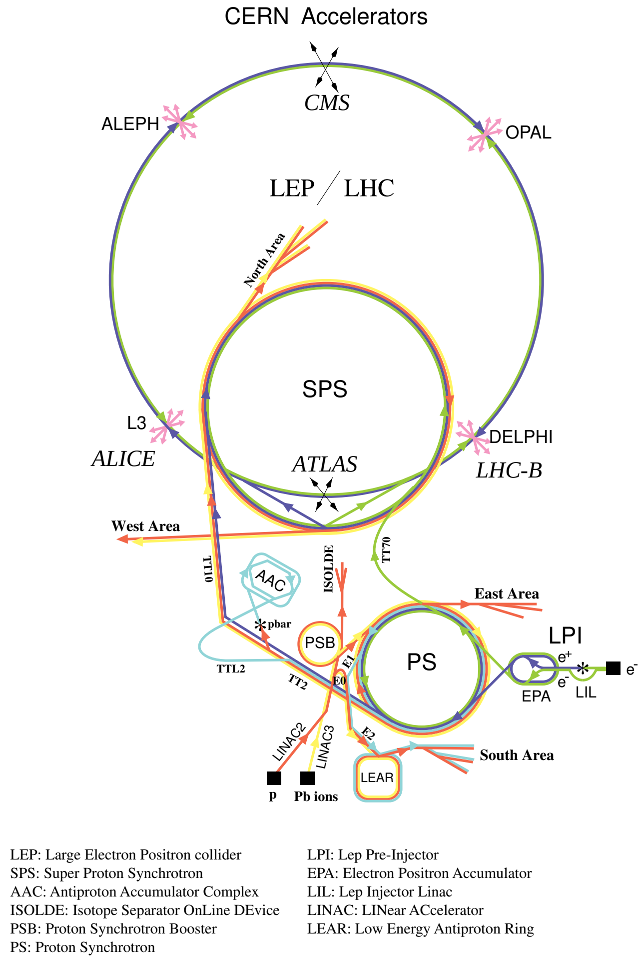

Figure 1.1: *Schematic view of the CERN accelerator complex.*

The beam line will be occupied with super-conducting NbTi bending magnets, quadrupoles for the beam optics and accelerating cavities. These magnets will house two separated beam lines with opposite magnetic fields of 8.4 T strength. The 1232 dipole magnets which are foreseen along the beam line will be $\sim 14.6\,\text{m}$ long.

At the interaction points, the bunches will have a transverse radius of $15\,\mu\text{m}$ and the length of the bunch will be 30 cm. This means that the position of the vertex will have a rather large spread along the beam direction, the effective spread of the distribution of the vertex position is expected to be 5.5 cm (r.m.s) along the beam direction.

1.2.2 Particle Production Rates

In Figure 1.2 some important production cross-sections and interaction rates are shown as a function of the centre-of-mass energy $\sqrt{s}$. The total cross-section is estimated to be between 90 and 130 mb. This means that on average there will be about 20 interactions in the centre of the detectors per bunch crossing (i.e. every 25 ns) at full luminosity $\mathcal{L} = 10^{34}\,\mathrm{cm}^{-2}\mathrm{s}^{-1}$. Small angle elastic and inelastic proton-proton scattering will be the most numerous and will dominate the 20 underlying events per bunch crossing. The total integrated luminosity is expected to be 10^5 events/(pb × year).

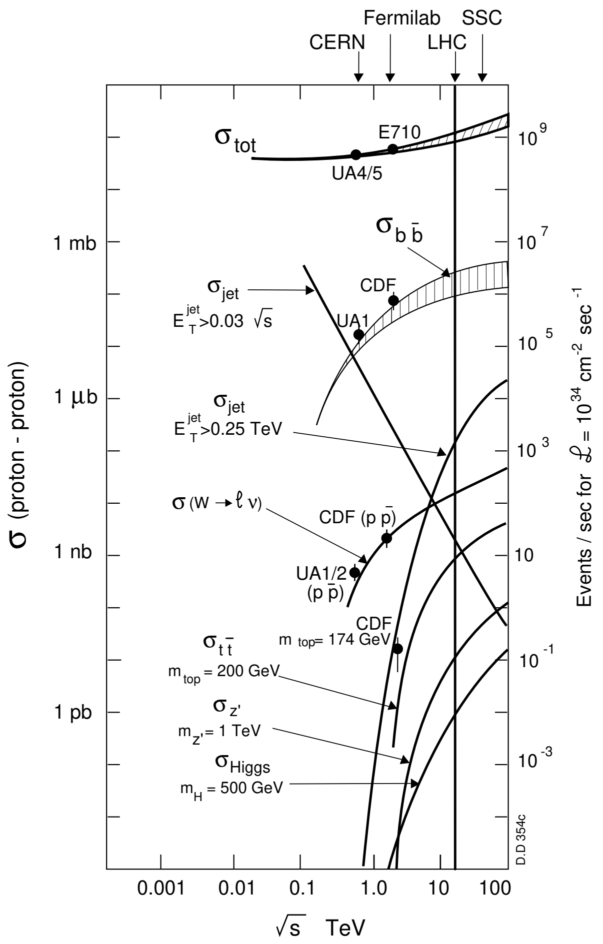

Figure 1.2: *The cross-section of some characteristic processes* [JAR:90]. *The centre-of-mass energy of LHC is indicated at the top. At $\sqrt{s} = 14\,\mathrm{TeV}$ the production of the Higgs is eleven orders of magnitude less frequent than small angle p-p scattering.*

The LHC will be a p-p collider with a centre-of-mass energy $\sqrt{s} = 14\,\mathrm{TeV}$. At full luminosity $\mathcal{L} = 10^{34}\,\mathrm{cm}^{-2}\mathrm{s}^{-1}$ the collision rate will be 10^9 collisions/s and the total integrated luminosity 10^5 events/(pb × year).

1.3 Physics at LHC and Detector Requirements

One of the main goals of LHC is to study the actual mechanism for symmetry breaking in the electroweak sector ($SU(2) \times U(1)$) of the **S**tandard **M**odel (SM). This phenomenon is associated with the nature of the Higgs mechanism, the existence of the Higgs particle and the behaviour of the cross-sections involving the gauge bosons, $W^\pm$ and Z. The LHC is designed to explore all the range of "allowed" Higgs masses and more, hence the planned experiments either must find the Higgs boson or contradict the Standard Model. In this section we will discuss the Higgs production and decay channels for the whole range of Higgs masses.

At the LHC heavy fermions (bottom and top-quarks) will be produced in large quantities. Hence, beside the Higgs search also B physics and the study of top-quark production and decay will be interesting issues for the LHC physics programme.

All these examples for LHC physics are used as benchmark processes for the detector design. In this Section we discuss briefly these benchmark processes and show their impact on the design of the various LHC detectors.

1.3.1 The Standard Model Higgs Boson

The most prominent benchmark processes for the detector design at LHC are the different Higgs-decay channels for the Higgs-mass range from $80\,\mathrm{GeV}/c^2$ to $1\,\mathrm{TeV}/c^2$. The Higgs coupling to other particles is proportional to their masses. It couples to quarks and leptons of mass m_f with a strength $g\frac{m_\mathrm{f}}{2M_\mathrm{W}}$. If the Higgs mass is very large, the couplings of the Higgs to itself and to longitudinally polarised gauge bosons become large. Requiring that these couplings remain weak enough that perturbation theory is applicable implies that $M_\mathrm{H} \leq 1\,\mathrm{TeV}/c^2$. This becomes more clear by pointing out that the width of the Higgs boson is proportional to the cube of its mass (for $M_\mathrm{H} > 2M_\mathrm{Z}$) and that a boson of mass $1\,\mathrm{TeV}/c^2$ has a width of Γ_H of $500\,\mathrm{GeV}/c^2$ (see Figure 1.3) and hence dissolves into the background. At the moment the lower limit of the Higgs mass is $94.1\,\mathrm{GeV}/c^2$ [DEL:99] (at $95\,\%$ confidence level) since it has not been discovered yet with LEP2. The Standard Model prefers a value for the Higgs mass close to $100\,\mathrm{GeV}/c^2$. In the **M**inimal **S**uper-symmetric extension of the **S**tandard **M**odel (MSSM) a family of Higgs bosons is predicted with an upper limit for the lightest super-symmetric Higgs boson of $130\,\mathrm{GeV}/c^2$.

Higgs Production

The production cross-section of the Higgs is typically 1 pb, assuming the Higgs mass with $500\,\mathrm{GeV}/c^2$. This corresponds to 10^5 produced Higgs bosons per year (or 1 Higgs boson every 2 minutes). The cross-section increases rapidly for a low-mass Higgs. The most dominant production mechanisms are the gluon-gluon fusion and the WW(ZZ) fusion. Figure 1.4 shows the Feynman-Diagrams for these two processes. Less important production channels are $t\bar{t}$ fusion and W or Z Bremsstrahlung [JAR:90].

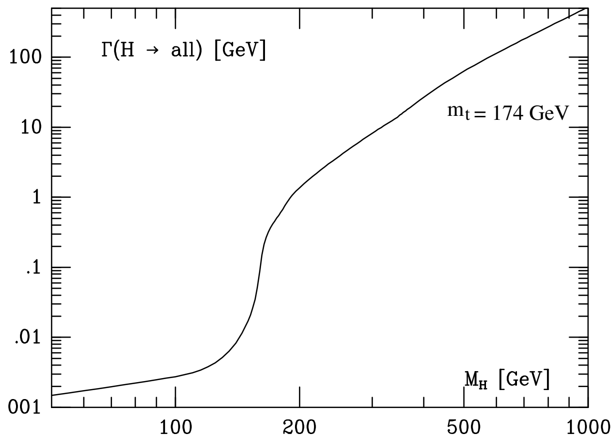

Figure 1.3: *Total Higgs width* $\Gamma_{\rm H}$ *as a function of* $M_{\rm H}$.

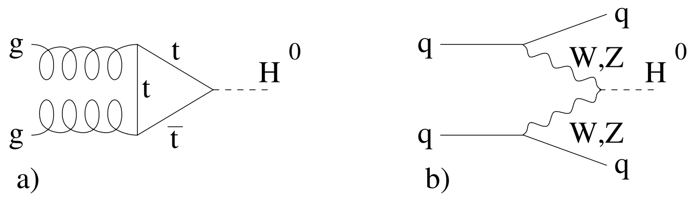

Figure 1.4: *The most dominant channels for the Higgs production: a) gluon-gluon fusion; b)* WW *and* ZZ *fusion.*

Higgs Decay

In Figure 1.5 the branching ratios are shown for Higgs masses between 50 and 600 GeV/c^2. Only a few decay channels of the Higgs boson are accessible to experimental observation since the decay channels have either small branching ratios, or they are obscured by a large background of events. Statistics will be the limiting factor in the detection of the Higgs boson, in particular for Higgs masses approaching 1 TeV/c^2.

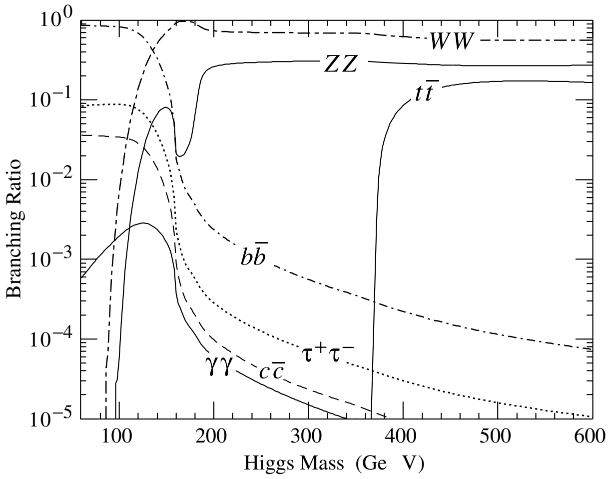

Figure 1.5: *Branching ratios of the Higgs.*

- **Low-Mass Higgs Boson ($M_{\mathrm{H}} < 120\,\mathrm{GeV}/c^2$):**
  Below the WW or ZZ threshold ($M_{\mathrm{H}} < 2M_{\mathrm{Z}}$), the dominant decay into the heaviest accessible pair of quarks ($\mathrm{H} \rightarrow \mathrm{b\bar{b}}$) is swamped by the QCD background (the direct $\mathrm{b\bar{b}}$ cross-section is very high, see Figure 1.2). Another decay channel in this regime can be the decay $\mathrm{WH} \rightarrow \mathrm{l}\nu\gamma\gamma$, which has almost no background, but unfortunately the production rate is very small. The third decay channel $\mathrm{H} \rightarrow \gamma\gamma$ suffers an enormous background from $\mathrm{q\bar{q}} \rightarrow \gamma\gamma$, $\mathrm{gg} \rightarrow \gamma\gamma$, $\mathrm{gq} \rightarrow \mathrm{q}\gamma\gamma$ and $\mathrm{Z} \rightarrow \mathrm{e^+e^-}$ processes, where the jets or $\mathrm{e}^{\pm}$ fake a γ. These backgrounds can be reduced with excellent photon resolution and excellent γ/jet and $\gamma/\mathrm{e}^{\pm}$ discrimination. Hence an electromagnetic calorimetry with excellent performance is required.

- **Intermediate-Mass Higgs Boson ($120\,\mathrm{GeV}/c^2 < M_{\mathrm{H}} < 800\,\mathrm{GeV}/c^2$):**
  In this mass region the decay $\mathrm{H} \rightarrow \mathrm{ZZ}^{(*)} \rightarrow \mathrm{l^+l^-l^+l^-}$ provides a very clean signature of the Higgs boson. For the range $M_{\mathrm{H}} < 2M_{\mathrm{Z}}$ one of the two Z bosons is virtual. For a Higgs mass of $150\,\mathrm{GeV}/c^2$ one expects ~ 550 such events per year. The four leptons have a high transverse momentum ($5\,\mathrm{GeV}/c < p_{\mathrm{T}} < 50\,\mathrm{GeV}/c$). The natural Higgs width Γ_{H} is small in this regime (see Figure 1.3) and the background is mainly coming from prompt muons, decay muons, hadronic punch-through, neutrons and muon induced electromagnetic secondaries. To achieve a good acceptance for such kind of events, the geometrical and kinematic acceptance for leptons has to be maximised, the significance of the signal will depend on the four-lepton mass resolution. Hence a good lepton energy and momentum resolution at the level of 1 % is necessary. For large Higgs boson masses the Higgs width increases rapidly and the signal will be rate limited, hence the accelerator luminosity becomes more important than the detector performance.

- **Heavy-Mass Higgs Boson ($M_{\mathrm{H}} > 800\,\mathrm{GeV}/c^2$):**
  For a heavy Higgs boson the channel $\mathrm{H} \rightarrow \mathrm{ZZ} \rightarrow \mathrm{l^+l^-}\nu\bar{\nu}$ becomes six times more frequent than $\mathrm{H} \rightarrow \mathrm{ZZ} \rightarrow \mathrm{l^+l^-l^+l^-}$ and can be detected with the measurements of two high-p_{T} leptons and a high missing E_{T} due to the escaping neutrinos. Also the channels $\mathrm{H} \rightarrow \mathrm{WW}, \mathrm{ZZ} \rightarrow \mathrm{l}^{\pm}\nu\mathrm{2jets}, \mathrm{2l}^{\pm}\mathrm{2jets}$ provide promising signatures for a heavy Higgs boson.

1.3.2 Other Proton-Proton Physics Issues

In this section further examples of benchmark processes besides the Higgs search are discussed which had an impact on the detector design.

Minimal Super-Symmetric Extension of the Standard Model (MSSM)

The simplest extension of the Standard Model (MSSM) has two Higgs doublets whose neutral components have vacuum expectation values v_1 and v_2. The physical particle spectrum contains one charged Higgs boson ($\mathrm{H}^{\pm}$), two neutral scalars (h,H) and one pseudoscalar (A). The mass of the lightest of these scalars depends upon the top quark mass, the ratio $v_2/v_1 \equiv \tan\beta$, and the masses of other super-symmetric particles. At large $\tan\beta$ and

$m_{\mathrm{top}} = 174\,\mathrm{GeV}/c^2$ there is a bound $M_{\mathrm{h}} < 130\,\mathrm{GeV}/c^2$. The bound reduces as $\tan\beta$ is lowered. The MSSM Higgs searches require efficient secondary vertex detection for τ leptons and b-quarks as well as high-resolution calorimetry for jets and missing transverse energy.

Super-Symmetric Searches

If **SU**per-**SY**mmetric (SUSY) particles exist, they will be produced and detected at the LHC for masses up to $2\,\mathrm{TeV}/c^2$. The lightest SUSY particle is stable, but hardly interacting with matter. Hence the search for super-symmetric particles sets stringent requirements on the hermiticity and the missing E_{T} capability of the detector.

Top Physics

As already mentioned before, the LHC will provide us with a large number of top-quarks. The $\mathrm{t\bar{t}}$ cross-section will be about 1 nb (see Figure 1.2). This high statistics of top-quarks will allow to obtain a top-mass resolution limited merely by theoretical uncertainties rather than statistics. Furthermore it will be possible to study its decay channels in detail such as $\mathrm{t} \rightarrow \mathrm{bH}^+$ or $\mathrm{t} \rightarrow \mathrm{Zc}$.

B Physics

The main issue of B physics is the observation of CP violation in the $\mathrm{B}^0_{\mathrm{d}}$ system, and the goal is to measure the three interior angles of the unitarity triangle corresponding to the **C**abibbo-**K**obayashi-**M**askawa (CKM) matrix. The investigations of $\mathrm{B\bar{B}}$ mixing in the $\mathrm{B}^0_{\mathrm{s}}$ system, rare b decays and general spectroscopy of states with b-quarks will be of great interest. Precise secondary vertex determination and full reconstruction of final states with relatively low-p_{T} particles (e.g. $\mathrm{B}^0_{\mathrm{d}} \rightarrow \mathrm{J}/\Psi \mathrm{K}^0_{\mathrm{s}}$ followed by $\mathrm{J}/\Psi \rightarrow \mathrm{l}^+\mathrm{l}^-$) are important. Obviously low-p_{T} lepton first-level trigger thresholds as well as second-level triggering capability are necessary requirements for the experiments.

During the initial low-luminosity running ($\mathcal{L} = 10^{33}\,\mathrm{cm}^{-2}\mathrm{s}^{-1}$), when b-quark identification is not hindered by pile-up in the detectors, B physics investigations can be performed also with the general-purpose experiments [EER:92]. However, a dedicated B physics experiment – LHCb [LHC:98] – is planned on one of the low-luminosity interaction points.

Other Symmetry-Breaking Mechanisms

Nature maybe has not chosen the Higgs mechanism as the mechanism responsible for the electroweak symmetry breaking. Here, I want to introduce briefly one concept which could replace the Higgs mechanism: the technicolor models.

Technicolor models replace the elementary Higgs bosons of the SM or SUSY with dynamical condensates and provide a dynamical means of breaking electroweak symmetry [WEI:79, SUS:79]. It assumes the existence of technifermions possessing a technicolor charge. Chiral symmetry is broken by techniquark condensates giving rise to Goldstone bosons, the technipions, which are the longitudinal degrees of freedom of the W and the Z gauge bosons.

ATLAS may be able to detect the single production of a technipion if it decays to heavy quarks. Also the search for a technirho resonance decaying to a pair of gauge bosons, or to a technipion and a gauge boson will be possible [ATL:99].

Other Searches

New heavy gauge bosons W′ and Z′ could be accessible to the LHC for masses up to 5–6 TeV/c^2. Therefore high-resolution lepton measurement and charge identification are needed even in a p_T range up to a few TeV/c.

Also searches for leptoquarks and investigations of quark and lepton compositeness will be performed at LHC.

1.3.3 Experiments

In order to exploit the full discovery potential of LHC two general-purpose proton-proton experiments (ATLAS and CMS) and two specialised experiments (ALICE and LHCb) will be installed at the beam crossings (see Figure 1.1).

The main difference between the two general-purpose experiments lies in their magnet configurations for muon spectroscopy. The choice of the magnet system strongly influences the geometry of the detector.

- **ATLAS:**
  The ATLAS (**A T**oroidal **L**HC **A**pparatu**S**) experiment is characterised by the following magnet configuration: A super-conducting solenoid will be installed around the Inner-Detector cavity and large super-conducting air-core toroids consisting of independent coils will be arranged outside the calorimetry. This concept offers almost no constraints on calorimetry and Inner Detector allowing noncompromised technological solutions and a high-resolution, large-acceptance and robust Muon Spectrometer with excellent stand-alone capabilities.

  ATLAS will be 22 m high, 44 m long, and will have a weight of $\sim$ 6000 tons.

  The ATLAS experiment will be explained in greater detail in the next section (see also [ATL:94]), the performance of its Muon Spectrometer is subject of this thesis (see also [ATM:97]).

- **CMS:**
  The CMS (**C**ompact **M**uon **S**olenoid) experiment is based on a single, large, super-conducting solenoidal magnet (14 m long and 3 m inner radius) generating a uniform

magnetic field of 4 T. The choice of a strong field leads to a compact design for the Muon Spectrometer without compromising the momentum resolution up to pseudo-rapidities[1] of 2.5.

CMS will be 14 m high, 20 m long, and will have a weight of $\sim$ 12,000 tons. For more detailed information see [CMS:94].

- **ALICE:**
  It is planned to convert the existing L3 detector into the ALICE (**A** **L**arge **I**on **C**ollider **E**xperiment) experiment to investigate Pb-Pb collisions. This heavy-ion detector will be used to study physics of strongly interacting matter at extreme energy densities. For more detailed information see [ALI:95].

- **LHCb:**
  This dedicated B physics experiment at the LHC will be built in the DELPHI pit. It is an open-geometry forward collider detector which is designed to fully exploit the B physics potential of the LHC. The large Lorentz boost of accepted B-mesons allows precise decay-time measurements, which are complemented by excellent particle identification and efficient muon triggers. For more detailed information see [LHC:98].

The most important benchmark processes for the general-purpose experiments at LHC (ATLAS and CMS) are the different Higgs-decay channels for a Higgs-mass range from 80 GeV/c^2 to 1 TeV/c^2. Besides a large acceptance and maximum η coverage, very good electromagnetic calorimetry for electron and photon identification, efficient missing E_T calorimetry and a high four-lepton-mass resolution – requiring a high-resolution Muon Spectrometer – are necessary to be able to discover the Higgs in its entire mass range. In general, these properties will allow to explore the full discovery potential of the LHC.

[1]The pseudo-rapidity η is defined as $\eta \equiv -\ln\tan(\theta/2)$, where θ is the polar angle with respect to the beam line.

1.4 The ATLAS Detector

The ATLAS collaboration proposes to build a general-purpose proton-proton detector which is designed to exploit the full discovery potential of LHC [ATL:94]. The collaboration submitted a Letter of Intent in 1992, a Technical Proposal in 1994 and **T**echnical **D**esign **R**eports (TDRs) for each subsystem including most of the final specifications. Construction started in 1998 and the experiment should be ready for the start of LHC in 2005. Figure 1.6 shows a 3D view of the final design of the whole ATLAS experiment.

As pointed out in Section 1.3, many of the interesting physics questions at the LHC require high luminosity. A variety of signatures is important to achieve robust and redundant physics measurements with the ability of internal cross checks. The goal to exploit the full physics potential of LHC and the requirements introduced in Section 1.3 lead to the following basic design considerations:

- very good electromagnetic calorimetry for electron and photon identification and measurements, complemented by hermetic jet and missing E_{T} calorimetry;
- efficient tracking at high luminosity for lepton-momentum measurements, for b-quark tagging, and for enhanced electron and photon identification, as well as τ and heavy-flavor vertexing and reconstruction capability of some B-decay final-states at lower luminosity;
- stand-alone, precision muon-momentum measurements up to highest luminosity, and very low-p_{T} trigger capability at low luminosity;
- large acceptance and maximum η coverage.

1.4.1 The Inner Detector

The ATLAS Inner Detector is shown in Figure 1.7. It combines high-resolution detectors at inner radii with continuous tracking elements at outer radii, all contained in a solenoidal magnet with a central field of 2 T. For more detailed information see [ATI:97].

The silicon-pixel vertex-detector consists of three barrel layers of 140 million pixels (each 50 μm in r-φ direction and 300 μm in the direction along the beam line) and four disks on each side between radii of 11 cm and 14 cm aiming for a point resolution of $\sigma_{r,\varphi} = 12\,\mu$m and $\sigma_z = 60\,\mu$m. This high resolution allows to reconstruct the track origin to find secondary decay vertices. The readout chips must withstand over 300 kGy of ionising radiation and over $5 \cdot 10^{14}$ neutrons/cm^2 in ten years of operation.

The silicon strip detectors – **S**emi **C**onductor **T**racker (SCT) – with a pitch of 80 μm are mounted in four barrel layers at radii of 30, 37.3, 44.7 and 52 cm in order to provide four precision measurements per track in the intermediate radial range, contributing to the measurement of momentum, impact parameter and vertex position. The spatial resolution will be $\sigma_{r,\varphi} = 18\,\mu$m and $\sigma_z = 580\,\mu$m.

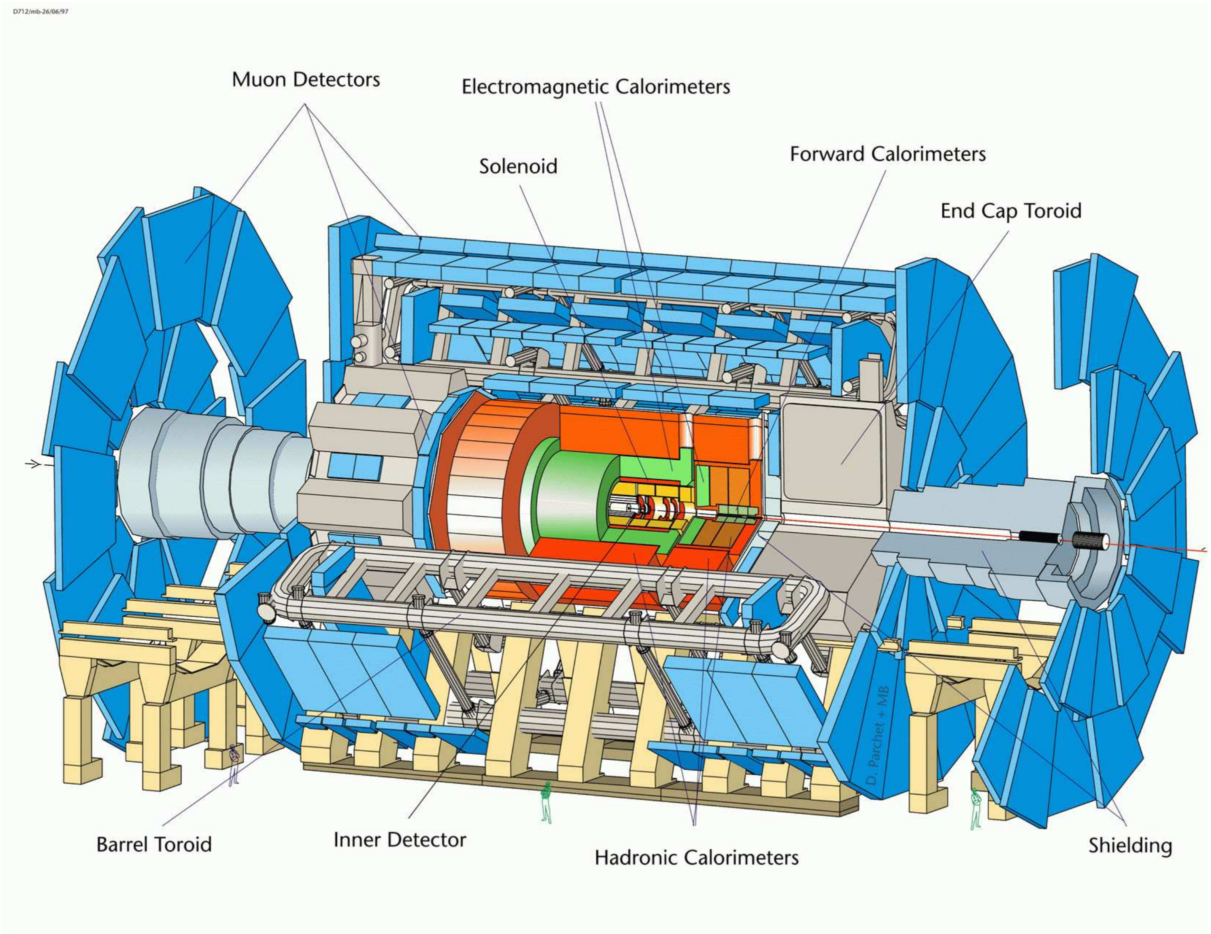

Figure 1.6: *3D view of the ATLAS detector.*

The **T**ransition **R**adiation **T**racker (TRT) consists of 420,000 proportional drift tubes with a diameter of 4 mm. It is divided into a barrel part and several forward wheels. The detector is operated with a $Xe/CF_4/CO_2$ gas mixture optimised for the detection of X-rays created as transition radiation in stacks of thin radiators between the tubes. The single-wire resolution will be 170 μm and the efficiency will be $> 50\,\%$ even for the highest rates (15 MHz). Two different discriminator thresholds will be used to distinguish between tracking hits (only lower threshold) and transition-radiation hits (both thresholds).

1.4.2 Calorimetry

The ATLAS calorimetry is shown in Figure 1.8. It consists of an electromagnetic calorimeter and a hadronic calorimeter. A barrel cryostat around the inner cavity contains the barrel electromagnetic **L**iquid **Ar**gon (LAr) calorimeter and the coil of the solenoid magnet. Two end-cap cryostats enclose the electromagnetic and hadronic end-cap calorimeters as well as the integrated forward calorimeter. For more detailed information see [ATC:96].

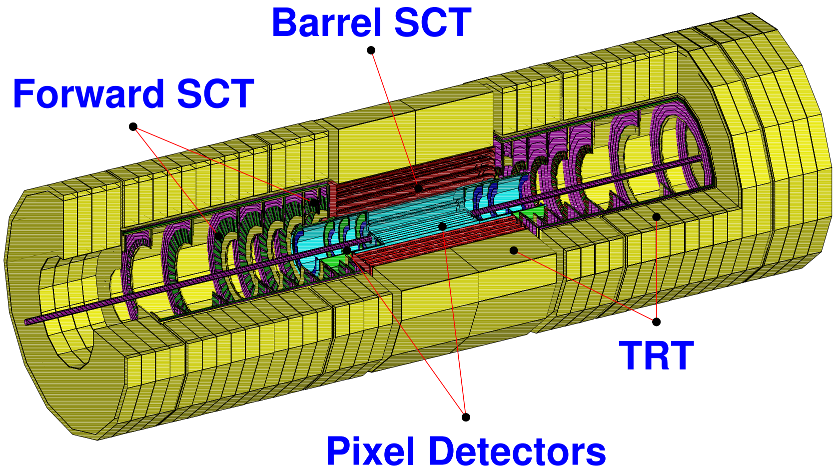

Figure 1.7: *Atlas Inner Detector consisting of a pixel detector system, the SCT and the TRT. The whole Inner Detector has a length of* 6.8 m *and a radius of* 1.15 m.

- **The Electromagnetic Calorimeter:**
The electromagnetic calorimeter is a lead-LAr detector with accordion shaped Kapton electrodes and lead absorber plates over its full coverage[2]. The LAr sampling technique is radiation resistant and provides long-term stability of the detector response, excellent hermiticity, good energy resolutions, and relatively easy detector calibration. The total thickness of the electromagnetic calorimeter is $> 24\,X_0$ in the barrel part and $> 26\,X_0$ in the forward region. The segmentation of the calorimeter will be $\Delta\eta \times \Delta\varphi \approx 0.025 \times 0.025$, aiming for an energy resolution of $\Delta E/E = 10\,\%/\sqrt{E} \oplus 1\,\%$ (E in GeV). The energy-scale precision will be 0.1 % and the measurement resolution of the shower direction in θ will be $\sim 50\,\mathrm{mrad}/\sqrt{E}$ (E in GeV).

- **The Hadronic Calorimeter:**
The barrel hadronic calorimeter will have an inner radius of 2.28 m and an outer radius of 4.23 m. The hadronic calorimeter uses different techniques and devices as best suited for the different requirements and the radiation environment. The total thickness is 11 interaction lengths λ at $\eta = 0$, including $1.5\,\lambda$ of the outer support. In the range of $|\eta| < 1.6$ a sampling calorimeter is used with iron as absorber material and scintillating tiles (3 mm thick) as active material (TILE Calorimeter). The signals produced on both sides of the scintillating tiles are read out by wavelength-shifting fibres into two separate photo-multipliers. The resulting segmentation of the hadronic calorimeter will be $\Delta\eta \times \Delta\varphi \approx 0.1 \times 0.1$. In the range of $1.5 < |\eta| < 4.9$ a hadronic LAr calorimeter is used. The end-cap hadronic calorimeter extends up to $|\eta| < 3.2$ and is a copper-LAr detector with parallel plate geometry. The high-density forward calorimeter covers the region of $3.2 < |\eta| < 4.9$ with the front face about 5 m from the interaction point (high level of radiation). The detector is based on rods filled with LAr in a copper and tungsten matrix. The expected energy resolution for the hadronic calorimeter is $\Delta E/E = 50\,\%/\sqrt{E} \oplus 3\,\%$ for $|\eta| < 3$ and $\Delta E/E = 100\,\%/\sqrt{E} \oplus 10\,\%$ for $3 < |\eta| < 4.9$.

[2]Barrel part: $|\eta| < 1.475$, end-cap parts: $1.375 < |\eta| < 3.2$.

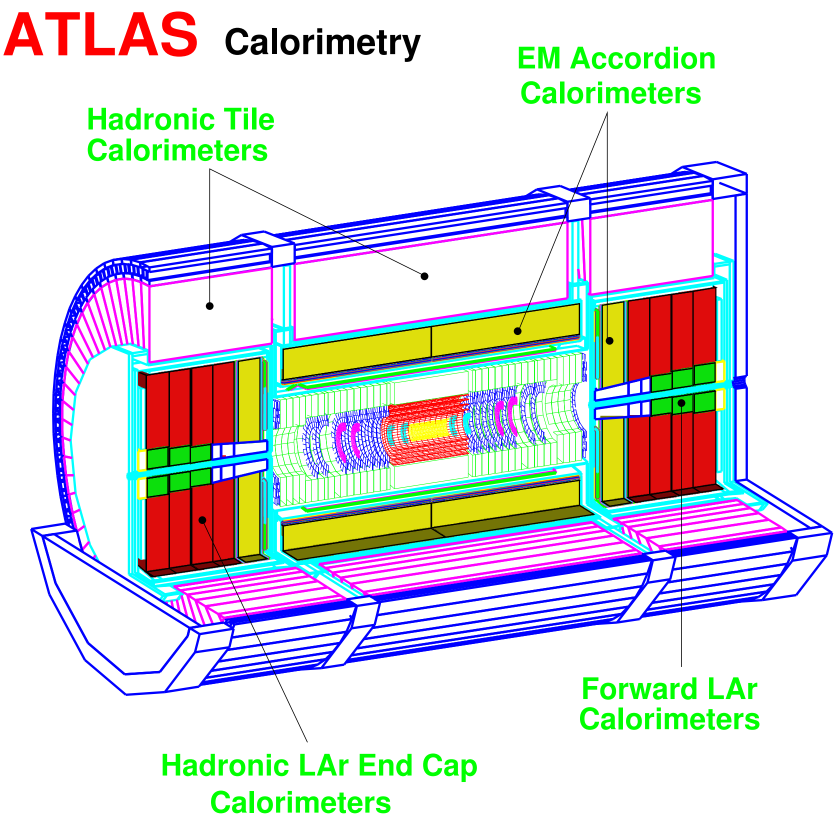

Figure 1.8: *Layout of the ATLAS calorimetry system.*

1.4.3 The Muon Spectrometer

The Muon Spectrometer dominates the size of the ATLAS experiment with its outer diameter of $\sim 22\,\mathrm{m}$. Figures 1.9 and 1.10 show two cuts through the Muon Spectrometer.

The ATLAS Muon Spectrometer is based on the magnetic deflection of muon tracks in a system of three large super-conducting air-core toroid magnets instrumented with separate-function trigger and high-precision tracking chambers. The design and performance of the Muon Spectrometer must satisfy the following requirements:

- the largest possible discovery reach for expected and unexpected new physics, with minimal systematic biases;
- good discrimination against high levels of charged and neutral particle background from minimum-bias events and radiation;
- safe and reliable operation in difficult environmental conditions for the anticipated lifetime of the LHC.

The operational environment of the Muon Spectrometer is described in Chapter 2. The discovery potential of the spectrometer has been optimised on the basis of selected benchmark processes.

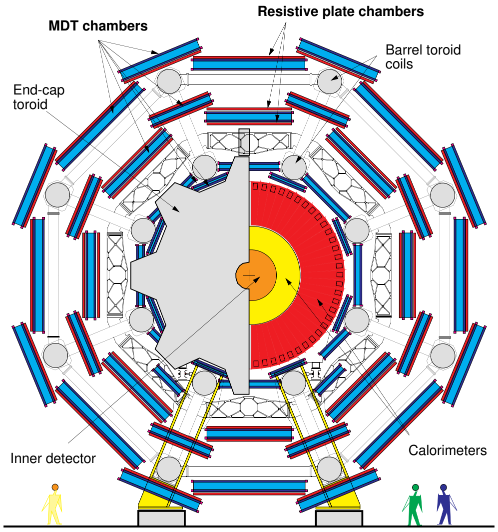

Figure 1.9: *Transverse view of the ATLAS Muon Spectrometer.*

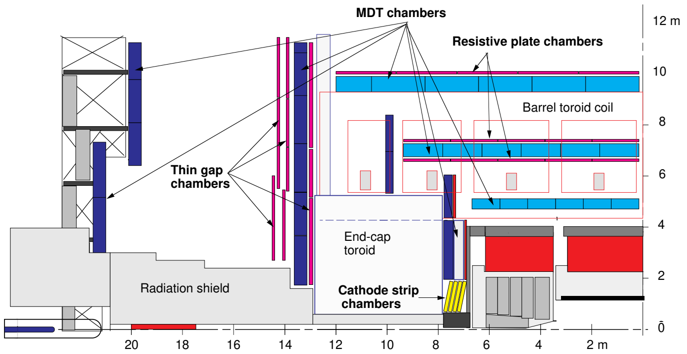

Figure 1.10: *Side view of one quadrant of the ATLAS experiment.*

Based on the discussion from Section 1.3 the important parameters that need to be optimised for maximum physics reach are:

- Resolution: momentum and mass resolutions at the level of 1 % are essential for the reconstruction of narrow two- or four-muon final states on top of high background levels, such as the intermediate-mass Higgs, and for reliable charge identification. A transverse momentum resolution that is constant over the full rapidity range is desirable.

- "Second coordinate" measurement: a measurement of muon tracks in the non-bending projections with an r.m.s spatial resolution of 5–10 mm is required for safe track reconstruction and reliable momentum determination.

- Rapidity coverage of track reconstruction: all physics channels profit from a pseudorapidity coverage up to $|\eta| \approx 3$ and good hermeticity, in particular rare high-mass processes.

- Trigger selectivity: transverse momentum thresholds of 10–20 GeV/c are adequate for high-mass states, which will be in the focus of LHC physics at nominal luminosity. Lower thresholds of $p_{\mathrm{T}} \approx 5\,\mathrm{GeV}/c$ are required for CP violation and beauty physics.

- Trigger coverage: adequate trigger efficiencies can be obtained with a pseudo-rapidity coverage smaller than that of the precision chambers. The actual requirements are mostly determined by processes at the opposite ends of the LHC mass scale: the need for good acceptance for rare high-mass Higgs particles, and the need for very high statistics to study small rate asymmetries due to CP violation in the B sector. A trigger coverage of $|\eta| < 2.4$ is found to be sufficient.

- Bunch-crossing identification: the LHC bunch-crossing interval of 25 ns sets the scale for the required time resolution of the first-level trigger system.

Achieving a resolution $\Delta p_\mathrm{T}/p_\mathrm{T} \approx 10\,\%$ for $p_\mathrm{T} = 1\,\mathrm{TeV}/c$ dictates the combination of the bending power in the central rapidity region, and of the precision with which the muon instrumentation must measure the sagitta of the particles.

Magnet System

The magnet system consists of three air-core super-conducting toroids with an open structure to minimise the contribution of multiple scattering to the momentum resolution. The toroidal design of the magnet system made it possible to provide a high-resolution, large-acceptance and robust stand-alone Muon Spectrometer. A combined optimisation of the magnet-field strength and its radius, constrained by magnet-fabrication costs and by space limitations in the experimental cavern, led to the air-core toroid magnet configuration providing a bending power at $\varphi = 0$ of $\int B\,\mathrm{d}l = 2\,\mathrm{Tm}$ at $\eta = 0$ up to $\int B\,\mathrm{d}l = 9\,\mathrm{Tm}$ at $|\eta| = 2.8$ (see Figure 1.12, the integral is calculated from the inner muon station to the outer muon station). The average toroidal magnetic field will be $\sim 0.5\,\mathrm{T}$. A big advantage of the toroidal magnetic field is the fact that the bending power increases with higher pseudo-rapidities.

The barrel toroid extends over a length of 25 m, with an inner bore of 9.4 m and an outer diameter of 20.1 m. The two end-cap toroids are inserted in the barrel at each end. They have a length of 5 m, an inner bore of 1.64 m and an outer diameter of 10.7 m. Each toroid consists of eight flat coils assembled radially and symmetrically around the beam axis. The barrel-toroid coils are contained in individual cryostats, whereas the eight end-cap toroid-coils are assembled in a single, large cryostat. Figure 1.11 shows a 3D view of the muon magnet system.

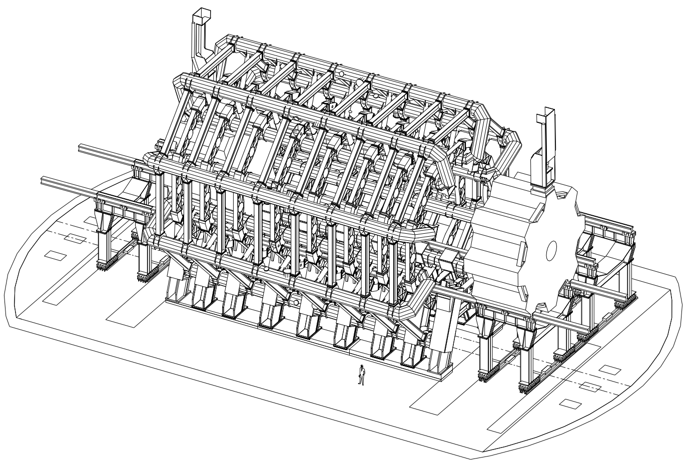

Figure 1.11: *3D view of the super-conducting air-core toroid magnet system.*

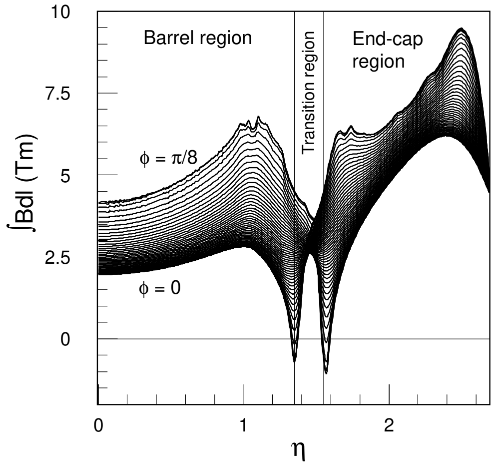

Figure 1.12: *Toroid bending power $\int B\,\mathrm{d}l$ of the azimuthal field component as a function of η.*

Muon Instrumentation

The ATLAS Muon Spectrometer will measure the trajectories of particles at three stations of chambers.

In the barrel ($|\eta| < 1$) they will be arranged in three cylinders concentric with the beam axis at radii of about 5 m, 7.5 m and 10 m. In this η-region the particles are measured near the inner and outer field boundaries, and inside the field volume, in order to determine the momentum from the sagitta.

The end-cap chambers will cover the pseudo-rapidity range $1 < |\eta| < 2.7$ and are arranged in four disks at distances of 7 m, 10 m, 14 m and 21–23 m from the interaction point. In the forward region, for $|\eta| > 1.4$, the magnet cryostats do not allow the positioning of chambers inside the field volume. Instead, the chambers are arranged to determine the momentum with the best possible resolution from a point-angle measurement.

The ATLAS Muon Spectrometer consists of four different chamber technologies:

- **Precision Chambers:**
  For the precision measurement of muon tracks in the principal bending direction of the magnetic field, **M**onitored **D**rift **T**ube (MDT) chambers are used except in the innermost ring of the end-cap inner-station ($2 < |\eta| < 2.7$), where particle fluxes are highest. This thesis is devoted to a detailed study of the performance limits of the ATLAS Muon Spectrometer with the main focus on the MDT system. The layout of the MDT chambers will be explained in Section 1.5.
  In the innermost ring of the end-cap inner-station **C**athode **S**trip **C**hamber**s** (CSCs) are employed (see Figure 1.10). The CSCs are multi-wire proportional chambers with cathode strip readout and with a symmetric cell in which the anode-cathode spacing is equal to the anode-wire pitch. A spatial resolution of 60 μm (r.m.s) has been measured. A transverse coordinate is obtained from the strips parallel to the anode wires, which form the second cathode of the chamber.

- **Trigger Chambers:**
  These chambers will provide the trigger function, the bunch-crossing identification and the measurement of the "second coordinate" (coordinate along the magnetic field line). In the barrel this information is provided by three stations of **R**esistive **P**late **C**hamber**s** (RPCs). They are located on both sides of the middle MDT station, and either directly above or directly below the outer MDT station. These chambers are gaseous parallel-plate chambers with a typical space-time resolution of 1 cm $\times$ 1 ns. Each chamber is made of two rectangular detector layers, each one read out by two orthogonal series of pick-up strips: The η-strips are parallel to the MDT wires and provide the bending view of the trigger detector; and the φ-strips, orthogonal to the MDT wires, provide the "second coordinate" measurement which is important for the off-line pattern recognition.
  In the end-caps, three stations of **T**hin **G**ap **C**hambers (TGCs), located near the middle MDT station will be installed. The TGCs have a structure similar to multi-wire proportional chambers, with the difference that the anode-wire pitch (1.8 mm)

is larger than the cathode-anode distance (1.4 mm). Signals from the anode wires, arranged parallel to the MDT wires, provide the trigger information together with readout strips arranged orthogonal to the wires, that also provide a measurement of the "second coordinate".

1.4.4 The Trigger Scheme

The role of the trigger system is to select bunch crossings containing interesting interactions. The data-acquisition will be able to record events with a rate of ~ 100 Hz (10–100 MB/s). Hence the task of the trigger is to reduce the vast interaction rate of 10^9 Hz to 100 Hz of interesting events.

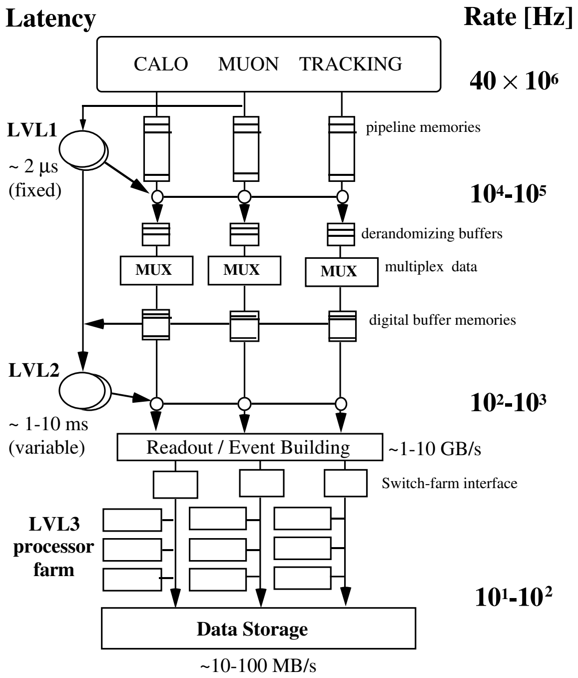

Figure 1.13: *The ATLAS three-level trigger architecture.*

The ATLAS trigger is organised in three trigger levels (LVL1, LVL2 and LVL3) as shown in Figure 1.13. The LVL1 trigger uses reduced-granularity data from a subset of detectors. The LVL2 trigger uses full-granularity, full-precision data from most of the detectors, but examines only regions of the detector flagged at LVL1 as containing interesting information. The LVL3 trigger uses the full event data for the final selection of events for off-line analysis.

The LVL1 trigger accepts data at the full LHC bunch-crossing rate of 40 MHz (every 25 ns). The latency, which is the time to form and distribute the LVL1 trigger decision, is 2 μs and the maximum output rate is limited to 100 kHz by the capabilities of the sub-detector readout systems and the LVL2 trigger. During the LVL1 processing, the data from all parts of the ATLAS detector are held in pipeline memories. The LVL1 trigger must identify unambiguously the bunch crossing containing the interaction of interest and introduce negligible dead-time.

The LVL2 trigger reduces the rate from about 100 kHz after LVL1 to 1 kHz. To minimise the latency, only data from regions of interest, defined by LVL1, are transferred to the trigger processors. Also data from different regions of interest are processed in parallel where possible.

After an event is accepted, the full data are sent to the LVL3 processors via the event builder. At LVL3 a complete event reconstruction is possible with decision times up to about 1 s. The LVL3 system must achieve a data storage of 10–100 MB/s by reducing the event rate and the event size. For some triggers, such as Higgs boson candidates, the full event size of about 1 MB will be recorded.

The ATLAS detector will be a general-purpose proton-proton detector, designed to exploit the full discovery potential of LHC. Its Inner Detector is implemented in three different technologies and will measure the particle tracks in a solenoidal magnetic field. The silicon-pixel vertex-detector, the silicon-strip detectors (SCT) and the TRT will provide the vertex position with a resolution of $\sigma_{r,\varphi} = 12\,\mu$m and $\sigma_z = 60\,\mu$m. The electromagnetic calorimeter (LAr calorimeter) is aiming for an energy resolution of $\Delta E/E = 10\,\%/\sqrt{E} \oplus 1\,\%$ (E in GeV). For the hadronic calorimeter (LAr and TILE calorimeter) we expect a resolution of $\Delta E/E = 50\,\%/\sqrt{E} \oplus 3\,\%$ for a large η range.
The Muon Spectrometer will measure the sagittas of the muon tracks in a toroidal magnetic field with three chamber stations, aiming for a resolution of $\Delta p_{\mathrm{T}}/p_{\mathrm{T}} \approx 10\,\%$ for $p_{\mathrm{T}} = 1\,\mathrm{TeV}/c$. MDTs and CSCs are used as precision chambers, the trigger is provided by RPCs and TGCs.

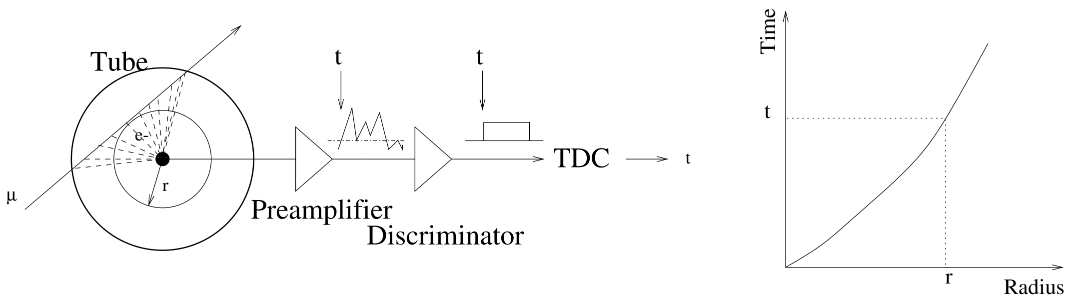

Figure 1.14: *Principle of the MDT operation. The electron-drift time is measured and converted to a distance via a space-time relationship (rt-relation).*

1.5 Muon Precision Drift Chambers

The sagittas of muon tracks are measured by precision chambers in an inner, middle and outer muon station (see also [HES:98]). A muon with $p_T = 1\,\text{TeV}/c$ shows a sagitta of $\sim 500\,\mu$m in an average magnetic field of 0.5 T; thus a momentum resolution of 10 % requires a sagitta-measurement accuracy of $50\,\mu$m. The relative position of the muon chambers in the inner, middle and outer station will be monitored by an optical alignment system. The basic elements of these chambers are Aluminium[3] drift tubes (MDTs) with an outer diameter of 3 cm (wall thickness of $400\,\mu$m) and a $50\,\mu$m central wire (W/Re 97/3, gold-plated 3 % by weight) that is connected to positive high voltage.

1.5.1 The Principle of Operation

The principle of operation is shown in Figure 1.14. A muon crossing the MDT ionises the detector gas along its track, the electrons are drifting towards the wire in the electric field and are multiplied in an avalanche process close to the wire due to the high field. The movement of the electrons and ions induces a current on the wire that is read out at one end of the tube by a current sensitive preamplifier. After discriminating the signal, a **T**ime to **D**igital **C**onverter (TDC) stores the arrival time of the pulse, such measuring the drift time of the ionisation electrons. The drift time is then converted to a distance using the space-time relationship, which will be often referred to as “rt-relation” throughout this work. If the drift velocity depends only weakly on the electric field, the rt-relation is almost linear. Hence we call it a “linear” gas, otherwise we speak of “non-linear” drift gases. The rt-relation is obtained by a so-called auto-calibration procedure [VIE:96, CRE:97]. The detailed analysis of the contributions to the spatial resolution that can be obtained with such a drift tube is discussed in [RIE:97b]. The performance of MDT chambers in a high-rate environment and the dependence on the environmental parameters is subject of this thesis.

The MDT chambers consist of two multilayers separated by a support structure. Each

[3]ALUMAN-100, German DIN norm AlMn-DIN-1700.

multilayer combines three[4] or four[5] layers of tubes (see Figure 1.15). The support structures provide accurate positioning of the two multilayers with respect to each other and mechanical integrity under effect of gravity and temperature. An X-ray Tomograph will be used to check the wire-position accuracy before the chambers are installed [GSC:97]. The MDT in-plane alignment system will monitor the wire displacement[6] in the experiment with an accuracy of 10 μm or better (see Figure 1.15). The 1194 MDT chambers will cover an area of 5500 m^2. The total number of readout channels is 370,000.

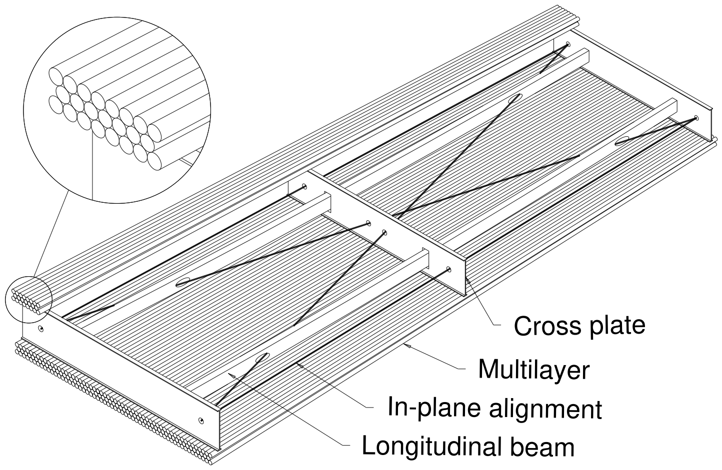

Figure 1.15: *Two multilayers of MDT tubes each consisting of three or four layers are glued to a support frame ("spacer structure") to form a chamber.*

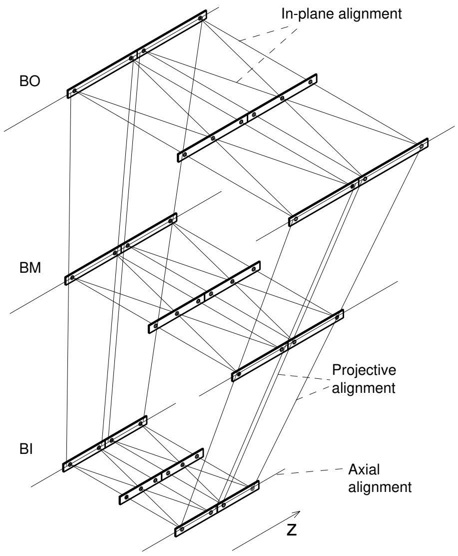

Figure 1.16: *The projective alignment system in the barrel region.*

1.5.2 The Projective Alignment System

The momentum measurement in the Muon Spectrometer will be a sagitta measurement in triplets of precision chambers. The level of accuracy is determined by the spatial resolution of the precision chambers as well as by the exact knowledge of the positions of the chambers with respect to each other. This information will be provided by the projective alignment system.

The arrangement of the light rays for the alignment of barrel towers is shown in Figure 1.16. In this projective layout, and in linear approximation, the correction to the measured sagitta of the muon trajectory is a function of six chamber-displacement parameters. Four laser rays monitored with two-dimensional optical sensors therefore provide for an over-constrained measurement of chamber movements. The projective monitoring is implemented in RASNIK technology [ATM:97].

[4]In the middle and outer station.

[5]In the inner station.

[6]Such displacements are inferred from relative movements of the three cross-plates which are part of the chamber support structure.

In order to control the relative positioning of chamber stations inside each sector, the distance and the direction of the axial laser rays are monitored with silicon sensors mounted on a stiff reference frame.

The optical alignment system must measure the relative position of the inner, middle and outer muon station with an accuracy such that the maximum alignment contribution to the sagitta measurement is $< 30\,\mu$m. Section 8.1.1 introduces briefly some methods of calibrating the alignment system.

1.5.3 Contributions of this Thesis

At the start of this thesis the Technical Design Report for the Muon Spectrometer was in preparation. During this phase and before most of the design-work for the MDTs was done. However, the following major points had no or no final answer:

- **The MDT Drift Gas:**
  At the time of the Technical Design Report the baseline gas was $Ar/N_2/CH_4$ 91/4/5. This drift gas had excellent drift properties (linear space-time relationship, small maximum drift time), but unfortunately showed aging effects already after an accumulated charge of $\frac{1}{5}$ to $\frac{1}{2}$ of the amount that is expected during ten years of ATLAS operation. During the work for this thesis a viable solution was found and established as the new baseline gas (Ar/CO_2 93/7). The space-charge effects at high background rates, which depend on the drift properties of the drift gas were understood and quantified.

- **The Full Analysis of Systematic Effects:**
  The main drawback of Ar/CO_2 93/7 is that the non-linear space-time relationship entails a much stronger dependence on environmental parameters (background radiation, temperature, gas pressure, magnetic field, ...). A full analysis of systematic effects under realistic LHC operating conditions is presented in this thesis. The magnitude of these effects and possibilities to correct for them as well as their impact on the performance of the Muon Spectrometer were investigated and understood in detail.

- **The Front-End Electronics:**
  The high-rate studies showed that one has to correct for the baseline shift at the highest expected background rates. Otherwise the resolution would deteriorate by $\sim 10\,\mu$m. Hence an active circuit for baseline restoration was included into the front-end chip-design. The new baseline gas necessitated another revision of the front-end electronics. Due to the longer maximum drift time and the non-linearity of the space-time relationship of the new baseline gas, the tail cancellation had to be extremely "soft" to avoid multiple hits. Measurements made for this thesis showed this problem and triggered a rethinking of the shaping scheme. In the June 1999 ATLAS week the decision was taken, that bipolar shaping (instead of unipolar shaping with baseline restoration) will be used for the MDT system.

- **The Calibration of the Absolute Mass Scale:**
  The absolute momentum scale (i.e. the absolute mass scale) of the Muon Spectrometer has to be calibrated with an accuracy of $\sim 1\,\%$. This work introduces a method using $Z \rightarrow \mu^+\mu^-$ which can calibrate systematic errors to the magnetic field at the same time as the energy loss in the calorimeters at the 10^{-3} level.

This thesis is devoted to giving the answers to the above mentioned open questions. Chapter 2 introduces the operational environment of the Muon Spectrometer and deduces the requirements for the precision drift chambers. Chapter 3 discusses the means of simulation which were used to make predictions on the performance of various drift gases and finally made it possible to find the new baseline gas. The set-ups for the complete set of measurements which was necessary to test the baseline gas is described in Chapter 4. In Chapter 5 the results of measurements and simulations are presented and the working point is defined. The most important characteristics of the drift gas is the spatial resolution in a wide range of background rates (0–1500 Hz/cm), which is the subject of Chapter 6. Chapter 7 is devoted to systematic errors to the track-position measurement in one tube due to changes of the environmental parameters. Finally, Chapter 8 analyses systematic errors to the momentum measurement and proposes a method to calibrate the absolute mass scale.

The basic elements of the muon precision drift chambers are drift tubes (MDTs) with a diameter of 3 cm and a 50 μm central wire that is connected to HV. Three or four layers of drift tubes will be glued together to one multilayer; two multilayers separated by a spacer will form one chamber. The drift time of electron clusters that are produced by a muon traversing a tube will be measured and translated into a distance between the track and the wire.
The alignment of the three chamber stations in one tower and hence the sagitta corrections will be provided by four laser rays with two-dimensional optical sensors.
This thesis deals with the challenging search for a suitable drift gas and with front-end electronics studies. Furthermore a new method of calibrating the absolute mass scale has been developed.

Chapter 2

Environment and Requirements for the Muon Chambers in ATLAS

2.1 Introduction

In Section 1.3 the detector requirements that are necessary to achieve maximum physics reach were derived from the LHC research program. In Section 1.4.3 those thoughts were translated into requirements for the ATLAS Muon Spectrometer. In this chapter we will introduce the operational environment of the Muon Spectrometer and afterwards concentrate on the requirements for the muon chambers and the single-tube operation. The main performance numbers of the spectrometer are momentum resolution and pattern-recognition efficiency in the given background environment. These numbers define the specifications for the chamber construction and the single-tube operation and set the boundaries for the search for a viable solution.

2.2 Operational Environment

2.2.1 Rate Environment

The high level of particle fluxes in the Muon Spectrometer has a major impact on the design of the whole system. They define parameters such as the rate capability of single tubes and the aging properties, and are one important input for the choice of the baseline gas and the front-end electronics. The background sources in the Muon Spectrometer can be classified into two categories:

- **Primary background:**
  Primary collision products penetrating into the Muon Spectrometer through the calorimeters, which are correlated in time with the p-p interaction. Conventional

sources of primary background are semileptonic decays of light ($\pi, \mathrm{K} \to \mu\mathrm{X}$) and heavy ($\mathrm{c, b, t} \to \mu\mathrm{X}$) flavours, gauge Boson decays ($\mathrm{W, Z}, \gamma^* \to \mu\mathrm{X}$), shower muons and hadronic punch-through. At small $p_\mathrm{T} < 10\,\mathrm{GeV}/c$, the largest source of background are muons from π/K decays in flight; depending on pseudo-rapidity, muons with momenta of 3–6 GeV/c will be absorbed in the calorimeters. At moderate $p_\mathrm{T} > 10\,\mathrm{GeV}/c$, top and Z decays also give a sizeable contribution.

- **Radiation background:**
  Background consisting mostly of neutrons and photons in the 1 MeV range, produced by secondary interactions in the forward calorimeter, shielding material, the beam pipe and machine elements. Low-energy neutrons, which are an important component of the hadronic absorption process, escape the absorber and produce a gas of low-energy photon background through nuclear n-γ processes. This background enters into the spectrometer from all directions and is not any longer correlated in time to the primary p-p interaction. Using the MDTs as an example, typical detection efficiencies for photons are at the level of 1 %, and those for neutrons one order of magnitude smaller. Notwithstanding these low sensitivities, the low energy neutral particle background will dominate the counting rates in most areas of the spectrometer (see Figures 2.1 and 2.2).

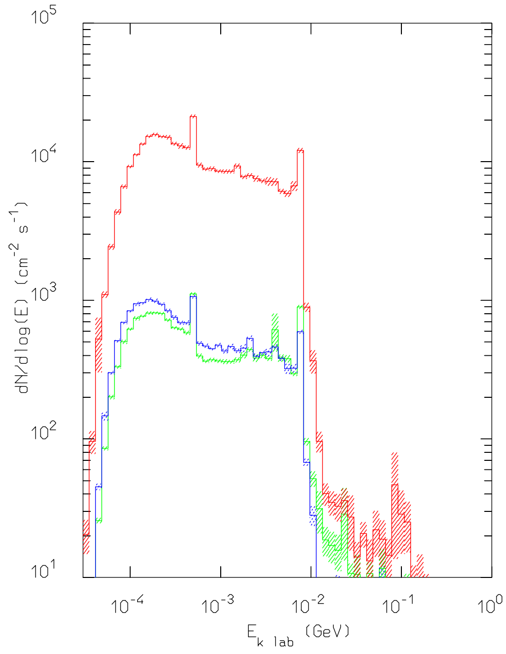

Figure 2.1: *The expected photon flux as a function of photon energy in different regions of the Muon Spectrometer (top curve: $2.3 < |\eta| < 2.7$, middle curve: $1.4 < |\eta| < 2.3$ and bottom curve: $|\eta| < 1.4$).*

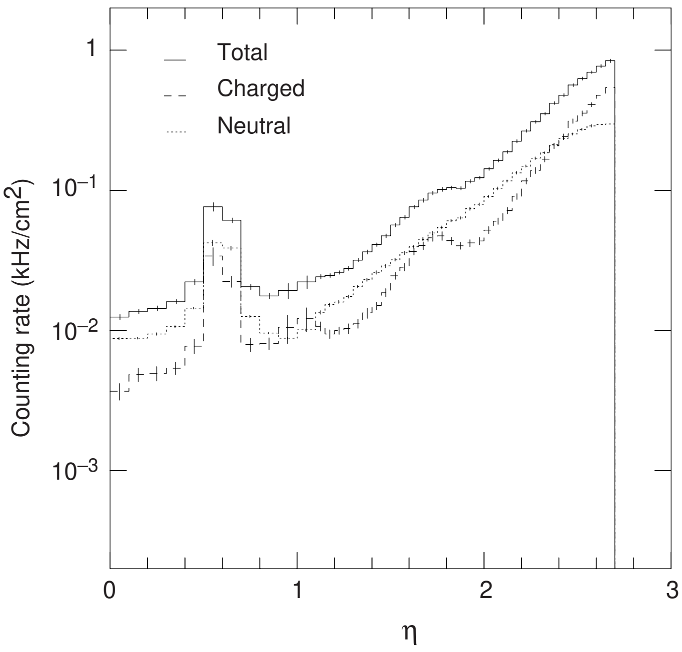

Figure 2.2: *The expected counting rate per cm^2 in the inner muon station. In the inner station the MDT chambers cover a region of $|\eta| < 2$. The detection efficiencies were measured and supplemented with Monte Carlo simulations.*

The neutron and photon fluxes have been computed [BAT:94, FER:95, FER:97] taking into account the material distribution and the magnetic field in the ATLAS detector and the experimental hall. The various mechanisms by which these neutrons and photons induce detectable signals in gaseous detectors are summarised in [ATL:94, Section 4.1.2]. To obtain actual detection efficiencies, two approaches were used: Prototypes were exposed to neutron and photon sources, and the detection efficiency measured at several known particle energies [BAR:94]. These measurements were supplemented with Monte Carlo simulations, reproducing the detailed chamber structures and the calculated neutron and photon-energy spectra. According to these studies, the neutron sensitivity of one MDT is $\sim 10^{-3}$ [ATM:97], and the γ sensitivity in average over our expected photon-energy distribution is measured to be $\sim 4.5 \cdot 10^{-3}$ [BAR:94]. Simulations determined the average energy deposit of a background photon to be $\sim 36\,\mathrm{keV}$ at a magnetic field of 0.6 T [BOY:97].

The uncertainties of the count-rate calculations have been quantified and the following contributions have been identified:

- the combination of the uncertainties attached to the total p-p cross-section and to the multiplicity produced in the primary collisions, is estimated at $\pm 30\,\%$;
- limited knowledge of the showering process in the absorber, and of the (n,γ) cross-sections could conspire to modify the fluences by a factor of up to 2.5;
- the comparison of simulation results and laboratory measurements on chamber sensitivities conservatively suggests that the numbers assumed could be in error by a factor of up to 1.5.

A conservative linear superposition of these uncertainties yields a factor of five. The ATLAS muon instrumentation is therefore designed to operate at a nominal luminosity of $\mathcal{L} = 10^{34}\,\mathrm{cm}^{-2}\mathrm{s}^{-1}$, allowing for a safety factor of five on the background rate.

Consequently the highest background rates for one MDT will be 1500 Hz per cm wire length (tube diameter of 3 cm, factor of five included, see Figure 2.2 at $|\eta| = 2$) or 300 kHz per tube (the length of tubes on the "hottest" spot is $\sim 2\,\mathrm{m}$), respectively. These numbers were the main input for the high-rate tests that were performed in the test beam and are presented in this thesis.

2.2.2 Temperature Environment

Temperature differences in the Muon Spectrometer are estimated to be about 3 K [ATM:97]. For the stability of the MDT operation diurnal temperature variations are of greater importance since they introduce systematic errors to the muon-track-position measurements (see Chapter 7). Such temperature variations in the cavern will be at the level of $\Delta T = \pm 1\,\mathrm{K}$.

Temperature variations induce direct changes of the space-time relationship due to the temperature dependence of the drift velocity and the gas gain. Moreover temperature-induced chamber deformations cause non-concentricities of the wires in the tubes that also represent one source of systematic errors to the position measurement. These effects have been measured and simulated in detail and are presented in Chapter 7.

2.2.3 Vibrations

The spectrum of seismic vibrations in the LEP tunnel has been measured [BAL:93]. The amplitudes are much too small to be of concern.

A more serious problem are vibrations induced by compressors, pumps, liquid helium flow in the toroid coils, air currents, etc.. Initial studies and measurements on LEP detectors and their extrapolation to LHC experiments indicate that vibrational amplitudes of the wire at the level of 10 μm r.m.s cannot be excluded.

> **The Muon Spectrometer will have to operate in a high-rate environment. Background consisting mostly of neutrons and photons in the 1 MeV range will lead to count rates of up to 1500 Hz/cm including a factor five for safety. This translates into count rates of up to 300 kHz per tube.**
> **Temperature variations are expected to be at the level of $\boldsymbol{\Delta T = \pm 1}$ K.**
> **Vibrations of the chamber-support structure might cause wire vibrations at the level of 10 $\boldsymbol{\mu}$m r.m.s.**

2.3 Performance Requirements

2.3.1 Momentum resolution

Physics requirements set the scale for the momentum resolution of about 10 % for the most energetic muons expected at LHC, i.e. muons with a transverse momentum of about 1 TeV/c. Figure 2.3 shows the individual contributions to the momentum resolution in the barrel region of the spectrometer. We see that for low-energy muons the momentum resolution is limited by multiple scattering of the muons in the spectrometer material. For high-energy muons the momentum resolution is limited by alignment errors and the MDT resolution which was assumed to be 80 μm for this simulation.

2.3.2 Reconstruction Efficiency

Another important performance number connected with the muon chambers is the pattern-recognition efficiency, i.e. the efficiency to reconstruct muon tracks correctly. The high background levels resulting in large chamber occupancies (up to 16 % for a maximum drift time of 700 ns) and hit rates (up to 300 kHz per tube), put severe requirements on the single-tube efficiency and rate capability. The occupancy is defined as the fraction of time where the MDT is occupied by an event i.e. the MDT is not able to measure a muon track. This number, which directly influences the pattern-recognition efficiency is the main argument for a fast drift gas. Figure 2.4 shows the pattern-recognition efficiency and the fake-track

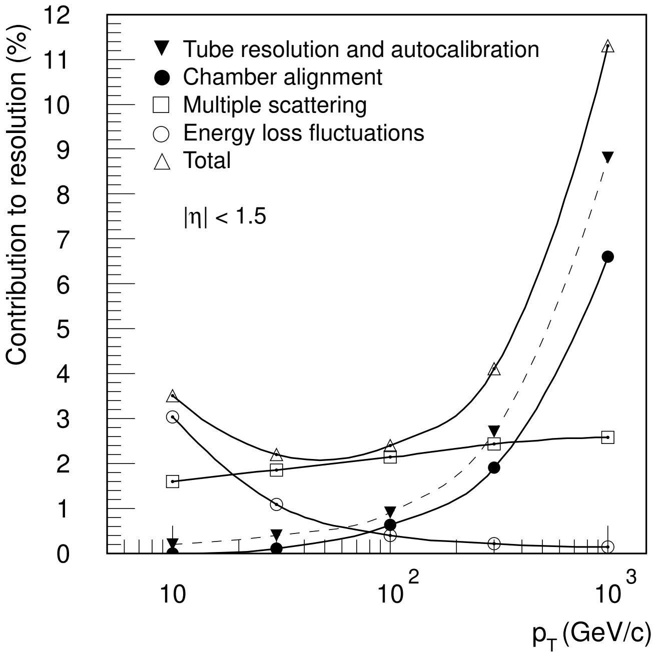

Figure 2.3: *Individual contributions to the muon momentum resolution as a function of* p_T*. The average single-wire resolution was assumed to be* $80\,\mu$m.

rate (number of wrongly reconstructed tracks) for different background levels and layout schemes. The simulation was done assuming a maximum drift time of 480 ns and an MDT hit efficiency of 99 %, where hit efficiency is defined as the MDT efficiency in absence of any correlated (i.e. above all no δ-electrons) or uncorrelated background particles. The 3σ-efficiency[1] was 84 % for background level 5. However, the pattern-recognition efficiency for high background rates depends crucially on the maximum drift time. The baseline gas Ar/CO_2 93/7 has a longer maximum drift time than assumed in the simulation shown in Figure 2.4.

2.4 Chamber Construction

From the performance requirements, which were discussed in the previous section, requirements for the chamber construction have been derived. A detailed description of the chamber construction is presented in [ATM:97], and results on the achieved accuracy are reported. Here, I want to summarise the mechanical requirements for the production of the MDT precision chambers, that are necessary to reach the desired precision of the momentum resolution.

The MDT chambers consist of two multilayers each combining three or four layers of tubes. Three cross-plates and two long-beams form the support structure (spacer structure) which separates and supports the two multilayers (see Figure 1.15).

[1]For a definition of the 3σ-efficiency see Section 5.6.

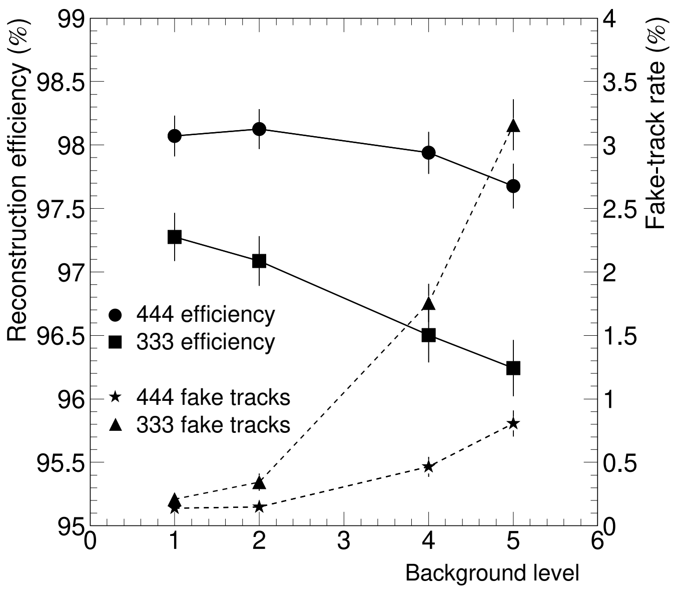

Figure 2.4: *Pattern-recognition efficiency as a function of the background level. A background level of five refers to a safety factor of five on top of the nominal background rate derived from simulation. "444" indicates a chamber configuration with four layers of tubes per multilayer, "333" indicates three layers.*

The individual chamber parts have to fulfil the following requirements:

- The elements of the spacer structure are three cross-plates and two long-beams connecting the cross-plates. The distance between the tube centre and the wire has to be less than $100\,\mu$m r.m.s over the whole tube length to limit the deviations from the ideal rt-relation (see Chapter 7). Therefore the spacer frame must guide the multilayers along the wire trajectories.

- The sag of the wires must be controllable within $10\,\mu$m up to a wire length of 4 m.

- The wires of the chamber must be placed with respect to alignment fiducials with an accuracy of $20\,\mu$m.

- The internal optical alignment system mounted on the spacer structure must monitor the displacement of the middle cross-plate due to temperature gradients at the few micron level.

- The leak rate for a single tube must be $< 10^{-8}$ bar l/s.

- The wire tension (350 g) must have an r.m.s of < 7 g.

- The wire of a single tube has to be positioned to $10\,\mu$m r.m.s (in projection) with respect to the outer tube wall at a few designated positions along the tube axis.

2.5 Single-Tube Operation

The performance requirements that have been described in Section 2.3 translate into requirements for all the individual parts of the system. Here, I want to summarise the prerequisites for the single-tube operation which contribute to the momentum resolution and the reconstruction efficiency. However, the system performance obviously also depends on system aspects such as the performance of the alignment system, the calibration of the energy loss in the calorimeters and the calibration of the magnetic field. Chapter 8 deals with such system aspects.

2.5.1 Prerequisites for an Excellent Momentum Resolution

Spatial Resolution

The single-tube resolution is directly connected to the momentum resolution for high energy muons. The requirement is an average spatial resolution in a single tube of $80\,\mu$m. One can arrive at such resolution levels by using gases with low diffusion coefficients and/or high gas pressure. Also a low threshold level or a high gas gain improve the resolution. Therefore the electronics-noise level plays an important role since the threshold level has a lower limit of approximately $5 \times \sigma_{\text{noise}}$ to avoid spurious noise hits (for noise measurements see Chapter 5).

At high background rates space-charge effects and electronics effects degrade the resolution significantly. Those effects have been studied and understood in detail (see Chapter 6). In order to achieve a spatial resolution of $80\,\mu$m even in the “hottest” regions of the detector, specially designed front-end electronics with baseline restoration or bipolar shaping had to be developed. The background rate also imposes limits on the drift properties of a drift gas because the background-induced resolution deterioration grows with the non-linearity of the space-time relationship. Hence one prefers linear drift gases.

The single-tube spatial resolution also has a small impact on the pattern-recognition efficiency since with degraded resolution the reconstruction of fake tracks becomes more probable.

B-Field Dependence of the Space-Time Relationship

The drift of the electrons is affected by the magnetic field, so we have to use different space-time relationships in different magnetic-field regions of the detector. We derive the rt-relation by a so called “auto-calibration” procedure [VIE:96, CRE:97]. For this procedure we have to use the tracks from a certain region of a chamber, so if the magnetic field changes a lot over this region we only derive an average rt-relation and the resolution decreases. To minimise this effect one prefers a gas where the space-time relationship has a weak dependence on the magnetic field. Usually slow drift gases show a smaller B-field dependence than faster ones (see Chapter 5).

Systematic Errors to the Space-Time Relationship

The drift velocity v_{D} is a function of $\frac{E}{\rho}$. Hence environmental changes that influence either the electric field E or the gas density ρ affect the drift velocity in a tube and consequently the rt-relation. If the rt-relation changes after auto-calibration, the momentum resolution degrades, because systematic errors to the track-position measurement occur. Chapter 7 discusses the reasons and the impact of such systematic errors to the rt-relation. In linear drift gases the drift velocity v_{D} depends only weakly on the quotient $\frac{E}{\rho}$. Therefore linear drift gases show higher operational stability and hence are clearly preferred.

Strong variations of the rt-relation caused by big changes of the environmental parameters will degrade also the reconstruction efficiency.

Wire Vibrations

Some causes of vibrations of the MDT system have been briefly described in Section 2.2.3. Such vibrations of the support structure can cause wire vibrations. A second reason for wire vibrations is the stochastic repulsion of the wire by positively charged ions created in the avalanche.

Since the wire-location precision has to be 20 μm r.m.s wire vibrations should be significantly smaller. If necessary, relatively simple damping discs will be implemented as integral parts of the MDT chamber mounts.

For highest possible momentum resolution one would prefer a slow and linear drift gas with a low diffusion coefficient.
Fast, but also low-noise (low threshold) read-out electronics is desired.
For high background rates baseline restoration or bipolar shaping is necessary.

2.5.2 Prerequisites for a High Reconstruction Efficiency

MDT Efficiency

The reconstruction efficiency is linked directly to the MDT efficiency. We distinguish two kinds of efficiencies:

- **Hit Efficiency:**
  The requirement is a hit efficiency of $> 99\,\%$. That means that in more than $99\,\%$ of the cases a drift tube gives a hit once a muon has been traversing the tube. Even for the highest background rates and large baseline shifts the hit efficiency was always

measured to be well above 99.5 %; without baseline shift the hit efficiency was around 99.95 % (see Section 5.6). This fact helps the pattern recognition significantly since it can almost be excluded that a muon traversed a tube which did not show a signal. To improve this kind of efficiency the threshold level has to be lowered. Since the threshold level has a lower limit at $5 \times \sigma_{\text{noise}}$ the noise level has to be kept on a minimum level. Noise measurements show that the first chamber prototypes showed a noise level very close to the theoretical minimum (see Chapter 5).

- **3σ-Efficiency:**
  The 3σ-efficiency is the probability, that the trajectory of a muon traversing the tube is measured with an accuracy better than three times the resolution. For a more detailed discussion see Section 5.6. Since the occupancy is responsible for the degradation of the 3σ-efficiency with rate, fast drift gases and front-end electronics schemes with short dead-times are preferred.

The MDT efficiency also has a certain impact on the momentum resolution since it determines how many tubes can be used for the track fit.

Afterpulsing Behaviour

Afterpulses are secondary hits occurring after a muon signal with a delay of equal or bigger the maximum drift time (see Section 5.4). Afterpulses are a sign for incomplete quenching behaviour of the drift gas. If they become frequent they can reduce the pattern-recognition efficiency due to additional "noise" hits. They also contribute to the occupancy. An afterpulsing rate at the one percent level is still tolerable.

Multiple Hits

If one muon event gives multiple hits[2], the information, which one of them corresponds to the leading edge, is lost. Hence the reconstruction efficiency decreases. Furthermore there is an upper limit of hits given by the TDC LVL1 buffer. Once this buffer is full, additional hits will be lost. Therefore front-end electronics providing only one hit per muon will be used (see Chapter 5 and [ALE:99b]).

From the point of view of reconstruction efficiency one would suggest a fast and linear drift gas with good afterpulsing behaviour.
The front-end electronics has to provide only one hit per signal without introducing long dead times. Furthermore, low-noise front-end electronics is required.

[2]I.e. the muon signal causes more than one threshold crossing (hits), see Section 5.5.

2.5.3 Prerequisites for a High System Stability

MDT Aging

The high background rates and the aim for good momentum resolution are the driving considerations for the MDT operation requirements. One of the biggest concerns is the possible degradation of the drift chamber performance due to large amounts of charge deposit on the wire. Assuming the rates given above together with a gas gain of 2×10^4 we expect a charge deposit of 0.6 C per cm of wire for ten years of high luminosity LHC running (including a safety factor of five). Such a high amount of charge can cause aging effects resulting from deposits of various kinds on the wire and the cathode. These deposits can either reduce the MDT performance or even completely destroy a tube. To minimise these effects we want to operate the chamber at the lowest possible gas gain that is still compatible with our requirements on resolution. The aging problem also puts severe constraints on the choice of gas and construction materials.

It has been found in extensive aging studies that gas mixtures containing hydrocarbons (e.g. CH_4) produce thin deposits on the wire and on the cathode which affect the performance (aging). Up to now no linear drift gas without organic compounds has been found, although some gases with CF_4 come close. The baseline gas (Ar/CO_2 93/7) shows no aging but is rather non-linear [SPE:97].

Streamer Rate

Streamers produce up to 100 times bigger charge deposits on the wire than proportional signals. In order to keep the charge deposit low, the streamer rate has to be smaller than 1 % (for streamer-rate measurements see [BOY:95]). A high streamer rate is due to incomplete quenching behaviour of a drift gas.

Extensive aging studies give evidence that compounds like CH_4 accelerate tube aging. Up to now no appropriate linear drift gas without organic compounds has been found.

2.6 Searching for a Viable Solution

All the conditions for a stable and high-performance MDT system have to be taken into account for the choice of the front-end electronics and the drift gas. It has been shown that some of the requirements are even contradictory (e.g. slow versus fast drift gas). Since many of the single-tube performance requirements depend on the background rate, a detailed study and understanding of the high-rate behaviour of drift tubes plus its readout electronics was necessary. The search for a suitable new baseline gas was triggered by aging results. The former baseline mixture ($Ar/N_2/CH_4$ 91/4/5) showed strong aging damage at already $\frac{1}{5}$ to $\frac{1}{2}$ of the charge deposit which is expected during ten years of ATLAS operation [SPE:97]. Only gas mixtures not containing organic compounds did not show aging effects.

Measurements with a prototype chamber in a high-rate environment (X5, GIF, see Chapter 4) made a profound understanding of different high-rate effects possible. The results allowed an accurate description of the high-rate performance of drift tubes, which was implemented into GARFIELD [VEE:98], a program to simulate the response of drift chambers.

Since the spatial-resolution requirement of $80\,\mu$m seemed to be the most important and maybe tightest limit in a high-background environment, the resolutions of different drift gases were simulated and optimised. It was found in the simulation that the non-linear Ar/CO_2 gas mixtures are compatible with the $80\,\mu$m limit. In a second step, the maximum drift time was minimised by reducing the CO_2 content. It is well known that CO_2 in this mixture is crucially needed as quenching gas. Unfortunately, effects of incomplete quenching behaviour (afterpulsing rate and streamer rate) could not be predicted by the simulation.

The predictions of the simulations were confirmed by measurements (GIF). Several Ar/CO_2 mixtures were tested and the optimum compromise between afterpulsing rate and maximum drift time was found: Ar/CO_2 93/7 was established as baseline gas.

Now the different systematic errors to the track-position measurement which were imposed by the non-linearity of the drift gas had to be understood quantitatively. Again, measurements and simulations showed very good agreement. It was shown that the biggest effects can be corrected for, even though this of course translates into a loss of robustness of the system.

All the measurements and simulations done to arrive at this complete understanding of high-rate effects and systematic effects are described in this thesis.

The choice of a rather slow and non-linear gas as baseline gas had also a big impact on the front-end electronics design. To avoid multiple hits, bipolar shaping with fixed dead time was found to be the most robust and practical solution.

Chapter 3

Detector-Physics Simulation

3.1 Introduction

The simulation of the detector response to charged particle tracks without high-rate effects was already discussed in detail in [RIE:97b]. This chapter gives a quick overview over the different methods used in drift-tube simulation. The work presented here served as a basis for the simulation of the drift-tube performance at high background rates.

Three programs were used for simulating the response of the MDT to charged particle tracks: HEED [SMI:95], MAGBOLTZ [BIA:98] and GARFIELD [VEE:98]:

- The HEED program computes in detail the energy loss of fast charged particles in gases, taking δ-electrons and optionally multiple scattering of the incoming particle into account. The program can also simulate the absorption of photons through photo ionisation in gaseous detectors.

- The MAGBOLTZ program computes electron-transport parameters for a large variety of gases and mixtures of gases. The program is based on the numerical solution of the Boltzmann transport equation.

- GARFIELD is a program for the two or three dimensional simulation of drift chambers. It is interfaced to MAGBOLTZ and HEED and computes field maps, electron and ion drift lines, drift-time tables and arrival-time distributions, signals induced on the wires by moving ions and electrons, etc..

Using the programs described above we are able to simulate the detector-physics processes in detail.

3.2 From the Muon Track to the Signal

3.2.1 Ionisation along the Particle Track

The muon interacts electromagnetically along its track, thereby causing ionisation of the detector gas. Since the interactions are independent, the number of interactions per unit of track length is Poisson distributed resulting in an exponential distribution of the distances between the interaction points.

The main interactions liberating electrons are the following:

- The muon ionises a gas atom creating a primary electron that can have sufficient energy to cause gas ionisation itself.
- The muon excites a gas atom which returns to the ground state via one of many possible mechanisms. It can deposit charge in the gas volume by emitting an Auger electron or by emitting a photon which (rarely) itself causes ionisation in that gas via the photo effect.

Since the range of the primary electrons is on average quite small the gas is left with clusters of electron-ion pairs along the muon track. The energy deposit is normally characterised by the number of clusters per unit of length and the number of electrons per cluster. In Ar-based gases at 3 bar gas pressure we find about 100 clusters/cm (calculation with HEED for 100 GeV muons) and typically three ionisation electrons per cluster (see Figure 3.2).

The energy deposited by the muon in the gas volume depends on the muon energy in the characteristic way described by the Bethe Bloch formula (Figure 3.1).

Figure 3.2 shows the number of ionisation electrons created by the primary electrons (cluster-size distribution) as simulated by HEED. Although most of the primary electrons have a very short range, there is a small fraction of very high-energetic electrons (δ-electrons) creating tracks up to a length of several mm.

3.2.2 Drift of the Electrons

The electrons created by the muon along its track drift towards the wire along the electric field lines. The drift of the electrons can be characterised by the drift velocity and the longitudinal and transverse diffusion. These parameters are calculated using MAGBOLTZ. Figure 3.3 shows the electron drift velocity as a function of E/p, where E is the electric field and p the gas pressure at 295 K. Figure 3.4 compares MAGBOLTZ calculations with measurements. We see very good agreement for $r > 4$ mm. At smaller radii the residual distribution is non-Gaussian [DEI:98] due to cluster-position fluctuations (see Section 3.3) and hence the measured drift velocity – obtained by a Gaussian fit to the residual distribution – gets systematically shifted to higher values.

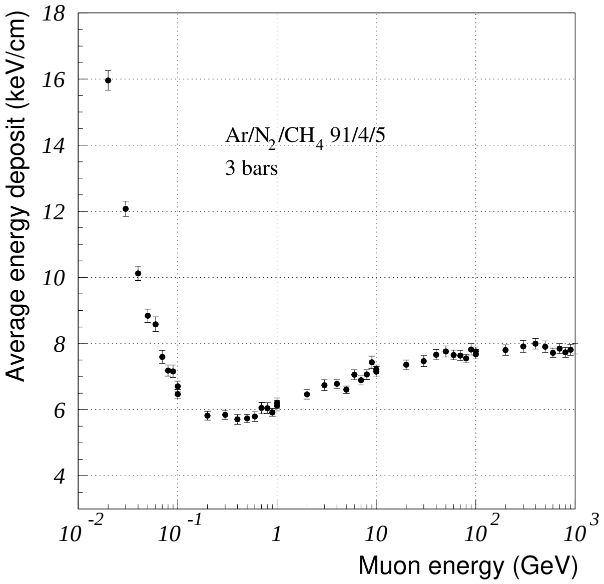

Figure 3.1: *Energy deposited in the gas* $Ar/N_2/CH_4$ 91/4/5 *at a pressure of* 3 bar *absolute for different muon energies, calculated with HEED.*

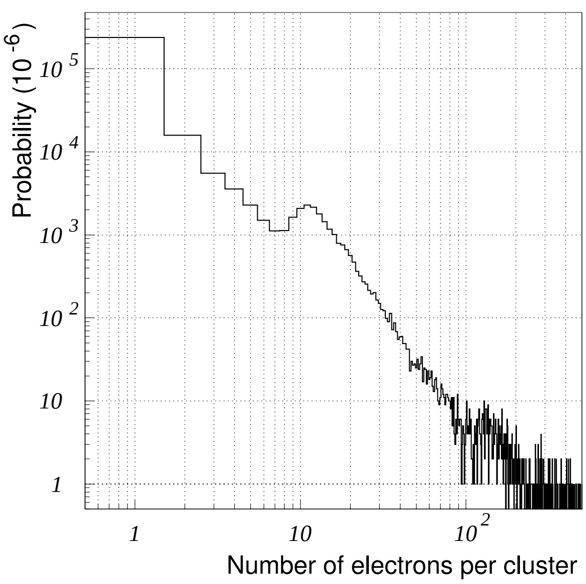

Figure 3.2: *Cluster-size distribution given by HEED, i.e. the number of ionisation electrons liberated by one primary electron.*

$Ar/N_2/CH_4$ 91/4/5 has a drift velocity which depends only weakly on the electric field giving a linear space-time relationship. We call it a linear gas. For Ar/CO_2 the drift velocity depends strongly on the electric field, hence we call it non-linear.

Figure 3.5 shows the longitudinal diffusion as a function of E/p and $T = 295\,\mathrm{K}$. We see that the Ar/CO_2 mixture shows considerably less diffusion compared to the $Ar/N_2/CH_4$ mixture.

In Figures 3.4 and 3.6 the gas gain of $G = 2 \times 10^4$ determined the high voltage on the wire.

3.2.3 The Avalanche Process

As the drifting electrons approach the wire, they gain enough energy to ionise the counting gas and an avalanche process starts. Typical amplification factors used in drift chambers are 10^4 to 10^5. The amplification is a statistical process which for a cylindrical geometry is well described by a Polya [ALK:70] distribution.

$$f(x) \propto x^{\Theta} e^{-(1+\Theta)x} \; , \tag{3.1}$$

where Θ is a parameter between 0 and 1.

MAGBOLTZ calculates the Townsend coefficient, so in principle one can find the gas gain for a given voltage by integrating this coefficient. The Townsend coefficient α describes the

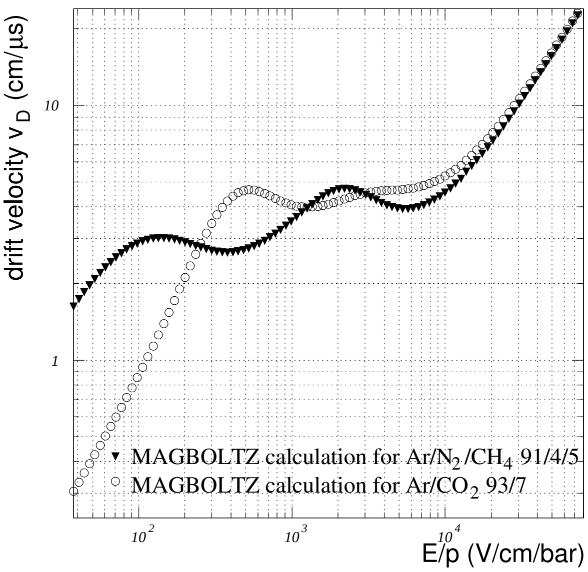

Figure 3.3: *Drift velocity as a function of E/p ($T = 295\,\mathrm{K}$).*

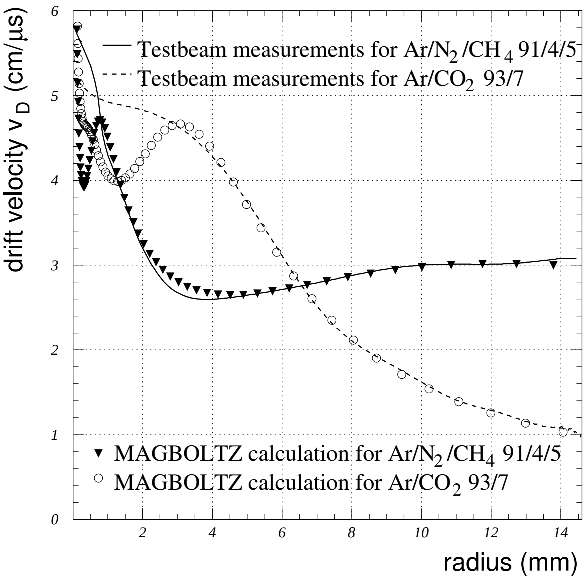

Figure 3.4: *Drift velocity as a function of the radius r (gas gain $G = 2 \times 10^4$).*

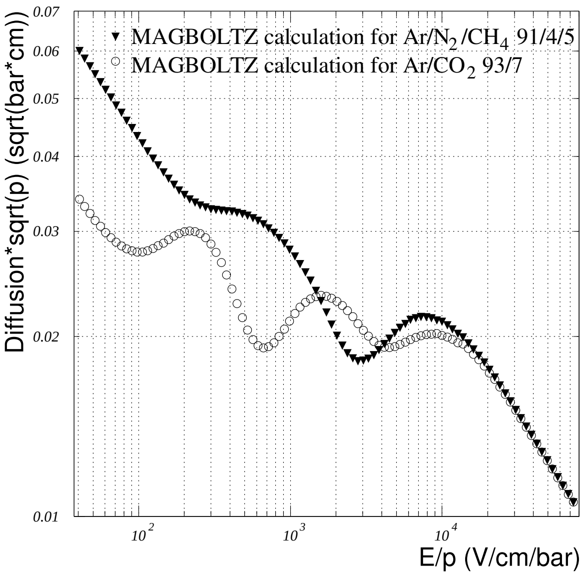

Figure 3.5: *Longitudinal diffusion as a function of E/p ($T = 295\,\mathrm{K}$).*

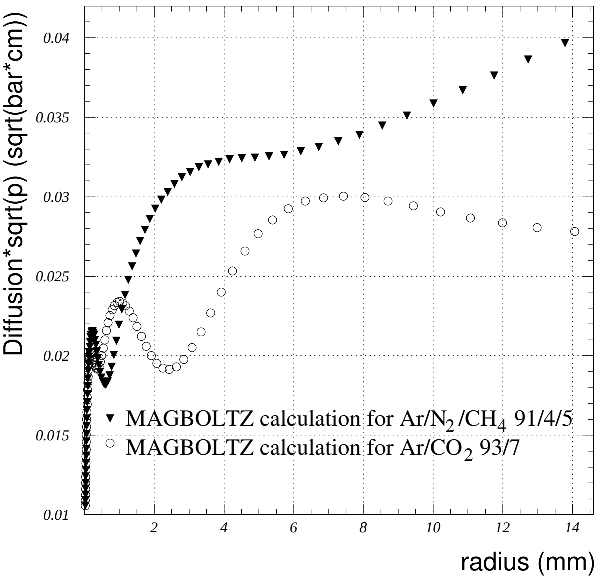

Figure 3.6: *Longitudinal diffusion as a function of the radius r (gas gain $G = 2 \times 10^4$).*

increase in the number of free electrons over a path length dr. This quantity depends in a complicated manner on the electron energy and distribution and thus on the electric field and the gas mixture. The total gas-amplification factor is given by (a is the wire radius)

$$\frac{N}{N_0} = \exp\left[\int_a^{r_{\min}} \alpha(r)\,\mathrm{d}r\right] = \exp\left[\int_{E(a)}^{E_{\min}} \frac{\alpha(E)}{\mathrm{d}E/\mathrm{d}r}\,\mathrm{d}r\right] . \tag{3.2}$$

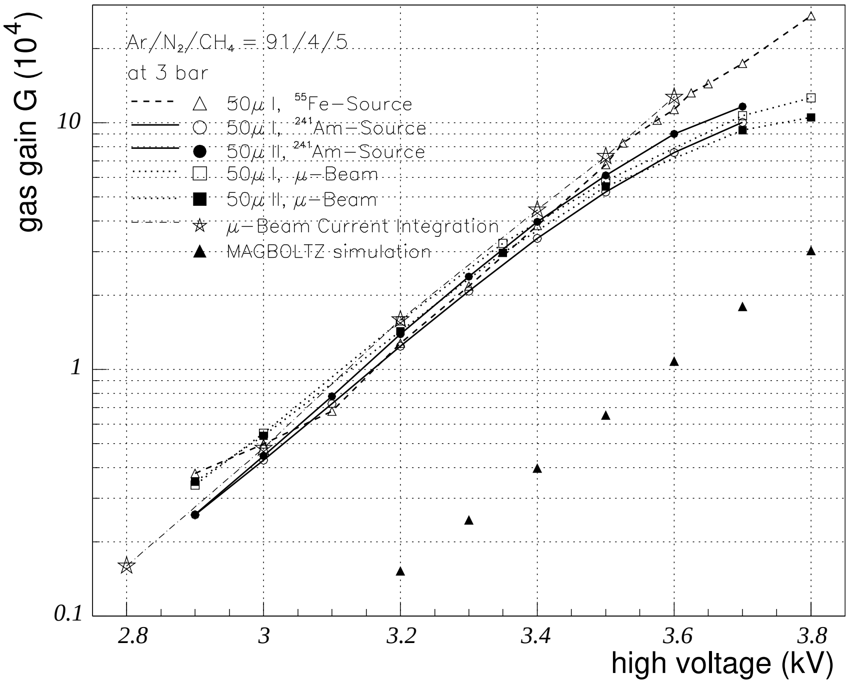

Figure 3.7: *Amplification Factor simulated by MAGBOLTZ compared to measurements* [DEI:96a].

Since the avalanche multiplication is an exponential process, small uncertainties in the Townsend coefficient result in large uncertainties of the gas gain and the theoretical values differ significantly from the measurements (see Figure 3.7). Therefore the amplification factor for a given voltage was taken from measurements and given to GARFIELD as an input parameter. The avalanche simulation in GARFIELD is done by choosing the gain randomly from the given Polya distribution and reconstructing the average avalanche process for each incoming electron.

3.2.4 The Induced Current Signal

The simulation of the induced current signal is the most critical point in the whole simulation chain. The movement of the ions and electrons created in the avalanche induces a current on the wire. Figure 3.8 shows measured values for the ion mobility used for this simulation.

Since close to the wire the electric field varies strongly, the peak of the induced current signal depends strongly on the actual position of the creation of the charge. Also the electric field within the avalanche may be distorted by the surrounding ions.

Detailed studies of the electron and ion part of the signal have been performed in [RIE:97b]. It was found that for the simulation of the spatial resolution it is sufficient to calculate the induced current signal by tracking the ions from the wire surface according to the field-dependent ion mobility. The electron component was neglected. The simulated signal shape was matched to measured signals by adjusting the constants of a pole/zero filter [RIE:97b, Chapter 4].

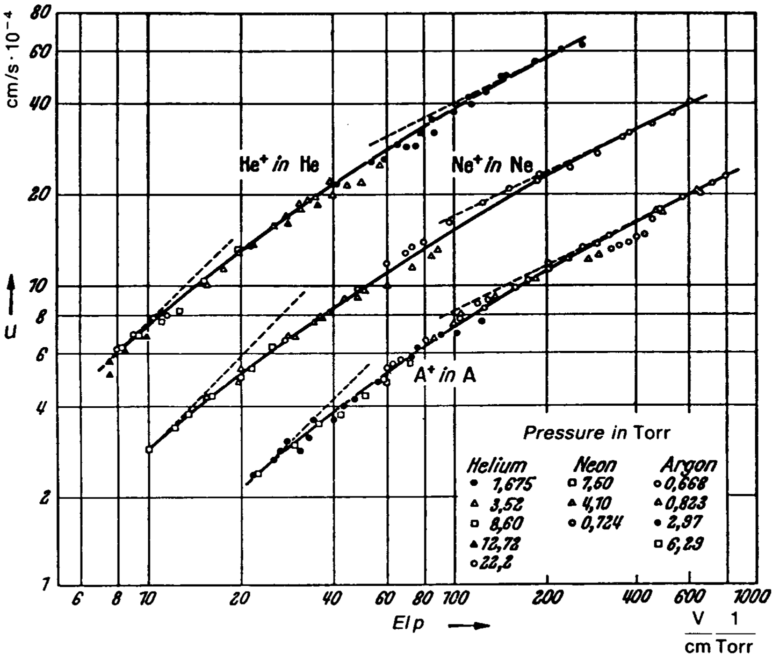

Figure 3.8: *Ion velocities for different gases. For low fields the mobility (slope of the ion velocity) is constant, for high fields it falls off as* $1/\sqrt{E}$ [BLU:93]. *Since we expect* E/p *values of up to* $200\,\mathrm{V}/(\mathrm{cm} \times \mathrm{Torr})$ *the signal shape and the pulse height will definitely be affected by the varying ion mobility.*

3.2.5 Signal Characteristics

According to Ramo's theorem [RAM:39] the current signal induced on an electrode is given by

$$i(t) = -\frac{q}{V} v(t) E(r(t)), \qquad v(r(t)) = \mu E(r(t)) \ , \tag{3.3}$$

where q is the charge moving with a velocity $v(t)$ at a position $r(t)$. Using the expression for a cylindrical field $E(r) = \frac{V_0}{r \ln \frac{b}{a}}$ and assuming a constant ion mobility[1] μ one gets:

$$\begin{aligned} i(t) &= \frac{q}{2 \ln \frac{b}{a}} \frac{1}{t + t_0} \ , \qquad t = 0 \ldots t_{\max}^{\mathrm{ion}} \ , \\ t_0 &= \frac{\ln \frac{b}{a}}{2 V_0 \mu} a^2 \ , \\ t_{\max}^{\mathrm{ion}} &= \frac{\ln \frac{b}{a}}{2 V_0 \mu} (b^2 - a^2) \ , \end{aligned} \tag{3.4}$$

[1]This assumption is true for $r > 100\,\mu$m.

with $b = 1.46\,\mathrm{cm}$ the tube radius, $a = 25\,\mu\mathrm{m}$ the wire radius, $\mu = 0.51\,\mathrm{cm}^2/\mathrm{Vs}$ the ion mobility at 3 bar gas pressure [LAN:57], $V_0 = 3270\,\mathrm{V}$ the wire potential[2] and $t_{\max}^{\mathrm{ion}}$ the maximum ion drift time.

With these equations and the numbers given above one can calculate the parameters:

$$t_0 = 11.9\,\mathrm{ns} \qquad \text{and} \qquad t_{\max} = 4.07\,\mathrm{ms}\,. \tag{3.5}$$

The passage of particles through muon drift tubes was simulated using GARFIELD, MAGBOLTZ and HEED. The full chain from the ionisation along the particle track, the drift of electrons, the avalanche process, the creation of the signal to the processing of the electronics signal was simulated. Apart from the gas gain, which had to be measured, there were no free parameters in the simulation.

3.3 Contributions to the Drift-Tube Resolution at Low Rates

The individual contributions to the drift-tube resolution without background rate have been studied in [RIE:97b]. Simulating the drift-tube response in a way it was described before and switching off individual contributions in the simulation it was possible to study the amplitude of each effect and learn about its impact. The following contributions have been found:

- **Cluster-Position Fluctuations:**
  Since we expect about 100 clusters/cm, their average distance is about $100\,\mu\mathrm{m}$. Close to the wire this can translate into drift-time differences for two tracks at the same distance from the wire depending on the actual position of the clusters. Hence this effect deteriorates the spatial resolution close to the wire.

- **Diffusion:**
  It was found that diffusion has a major impact on the resolution of $\mathrm{Ar/N_2/CH_4}$ 91/4/5. In $\mathrm{Ar/CO_2}$ mixtures the diffusion has only little impact. The difference of the diffusion coefficients of these two gases was already shown in Figure 3.6. Without diffusion the difference in resolution between these mixtures is only due to the different drift velocities (see Figure 3.4).

- **Charge Fluctuations:**
  Charge fluctuations have the biggest effect on the resolution by causing different signal rise times which result in different threshold crossing times. This effect we

[2] This corresponds to a gas gain $G = 2 \times 10^4$ in $\mathrm{Ar/N_2/CH_4}$ 91/4/5 at 3 bar.

call time slewing. Also the reduced resolution close to the wire is due to charge fluctuations. This contribution can be reduced by using faster electronics or lower thresholds. In Chapter 5 a time-slewing correction was tested with test-beam data.

- **Gas-Gain Fluctuations:**
  Gas-gain fluctuations have only a very small effect on the resolution since they are much smaller than charge fluctuations.

- **Noise:**
  Noise affects the resolution directly by causing additional jitter on the threshold-crossing time and indirectly by imposing a lower limit on the threshold, which was chosen to be $5 \times \sigma_{\text{noise}}$ to avoid noise hits. Measurements of the noise level in prototype MDT chambers are presented in Section 5.2.

According to an optimisation in terms of spatial resolution performed in [RIE:97b], the following working parameters have been chosen: the MDTs will work at a gas pressure of 3 bar, a gas gain of 2×10^4 or more and a preamplifier and shaper peaking time of $t_{\text{p}} = 15\,\text{ns}$. The minimum threshold level is $5 \times \sigma_{\text{noise}}$. For the investigations presented in this thesis these parameters are regarded as unchangeable values, since some of them had an impact on the design of the gas system or the chambers themselves. The studies shown throughout this thesis do not have any impact on the chamber construction, but try to optimise the MDT performance by choosing a suitable drift gas and read-out electronics.

The individual contributions to the resolution of drift tubes without background rates were identified: cluster-position fluctuations, diffusion, charge fluctuations, gas-gain fluctuations and electronics noise.

Chapter 4

Creating the High-Rate Environment in the Test Beam

4.1 The Gamma Irradiation Facility

The rate studies described here were made in the **G**amma **I**rradiation **F**acility (GIF) in the SPS beam line X5 (see Figure 4.1).

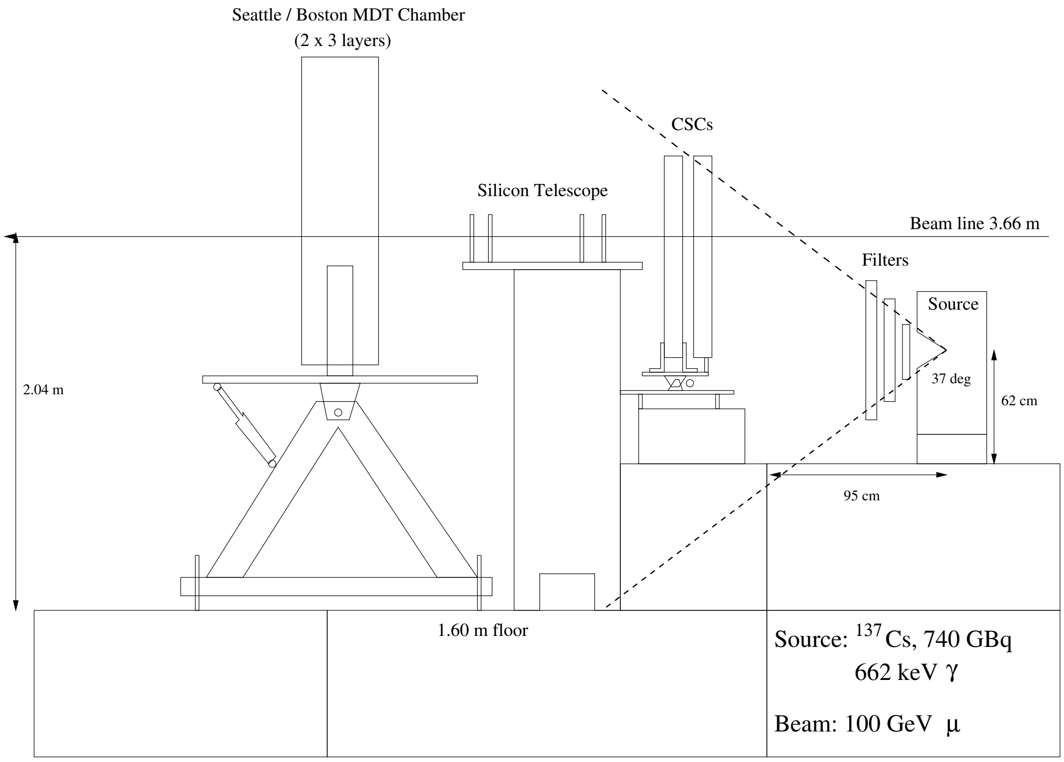

Figure 4.1: *The set-up in the X5-GIF zone.*

This common test facility of the ATLAS and CMS groups has a 100 GeV muon beam and a ^{137}Cs source with an activity of 740 GBq emitting 662 keV γ's, which deposit on average an energy of about 36 keV in our MDTs, and hence simulate well the photon background in ATLAS. The actual γ rate can be adjusted by choosing an appropriate combination of several lead filters.

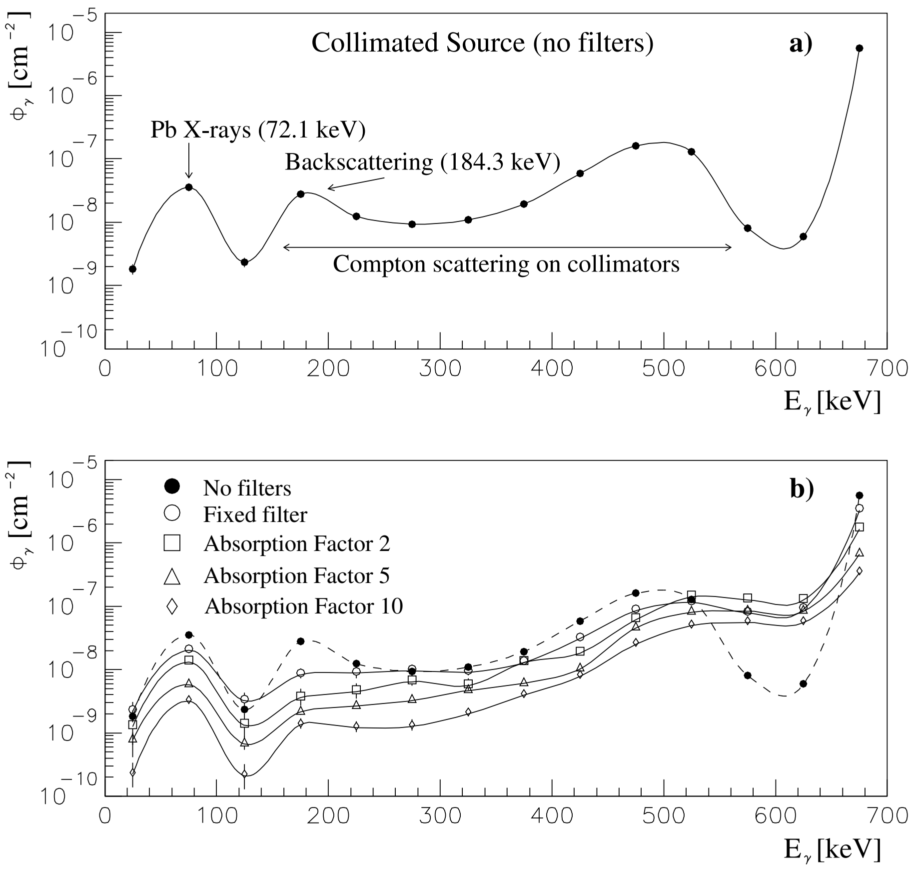

Figure 4.2: *γ spectrum at* 117.4 cm *from the source in free air: (a) Spectral contributions with collimators but without filters. (b) Spectra for different filter configurations.*

Figure 4.2 (a) shows the full γ spectrum of the source with collimators but without any filters [CMS:97]. The dominant contribution is the 662 keV line at the upper limit of the spectrum. At lower energies one sees a continuum due to Compton scattering in the collimators and the 72.1 keV Pb escape peak. Putting filters in front of the source not only attenuates the emission but also smoothens the spectrum by enhancing Compton scattering (see Figure 4.2 (b)).

There is a curved filter permanently fixed in place to flatten the planes of equal γ flux perpendicular to the beam axis. This avoids a lateral dependence of the count rate in the detectors under study. However, as the measured rate profile in Figure 4.3 shows, these collimators are not perfect.

By varying the combination of filters one can obtain attenuation factors ranging between 1 and 300 as indicated in Figure 4.3 above the solid lines. For each curve (filter combination)

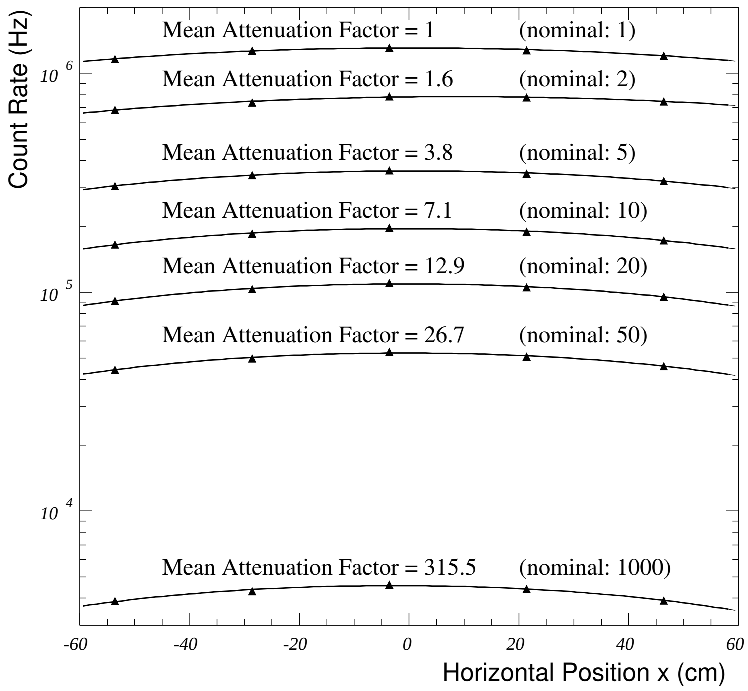

Figure 4.3: *Rate profile along the x-coordinate at $z = 1.72\,\mathrm{m}$ (z-axis parallel to the muon beam, x-axis horizontal). The source is positioned at $x = z = 0$. For the measurement a $6 \times 6\,\mathrm{cm}^2$ scintillator was used. The solid lines represent quadratic fits to the measured points. The true (calibrated) attenuation factors are lower than the nominal ones.*

this mean attenuation A is defined as

$$A = \frac{\frac{1}{L}\int_{x_{\min}}^{x_{\max}} R_{\text{no filter}}(x)\,\mathrm{d}x}{\frac{1}{L}\int_{x_{\min}}^{x_{\max}} R_{\text{filter}}(x)\,\mathrm{d}x}\,, \tag{4.1}$$

where $x_{\min}$ and $x_{\max}$ are the projections of the tube ends onto the plane with $z = 1.72\,\mathrm{m}$ (z-axis parallel to the muon beam, x-axis horizontal), $L = x_{\max} - x_{\min}$ the projected tube length and $R(x)$ the count rate parametrised as shown in Figure 4.3.

All the measurements of the MDT performance presented in this thesis were made in the GIF zone in X5.

The GIF zone has a 100 GeV muon beam and provides a ^{137}Cs source with an activity of 740 GBq, emitting 662 keV γ's. These photons deposit on average 36 keV in our MDTs and are therefore simulating well the photon background in ATLAS. The MDT count rate can be adjusted by choosing different lead filters in front of the source.

4.2 Set-up for the $Ar/N_2/CH_4$ 91/4/5 Measurements

The tubes that we used for these investigations were part of the Seattle/Boston EMS end-cap chamber prototype consisting of two triple layers of drift tubes with a typical length of $\sim$ 2 m. The chamber was installed in the GIF zone in the X5 beam line (see Section 4.1). The tubes were operated with "Datcha Gas" ($Ar/N_2/CH_4$ 91/4/5) at 3 bar pressure and with a gain of $G_0 = 2 \times 10^4$. The discriminator threshold was set to $\sim 5 \times \sigma_{\text{noise}}$ to suppress noise hits, which was about the 25^{th} p.i.e (**p**rimary **i**onisation **e**lectron[1]). The working parameters are summarised in Table 4.1.

Drift Tube Parameters	
inner tube radius	1.46 cm
outer tube radius	1.50 cm
tube length	1.90 m
wire diameter	50 μm W/Re 97/3
gas	$Ar/N_2/CH_4$ 91/4/5
gas pressure	3 bar absolute
gas gain G_0	2×10^4 (3270 V)
maximum electron drift time	480 ns
maximum ion drift time	$\sim$ 4 ms
preamp + shaper peaking time	15 ns
noise level σ_{noise}	4.5 p.i.e (see text)
discriminator threshold	25 p.i.e (see text)
γ-rate per wire length	0 Hz/cm – 1853 Hz/cm
γ-rate per tube	0 kHz – 333.5 kHz

Table 4.1: *Working parameters of the drift tubes.*

The external reference system for the resolution and efficiency measurements was ODYSSEUS [DEI:99], a beam telescope consisting of six Silicon micro-strip detectors with 7 μm resolution each. Four out of the six planes measure the precision coordinate perpendicular to the MDT wires, the other two detectors give us the "second coordinate" parallel to the wires. By extrapolation of the silicon-telescope track to the chamber we get a prediction accuracy of 15 μm.

The silicon detectors cover an area of $5.1 \times 5.1\,\text{cm}^2$. Thus in both multilayers there is a "flower" of seven MDTs lying partly within the window defined by ODYSSEUS. For our purposes we only used the downstream "flower" (see Figure 4.5).

As front-end electronics (see Figure 4.6) we used BNL preamplifiers [BNL:73] and different kinds of shapers which will be explained in Section 4.3.

The signals from tubes n^o 1, 3, 4, 6 and 7 were then split and discriminated with two different thresholds (25 and 100 p.i.e) before being registered by TDCs. The high threshold

[1] One primary ionisation electron as a unit of signal height is defined as the peak of a pulse created by a single ionisation electron.

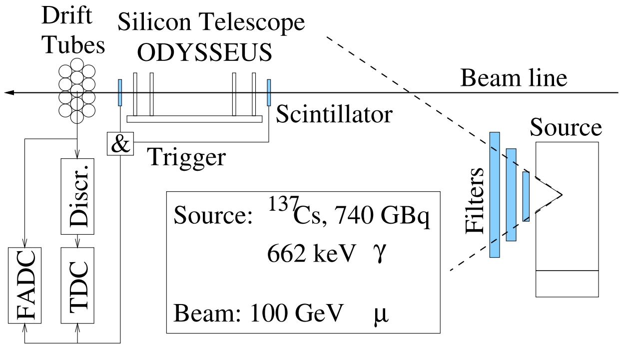

Figure 4.4: *Sketch of the set-up in the GIF zone. Figure 4.5 shows the enlargement of the drift tubes which were read out.*

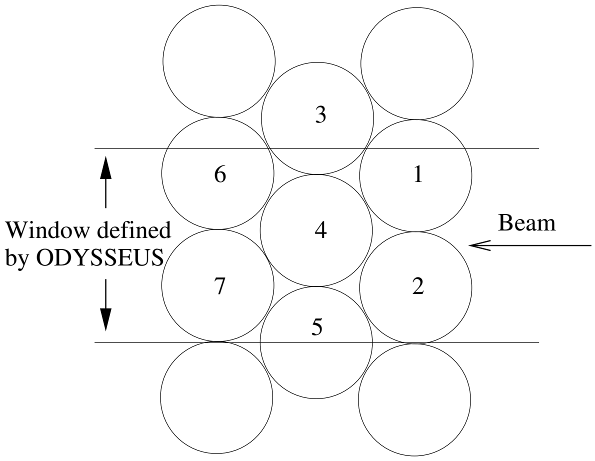

Figure 4.5: *The "flower" of the seven drift tubes in the downstream multi-layer of the Seattle/Boston chamber which were covered by the silicon telescope.*

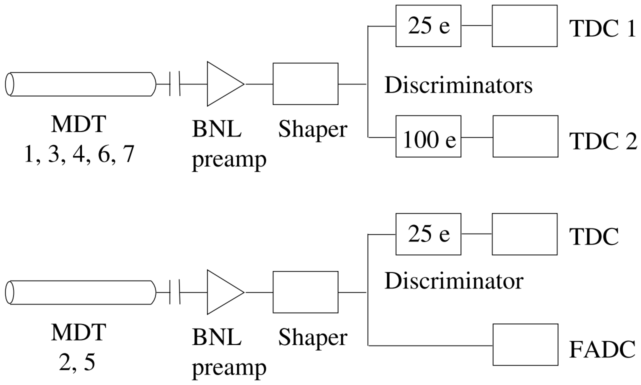

Figure 4.6: *The readout chain of the 7 tubes analysed in this study.*

was used for time-slewing correction and double-track separation studies (see Section 6.1.3 and [ALE:98b]).

The signals from tubes n^o 2 and 5 were also split, but here the second signal half was fed into an FADC (**F**lash **A**nalog to **D**igital **C**onverter) allowing us to look at complete pulse shapes.

The MDT chamber was located in front of the ^{137}Cs source, its distance to the source was ~ 4 m. By choosing different lead filters the background rate was adapted. Although the γ flux of the source should be homogeneous in a plane perpendicular to the beam axis (curved lead filter, see Section 4.1), there is still a slight dependence of the rate on the x-coordinate. At the end of the 1.90 m long tubes the rate is between 84 and 91 % of the rate in the middle (Figure 4.7). Within the beam-centered trigger area of 10 cm width the rate can be considered as being constant.

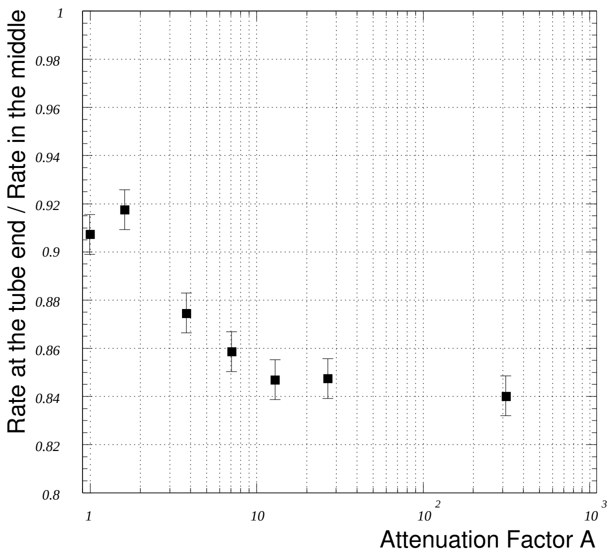

Figure 4.7: *Ratio between the rates at the ends and in the middle of the tubes as a function of the attenuation factor.*

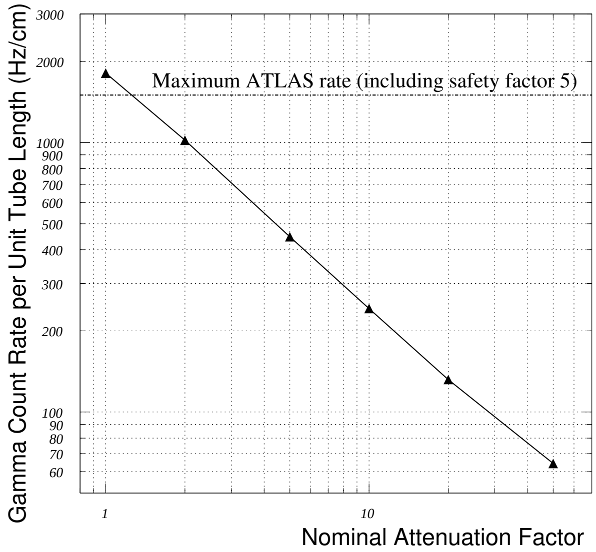

Figure 4.8: *γ count rate per unit tube length as a function of the nominal attenuation factor. The triangles give the rates which are experimentally accessible by an appropriate combination of the lead filters.*

Figure 4.8 shows the γ rate per unit tube length as a function of the attenuation factor. The maximum ATLAS rate of about 1500 Hz/cm (horizontal line) is well within the scope of the X5 set-up.

High-rate measurements have been performed with the Seattle/Boston EMS prototype chamber. The drift gas was $Ar/N_2/CH_4$ 91/4/5 at 3 bar gas pressure. The threshold level was at 25 p.i.e, which corresponded to $\sim 5 \times \sigma_{\mathrm{noise}}$. The gas gain was $G_0 = 2 \times 10^4$. The background rate was varied from 0 to 1853 Hz/cm (high local rate) corresponding to 0 to 333.5 kHz per tube (high rate per tube).

4.3 Signal-Shaping Schemes

In order to investigate the impact of the shaping on the single-tube resolution, three different shaping schemes were applied. Example pulses for each of them are shown in Figure 4.10. The impact of the shaping scheme on high rate MDT performance is mainly determined by the amount of baseline shift (see Section 6.2.1).

On the BNL shapers, consisting in principle of two pole/zero filters in series (each of them behaving as in Equation (4.2)), the time constants τ can be adjusted with potentiometers on the board to give different transfer functions:

$$f(s) = \frac{s + \frac{1}{\tau_1}}{s + \frac{1}{\tau_2}}\,, \qquad \text{with} \qquad \begin{array}{l} \tau_1 = R_1 C \\ \tau_2 = \frac{R_1 R_2 C}{R_1 + R_2} \\ \tau_1 > \tau_2 \end{array} \,. \tag{4.2}$$

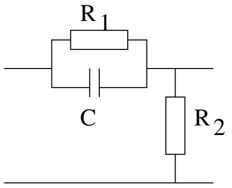

In the first pole/zero filter only R_1 is adjustable, in the second one R_1 and R_2.

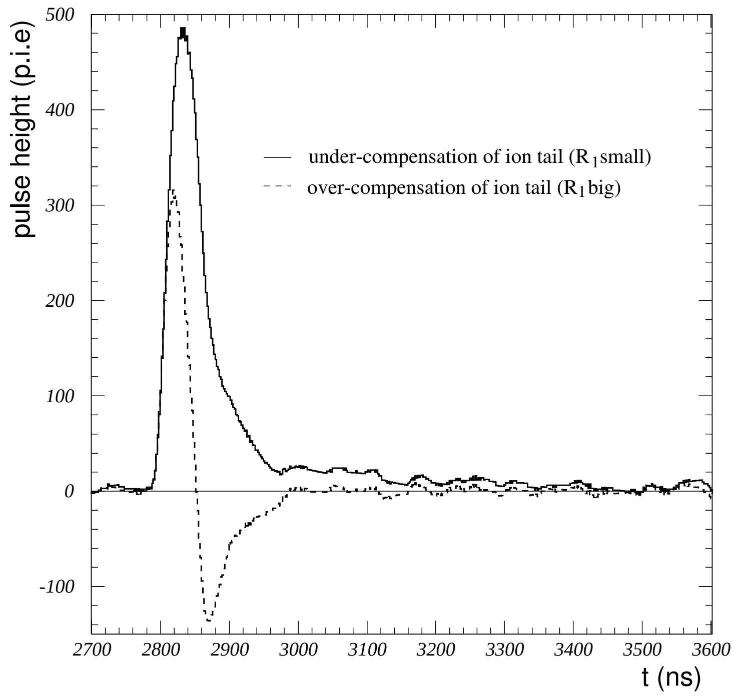

Figure 4.9: *Real muon pulses were convoluted with the transfer function of a pole/zero filter. Depending on the potentiometer settings on the shaper board the ion tail can be under-compensated ($C = 20\,\mathrm{pF}$, $R_1 \approx 100\,\Omega$, $R_2 = 1\,\mathrm{k}\Omega \rightarrow \tau_1 = 2\,\mathrm{ns}$, $\tau_2 = 1.8\,\mathrm{ns}$, solid line) or over-compensated ($C = 20\,\mathrm{pF}$, $R_1 \approx 8.4\,\mathrm{k}\Omega$, $R_2 = 1\,\mathrm{k}\Omega \rightarrow \tau_1 = 168\,\mathrm{ns}$, $\tau_2 = 17.9\,\mathrm{ns}$, dashed line). For the unipolar shaping with undershoot the second case was chosen.*

- **Unipolar Shaping:**
  This shaping scheme was optimised for a good trailing edge resolution, since the signal trailing edge contains important information about the bunch crossing time and can help to reject out-of-time background pulses. The tail ($\propto \frac{1}{t_0+t}$, $t_0 \approx 12\,\mathrm{ns}$) of the ion signal was compensated by carefully adjusted τ-constants. The cancellation of the tail is not possible for the whole ion drift time since the pole/zero filters provide only exponential functions for compensation. Nevertheless a reduction to a few per cent is possible, depending on the event position along the wire. Table 4.2 shows the time constants which were used for unipolar shaping.

	τ_1 (ns)	τ_2 (ns)
first pole/zero filter	42.0	1.9
second pole/zero filter	2.0	1.8

Table 4.2: *Time constants of the pole/zero filters for unipolar shaping.*

- **Unipolar Shaping with Undershoot:**
For high background rates the baseline shift and baseline fluctuations contribute to resolution deterioration. In order to minimise these effects, the R_1-values in the two filters were put to the highest possible values. Such settings over-compensate the ion tail and produce an undershoot leading to a quicker restoration of the baseline (see Figure 4.9). Table 4.3 shows the time constants which were used for unipolar shaping

	τ_1 (ns)	τ_2 (ns)
first pole/zero filter	42.0	1.9
second pole/zero filter	168.0	17.9

Table 4.3: *Time constants of the pole/zero filters for unipolar shaping with undershoot.*

with undershoot. The negative undershoot was about 20 % of the positive pulse.

- **Bipolar Shaping:**
The final electronics will avoid a baseline shift. This new electronics is not available yet; in the test beam the baseline shift was avoided with bipolar shaping. Since the signal is compensated by an undershoot, the baseline stays fixed. Our bipolar shapers had twice the peaking time of our unipolar shapers. Therefore the resolution is worse with and without background rate. But this did not affect the main objective of studying bipolar shaping, namely avoiding baseline shift and baseline fluctuations.

Data with three different shaping schemes were taken in order to investigate the impact of the shaping scheme on the high-rate resolution-deterioration. Unipolar shaping, unipolar shaping with undershoot and bipolar shaping was used. The baseline shift can be avoided by using an appropriate shaping scheme (bipolar shaping).

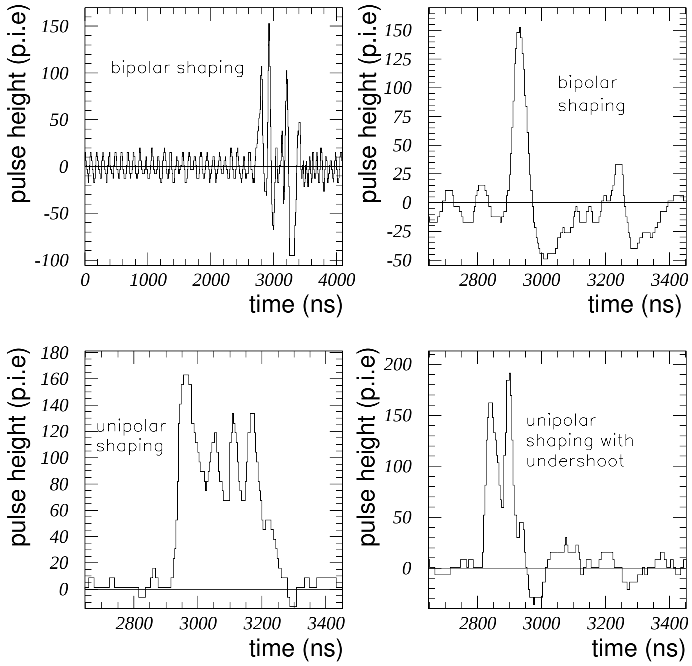

Figure 4.10: *Different kinds of pulse shaping, example pulses.*

4.4 Set-up for the Ar/CO_2 Measurements

These measurements were designed to show the gas properties of Ar/CO_2 mixtures, hence only the space-charge effects of resolution deterioration (gain drop and field fluctuations, see Section 6.2.2) were investigated. In order to minimise the electronics effects of resolution deterioration (baseline shift and baseline fluctuations, see Section 6.2.1) the total count rate per tube was kept low by shielding the entire tube with lead blocks apart from ~ 10 cm around the beam line.

For our investigations single tubes equipped with BNL preamplifiers and shaping amplifiers [BNL:73] were used. The shaping amplifiers were adjusted to give maximum undershoot. This shaping scheme was discussed as unipolar shaping with undershoot in Section 4.3. Figure 4.11 shows the readout chain. An FADC and a TDC were read out for each tube. The discriminator threshold was set to $5 \times \sigma_{\text{noise}}$ which corresponded to 20 p.i.e.

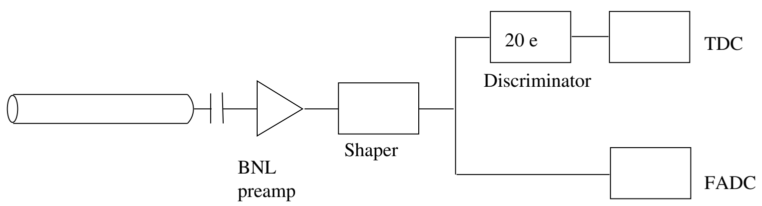

Figure 4.11: *The readout chain of the tubes analysed in this study.*

The tubes were operated with different Ar/CO_2 mixtures (Ar/CO_2 90/10, Ar/CO_2 92/8, Ar/CO_2 93/7, Ar/CO_2 94/6). The gas-mixing facility used digital flow meters with an error of $\sim 0.5\,\%$. This corresponds to an error of smaller than $0.1\,\%$ absolute in the final gas mixture (Ar/CO_2 93/7 $\rightarrow$ Ar/CO_2 93.07/6.93 or Ar/CO_2 92.93/7.07). A pressure of 3 bar was applied and gas gains of 2×10^4 and 4×10^4 were used.

The working parameters are summarised in Table 4.4.

Drift Tube Parameters	
inner tube radius	1.46 cm
outer tube radius	1.50 cm
tube length	$\sim$ 1 m
wire diameter	50 μm W/Re 97/3
gas	Ar/CO_2 90/10, 92/8, 93/7, 94/6
gas pressure	3 bar absolute
gas gain G_0	2×10^4 / 4×10^4
maximum electron drift time	610 ns – 950 ns
maximum ion drift time	$\sim$ 4 ms
preamp + shaper peaking time	15 ns
noise level σ_{noise}	3.8 p.i.e (see text)
discriminator threshold	20 p.i.e (see text)
γ-rate per wire length	0 Hz/cm – 3060 Hz/cm
γ-rate per tube	0 kHz – 9 kHz

Table 4.4: *Working parameters of the drift tubes.*

The external reference system was ODYSSEUS [DEI:99], a beam telescope consisting of six Silicon micro-strip detectors with 7 μm resolution each. Four out of the six planes measure the precision coordinate perpendicular to the MDT wires, the other two detectors give us the “second coordinate” parallel to the wires. By extrapolation of the silicon-telescope track to the tube position we get a prediction accuracy of 10 μm. The tubes were located between the silicon-telescope planes.

The rates per unit tube length for different lead filters are listed in the table below:

nominal filter factor	rate per unit tube length (Hz/cm)
2	3060
5	1400
10	810

Measurements without background rate and with the rates mentioned above have been performed.

High-rate measurements have been performed with single tubes. As a drift gas different Ar/CO_2 mixtures have been used at 3 bar gas pressure. The threshold level was set to 20 p.i.e, which corresponded to $\sim 5 \times \sigma_{noise}$. The gas gain was $G_0 = 2 \times 10^4$ and $G_0 = 4 \times 10^4$. The background rate was varied from 0 to 3060 Hz/cm (high local rate), the count rate per tube was kept low.

Chapter 5

Defining the Working Parameters

5.1 Introduction and Strategy

As already described in Chapter 2, the gas choice is one of the most critical issues for the MDT system. Many different aspects have to be considered, especially the high-rate environment. The drift gas Ar/CO_2 93/7 was found during the work for this thesis and its advantages and disadvantages are analysed in this and the following two chapters. Since $Ar/N_2/CH_4$ 91/4/5 is the drift gas, which has been favoured for a long time due to its linear rt-relation, we will also focus on the comparison between this gas and the new baseline gas. As a benchmark for the gas choice we want to use the single-tube performance (see also Section 2.5 and [ATM:95]):

- **Resolution:**
  The resolution of one single MDT has to be better than $80\,\mu$m. This upper limit is necessary to achieve a muon-momentum resolution of $\sim 10\,\%$ for muons with a transverse momentum of $p_T = 1\,\text{TeV}/c$. Detailed investigations, presented in Chapter 6, show, that Ar/CO_2 mixtures have an average resolution of $\sim 50\,\mu$m without background rate (with time slewing correction) and are still compatible with the $80\,\mu$m-limit for the highest expected background rates (1500 Hz/cm including an uncertainty factor of five for safety). The noise level determines the threshold level ($5 \times \sigma_{\text{noise}}$) and hence has an important impact on the spatial resolution. Noise measurements are presented in this chapter which show that with first prototype chambers the theoretical minimum-noise level was almost achieved.

- **Efficiency:**
  The hit efficiency of one MDT without background rate has to be at least 99 %. This requirement is satisfied by most of the drift gases at a gas pressure of 3 bar and a threshold of $\sim$ 20 p.i.e. For high background rates – we expect count rates of up to 300 kHz per tube – the occupation time of the drift tubes becomes important. A maximum drift time of $t_{\max} \approx 700\,\text{ns}$ (baseline gas Ar/CO_2 93/7) translates into an occupancy of 16 %. This is the main reason why fast drift gases are preferred. Measurements and simulations determining the maximum drift time are presented

in this chapter. The 3σ-efficiency was measured and simulated as a function of the background rate.

- **Aging, Linearity of the Space-Time Relationship:**
  Operating at a gas gain of $G_0 = 2 \times 10^4$ (baseline) the charge deposit will be 0.6 C/cm in ten years of ATLAS operation. Many drift gases show aging (decrease of the pulse height, high count rates) when being exposed to such conditions. It has been found in extensive aging studies that gas mixtures containing organic compounds (e.g. CH_4) produce thin deposits on the wire and on the cathode which affect the performance (aging) and therefore are not appropriate for the use in ATLAS, even though their drift properties are sometimes very good (e.g. linear rt-relation). The baseline gas (Ar/CO_2 93/7) shows no aging but is rather non-linear. In Chapter 7 consequences of this non-linearity are investigated.

- **B-Field Dependence:**
  The B-field dependence of the rt-relation should be as small as possible (i.e. small Lorentz angle). In this respect slower drift gases (small Lorentz angle) are preferred. In this and the following chapters simulations of the resolution and the systematic error to the rt-relation due to magnetic field differences are presented for the baseline gas (Ar/CO_2 93/7).

- **Afterpulsing Behaviour:**
  Afterpulses are a sign for incomplete quenching behaviour of the considered gas. Therefore the afterpulsing rate has to be as low as possible. The afterpulsing behaviour for several Ar/CO_2 mixtures was measured and is presented in this chapter.

- **Streamer Rate:**
  The streamer rate has to be smaller than 1 %. Measurements for Ar/CO_2 80/20 showed that it is smaller than 0.5 % for gas gains up to 4×10^4. For Ar/CO_2 93/7 the streamer rate was measured to be < 0.1 % for a gas gain of 4×10^4.

In addition to the gas choice, the front-end electronics scheme had to be considered. The main reason for that was the hit multiplicity which turned out to be > 1 for Ar/CO_2 mixtures due to the longer maximum drift time and the non-linearity of the rt-relation.

This chapter discusses measurements from the test beam and simulations for several Ar/CO_2 mixtures and compares them to simulations of other drift gases. The following two chapters are devoted to defining the working parameters of the baseline gas Ar/CO_2 93/7 and give evidence that a viable solution has been found. Chapter 7 will focus on the main disadvantage of all Ar/CO_2 mixtures, the non-linear rt-relation. Finally, Section 7.5 will conclude on the discussion of the drift gas and summarise the working parameters of the baseline gas.

The measurements described in this chapter were performed in the GIF zone in the SPS beam line X5 (see Chapter 4).

5.2 Electronics-Noise Measurements

5.2.1 Introduction

A low discriminator threshold is inevitable for high spatial resolution. Since the noise level determines the minimum threshold level ($5 \times \sigma_{\text{noise}}$), it has been tried to come close to the theoretical noise level. This section shows measurements with two prototype chambers (EMS and BOS) equipped with electronics similar to the final design, and identifies the most important sources of noise. It is shown that the measurements come very close to the theoretical minimum-noise level (see also [ALE:98a]).

Several different methods of measuring the noise level will be introduced. They all agree within the error bars. Differences between the two prototype chambers are due to the different capacitances to the ground in front of the preamplifier.

5.2.2 Pulser Measurements (on the EMS Chamber)

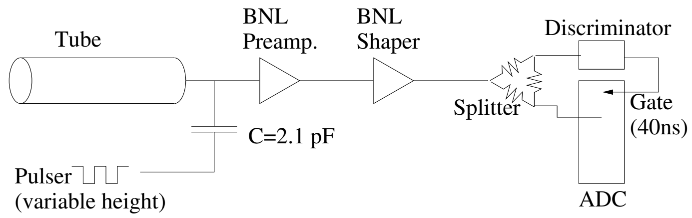

Figure 5.1: *Experimental set-up for the noise measurement using a pulser and a capacitor for calibrating the ADC. The ADC gate was chosen to be 40 ns.*

The measurements were performed in the X5 test beam with the upstream half of the Seattle/Boston EMS chamber[1] equipped with BNL preamplifiers [BNL:73] and shapers. The tube was connected to the preamplifier with a 5 cm cable. The preamplifier and shaper peaking time t_p was 15 ns. The set-up is shown in Figure 5.1. For this noise measurement the high voltage was switched off but the HV cables were still connected.

The ADC was calibrated by injecting well defined amounts of charge into the preamplifier. A voltage step U through a capacitor C injects a charge q of

$$q = C \cdot U \ , \tag{5.1}$$

so by varying the pulse height we derive the desired calibration curve.

The nominal capacitance C_{nom} of the capacitor was 1.8 pF. The true capacitance C was larger because of additional parallel capacitances from the wires etc.; hence the capacitance was measured to be $C = (2.09 \pm 0.05)$ pF.

[1] Note, that the resolution studies for $Ar/N_2/CH_4$ 91/4/5 have been performed on the EMS downstream half. There the preamplifiers were located on hedgehog boards with a similar design as on the BOS chamber (see below). Also the noise level in the EMS downstream half was similar to that measured on the BOS chamber.

Since the shaper output signal shows significant undershoot, an ADC gate of 40 ns was chosen in order to integrate only the positive part of the signal.

For gates slightly longer than two times the preamplifier peaking time ($t_\mathrm{p} = 15\,\mathrm{ns}$) the charge-sensitive ADC readings correspond very well to an amplitude measurement. Still, this represents a source of a systematic error, which can be estimated to about 20 %.

Figures 5.2 and 5.3 show the ADC calibration. One obtains the following relationship between the charge q injected into the preamplifier and the ADC channel number N_ADC:

$$q = C \cdot [(-1.596 \pm 0.702) + (0.068 \pm 0.001) \cdot N_\mathrm{ADC}] \ , \tag{5.2}$$

with C in pF and q in fC.

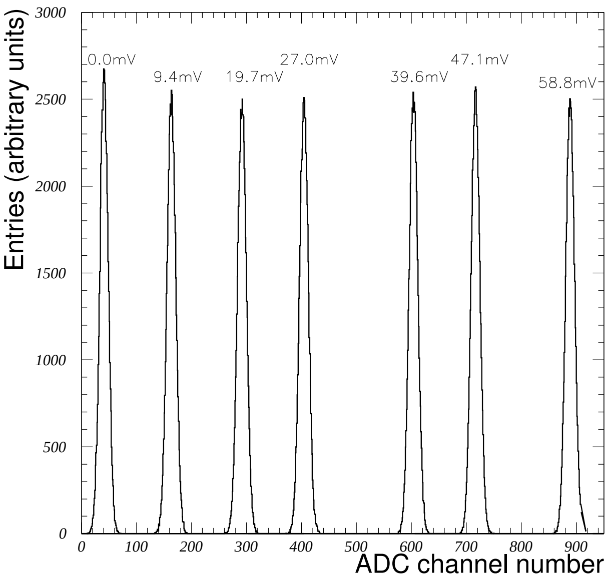

Figure 5.2: *ADC readings for different pulser voltages.*

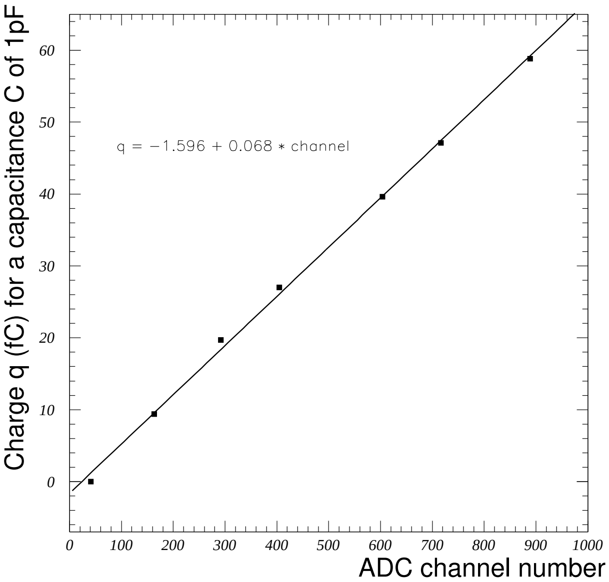

Figure 5.3: *Straight line fit to the data yielding the relationship between charge and channel number.*

The width of the ADC value distributions in Figure 5.2 corresponds to the noise level that we want to measure. Figures 5.4 and 5.5 show Gaussian fits to the first distribution (0 mV, $\chi^2 = 2.131$) and the last distribution (58.8 mV, $\chi^2 = 1.015$). The not perfectly Gaussian shape of the first distribution is probably due to a non-linearity of the ADC for negative input voltages. The "perfect" Gaussian shape of the second distribution shows that there are no noise contributions from pick-up or oscillations down to a level of $< 10^{-3}$.

According to the Gaussian fits in Figure 5.4, 5.5 and all the others shown in Figure 5.2, the σ of the distribution is 7.64 ± 0.02 channels which – using Equation (5.2) – corresponds to a σ in terms of charge of (capacitance C in pF)

$$\sigma = C \cdot (0.520 \pm 0.008)\,\mathrm{fC} \equiv C \cdot (3250 \pm 50)\,\mathrm{e}^- \ , \tag{5.3}$$

hence we obtain the **E**quivalent **N**oise **C**harge (ENC):

$$\mathrm{ENC} = C \cdot (3250 \pm 650)\,\mathrm{e}^- \approx (6780 \pm 1400)\,\mathrm{e}^- \ , \tag{5.4}$$

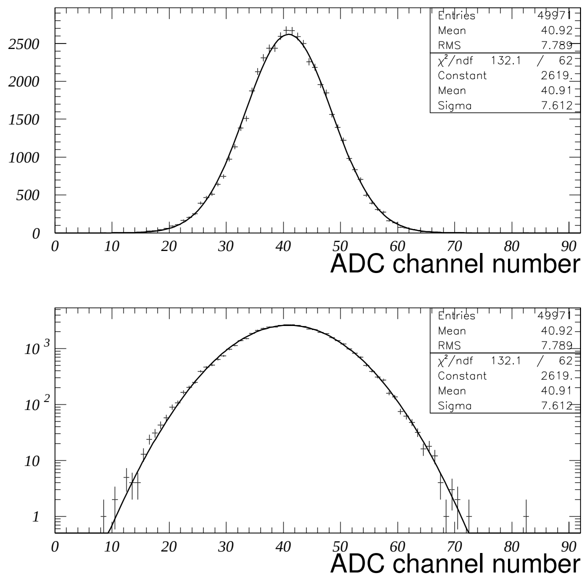

Figure 5.4: *Histograms of the ADC readings for a pulser voltage of* 0 mV. *The imperfection of the Gaussian distribution is probably due to an ADC non-linearity for negative input voltages.*

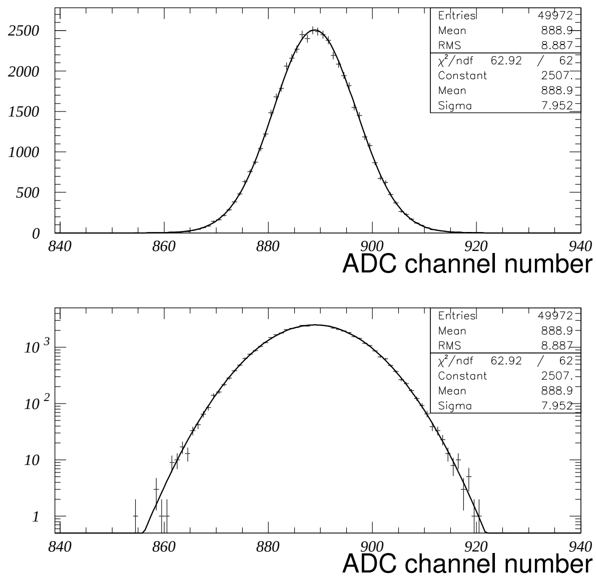

Figure 5.5: *Histograms of the ADC readings for a pulser voltage of* 58.8 mV. *The distribution is "perfectly" Gaussian.*

with the capacitance $C = (2.09 \pm 0.05)\,\mathrm{pF}$. In Equation (5.4) the above mentioned additional error of 20 % due to the translation of the charge-sensitive ADC readings into a signal amplitude was taken into account.

In order to get this number in units of primary ionisation electrons (p.i.e) one has to calculate the fraction of charge collected during the peaking time t_p of preamplifier and shaper.

The current signal induced on the wire was already discussed in Section 3.2.5. According to Equation (3.4) the induced signal has a form $\propto \frac{1}{t_0+t}$, where t_0 was calculated to be 11.9 ns for our set of working parameters.

The peaking time t_p of the preamplifier and shaper was 15 ns. Since for this calculation the peaking time of a real signal (not a δ-pulse) has to be taken into account, we set $t_\mathrm{p} < t_\mathrm{p}^\mathrm{signal} = (20 \pm 2)\,\mathrm{ns}$. Hence the fraction R_q of charge arriving before the peaking time $t_\mathrm{p}^\mathrm{signal}$ is given by

$$R_q = \frac{\int_0^{t_\mathrm{p}^\mathrm{signal}} \frac{1}{t+t_0}\,\mathrm{d}t}{\int_0^{t_\mathrm{max}^\mathrm{ion}} \frac{1}{t+t_0}\,\mathrm{d}t} = \frac{\ln\left(\frac{t_\mathrm{p}^\mathrm{signal}+t_0}{t_0}\right)}{\ln\left(\frac{t_\mathrm{max}^\mathrm{ion}+t_0}{t_0}\right)} = (7.7 \pm 0.5)\,\% \,. \tag{5.5}$$

So for a gas gain G of 2×10^4 one p.i.e induces the charge of $R_\mathrm{q}G = (1550 \pm 100)\,\mathrm{e}^-$ in the time $t_\mathrm{p}^\mathrm{signal}$.

Now the numbers in Equation (5.4) can be expressed in p.i.e ($C = (2.09 \pm 0.05)\,\text{pF}$):

$$\boxed{\sigma_{\text{noise}} = C \cdot (2.1 \pm 0.5)\,\text{p.i.e} = (4.4 \pm 1.1)\,\text{p.i.e}\,.} \tag{5.6}$$

Unfortunately, this measurement method suffers from a large error due to the translation of the ADC readings into a signal amplitude. However, the "perfect" Gaussian shape of the electronics noise was demonstrated.

Pulser measurements on the EMS chamber resulted in a $\boldsymbol{\sigma_{\text{noise}}}$ of (4.4 ± 1.1) p.i.e. The translation of ADC readings into signal amplitudes represents the main source of errors. The "perfect" Gaussian shape of the noise distribution ($\chi^2 = 1.015$) suggests that the system does not suffer from pick-up or oscillations.

5.2.3 Rate Measurements (on the EMS Chamber)

As a second method to determine the noise level, the noise count rate was measured as a function of threshold. This measurement was performed with and without high voltage on the wire.

Noise level without high voltage

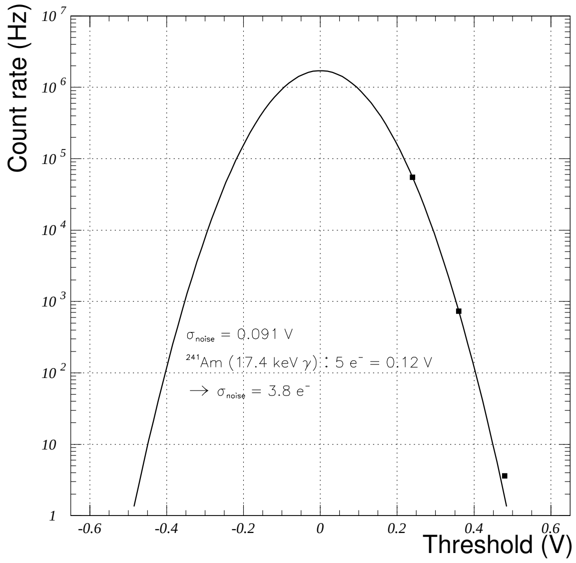

Figure 5.6: *Noise level without high voltage on the wire.*

Figure 5.6 shows a Gaussian fit to the measurements with the maximum forced to zero. To convert the voltage into units of p.i.e, pulses of 17.4 keV photons which leave a localised cluster of 670 primary ionisation electrons in the counting gas, were recorded. Dividing the pulse height by 670 yields the voltage corresponding to a single p.i.e. The measurement result for this set-up was: 1 p.i.e $\equiv$ 0.0242 V.

Hence in terms of primary ionisation electrons the σ_{noise} is

$$\boxed{\sigma_{\text{noise}} = 3.8\,\text{p.i.e}\ ,} \tag{5.7}$$

which is – within the expected errors – in accordance with the value given in Equation (5.6).

The statistical errors on the result given in Equation (5.7) are about 0.1 %, but the systematic error can be much larger due to forcing the maximum of the Gaussian distribution in Figure 5.6 to zero which relies on a base line exactly at 0 mV. Nevertheless this measurement displays the actual noise level with much higher accuracy than the measurement described in Section 5.2.2.

By using expression (5.5) we can calculate the ENC for the σ_{noise} given in Equation (5.7):

$$\text{ENC} = R_{\text{q}} G \sigma_{\text{noise}} \approx 5880\,\text{e}^- \ . \tag{5.8}$$

Noise level with high voltage

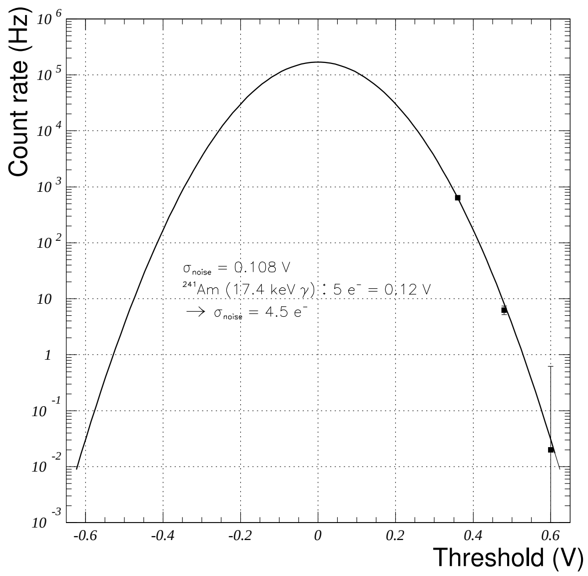

Figure 5.7: *Noise level with high voltage on the tube switched on.*

Figure 5.7 shows the noise level with 3270 V on the wire (cathode voltage 0 V). The cosmic rate, which was 56.78 Hz for our 190 cm long tube, had to be subtracted from the measured value. Like for the case with the high voltage switched off, a Gaussian distribution with the maximum forced to zero was fitted.

With the calibration given before we obtain

$$\boxed{\sigma_{\text{noise}}^{\text{hv on}} = 4.5\,\text{p.i.e} = \sqrt{\sigma_{\text{noise}}^2 + (2.4\,\text{p.i.e})^2}\ .} \tag{5.9}$$

Hence the additional contribution of the high voltage is 2.4 p.i.e. One can eliminate this contribution by either using a more stable HV supply or filtering the HV with an appropriate low-pass filter. The noise level of the BOS chamber did not change when switching on the high voltage (see Section 5.2.4).

The rate measurements showed a noise level of 3.8 p.i.e. This measurement method displays the noise level with much higher accuracy than the pulser measurements. Switching on the HV lead to an enhancement of electronics noise, which can be eliminated by filtering the HV with an appropriate low-pass filter.

5.2.4 Noise Measurements (on the BOS Chamber)

These measurements were performed in the H8 test beam. The BOS chamber was equipped with BNL preamplifiers [BNL:73] on the hedgehog board[2]. The high-voltage end and the electronics end were protected by a Faraday cage.

The signal was shaped by the BNL-shapers, 48 of them on one board in a crate, connected with 10 m long cables to the chamber.

The calibration of the signal amplification was performed with a ^{241}Am source + Mo foil: 1 mV of the output signal of the shapers corresponded to ~ 1.1 p.i.e at a gas gain of 2×10^4.

By histogramming the noise with a digital scope we got:

$$\boxed{\sigma_{\text{noise}} = (4.8 \pm 0.3)\,\text{p.i.e}\,.} \tag{5.10}$$

The measurements were done with the high voltage switched on, switched off and the high voltage cable unplugged. No significant change of the noise level was observed.

The difference between the noise level on EMS and on BOS cannot be explained by different wire lengths (EMS: $l = 1.9$ m, BOS: $l = 4.0$ m), since a longer wire decreases the ENC (see Equation (5.12), $R_1 = 0$):

$$\sigma_{\text{noise}} \propto \frac{1}{\sqrt{R_\text{t} + l \cdot r_\text{wire}}}\,, \tag{5.11}$$

where l is the length of the tube, r_wire the resistance of the wire per unit length ($r_\text{wire} \approx 44\,\Omega/\text{m}$) and $R_\text{t} = 382\,\Omega$ the termination resistor. Equation (5.11) would predict a $\sim 10\,\%$ smaller noise level for the BOS chamber than for the EMS chamber.

One reason for the additional noise on BOS is the additional capacitance of the signal traces on the hedgehog board between the tube and the preamplifier (see Section 5.2.5).

[2] I.e. the MDT front-end electronics board, adapted to the multilayer pin layout. The connections between the pins, plugged to the tubes, and the preamplifiers are implemented with signal traces with a length of ~ 10 cm. These hedgehog boards come close to the final design.

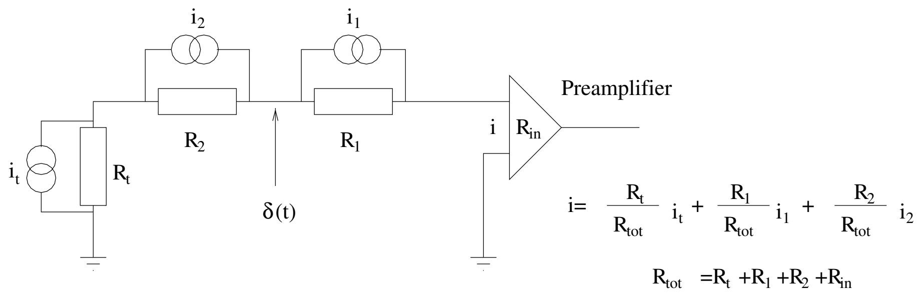

Figure 5.8: *Thermal noise can be modelled as a current source parallel to a noiseless resistor. R_1 and R_2 are the wire resistances left and right of the impact point* [RIE:97b].

Measurements on the BOS chamber yielded a σ_{noise} of (4.8 ± 0.3) p.i.e. The main difference to the EMS chamber is the connection of the tubes and the preamplifiers. On the BOS chamber these connections were implemented with signal traces on the hedgehog board, which comes close to the final design.

5.2.5 Calculation of the Noise Level and Comparison with the Measurements

The main contribution to the noise level is the thermal noise of the termination resistor. The derivation of the termination-resistor noise is given in [RIE:97b], here I want to summarise the results.

The thermal noise of a resistor R can be represented as a current noise source in parallel with a noiseless resistor R and having a mean square current magnitude of $i^2_{\text{r.m.s}} = \frac{4kT}{R}\mathrm{d}f$, where k is the Boltzmann constant, T the temperature of the resistor and $\mathrm{d}f$ the frequency interval [NIC:74].

Using the circuit shown in Figure 5.8, the following ENC in electrons is obtained:

$$\text{ENC} = \frac{\sqrt{R_\text{t}(R_1 + R_2 + R_\text{t})}}{R_2 + R_\text{t}} \frac{1}{e_0} \frac{e^n}{2^n} n^{-(n+\frac{1}{2})} \sqrt{t_\text{p} \frac{kT}{R_\text{t}} (2n)!}\,, \tag{5.12}$$

where n is the number of integrations of the preamplifier, e_0 is the electron charge and t_p the preamplifier peaking time. For the electronics used in the test beam we have to use $n \approx 3$, $t_\text{p} = 15\,\text{ns}$. Since we injected charge next to the preamplifier we have to set $R_1 = 0$.

Neglecting the wire resistance ($R_1 = R_2 = 0$) Equation (5.12) predicts a thermal noise of $\sim 3\,$p.i.e ([RIE:97b]) for the set-up used in the test beam.

If we take into account parasitic capacitance [HAZ:97], we get ($R_1 = 0$)

$$\mathrm{ENC} = \frac{1}{e_0}\frac{e^n}{2^n} n^{-(n+\frac{1}{2})} \sqrt{kT(2n)!} \left[\sqrt{t_\mathrm{p} \frac{R_\mathrm{t} + R_2 + R_\mathrm{N}}{(R_\mathrm{t} + R_2)^2}} + \sqrt{\frac{2C_\mathrm{in}^2 R_\mathrm{N}}{t_\mathrm{p}}} \right] , \tag{5.13}$$

where R_N is the noise resistance of the preamplifier, which is to a good approximation equivalent to the input impedance, and C_in the capacitance to ground in front of the preamplifier. The capacitance of the tube itself (8.7 pF/m) does not add to C_in as long as the tube is terminated (like in our case), but the end plug (6 pF) on the preamp side (the other one contributes far less) and the cables (signal traces) to the preamp have to be taken into account.

The BNL-preamplifier has a noise resistance of $R_\mathrm{N} \approx 100\,\Omega$. If we take into account the capacitance of one end plug plus the connections (EMS chamber: $\sim$ 9 pF), we calculate $\sigma_\mathrm{noise} = 3.5$ p.i.e, which comes very close to the measured $\sigma_\mathrm{noise} = 3.8$ p.i.e.

Since on the BOS chamber the connections between the tube and the preamplifier were implemented as signal traces ($\sim$ 10 cm), the capacitance is higher. An additional capacitance of $\sim$ 20 pF would explain the entire difference of the noise levels of $\sigma_\mathrm{noise}^\mathrm{BOS} - \sigma_\mathrm{noise}^\mathrm{EMS} = 1$ p.i.e. This seems to be too much, since the signal traces have a capacitance to the ground of $\sim$ 1 pF/cm. Nevertheless the calculated values are very close to the measurements.

Noise measurements on the Seattle/Boston EMS chamber were performed. The result was $\boldsymbol{\sigma_\mathrm{noise} \approx 3.8}$ p.i.e which has to be compared to a theoretical lower limit of $\sim$ 3.5 p.i.e resulting from thermal noise of the termination resistor (3 p.i.e) plus noise from the capacitance of the end plug (0.5 p.i.e).
Measurements on the Munich BOS chamber show a $\boldsymbol{\sigma_\mathrm{noise} \approx 4.8}$ p.i.e. Part of the difference to the noise level of the EMS chamber can be explained by additional capacitance in front of the preamplifier because of signal traces. The capacitance of the tube does not contribute since the tube is terminated.
The very good agreement between the theoretical and experimental noise level and the "perfect" Gaussian shape of the noise distribution shows that there is no noise contribution from pick-up or oscillations.

5.3 Gas-Gain Measurement

This section shows briefly the results of the gas-gain measurements. Only a relative measurement was performed, therefore the systematic error of the gas gain is estimated to be about 20 %. As a reference gas $Ar/N_2/CH_4$ 91/4/5 was used (see [DEI:96a]). The spectra of a ^{55}Fe source, emitting 5.9 keV photons, were compared and hence the gas gain calibrated.

Figure 5.9 shows the gas gains for different Ar/CO_2 mixtures at 3 bar gas pressure, a temperature of $\sim$ 295 K, a wire radius $a = 25\,\mu$m and a tube radius $b = 1.46$ cm. Using Diethorn's formula [DIE:56] the gas gains for other gas pressures or even other geometries can be calculated ($E(a)$ is the electrical field on the wire, $E_{\mathrm{min}}(\rho_0)$ and ΔV are the Diethorn parameters[3], see Table 5.1):

$$G = \left[\frac{E(a)\rho_0}{E_{\mathrm{min}}(\rho_0)\rho_{\mathrm{gas}}}\right]^{\frac{aE(a)\ln 2}{\Delta V}} \quad . \tag{5.14}$$

For our tube geometry, 3 bar gas pressure and the baseline mixture Ar/CO_2 93/7 a high voltage of 3080 V corresponds to a gas gain of 2×10^4.

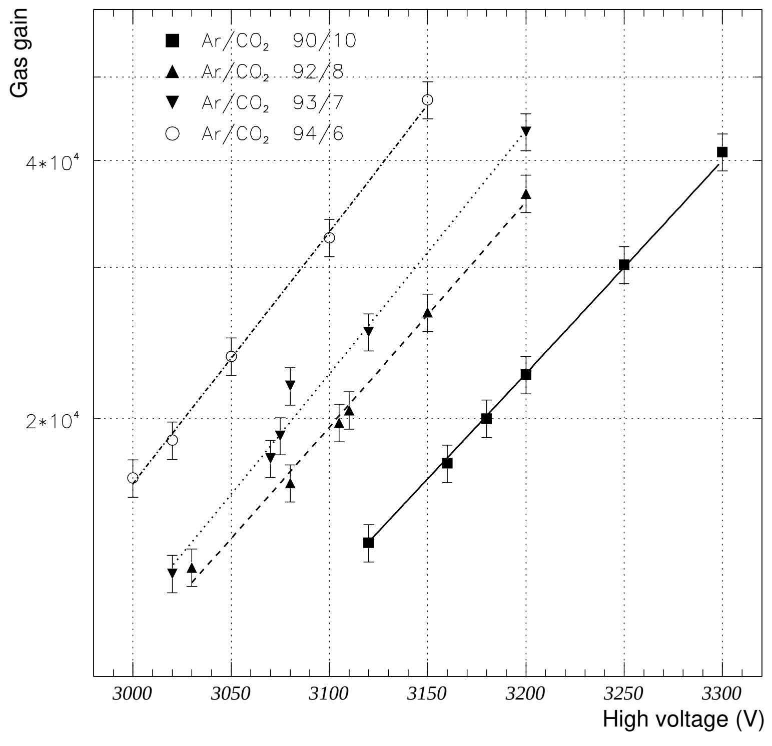

Figure 5.9: *Gas gains for different* Ar/CO_2 *mixtures. The Diethorn parameters resulting from the fits are listed in Table 5.1. Note that the plot shows only the statistical errors, the systematic errors due to the relative measurement are estimated to be about 20 %.*

[3]The parameter E_{min} stands for the electrical field at the start of the avalanche and ΔV for the ionisation potential of the drift gas.

gas mixture	$E_{\min}$(1 bar) (kV/cm)	ΔV (V)
Ar/CO_2 80/20	22	49
Ar/CO_2 90/10	20	43
Ar/CO_2 92/8	19	42
Ar/CO_2 93/7	24	34
Ar/CO_2 94/6	23	34

Table 5.1: *Diethorn parameters $E_{\min}$ and ΔV for different Ar/CO_2 mixtures. The errors on the parameters are about 10 %.*

A relative measurement was performed to obtain the gas gain as a function of the high voltage on the wire for several Ar/CO_2 mixtures. For the baseline mixture Ar/CO_2 93/7 at 3 bar gas pressure a high voltage of 3080 V corresponds to a gas gain of 2×10^4.

5.4 Afterpulsing

In the avalanche process next to the wire surface UV photons are generated. If such photons reach the conducting cathode, free electrons can be created by the photo-electric effect. These electrons will drift towards the wire, multiply and induce a – usually small – signal, which we call afterpulse. Hence these signals are expected to be separated in time from the first avalanche by at least the maximum drift time. Organic molecules, with their many degrees of freedom, have large photo-absorption coefficients over a range of wavelengths that is wider than that for noble gases. Thus they can be used as quench gases. Common quench gases are CH_4 and other hydrocarbons but also inorganic molecules like CO_2.

The afterpulsing rate is a number which quantifies whether a drift gas has a sufficient amount of quenching molecules. In order to distinguish between multiple hits and real afterpulses, only signal pulses were taken into account which showed no hit between the first threshold-crossing time and the time where afterpulses were expected. Figure 5.10 shows the principle. Dividing the number of entries around the maximum drift time by the number of first threshold crossings yields the afterpulsing rate which is plotted in Figure 5.11 for different CO_2 contents in Ar/CO_2 mixtures (3 bar gas pressure). We see that Ar/CO_2 93/7 has an afterpulsing rate of 3 % at a gas gain of $G = 2 \times 10^4$. Applying the same method to measurements with $Ar/N_2/CH_4$ 91/4/5 one obtains 0.25 %.

Afterpulses produce additional hits, but compared to the large uncertainties of the background rate (safety factor five), they are negligible. Since afterpulses are very short, they will not contribute significantly to the occupancy if a "time-over-threshold" TDC is used. However, the ATLAS front-end electronics scheme will introduce a dead time[4] after each

[4]This dead time will be approximately the maximum electron-drift time (~ 700 ns).

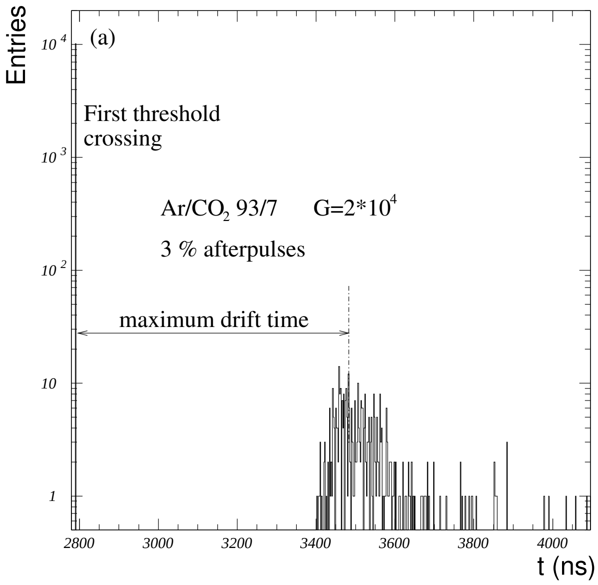

Figure 5.10: *The plot shows how the afterpulsing rate was determined: The number of all hits around and after the maximum drift time (*3400 ns – 4200 ns, $5 \times \sigma_{\text{noise}} = 20$ p.i.e *threshold for* $G = 2 \times 10^4$*) was divided by the number of first threshold crossings.*

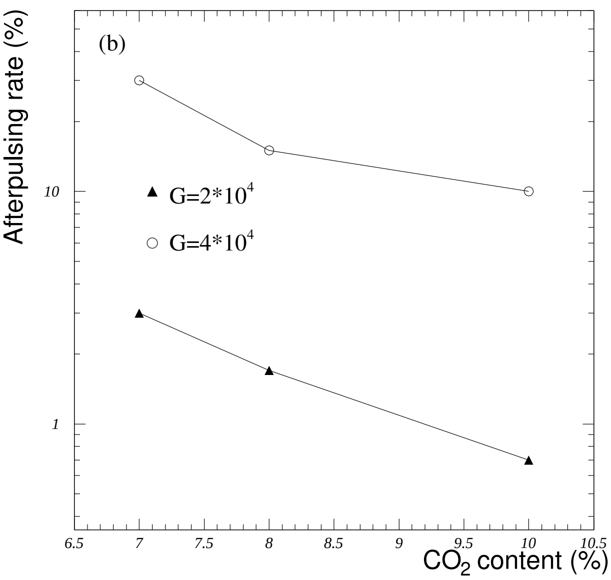

Figure 5.11: *The plot shows the dependence of the afterpulsing rate on the* CO_2 *content in* Ar/CO_2 *mixtures. With the same method we obtained an afterpulsing rate of* 0.25 % *for* $Ar/N_2/CH_4$ 91/4/5 *at a gas gain of* $G = 2 \times 10^4$.

hit which will on the one hand obscure afterpulses (see Figure 5.10, such afterpulses which arrive slightly before the maximum drift time) but on the other hand introduce additional dead time due to "late" afterpulses. This will raise the occupancy slightly.

However, afterpulses are a sign for incomplete quenching properties of a gas which might cause other problems (e.g. higher probability of discharges on damaged wires). The ATLAS Muon System will be able to cope with an afterpulsing rate of a few percent. Consequently afterpulses themselves in Ar/CO_2 are no problem at a gas gain of $G = 2 \times 10^4$. Nevertheless, for running with higher gas gains additional quench gases would have to be added.

The afterpulsing rate for different Ar/CO_2 mixtures was measured. For the baseline mixture Ar/CO_2 93/7 an afterpulsing rate of 3 % was found at a gas gain of 2×10^4 at 3 bar gas pressure. Such an afterpulsing rate is still tolerable but will raise the occupancy slightly.

5.5 Hit Multiplicity

Muons and also background events produce numerous clusters in the drift gas (see Chapter 3). Consequently the detected signal is a superpositions of the individual single-cluster signals. This leads to typical signal shapes showing several peaks and causing multiple threshold crossings (hits), depending on the threshold level. The sketch in Figure 5.12 shows a typical MDT signal and three different threshold levels, resulting in different hit multiplicities.

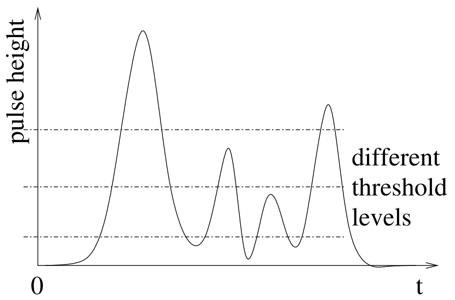

Figure 5.12: *A typical MDT signal for a muon or background event. The different threshold levels lead to different numbers of threshold crossings.*

Multiple hits per signal can cause readout occupancy and tracking[5] problems. Since the hit multiplicity strongly depends on the drift gas, it is necessary to check how the front-end electronics shaping scheme has to be adjusted to deliver only one hit per signal. This has been studied extensively and is described in [ALE:99b].

Due to the longer drift time (Ar/CO_2 93/7: $t_{\max} \approx 700\,\mathrm{ns}$) and the non-linearity of the rt-relation the hit multiplicity in Ar/CO_2 increases compared to faster, linear gases (e.g. $Ar/N_2/CH_4$ 91/4/5: $t_{\max} \approx 485\,\mathrm{ns}$). The main reason for this effect is that in a slow, non-linear drift gas the time difference between individual clusters arriving at the wire becomes bigger with longer drift distances. Therefore the pulse shapes usually show one high leading peak and many subsequent small peaks which often cause multiple threshold crossings (see Figure 5.12).

To compensate this behaviour and to achieve only one hit per signal for gases like Ar/CO_2 93/7, the tail cancellation has to be "soft"[6]. Consequently the trailing-edge resolution deteriorates significantly and the dead time increases slightly. Furthermore a big hysteresis is needed to achieve one single hit per signal. Figure 5.13 shows the hit multiplicity (GARFIELD simulations) for two gases as a function of the threshold (unipolar shaping). It can be seen that "soft" tail cancellation and large hysteresis results in 1 hit per signal.

Since the trailing-edge resolution deteriorates dramatically due to the "soft" tail cancellation, other shaping schemes, providing only one hit per signal were rethought. The main difference between different shaping schemes is the created occupancy and hence the 3σ-inefficiency, which is discussed in Section 5.6.

[5] The information whether a hit corresponds to a leading edge of a muon signal is lost.

[6] I.e. the long ion tail of the signal is not cancelled entirely.

Figure 5.14 shows the hit multiplicity using bipolar shaping for two different gases and different hysteresis (GARFIELD simulations). It can be seen that one hit per signal cannot be achieved. Only bipolar shaping with artificial dead time will provide one hit per signal.

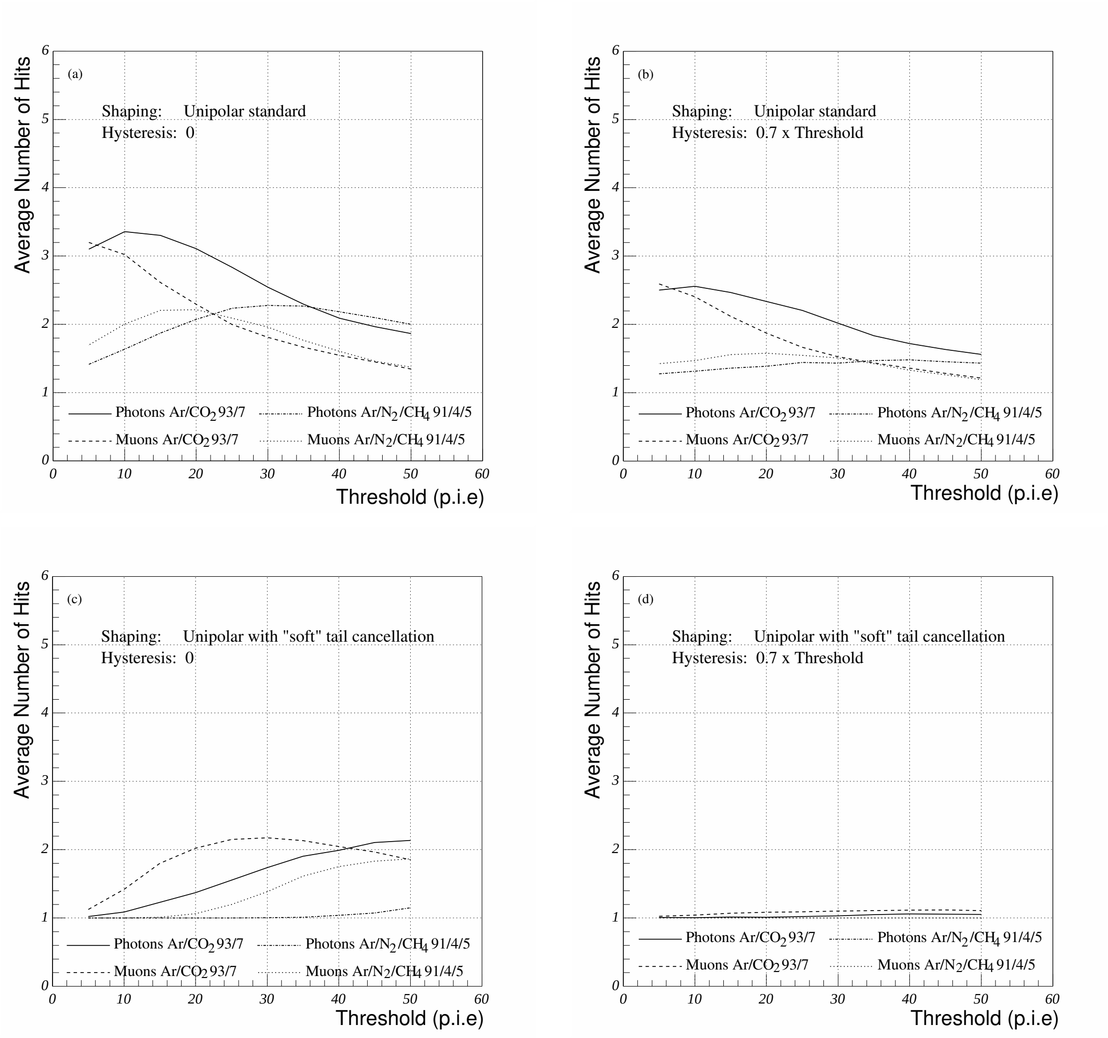

Figure 5.13: *Hit multiplicity as a function of the threshold for unipolar shaping* [ALE:99b]. *The figure compares* Ar/CO_2 93/7 *with* Ar/N_2/CH_4 91/4/5. *Plots (a) and (b) show the hit multiplicity for the standard unipolar shaping, (c) and (d) for unipolar shaping with a "soft" tail cancellation. We see that "soft" tail cancellation and large hysteresis result in a single hit per signal.*

The hit multiplicity was studied for different gas mixtures and different shaping schemes. To achieve only one hit per signal using the baseline gas Ar/CO_2 93/7 unipolar shaping with extremely "soft" tail cancellation or bipolar shaping with artificial dead time has to be used.

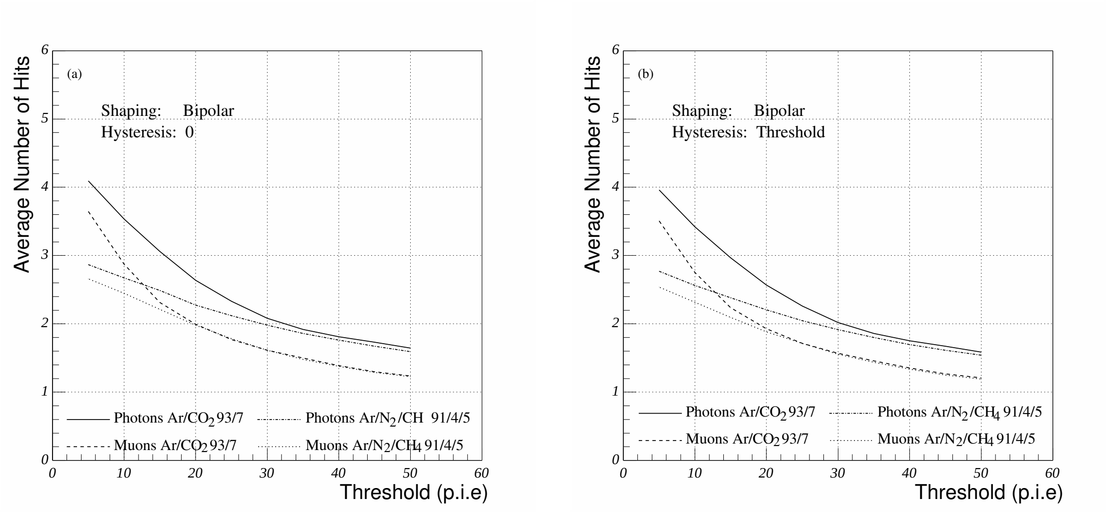

Figure 5.14: *Hit multiplicity as a function of the threshold for bipolar shaping* [ALE:99b]. *The figure compares* Ar/CO_2 93/7 *with* $Ar/N_2/CH_4$ 91/4/5. *One can see that the hit multiplicity is not affected by hysteresis settings. The number of hits is higher for* Ar/CO_2 93/7 *due to the longer drift time and the non-linearity of the rt-relation. Photons cause more hits due to the increased charge deposit.*

5.6 Efficiency

This section discusses the dependence of the MDT Efficiency on the background rate and the shaping scheme. We will consider two different efficiencies:

- The hit efficiency indicates the probability that a muon going through a tube is registered at all. No quality criterion is applied to the reconstructed hit radius.
- The 3σ-efficiency indicates the probability that a muon passing through a tube is detected and the reconstructed hit radius is within 3σ from the true value, where σ is the spatial resolution at the respective track radius. This efficiency definition thus characterises the importance of the tails in a residual distribution. The 3σ-inefficiencies are composed by inefficiencies due to δ-electrons ($\sim 5\,\%$) and by the occupancy which measures the percentage of time the drift tube is "dead" due to background events (which gave already a hit outside the 3σ-window). Obviously, the occupancy depends strongly on the maximum drift time and the background rate. Also the shaping scheme has a strong impact on the occupancy.

Both efficiencies have been measured using the information of ODYSSEUS as an external tracker.

5.6.1 Hit Efficiency

The hit efficiency remains very high even with a radiation background. Figure 5.15 shows the rate dependence of the hit inefficiency averaged over hit radii between 0 and 14 mm for the unipolar and the bipolar shaping ($Ar/N_2/CH_4$ 91/4/5 at 3 bar). In our average we exclude the 0.6 mm near the wall because in this domain the MDT starts becoming inefficient anyway [RIE:97a], and efficiency fluctuations as well as systematic errors due to wire displacements are bigger than the small rate-effect we are looking for.

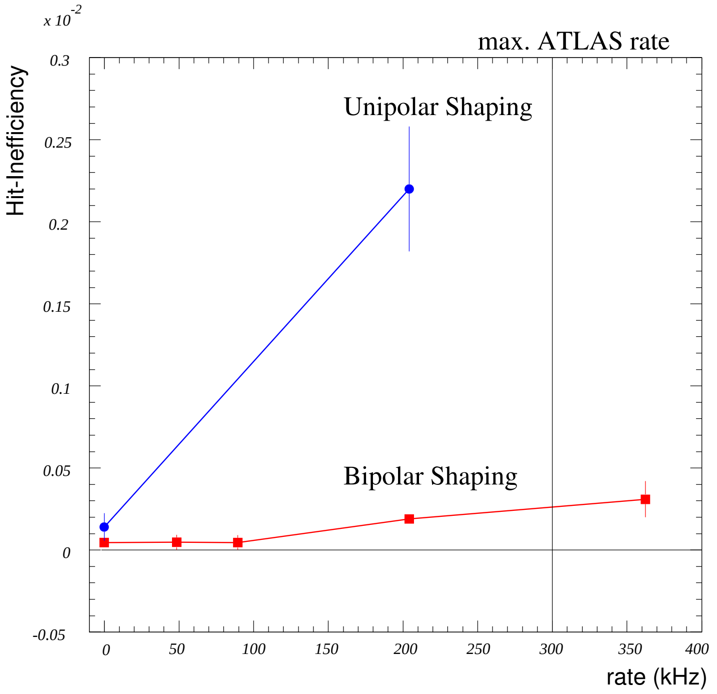

Figure 5.15: *Hit inefficiency as a function of the γ rate for unipolar and bipolar shaping (the threshold at* 0 kHz *is* 25 p.i.e*).*

The efficiency deterioration depends crucially on the shaping: It is most accentuated for the unipolar shaping due to its important negative baseline shift which increases the effective threshold (see Section 6.2.1). Therefore with a background more muon pulses stay below the threshold than without background. This effect however is very small: The maximum inefficiency is a few per-mille.

For the bipolar shaping there is no baseline shift. The tiny increase of inefficiency can be explained with the gain loss due to space-charge effects which – in a similar way as a baseline shift – translates into a higher effective threshold (see Section 6.2.2).

The hit efficiency was measured to be higher than 99.5 % for all shaping schemes even with a baseline shift due to high background rates. In the absence of a baseline shift (bipolar shaping) the hit efficiency was $>$ 99.95 %.

5.6.2 3σ-Efficiency

Measurements of the 3σ-Efficiency

The measurements of the 3σ-efficiency have been done with $Ar/N_2/CH_4$ 91/4/5. Since the maximum drift time of the baseline gas (Ar/CO_2 93/7) is bigger, the 3σ-efficiency will decrease stronger with the rate than for the gas presented here (see below). During track reconstruction typically only hits within three times the spatial resolution will be used. The amount of successfully reconstructed hits can be quantified by the 3σ-efficiency defined as

$$\eta_{3\sigma} = \frac{\text{hits with } |r(t_{\text{measured}}) - r_{\text{predicted}}| < 3\,\sigma(r_{\text{predicted}}, N_{\text{c}})}{\text{all tracks in a distance } r \text{ from the wire (given by ODYSSEUS)}} \,. \tag{5.15}$$

For the spatial resolution $\sigma(r, N_{\text{c}})$ at the track distance r and the count rate N_{c} we use the results of our measurements with ODYSSEUS which will be presented in Chapter 6, $r_{\text{predicted}}$ is the track distance predicted by ODYSSEUS and t_{measured} the measured drift time which is converted to a track distance by taking advantage of the rt-relation $r(t)$ (see Section 5.7).

Figures 5.16 and 5.17 show the rate dependence of the 3σ-efficiency. The 3σ-efficiency without background rate turned out to be only $\sim 90\,\%$, whereas we would expect an efficiency of about 95 % (5 % inefficiency due to δ-electrons). The discrepancy comes from the geometry in the test beam: The regarded tubes were located behind some support elements (spacer frame) which enhanced multiple scattering. Hence a certain number of muons was scattered outside the 3σ-window. However, apart from this offset the degradation with rate corresponds very well to the simulation presented in Figure 5.19 (unipolar shaping).

Since the probability for a δ-ray arriving earlier than the muon increases with the track radius, the 3σ-efficiency decreases from the wire to the wall. For an analogous reason the distance between two curves for different rates grows with increasing radius: The longer the drift time corresponding to the muon track, the bigger is the probability to have a background hit before the muon hit.

The dip near the wire is not due to δ-rays but to the (in principle incorrect) Gaussian treatment of the non-Gaussian errors of the rt-relationship in this domain [DEI:98].

Taking the average 3σ-efficiency over all radii r and plotting it versus the rate we obtain Figure 5.17. At the maximum ATLAS rate (safety factor five included) only 80 % of the muon hits would be reconstructed within 3σ. As mentioned above, these results represent the worst case, since the measurement region was located behind the spacer frame which caused an additional 3σ-inefficiency of about 5 %.

Double track separation can recover some of the shaded muon hits (see [RIE:97b, ALE:98b]).

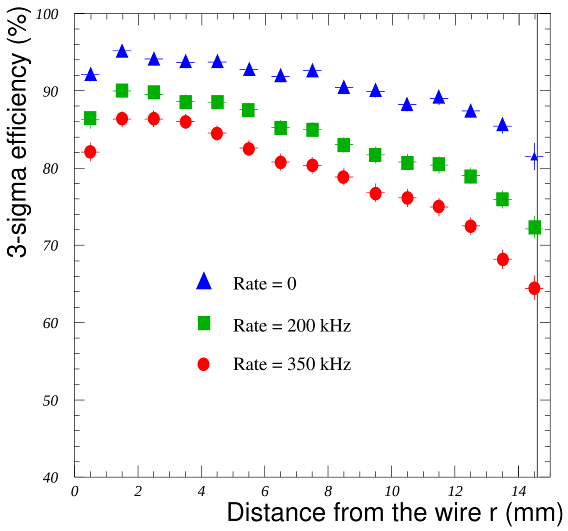

Figure 5.16: *3σ-efficiency as a function of the track radius for different γ rates. For this plot the unipolar shaping with maximum undershoot was used* ($Ar/N_2/CH_4$ 91/4/5).

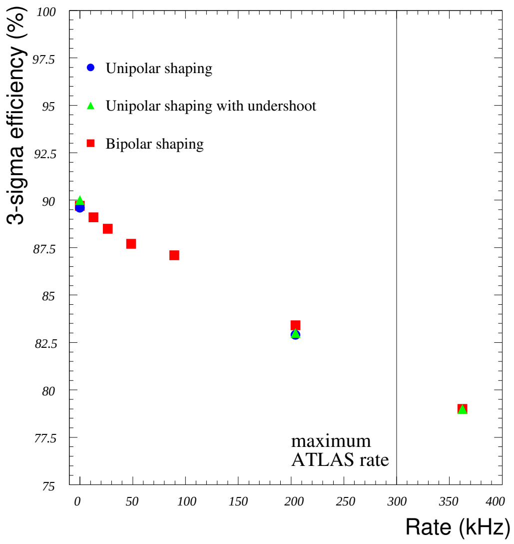

Figure 5.17: *3σ-efficiency averaged over r as a function of the γ rate, for the three shaping schemes studied* ($Ar/N_2/CH_4$ 91/4/5).

Simulated 3σ-Inefficiencies for Different Shaping Schemes

Due to the different maximum drift times of $Ar/N_2/CH_4$ 91/4/5 and Ar/CO_2 93/7 we expect the 3σ-inefficiencies to be different, too. Since the 3σ-efficiency at high background rates was only measured for $Ar/N_2/CH_4$ 91/4/5, the two gases were compared in the simulation. Besides the maximum drift time the shape of the rt-relation also influences the efficiency (see [RIE:97b]).

In the simulation background pulses with the desired frequency were superimposed to the muon signal. The inefficiency was obtained by counting the muon pulses which produced no hit at a 20 p.i.e discriminator threshold.

Figures 5.18 and 5.19 show the inefficiencies for different shaping schemes and readout scenarios. Obviously bipolar shaping and reading out all hits shows the lowest inefficiencies for both gases since the bipolar signal is rather short. However, reading out all hits (i.e. about three hits per signal) would demand a far higher capacity of the TDC LVL1 buffer. Furthermore we would lose the information, which one of the hits belongs to the leading edge. That would deteriorate the tracking efficiency. The other schemes presented in the plot only give one hit per signal. This is achieved by either introducing artificial dead time or only reading out the first hits. However, also “good” hits are suppressed by these measures. Hence the inefficiency increases. The unipolar shaping in the plot is also adapted to give one threshold crossing per signal, which implies “soft” tail cancellation for Ar/CO_2 93/7 and hence a prolongation of the dead time (see Section 5.5).

The $\sim 5\,\%$ inefficiency at 0 Hz is the inefficiency due to δ-electrons created by the muon in the tube wall.

Using bipolar shaping with a fixed dead time of 700 ns for Ar/CO_2 93/7 will result in 25 % 3σ-inefficiencies at the highest background rates (300 kHz). DICE [ART:95] simulations showed that such high inefficiencies do not degrade dramatically the pattern-recognition efficiency and are still tolerable. This shaping scheme was found to be the most convenient and robust solution for the MDT front-end electronics.

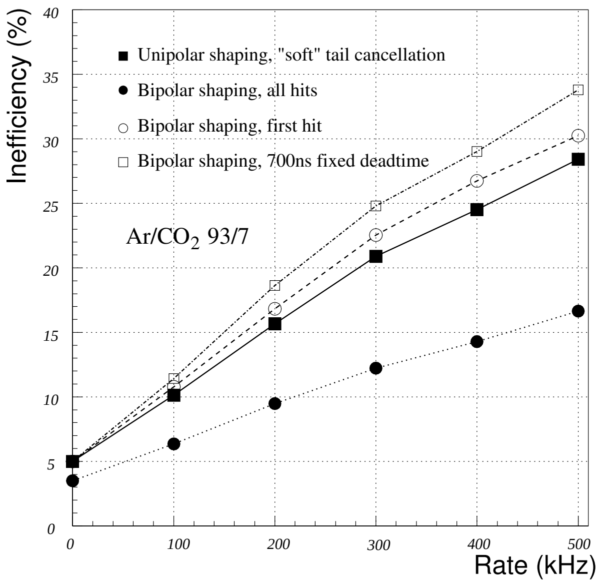

Figure 5.18: *Single-tube inefficiencies for* Ar/CO_2 93/7.

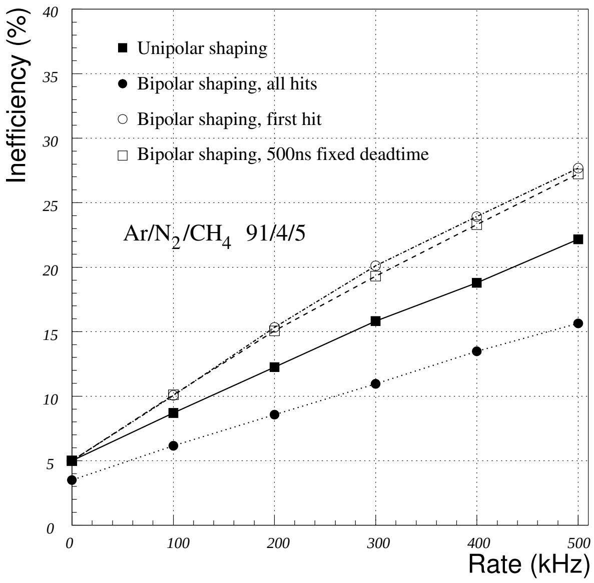

Figure 5.19: *Single-tube inefficiencies for* $Ar/N_2/CH_4$ 91/4/5.

The 3σ-efficiency was simulated for Ar/CO_2 93/7 and $Ar/N_2/CH_4$ 91/4/5 and different read-out schemes. For the baseline gas – due to the longer maximum drift time – the occupancy and hence the inefficiency grows faster with the background rate. Moreover there is an impact of the shaping scheme, which determines the average dead time after a signal. Bipolar shaping with a fixed dead time of 700 ns, providing only one hit per signal but causing inefficiencies up to 25 %, was found to be the most convenient and robust solution for the MDT front-end electronics.

5.7 Space-Time Relationship

The space-time relationships (rt-relations) were obtained from the test-beam measurements. Using the track prediction of the silicon telescope (ODYSSEUS), the distance between the muon track and the wire $r_{\text{predicted}}$ was calculated. Figure 5.20 shows the measured drift times t_{measured} (first hits) plotted versus $r_{\text{predicted}}$ for $Ar/N_2/CH_4$ 91/4/5. The residuals $\Delta r = r(t_{\text{measured}}) - r_{\text{predicted}}$ were filled into histograms for ~ 0.6 mm slices in r (see Figure 5.21). By fitting Gaussians to these distributions and matching the means with 0, $r(t_{\text{measured}})$ was found for each bin. The resolution for each r-bin is defined as the Gaussian σ of the residual distribution. During the operation of ATLAS the rt-relation will be obtained by auto-calibration [VIE:96, CRE:97].

In Figure 5.20 we can see a lot of hits with much smaller t_{measured} than expected. Those hits are due to background hits and δ-rays, which hide the muon signal. However, plot 5.21 gives evidence that even at the highest rates considered for ATLAS, the resolution (Gaussian σ of the residual distribution) is well defined. Hence the non-Gaussian tails are negligible for the resolution measurement but they have an important impact on the 3σ-efficiency (see Section 5.6.2).

It has been shown in [DEI:98], that close to the wire the residual distributions become significantly non-Gaussian. It was found that a combination of a Gaussian and an extreme value function ist more appropriate to describe the data. Here, these effects are neglected and the resolution was defined as described above for all r.

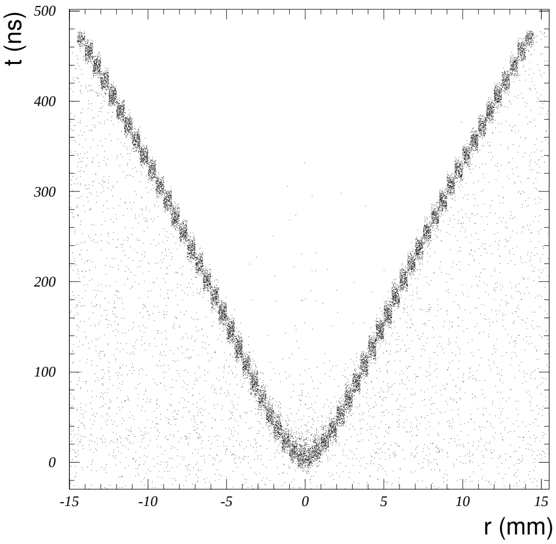

Figure 5.20: *Drift times t_{measured} versus the silicon-telescope predictions $r_{\text{predicted}}$ for $Ar/N_2/CH_4$ 91/4/5 at 3 bar and a gas gain of 2×10^4. The background rate is 333.5 kHz. The cascade-like form comes from the binning.*

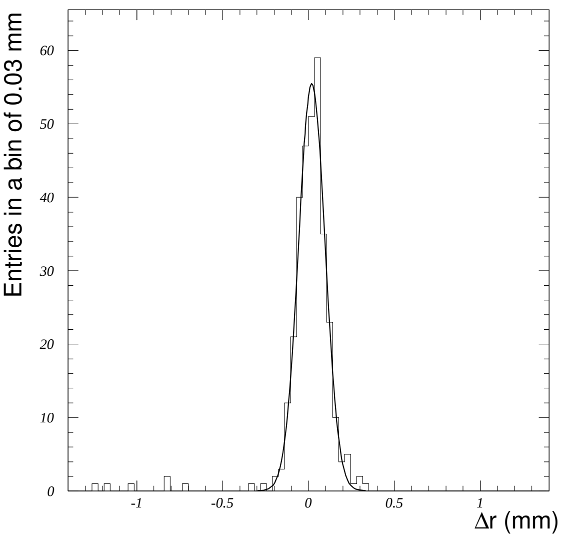

Figure 5.21: *Residual distribution of the raw data in a slice of 10.8 mm $< r_{\text{predicted}} <$ 11.4 mm. The background rate is 333.5 kHz.*

Figure 5.22 shows the rt-relations for several gas mixtures. The Ar/CO_2 mixtures are non-linear, i.e. the drift velocity changes with different electric fields ($E(r) \propto \frac{1}{r}$). Some drift velocities as a function of E/p are shown in Figure 3.3. Non-linear gases are far more sensitive to variations of the environmental parameters and hence cause systematic errors to the track-position measurement (see Chapter 7). For some gas mixtures containing CH_4 the drift velocity is almost independent of the electric field. Changes of the drift field due to space charge have hardly any impact, hence the resolution stays unchanged even for high background rates (see Section 6.1). So far, no linear gas without CH_4 has been found, although some gases containing CF_4 come close.

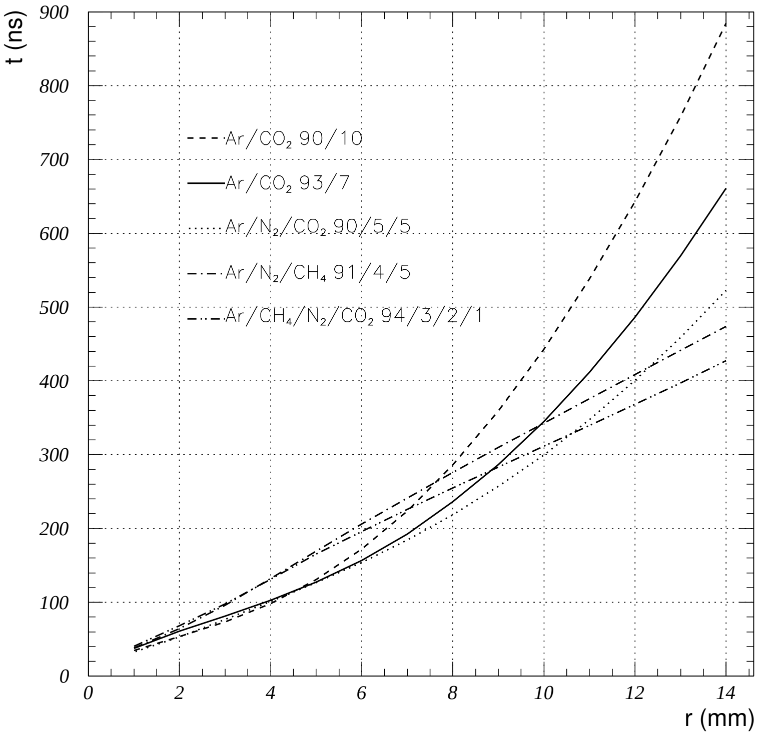

Figure 5.22: *Space-time relationships for different gas mixtures at a gas gain of* $G = 2 \times 10^4$ *and a gas pressure of* 3 bar.

Another important number is the maximum electron drift time $t_{\max}$ which has direct consequences on the occupancy. Figure 5.22 gives evidence that $t_{\max}$ decreases with the CO_2 content in Ar/CO_2 mixtures. An optimum in terms of highest possible drift velocity against lowest possible afterpulsing rate was found with the baseline-gas mixture Ar/CO_2 93/7 ($t_{\max} = 700\,\text{ns}$).

The rt-relations for several drift gases were measured and simulated. One important property of drift gases is the linearity of the rt-relation. Furthermore $t_{\max}$ is an important parameter which has to be minimised. Ar/CO_2 mixtures are non-linear drift gases and speed up with decreasing CO_2 content. The maximum drift time of the baseline mixture is $t_{\max} = 700\,\text{ns}$.

5.8 Impact of a Magnetic Field

With a magnetic field B parallel to the wire, the electrons do not travel on radial approach lines towards the wire, but under an angle Ψ (i.e. the Lorentz angle) which is approximately given by

$$\tan\Psi = \frac{eB}{m}\tau \,, \tag{5.16}$$

where $\frac{eB}{m}$ is the cyclotron frequency and τ is the mean time between collisions of the electrons with the gas molecules. Consequently the drift time t for a certain drift distance r will increase.

In order to understand the properties of Ar/CO_2 93/7 in the presence of a magnetic field parallel to the wire, GARFIELD simulations[7] with a magnetic field of $B = 0.5\,\mathrm{T}$ ($G = 2\times10^4$, $p = 3\,\mathrm{bar}$) have been done. Figure 5.23 shows measurements [MAC:82] and MAGBOLTZ [BIA:98] simulations of the Lorentz angle Ψ for Ar/CO_2 90/10 at a pressure $p = 1.02\,\mathrm{atm}$ in order to evaluate the validity of the simulations. It can be seen that the simulation yields a very good estimate of the effect of the magnetic field B. Plot 5.24 presents simulations of the Lorentz angle Ψ for several gases as a function of the radius r.

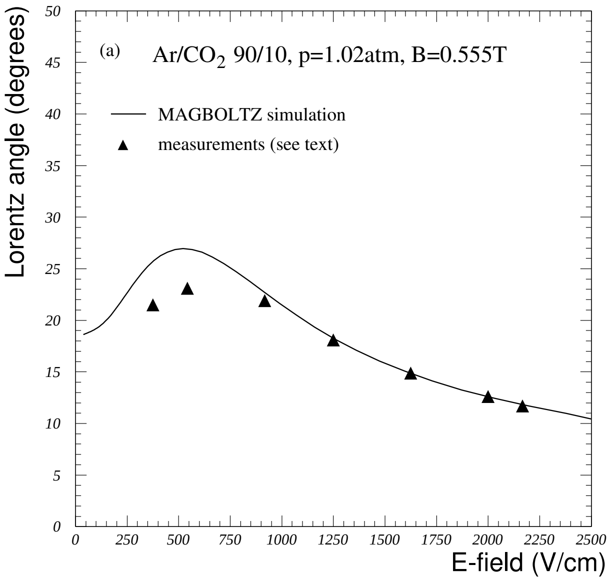

Figure 5.23: *Lorentz angle Ψ. Comparison of MAGBOLTZ* [BIA:98] *simulations with measurements* [MAC:82].

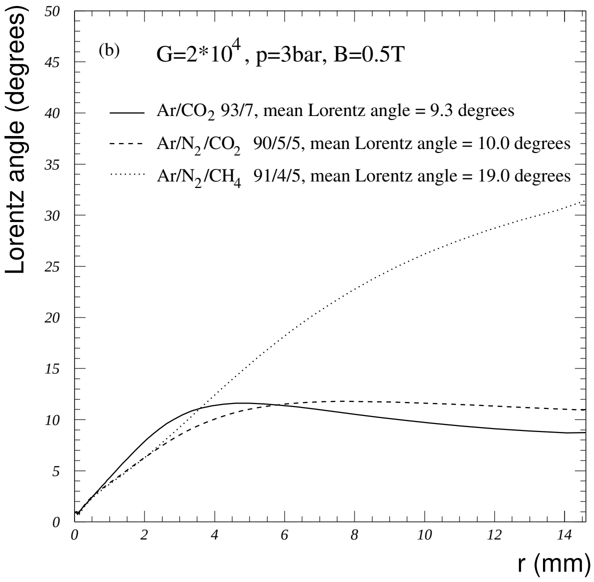

Figure 5.24: *Simulations of the Lorentz angle Ψ as a function of the drift radius r for three different drift gases.*

[7]The transport properties in the presence of a magnetic field B were simulated with MAGBOLTZ [BIA:98].

The following points have been found for Ar/CO_2 93/7:

- the Lorentz angle is $\langle\Psi^{0.5\,\mathrm{T}}\rangle = 9.3\,^\circ$ which is small compared to other gases,
- the maximum drift time t_{max} increases only slightly to $t_{\mathrm{max}}^{0.5\,\mathrm{T}} \approx 720\,\mathrm{ns}$ ($t_{\mathrm{max}}^{0\,\mathrm{T}} \approx 700\,\mathrm{ns}$ without magnetic field); nevertheless, the rt-relation changes introducing systematic errors to the track-position measurement (see Chapter 7),
- the resolution without background rate remains almost unchanged or improves slightly due to the decreased drift velocity ($\bar{\sigma}^{0.5\,\mathrm{T}} = 59\,\mu\mathrm{m}$ instead of $\bar{\sigma}^{0\,\mathrm{T}} = 60\,\mu\mathrm{m}$ without magnetic field, both values without time slewing correction,
- the high-rate behaviour is not influenced by a magnetic field of this strength; i.e. the high-rate deterioration of the resolution stays the same ($\bar{\sigma}^{0.5\,\mathrm{T}} = 87\,\mu\mathrm{m}$ for 1400 Hz/cm without time-slewing correction).

For the other simulated gases the impact of a magnetic field is higher (see Figure 5.24).

A magnetic field parallel to the wire changes the drift path of the electrons. The angle between the drift paths with and without magnetic field is called the Lorentz angle Ψ. For the baseline mixture an average Lorentz angle of $\langle\Psi^{0.5\,\mathrm{T}}\rangle = 9.3\,^\circ$ was found. Simulations showed that a magnetic field of 0.5 T has a small impact on the maximum drift time and only a negligible effect on the spatial resolution.

Chapter 6

Spatial Resolution

6.1 Resolution Studies on Different Drift Gases

The spatial resolution as a function of the drift distance r is defined as the width of the residual distribution in discrete slices in r (see Section 5.7, Figure 5.21). The residual distributions are obtained by comparing the track position $r_{\mathrm{predicted}}$, predicted by the reference system (ODYSSEUS), and the track position $r(t_{\mathrm{measured}})$, measured with the drift tube.

In order to be able to compare different drift gases we want to define one figure of merit which describes the spatial resolution conveniently. The average tube resolution is given by quadratically averaging the resolution as a function of r. However, we are more interested in the resolution for a track fit, for which hits are weighted by $\frac{1}{\sigma(r)^2}$. Hence a better figure of merit for our purposes is $\bar{\sigma}$, the **I**nverse **Q**uadratic **A**verage (IQA), defined by (b is the inner tube radius):

$$\bar{\sigma} = \frac{1}{\sqrt{\left\langle \frac{1}{\sigma^2} \right\rangle}} , \qquad \text{with} \qquad \left\langle \frac{1}{\sigma^2} \right\rangle = \frac{1}{b} \int_0^b \frac{1}{\sigma^2(r)} \, \mathrm{d}r \; . \tag{6.1}$$

This section will introduce high-rate measurements of the spatial resolution for several drift gases. From these results the profound understanding of high-rate effects was obtained, which is subject of Section 6.2. Obviously, the simulations which are shown here already involve the exact understanding of the different effects.

6.1.1 Spatial Resolution of $Ar/N_2/CH_4$ 91/4/5

The set-up for these measurements was described in Section 4.2. The measurements were performed with a high local background rate and a high rate on the tube in order to investigate both, high-rate space-charge effects and electronics effects.

Figure 6.1 compares measurements with GARFIELD [VEE:98] simulations. The spatial resolution as a function of the drift distance r is shown for no background and a count rate

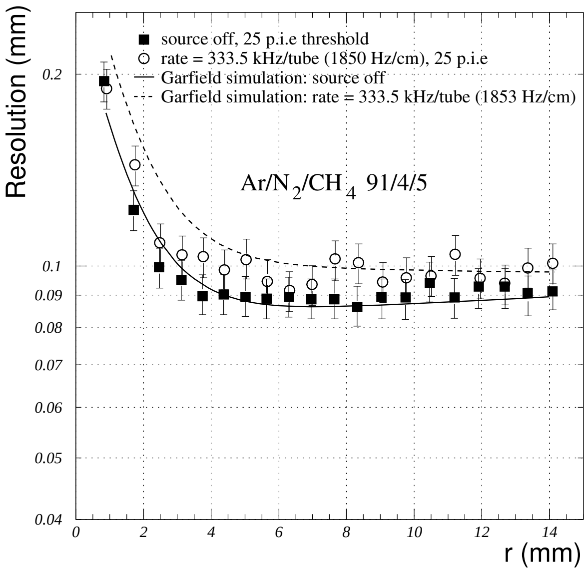

Figure 6.1: *Spatial resolution as a function of the drift distance ($G_0 = 2 \times 10^4$). Measurement and simulation for* $Ar/N_2/CH_4$ 91/4/5. *Space-charge effects and electronics effects contributed to the resolution deterioration.*

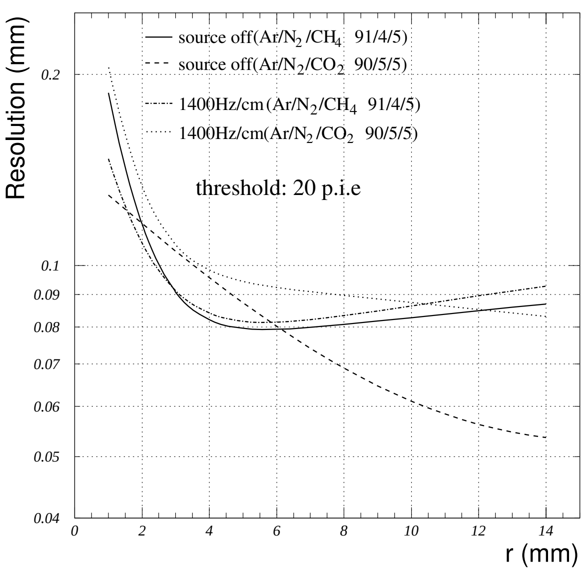

Figure 6.2: *GARFIELD simulations for* $Ar/N_2/CH_4$ 91/4/5 *and* $Ar/N_2/CO_2$ 90/5/5 *at* 1400 Hz/cm, *without any electronics effects. This plot can be compared with Figures 6.3 and 6.4.*

of 1850 Hz per cm tube length (333.5 kHz count rate of the tube). We see good agreement between the measurements and the simulations (gas gain without rate $G_0 = 2 \times 10^4$, $\sigma_{\text{noise}} = 4.5$ p.i.e, 25 p.i.e threshold, 3 bar gas pressure). The resolution deterioration is mainly caused by the baseline shift.

Figure 6.2 shows the simulated resolution for $Ar/N_2/CH_4$ 91/4/5 and $Ar/N_2/CO_2$ 90/5/5 with the same noise level ($\sigma_{\text{noise}} = 3.8$ p.i.e) and discriminator threshold (20 p.i.e) like for the measurements with the Ar/CO_2 mixtures (see below). The background rate is 1400 Hz/cm, the count rate of the tube is small ($\sim$ 4.5 kHz). Therefore only space-charge effects contribute to the resolution deterioration. This allows to compare the various drift gases. The linear drift gas $Ar/N_2/CH_4$ 91/4/5 shows only a very small resolution deterioration even at high background rates; the deterioration is mainly caused by the gain drop, whereas the resolution of $Ar/N_2/CO_2$ 90/5/5 deteriorates stronger with rate due to its non-linearity (field fluctuations, see Section 6.2).

Measurements and simulations of the resolution curves for $Ar/N_2/CH_4$ 91/4/5 agree very well. Electronics effects deteriorate the measured resolution moderately. By switching off electronics effects by reducing the count rate of the tube (only high local irradiation left) the deterioration for this gas as a function of rate vanishes almost entirely.

6.1.2 Spatial Resolution of Ar/CO_2 Mixtures

The spatial resolution was measured for Ar/CO_2 92/8, Ar/CO_2 93/7 and Ar/CO_2 94/6. The σ_{noise} was 3.8 p.i.e, the threshold was 20 p.i.e, which was approximately $5 \times \sigma_{\text{noise}}$. The exact set-up of these measurements is given in Section 4.4. Note that for these measurements the rate on the tube was kept low unlike for the measurements described above. The main reason for that was to simulate the ATLAS environment, where electronics effects of a resolution deterioration will be kept on a minimum (see Section 6.2) and to investigate the performance of the baseline gas Ar/CO_2 93/7.

Figures 6.3 and 6.4 compare the drift-radius dependence of the spatial resolution with GARFIELD [VEE:98] simulations. A detailed description of the way the simulations without rate effects were done can be found in Chapter 3, the rate effects are described extensively in Section 6.2. Simulations and measurements show very good agreement. The main effect of resolution deterioration for Ar/CO_2 mixtures – and for other non-linear gases – are the drift-field fluctuations due to space-charge fluctuations.

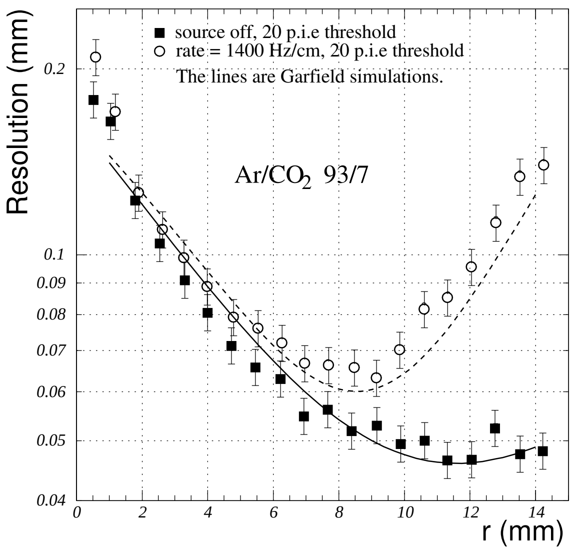

Figure 6.3: *Spatial resolution as a function of the drift distance ($G_0 = 2 \times 10^4$). Measurement and simulation for the* Ar/CO_2 93/7 *mixture. The shape of the resolution curve is very similar for all* Ar/CO_2 *mixtures.*

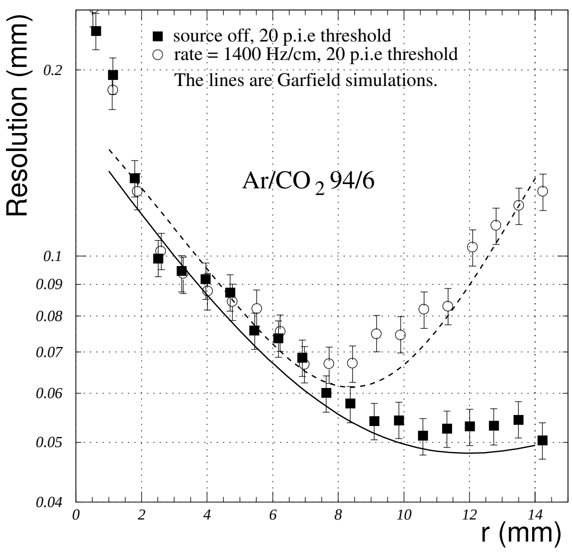

Figure 6.4: *Spatial resolution as a function of the drift distance ($G_0 = 2 \times 10^4$). Measurement and simulation for the* Ar/CO_2 94/6 *mixture.*

In Table 6.1 the values of $\bar{\sigma}$ for different gas mixtures are listed. For low background rates the Ar/CO_2 mixtures have a very much better resolution than linear and faster gases. Even at the highest background rates Ar/CO_2 mixtures still have better resolution.

gas mixture	$\bar{\sigma}(0\,\mathrm{Hz/cm})$ (μm)	$\bar{\sigma}(1400\,\mathrm{Hz/cm})$ (μm)	t_{max} (ns)
$Ar/N_2/CH_4$ 91/4/5 *	89	91	485
$Ar/N_2/CO_2$ 90/5/5 *	72	97	560
$Ar/CH_4/N_2/CO_2$ 94/3/2/1 *	95	98	440
Ar/CO_2 90/10 *	53	80	950
Ar/CO_2 92/8	56	81	770
Ar/CO_2 93/7	60	87	700
Ar/CO_2 94/6	66	88	630

Table 6.1: *Resolution $\bar{\sigma}$ (IQA) and maximum drift time t_{max} for different gas mixtures. The gases marked with * were only simulated. For all measurements and simulations the σ_{noise} was 3.8 p.i.e, the threshold was at 20 p.i.e and the gas gain was $G_0 = 2 \times 10^4$. The time-slewing correction was not applied. The errors on the values of $\bar{\sigma}$ are $3\,\mu$m.*

The spatial resolution of the non-linear Ar/CO_2 mixtures deteriorates significantly with rate due to drift-field fluctuations. Measurements and simulations agree very well. For the baseline gas Ar/CO_2 93/7 we expect – without time-slewing correction – a resolution of $\bar{\sigma}(0\,\mathrm{Hz/cm}) = 60\,\mu\mathrm{m}$ at low rates and $\bar{\sigma}(1400\,\mathrm{Hz/cm}) = 87\,\mu\mathrm{m}$ at the "hottest" points of the spectrometer.

6.1.3 Time-Slewing Corrections

Because of charge fluctuations in the leading edge of the signal, the rise time of the signal varies. This results in fluctuations of the threshold crossing time and therefore in degraded resolution. Since the information about the time slewing is still contained in the signal rise time, corrections can be applied.

In [RIE:97a], [RIE:97b] two different methods of time-slewing corrections are introduced. Those two methods are the second-threshold correction and the leading-edge-charge correction (see Figure 6.5).

1. **Second-Threshold Correction:**
   Data were taken with two discriminator thresholds (25 p.i.e and 100 p.i.e). In this method the noise causes a jitter on both threshold crossings (σ_t), consequently the difference between the two thresholds has an error of $\sigma_t\sqrt{2}$.

2. **Leading-Edge-Charge Correction:**
   This kind of time-slewing correction is the baseline for the ATLAS MDTs. In our measurements the leading-edge integral (20 ns width) was calculated from the FADC

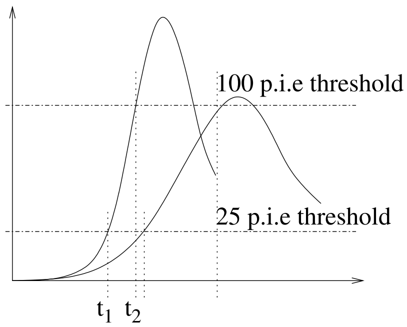

(a) Second-threshold correction

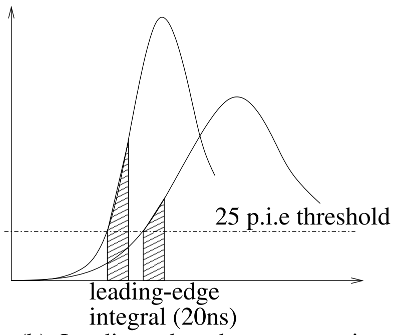

(b) Leading-edge-charge correction

Figure 6.5: *Time-slewing corrections. (a) shows the second-threshold correction: The time difference between the two threshold crossings supplies information about the slope of the leading edge. (b) shows the leading-edge-charge correction: The integral over a part of the leading edge contains the information about the slope of the leading edge.*

data. The noise level only affects the threshold crossing: The noise averages out for the leading-edge charge. This explains the better performance of this method.

In our study, both methods for time-slewing correction were tested with and without background using the unipolar shaping with undershoot.

In order to find the systematic deviations of the measured drift time from the ideal one, we determine the time residuals ($t(r)$ is the inverse function of the rt-relation $r(t)$)

$$\Delta t = t_{\text{measured}} - t(r_{\text{predicted by ODYSSEUS}}) \tag{6.2}$$

as a function of the drift time and the threshold-crossing time-difference (method 1) or the leading-edge charge (method 2). A 2-dimensional polynomial fit (2^{nd} order in the drift time and 4^{th} order in the threshold difference or leading-edge charge, respectively) was then performed. Figures 6.6 and 6.7 show two-dimensional projections of these polynomials for different drift time slices (each 100 ns).

The polynomials were used afterwards to determine the drift time corrections necessary to improve the resolution. The fit shown in Figure 6.6 provides Δt as a function of the drift time and the threshold difference. In the same way, Figure 6.7 provides Δt as a function of the drift time and the leading-edge integral. By measuring these two values for each incoming muon signal, the correction Δt could be predicted. Hence the new reconstructed track distance was calculated by $r(t_{\text{measured}} + \Delta t)$ instead of the uncorrected distance $r(t_{\text{measured}})$.

The uncorrected resolution curves with and without background together with the corrected curves are presented in Figures 6.8 and 6.9. The lines are drawn to guide the eye. The statistical error of the individual points is about 7 μm. Unfortunately the two starting points (i.e. the tube resolutions without any corrections) are not equal because tubes with different noise levels were used. The tube to which leading-edge-charge correction was applied had a higher noise level and hence worse resolution before the correction. Still, after correction both tubes have about the same resolution.

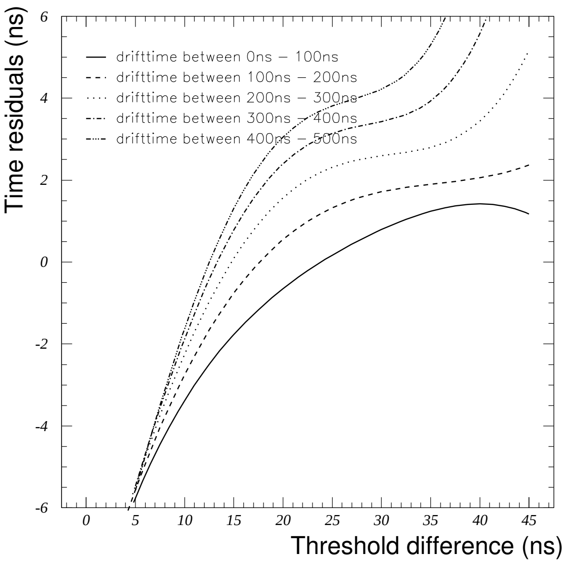

Figure 6.6: *Δt as a function of the threshold difference for the second-threshold correction. The projections become steeper with longer drift times because the leading edges become steeper.*

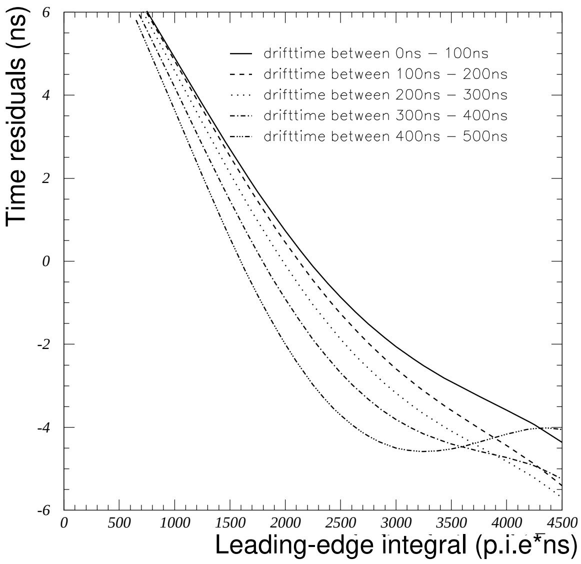

Figure 6.7: *Δt as a function of the leading-edge integral for the leading-edge-charge correction.*

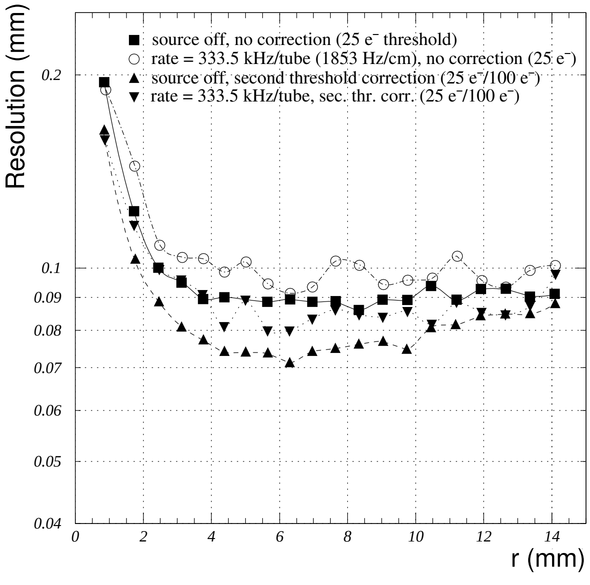

Figure 6.8: *Improvement of the resolution for the second-threshold correction.* e$^-$ *in the plot stands for* p.i.e.

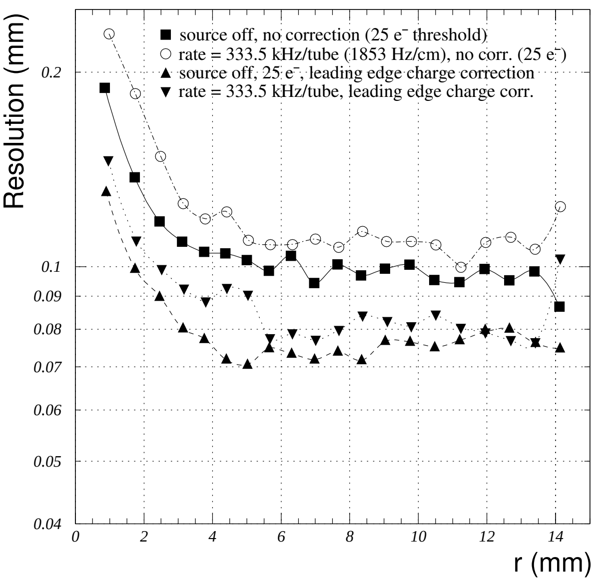

Figure 6.9: *Improvement of the resolution for the leading-edge-charge correction.* e$^-$ *in the plot stands for* p.i.e.

Calculating the IQA for the different resolution curves yields Table 6.2 for the second-threshold correction and Table 6.3 for the leading-edge-charge correction.

The improvement in both tables is calculated as the quadratic difference between the IQAs without and with correction. It can be seen that the leading-edge-charge correction gives

gas	IQA $\bar{\sigma}$ (all values in μm)					
	without background rate			with background rate 1853 Hz/cm, 333.5 kHz		
	no corr.	corr.	improvement	no corr.	corr.	improvement
$Ar/N_2/CH_4$ 91/4/5	95	79	53	102	86	55

Table 6.2: *Measured performance of the second-threshold correction. The errors are about 3 μm.*

gas	IQA $\bar{\sigma}$ (all values in μm)					
	without background rate			with background rate $Ar/N_2/CH_4$: 1853 Hz/cm, 333.5 kHz Ar/CO_2: 1400 Hz/cm, 4.5 kHz		
	no corr.	corr.	improvement	no corr.	corr.	improvement
$Ar/N_2/CH_4$ 91/4/5	104	79	68	119	87	81
Ar/CO_2 92/8	56	52	21	81	78	22
Ar/CO_2 93/7	60	56	22	87	82	29
Ar/CO_2 94/6	66	62	23	88	80	37

Table 6.3: *Measured performance of the leading-edge-charge correction. The errors are about 3 μm.*

better results than the second-threshold correction. The rate effect itself remains, but gets slightly extenuated, because time slewing as a consequence of baseline shift[1] and gain drop is reduced. Table 6.3 shows that a time-slewing correction is far less successful for the Ar/CO_2 mixtures because of the smaller diffusion coefficients (see Figure 3.6) and the smaller drift velocity (see Figure 3.4). Hence a jitter on the threshold-crossing time due to time slewing translates into smaller errors on the position measurement. The faster the Ar/CO_2 mixture gets the worse the spatial reolution becomes, but the acceleration of the gas also enhances the effectiveness of the time-slewing correction. Note that even with the highest background rate all three Ar/CO_2 mixtures have a spatial resolution $\bar{\sigma}$ of about 80 μm if a correction is applied. The leading-edge-charge correction is foreseen for the ATLAS MDT system.

Two kinds of time-slewing corrections were tested in the test beam. The leading-edge-charge correction is more effective than the second-threshold correction. The improvement of the resolution of the Ar/CO_2 mixtures is much smaller than for $Ar/N_2/CH_4$ 91/4/5 because the drift velocity and the diffusion coefficients are smaller. For the baseline gas with leading-edge-charge correction a resolution of $\bar{\sigma}_{corr}(0\,\mathrm{Hz/cm}) = 56\,\mu\mathrm{m}$ at low rates and $\bar{\sigma}_{corr}(1400\,\mathrm{Hz/cm}) = 82\,\mu\mathrm{m}$ at high background rates was measured.

[1]Only for $Ar/N_2/CH_4$ 91/4/5 measurements.

6.1.4 Resolution as a Function of Rate

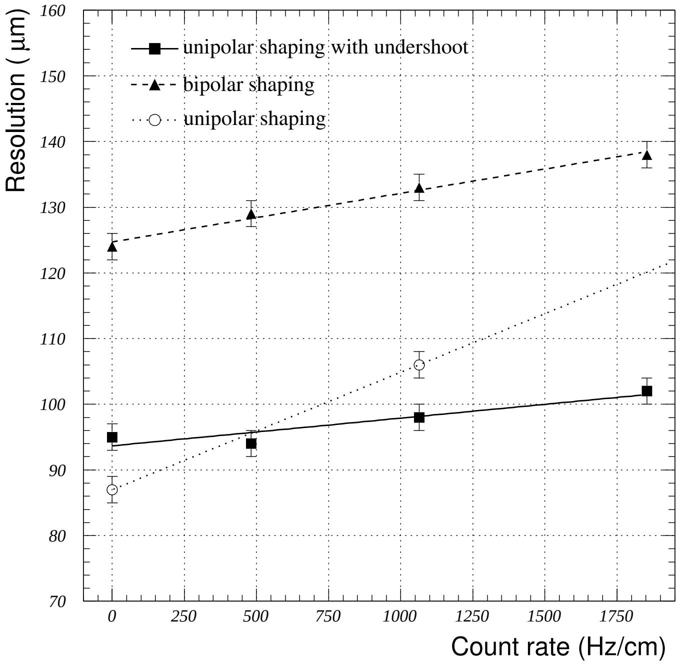

Figure 6.10: *Resolution $\bar{\sigma}$ (IQA) versus rate for different kinds of shaping* ($Ar/N_2/CH_4$ 91/4/5 *at* 3 bar *and* $G_0 = 2 \times 10^4$*). The IQA was calculated according to Equation (6.1).*

Figure 6.10 shows the deterioration of resolution with higher background rates for $Ar/N_2/CH_4$ 91/4/5 at 3 bar and $G_0 = 2 \times 10^4$. From the comparison of three shaping schemes (see Section 4.3) we can learn the following:

- **Resolution for Unipolar Shaping:**
  For this kind of shaping we can observe a fast deterioration of resolution with higher rates. This is due to the large baseline shift and baseline fluctuations (see Section 6.2.1).

- **Resolution for Unipolar Shaping with Undershoot:**
  The baseline shift and the baseline fluctuations were kept small due to the undershoot (see Section 6.2.1). Therefore this shaping shows a smaller deterioration of resolution with rate than unipolar shaping.

- **Resolution for Bipolar Shaping:**
  The bad resolution without background rate is due to the factor 1.3 higher noise level and the factor 2 bigger peaking time t_p for this kind of shaping in our test set-up. Another problem was, that the pulse heights after the bipolar shaping were a factor 4 smaller than after the unipolar shaping. Since the discriminators need a certain amount of charge to trigger a signal, this fact caused a time walk and hence worse resolution. This also explains the stronger resolution deterioration with rate than for the unipolar shaping with undershoot, because the gain drop boosted the time walk. With properly adjusted bipolar shaping we would expect a smaller deterioration with

background rate than for the other shaping schemes since baseline shift and baseline fluctuations are suppressed as it is shown in Section 6.2.1.

The main contributions to the resolution deterioration in Figure 6.10 are the baseline shift and the gain drop, which shift the threshold to higher primary ionisation electrons. This causes a rather linear degradation of the resolution with rate (→ linear fit in Figure 6.10). For a detailed description of the different contributions to high-rate resolution-deterioration see Section 6.2.

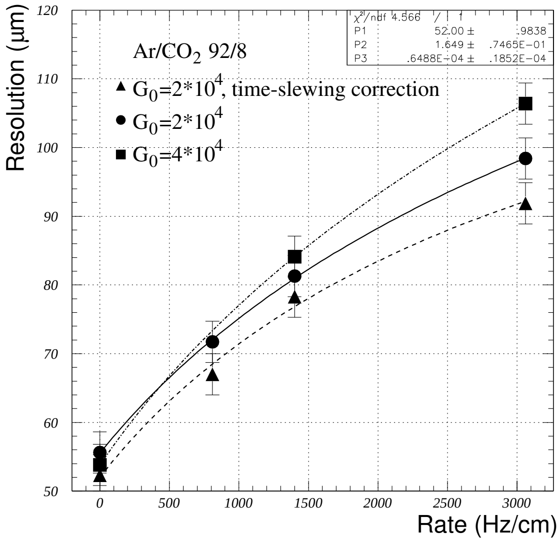

Figure 6.11: *Resolution $\bar{\sigma}$ (IQA) of* Ar/CO_2 92/8 *as a function of the rate.*

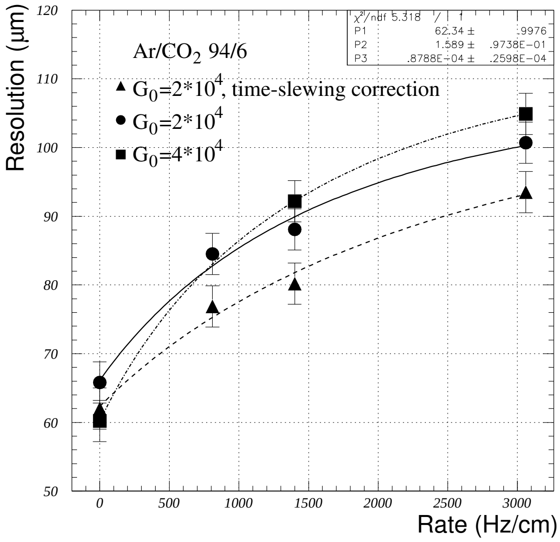

Figure 6.12: *Resolution $\bar{\sigma}$ (IQA) of* Ar/CO_2 94/6 *as a function of the rate.*

Figures 6.11, 6.12 and 6.13 show the IQAs $\bar{\sigma}$ as a function of rate for different Ar/CO_2 mixtures. The leading-edge-charge correction was used to correct for time slewing (full triangles). The highest background rates in ATLAS – including a safety factor five – are 1500 Hz/cm. The measurements presented in the plots go far beyond this rate. It can be seen that the resolution deterioration at a gas gain of $G_0 = 4 \times 10^4$ is more severe than for the lower gas gain because of almost twice the amount of space charge[2] being produced in the drift volume. For the higher gas gain the time-slewing correction is rather ineffective since the time-slewing contribution to the resolution is already quite small. For all three gas mixtures the resolution at a gas gain of 4×10^4 is slightly better without background rate but degrades quicker. At 1500 Hz/cm the resolution at the higher gain is always worse than for $G_0 = 2 \times 10^4$.

The fit functions in all three figures come from rather basic ideas. As discussed in Section 6.2 the prevailing high-rate effect is the field fluctuations. This effect grows with the square root of the background rate N_c (see Section 6.2.2). Hence the deterioration $\bar{\sigma}_{det}(N_c)$ is given by

$$\bar{\sigma}_{det}(N_c) = \sqrt{N_c} \cdot P2 \ , \tag{6.3}$$

where P2 determines the amplitude of the resolution deterioration. Using Equation (6.3) and taking into account that the deterioration $\bar{\sigma}_{det}(N_c)$ adds up quadratically with the

[2]Because of the higher gain drop for higher gas gains the amount of space charge does not increase linearly.

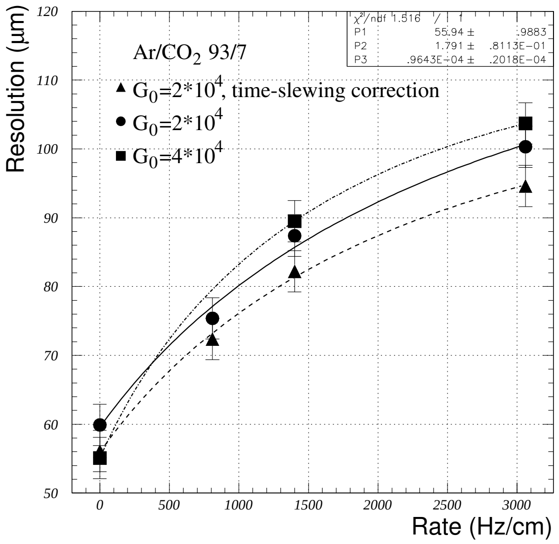

Figure 6.13: *Resolution $\bar{\sigma}$ (IQA) of* Ar/CO_2 93/7 *as a function of the rate.*

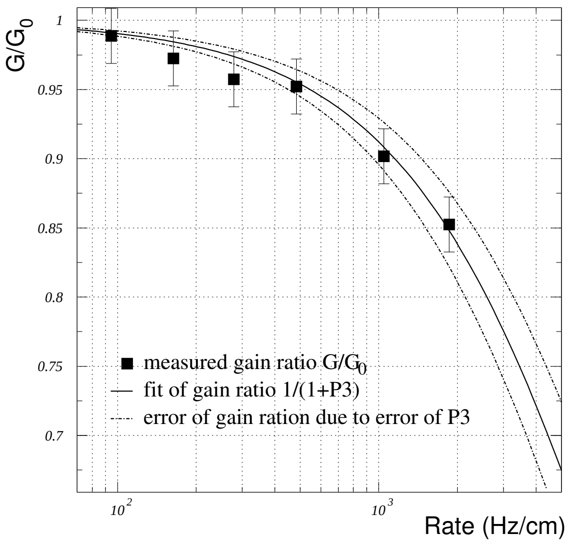

Figure 6.14: $G(N_\mathrm{c})/G_0 = \frac{1}{1+N_\mathrm{c}\cdot \mathrm{P3}}$ *extracted from the fit in Figure 6.13.*

resolution $\bar{\sigma}_0$ without background rate we can design a very simple fit function:

$$\bar{\sigma}(N_\mathrm{c}) = \sqrt{\bar{\sigma}_0^2 + \bar{\sigma}_{\mathrm{det}}(N_\mathrm{c})^2} = \sqrt{\mathrm{P1}^2 + N_\mathrm{c} \cdot \mathrm{P2}^2}\ , \tag{6.4}$$

where P1 stands for $\bar{\sigma}_0$. It turnes out, that this function does not fit to the data. This is due to the fact that a linear rise of the space charge with higher rates was assumed. This is obviously wrong because the gain drop reduces the space charge at high rates. Adding this effect to Equation (6.4) with a simple empirical function for $G(N_\mathrm{c})/G_0 \approx \frac{1}{1+N_\mathrm{c}\cdot P3}$ ($\mathrm{P2} \rightarrow \mathrm{P2} \cdot G(N_\mathrm{c})/G_0 = \frac{\mathrm{P2}}{1+N_\mathrm{c}\cdot \mathrm{P3}}$) yields:

$$\bar{\sigma}(N_\mathrm{c}) = \sqrt{\mathrm{P1}^2 + N_\mathrm{c} \cdot \left(\frac{\mathrm{P2}}{1 + N_\mathrm{c} \cdot \mathrm{P3}}\right)^2}\ . \tag{6.5}$$

Figure 6.14 shows the fitted gain ratio $G(N_\mathrm{c})/G_0 = \frac{1}{1+N_\mathrm{c}\cdot \mathrm{P3}}$ and compares it with measurements. The extraction of the gain drop from the high-rate resolution-deterioration fits very well to the measured data (see Section 6.2.2). In Figures 6.11, 6.12 and 6.13 the fit parameters for the time-slewing corrected resolution are printed in the right upper corner. The fit on the time-slewing corrected values turned out to be the most convenient since additional time slewing due to the gain drop is reduced.

The resolution deterioration with background rate was measured for different drift gases and shaping schemes. Whereas the resolution is degraded linearly for the linear drift gas since the prevailing effect is the baseline shift, in the Ar/CO_2 mixtures it deteriorates with $\sqrt{N_\mathrm{c}}$ because the dominant effect is the drift-field fluctuations due to the non-linearity of the gas. The gain drop can be extracted from the function $\bar{\sigma}(N_\mathrm{c})$ and agrees very well with the direct measurement.

6.2 Understanding of High-Rate Effects

The spatial resolution of drift tubes in the absence of a high background rate was already discussed in [RIE:97b] and [RIE:99]. Here we want to concentrate on the resolution deterioration due to high-rate effects (see also [ALE:98b] and [ALE:99c]). In the previous section the measurements have been presented which allow a qualitative and quantitative understanding of high-rate effects. We distinguish two groups of high-rate effects:

- **Electronics Effects:**
  The electronics effects depend on the total background rate of the tube, since for the readout all background pulses are relevant, independent of the position along the tube. The highest background rate per tube in ATLAS is 300 kHz. Two electronics effects have to be considered: baseline shift and baseline fluctuations. The quantitative understanding of these effects is crucial for the design of the front-end electronics.

- **Space-Charge Effects:**
  The space-charge effects depend on the rate per unit of length along the wire. The highest local rate in ATLAS is 1500 Hz/cm. At these rates the space charge of ion clouds drifting back to the cathode significantly changes both, the drift field and the gas gain. The resolution deterioration due to a change of the drift field depends on the non-linearity of a drift gas, the understanding of this effect therefore is an important input for choosing the drift gas for drift tubes operating in a high-background environment.

6.2.1 Electronics Effects

In this section we discuss in a quantitative way these two effects, which determine critically the design of the front-end electronics.

Since the signal trailing edge contains important information about the bunch-crossing time and would help to reject out-of-time background pulses, unipolar signal shaping preserving this information was investigated for the ATLAS MDT system. However, this kind of signal shaping requires active baseline restoration in order to reduce the electronics contribution to a resolution deterioration. It has been shown in Section 5.5 that, using the non-linear and relatively slow baseline gas, hit multiplicity represents a big problem for the read-out electronics. To avoid multiple hits, extremely “soft” tail cancellation is necessary which degrades heavily the trailing-edge resolution. According to that and due to considerations of robustness, this shaping scheme was abandoned.

Alternatively, bipolar shaping will be used which intrinsically avoids the electronics effects described below without additional active circuits; it has, however, the drawback of losing the information contained in the trailing edge of the signal.

In this section both shaping schemes are compared in terms of baseline shift and baseline fluctuations.

Baseline Shift

The tail of each signal caused by the ions drifting to the cathode is cancelled by the signal shaping to reduce dead time and pile-up.

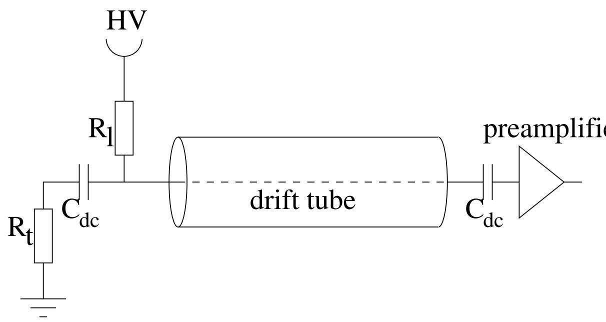

Figure 6.15: *Diagram of the drift tube and the read-out electronics (loading resistor $R_l = 1\,\mathrm{M}\Omega$, termination resistor $R_t = 380\,\Omega$, decoupling capacitors $C_{dc} = 500\,\mathrm{pF}$).*

While after each event the line charge on the wire recovers with a typical time constant of $2C_{dc}R_l = 1\,\mathrm{ms}$ (see Figure 6.15), the baseline will shift to negative values due to the AC-coupling between tube and front-end electronics. This shift will be quite small for one event but will sum up to rather big values at high background rates. Figure 6.16 (a) shows the principle. Subsequent muon pulses will start at the new baseline and hence the effective pulse heights decrease. The areas above and below the time axis have to cancel. This is the reason why an undershoot, which compensates already part of the muon signal ($\sim 20\,\%$ for unipolar shaping with undershoot), reduces the baseline shift. With bipolar shaping the whole charge of the muon pulse is compensated immediately after the signal, hence there is almost no baseline shift ($|\mathrm{baselineshift}| < 1\,\mathrm{p.i.e}$) and no baseline fluctuations (Figure 6.16 (b)), causing only a very small resolution deterioration of $\sigma_{\mathrm{shift}} - \sigma_{\mathrm{no\ shift}} < 1\,\mu\mathrm{m}$.

With our test electronics the baseline shift was measured for all three shaping schemes which were introduced in Section 4.3.

Figure 6.17 compares the baseline shifts for unipolar shaping with undershoot and bipolar shaping. As expected, at a background rate of 333.5 kHz per tube the baseline shift for bipolar shaping is negligible ($-1\,\mathrm{p.i.e}$), whereas for the unipolar shaping with undershoot the baseline is shifted by $-8.7\,\mathrm{p.i.e}$ (compare Figure 6.18). The non-linear dependence of the baseline shift on the background rate appears because a baseline shift reduces the additional charge per background pulse (the bigger the baseline shift is, the smaller becomes the area of the pulse above zero in Figure 6.16 (a)). Hence the bigger the baseline shift already is the less each subsequent pulse will contribute to a further increase of the baseline shift. Note that the baseline shift is only improved little by the $20\,\%$ undershoot of the unipolar shaping with undershoot. This is due to the fact that the baseline after each pulse returns to zero approximately exponentially. The $20\,\%$ undershoot cuts the maximum immediately after the pulse, but does not reduce too much the long tail. Hence the difference is very small. Nevertheless baseline fluctuations are reduced significantly (see below).

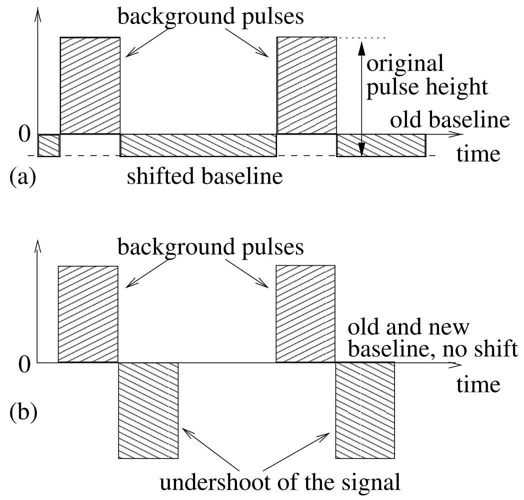

Figure 6.16: *Sketch explaining the origin of the baseline shift for unipolar shaping (a) and bipolar shaping (b). The rectangular pulses symbolise background pulses, the areas above and below the time axis have to cancel each other.*

A baseline shift deteriorates the resolution in the same way as a higher threshold level: The effective threshold level at high rates is the sum of the original threshold level and the absolute value of the baseline shift. Due to variations in cluster size or gain which cause varying slopes of the signal leading edges, the threshold-crossing times have a bigger jitter with higher thresholds. This effect is called time slewing (see Section 3.3) and is the reason for the resolution deterioration.

For these measurements preliminary ATLAS front-end electronics was used. The final front-end electronics will reduce the absolute value of the baseline shift to under 1 p.i.e.

Baseline Fluctuations

Since the distances between background pulses are not equally but exponentially distributed, and the energy deposit also varies, we do not expect the baseline to be constant but rather to fluctuate around a mean value, as seen in Figure 6.17. In (a) and (b) the width of the distribution is due to the noise level. In (c) the baseline fluctuations add quadratically[3] to the electronics noise σ_{noise}:

$$\sigma_{\mathrm{noise+fluct}} = \sqrt{\sigma_{\mathrm{noise}}^2 + \sigma_{\mathrm{fluct}}^2} \,. \tag{6.6}$$

Measuring the distribution of the baseline with ($\sigma_{\mathrm{noise+fluct}}$) and without background rate (σ_{noise}) and applying Equation (6.6) yields $\sigma_{\mathrm{fluct}} = 2.6$ p.i.e for unipolar shaping with undershoot at 300 kHz counting rate per tube. This number is highly dependent on the tail cancellation. For unipolar shaping without undershoot the baseline fluctuations σ_{fluct} increased to 6.4 p.i.e. For the bipolar shaping the distribution of the baseline level remains

[3]The distribution of the baseline fluctuations was approximated with a Gaussian distribution.

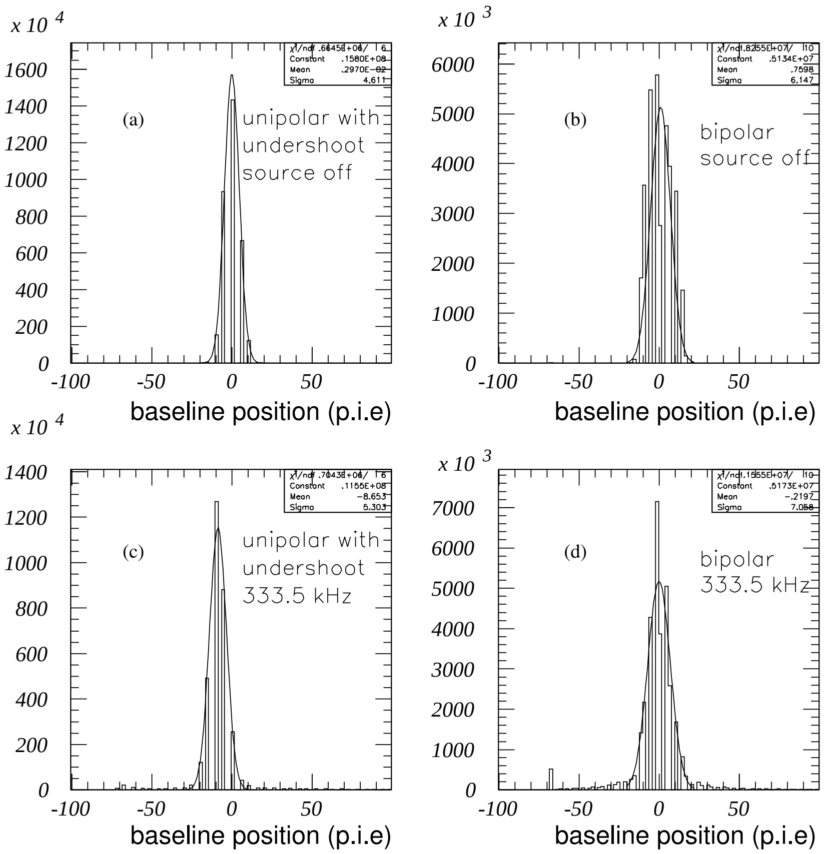

Figure 6.17: *Comparison of baseline shifts. The plots show histograms of the baseline (FADC readout) before the recorded muon pulse. In (a) and (b) the source was switched off, in (c) and (d) the photon background rate in the tube was* 333.5 kHz*. Comparing (a) and (c) one sees a baseline shift of* -8.7 p.i.e*; for the bipolar shaping the shift is much smaller (*-1 p.i.e*). The non-Gaussian tails in (d) are due to signal under- and overshoots after photon pulses.*

almost unchanged (see Figure 6.17 (b) and (d)) except for non-Gaussian tails due to signal under- and overshoots after a photon pulse. This means that bipolar shaping suppresses baseline fluctuations as well as baseline shift.

Baseline fluctuations cause a jitter on the threshold-crossing time because of the finite signal rise time, see Figure 6.19. Hence the resolution deteriorates.

Even though baseline fluctuations have only a minor direct impact on the resolution, they increase the minimum threshold level ($5 \times \sigma_{\text{noise}} \rightarrow 5 \times \sigma_{\text{noise+fluct}}$) which deteriorates the resolution significantly (see discussion of baseline shift and gain drop in Section 6.2.3). Hence baseline fluctuations should be kept to a minimum.

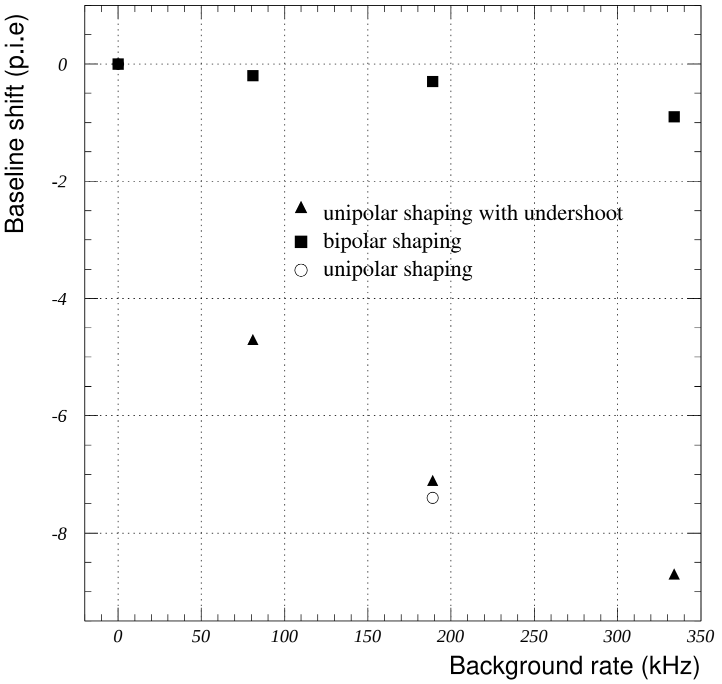

Figure 6.18: *Baseline shift as a function of the background rate for three different shaping schemes.*

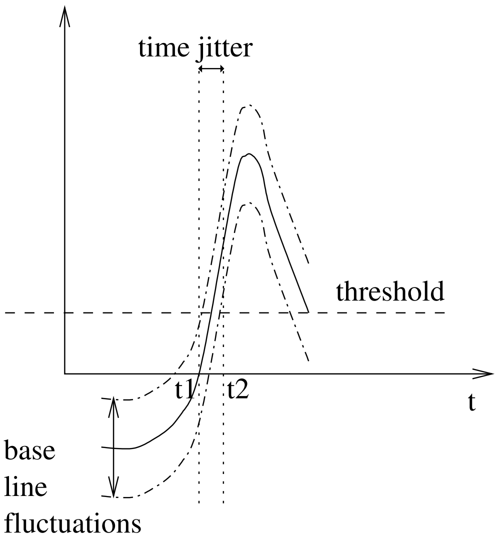

Figure 6.19: *Jitter on the threshold-crossing time caused by baseline fluctuations.*

The electronics effects of high-rate resolution-deterioration depend on the count rate per tube. Bipolar shaping will reduce these effects to a minimum. An expected absolute value of the baseline shift of < 1 p.i.e and baseline fluctuations of < 1 p.i.e will deteriorate the spatial resolution by less than $1\,\mu$m.

6.2.2 Space-Charge Effects

For our tube geometry and working point the ions created in the avalanche at the wire take about $t_{\mathrm{max}}^{\mathrm{ion}} \approx 4\,\mathrm{ms}$ to drift to the tube wall (cathode). The presence of ions in the drift region creates a space charge which modifies the electric field for subsequent events. This space charge lowers the electric field close to the wire and raises it close to the cathode.

Apart from considerations of tube lifetime during the ten years of ATLAS operation, the space-charge effects are the principal reason for a low gas gain ($G_0 = 2 \times 10^4$).

Gain Drop

Due to the decreased electric field at the anode wire the electron multiplication close to the wire is reduced and the gas gain drops $G_0 \to G$ (see Figure 6.20). The gain drop was measured by comparing the maximum of the distribution of the pulse integrals (i.e. the signal charges) with and without rate. Measurements are compared to an analytical model (see below) and show good agreement. The ratio of the gas gain at the worst expected background rate (1500 Hz/cm) and the gas gain without space charge G/G_0 will be of the order of 0.88 at a gas gain of $G_0 = 2 \times 10^4$.

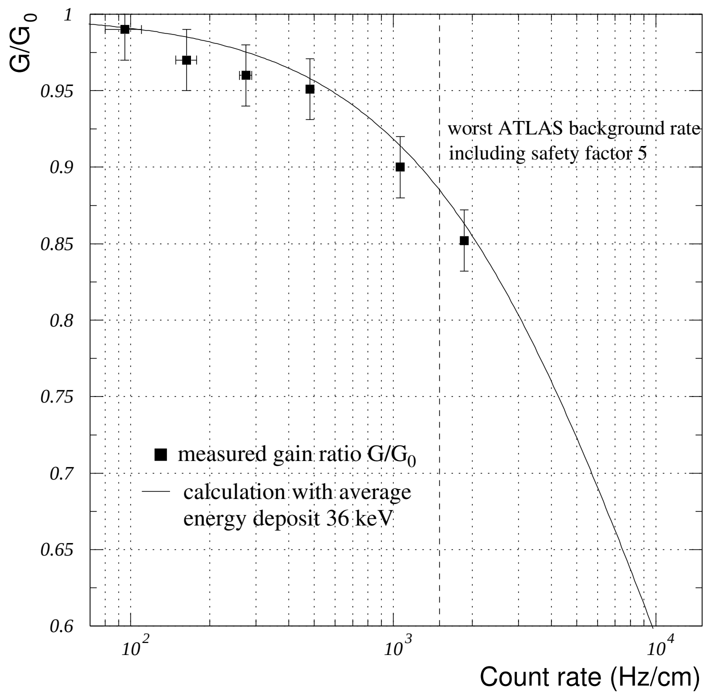

Figure 6.20: *Gain drop versus background rate for a gas gain of $G_0 = 2 \times 10^4$. The solid line is a calculation using an analytical model for the space charge (see below).*

The impact of a gain drop on the resolution can be understood in the following way: the signals are scaled down whereas the threshold remains fixed. Consequently the threshold gets effectively shifted to a larger number of primary ionisation electrons, which deteriorates the resolution.

Field Fluctuations

The space charge changes the drift field and hence the space-time relationship. Figure 6.21 shows a sketch of the drift fields without and with space charge (difference exaggerated). In Figure 6.22 the impact on the rt-relation is demonstrated for the non-linear baseline gas.

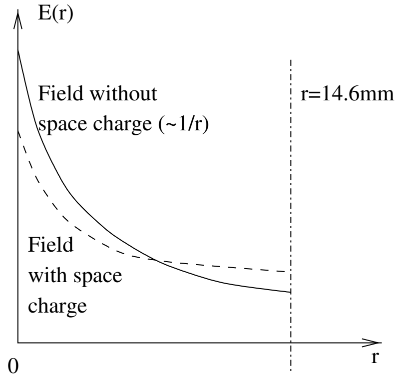

Figure 6.21: *Drift-field change due to space charge (exaggerated).*

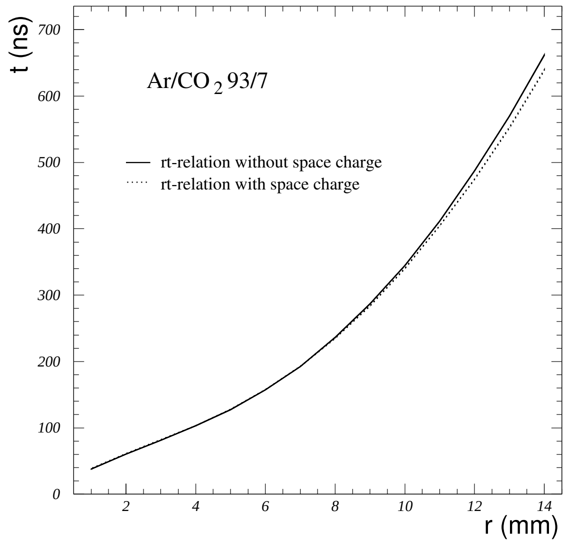

Figure 6.22: *Change of the rt-relation of a non-linear gas. For a linear gas the effect is much smaller because the drift velocity depends less on the field.*

If this space charge were constant for a given hit rate, the drift field would be constant and there would be no deterioration of resolution. However, the electrons drifting towards the wire are affected only by the charge within approximately 1 cm along the direction of the tube and in such a slice there are on average only 6 ion clouds (1500 Hz/cm). Since the actual number n of ion clouds is Poisson distributed around this number, the drift field varies and the resolution deteriorates. This effect is rather small for gases such as $Ar/N_2/CH_4$ 91/4/5, where the drift velocity depends only weakly on the electric field (linear gas), but becomes the dominating effect for gas mixtures like Ar/CO_2 (drift velocities see Figure 3.3 and 3.4). Whereas for $Ar/N_2/CH_4$ 91/4/5 the drift velocity is rather constant over big distances in r, it changes a lot with the electric field for the Ar/CO_2 mixture. This explains why the latter is much more sensitive to field fluctuations.

The resolution deterioration due to field fluctuations grows approximately with $\sqrt{\text{rate}}$ because the number n ($\langle n \rangle \approx (1\,\text{cm}) \cdot N_\text{c} \cdot t_\text{max}^\text{ion}$) of ion clouds having an impact on one muon has an uncertainty proportional to $\sqrt{n}$ (see Section 6.1.4).

Calculation of Field Change

The ion drift from the avalanche to the cathode takes several milliseconds $t_{\mathrm{max}}^{\mathrm{ion}} \approx 4\,\mathrm{ms}$. Their presence in the drift region creates a space charge which modifies the electric field for subsequent events. Since in our case the irradiated part of the tube is longer than the tube diameter we can approximate the space charge to be constant in the dimension along the wire and thus consider the problem to be two-dimensional. There are certainly limitations to this model, since assuming a count rate of $500\,\mathrm{Hz/cm^2}$ (that is $1500\,\mathrm{Hz/cm}$ tube wire), together with a maximum ion drift time of 4 ms there are on average only the ions of six events drifting in a 1 cm slice of the tube. Hence a two-dimensional approximation might be at the limit of validity. The comparison of simulations and measurements, however, shows good agreement.

1. **Exact Calculation:**

   The ion velocity depends on the electric field according to

$$v = \mu(E)\,E\,. \tag{6.7}$$

   Apart from the high-field region very close to the wire the ion mobility μ can be considered as constant. The density of space charge in the MDT can be calculated in the following way:

$$\frac{\mathrm{d}r}{\mathrm{d}t} = \mu E(r) \qquad \rightarrow \qquad \mathrm{d}t = \frac{\mathrm{d}r}{\mu E(r)}\,, \tag{6.8}$$

   where $\mathrm{d}t$ is the time it takes an ion to get from r to $r + \mathrm{d}r$. Multiplying $\mathrm{d}t$ by the amount of charge that is produced in the avalanche per second and dividing by the area between r and $r + \mathrm{d}r$ yields the charge density

$$\rho(r) = \frac{N_c G Q}{2r\pi\mu E(r)}\,, \tag{6.9}$$

   where N_c is the count rate per unit of length along the tube, Q is the average charge deposit per background event and G is the gas gain. In Equation (6.9) it has been assumed that the charge is equally distributed around the wire (no φ-dependence). This is not the case for most of the events, but still it is a quite good approximation, especially for high rates.

   Using Gauss' theorem we obtain:

$$\oint \vec{E}\,\mathrm{d}\vec{S} = q\,, \tag{6.10}$$

   where q is the total charge enclosed by the cylinder surface S. Evaluation of both sides and simplification yields the following expression:

$$2\pi r E(r) = \frac{\gamma}{\varepsilon_0} + \frac{1}{\varepsilon_0}\int_a^r 2\pi r' \rho(r')\,\mathrm{d}r'\,, \tag{6.11}$$

where γ is the line charge on the anode wire. Differentiation on both sides gives the differential equation

$$E(r)^2 + rE(r)\frac{\mathrm{d}E(r)}{\mathrm{d}r} = c_1 \qquad \text{with} \qquad c_1 = \frac{N_c GQ}{2\pi\mu\varepsilon_0} , \tag{6.12}$$

with the solution

$$E(r) = \sqrt{c_1}\,\frac{k}{r}\sqrt{1+\frac{r^2}{k^2}} , \tag{6.13}$$

where the integration constant k is determined by the boundary conditions. Since $E(r)$ has to obey the constraint

$$\int_a^b E(r)\,\mathrm{d}r = V_0 , \tag{6.14}$$

we obtain a transcendental equation for the parameter k:

$$k\ln\frac{b(k^2+k\sqrt{k^2+a^2})}{a(k^2+k\sqrt{k^2+b^2})} + \sqrt{k^2+b^2} - \sqrt{k^2+a^2} = V_0\sqrt{\frac{2\pi\mu\varepsilon_0}{N_c GQ}} . \tag{6.15}$$

This equation can be solved numerically. The parameter k has the dimension of a length and tells us a lot about the strength of the space-charge effect. For $k \gg b$, for example, we can neglect the second term in the square root in Equation (6.13), and the $1/r$ dependence of the drift field without space charge is restored.

gas mixture	E_{min}(1 bar) (kV/cm)	ΔV (V)
$Ar/N_2/CH_4$ 91/4/5	21	44
Ar/CO_2 80/20	22	49
Ar/CO_2 90/10	20	43
Ar/CO_2 92/8	19	42
Ar/CO_2 93/7	24	34
Ar/CO_2 94/6	23	34

Table 6.4: *Diethorn parameters E_{min} and ΔV for different gas mixtures. The errors are about 10 %. The values for* $Ar/N_2/CH_4$ 91/4/5 *are taken from* [DEI:96a, DEI:96b], *the others are from our own measurements (see Section 5.3).*

In order to take into account the gain drop, one has to calculate the line charge γ on the wire, which is given by

$$\gamma = 2\pi\varepsilon_0 aE(a) , \tag{6.16}$$

and to insert it into Diethorn's formula [DIE:56] describing the gas gain G as a function of γ:

$$G = \left[\frac{\gamma}{2\pi\varepsilon_0 aE_{\mathrm{min}}(\rho_0)\frac{\rho_{\mathrm{gas}}}{\rho_0}}\right]^{\frac{\gamma\ln 2}{2\pi\varepsilon_0\Delta V}} . \tag{6.17}$$

$E_{\min}(\rho_0)$ and ΔV are two gas-dependent parameters, ρ_{gas} is the gas density. The values of $E_{\min}$ and ΔV for several gas mixtures are listed in Table 6.4.

Since a different gas gain will produce a different amount of space charge, the electrical field on the wire surface and consequently the gas gain will change. Hence we have to iterate the two formulas (6.13) and (6.17). Usually they converge after only a few steps.

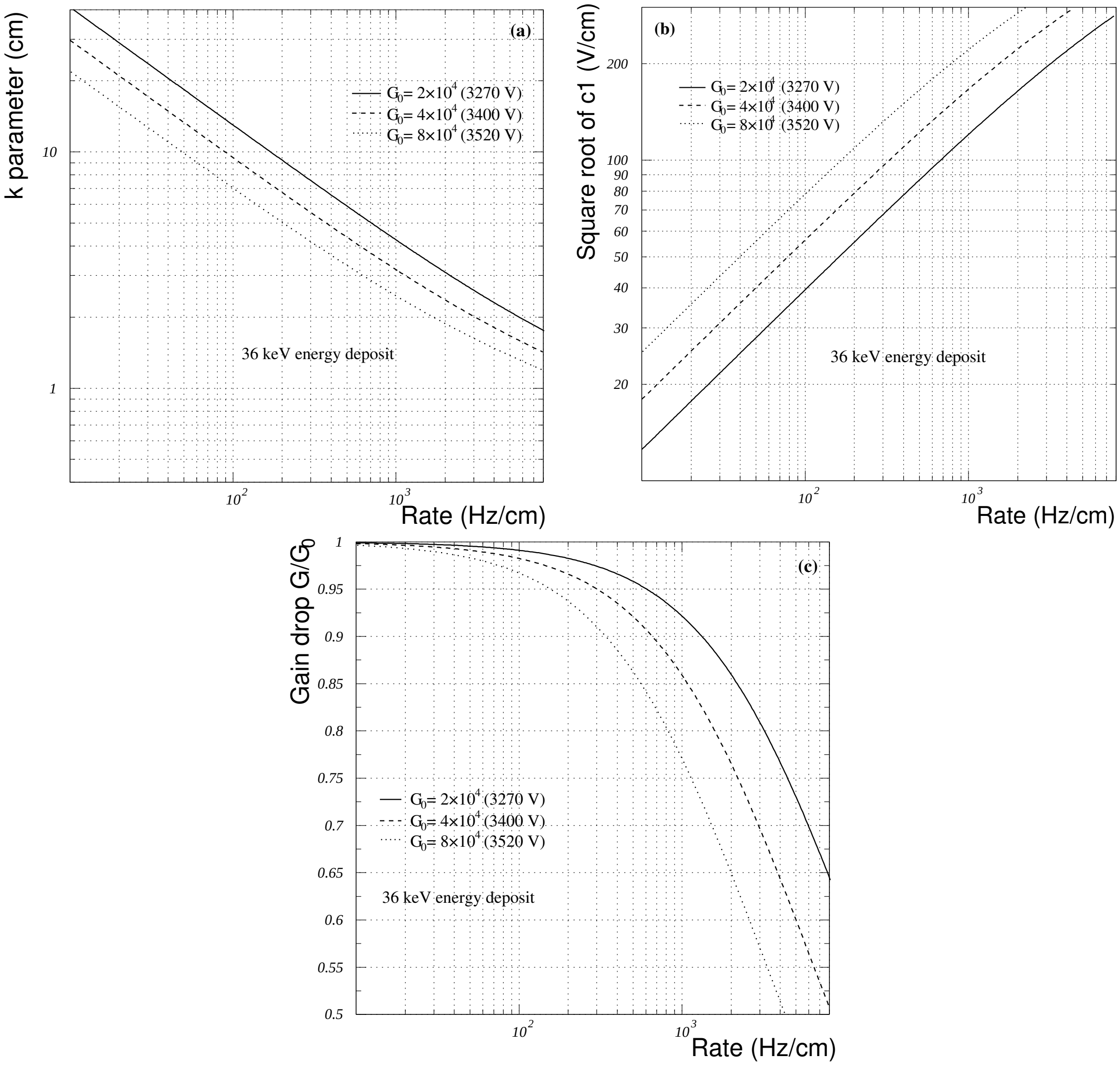

Figure 6.23: *Field parameters. These plots show the dependence of the different field parameters on the rate per unit wire length. Plot (a) shows the parameter k. For high rates k becomes smaller until $k \approx b$. Plot (b) shows the parameter $\sqrt{c_1}$ and (c) the gain drop. The assumed energy deposit per background event was* 36 keV.

Figure 6.23 shows the results obtained for k, $\sqrt{c_1}$ and G/G_0 as a function of the rate. All calculations are done for $Ar/N_2/CH_4$ 91/4/5, but the values are gas independent within a few per cent. Using this parameter set Equation (6.13) yields the electric field which was used for the simulations in Section 6.2.3.

2. **A First-Order Approximation:**

If $r \ll k$, which also means $k \gg b$ ($b = 1.46\,\mathrm{cm}$) we can expand Equations (6.13) and (6.15), and the two expressions reduce to

$$E(r) \approx \sqrt{c_1}\frac{k}{r} + \sqrt{c_1}\frac{r}{2k}\,, \qquad \text{and} \qquad k\ln\frac{b}{a} + \frac{b^2}{4k} = \frac{V_0}{\sqrt{c_1}}\,. \tag{6.18}$$

Solving for k gives the field

$$E(r) = \frac{V_0}{r\ln\frac{b}{a}}\left(1 - \frac{b^2 N_c G Q \ln\frac{b}{a}}{8\pi\epsilon_0\mu V_0^2}\right) + \frac{N_c G Q \ln\frac{b}{a}}{4\pi\epsilon_0\mu V_0}\,r\,. \tag{6.19}$$

This approximation is not valid (error $\mathcal{O}[25\,\%]$ at $1500\,\mathrm{Hz/cm}$) at the highest rates considered here. The first-order approximation overestimates the rate effect at high rates, especially for big radii.

The space-charge effects depend on the count rate per unit of wire length. The gain drop was measured to be $G/G_0 = 0.88$ at the highest rates. It shifts the effective threshold to higher values. Field fluctuations are the dominating effect for non-linear gases. A radial-symmetric analytical model was developed which can predict the gain drop with high accuracy and allows to calculate the drift field for a given rate.

6.2.3 Simulation of the High-Rate Resolution-Deterioration

The effects described above were introduced into the simulation. The drift field including the space charge of a given number of ion clouds was calculated with the simple radial-symmetric model introduced in Section 6.2.2. The number of ion clouds n was Poisson-distributed around the mean number of ion clouds $\langle n\rangle$, which we would expect at a given rate in a 1 cm slice perpendicular to the wire (e.g. at a background rate of $N_\mathrm{c} = 1400\,\mathrm{Hz/cm}$ we get $\langle n\rangle \approx (1\,\mathrm{cm}) \cdot N_\mathrm{c} \cdot t_\mathrm{max}^\mathrm{ion} \approx 5$ for a maximum ion drift time $t_\mathrm{max}^\mathrm{ion} = 3.8\,\mathrm{ms}$).

Figures 6.1 and 6.3 compare the predictions including all the electronics and space-charge effects with measurements for two very different drift gases. The good agreement between the test-beam data and the measurements made it possible to study the individual effects in greater detail.

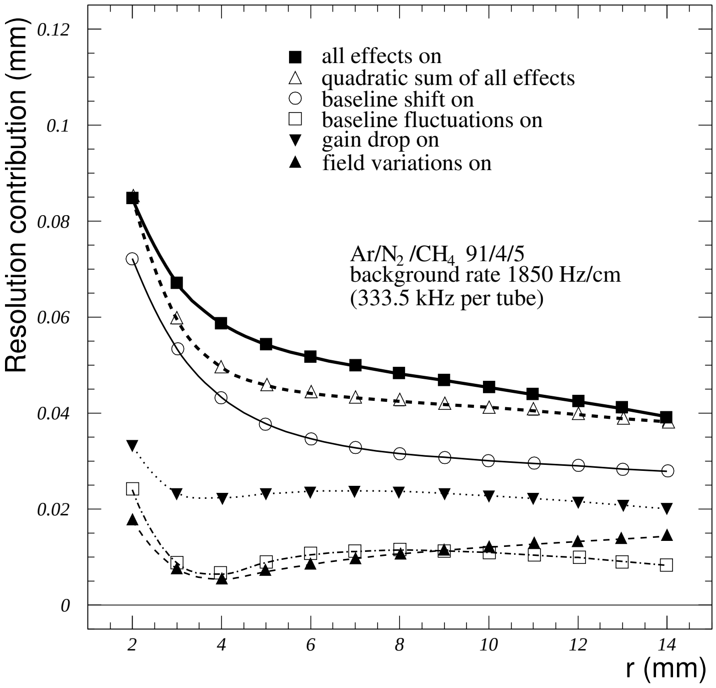

Figure 6.24: *Contributions to resolution deterioration. The background rate is* 1850 Hz/cm, *the drift gas* $Ar/N_2/CH_4$ 91/4/5 *and the gas gain* $G_0 = 2 \times 10^4$. *The statistical errors are about* 10 μm. *The lines are drawn to guide the eye.*

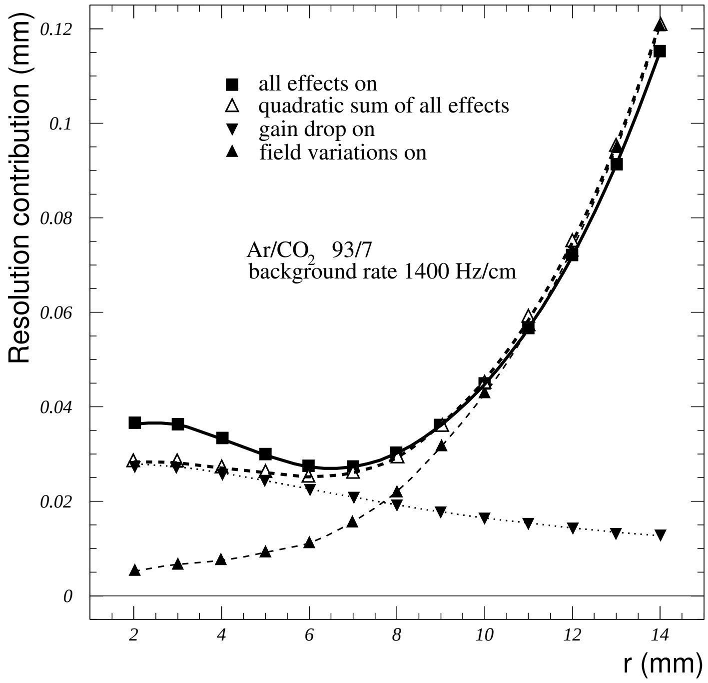

Figure 6.25: *Contributions to resolution deterioration. The background rate is* 1400 Hz/cm, *the drift gas* Ar/CO_2 93/7 *and the gas gain* $G_0 = 2 \times 10^4$. *The statistical errors are about* 10 μm. *The lines are drawn to guide the eye.*

Figures 6.24 and 6.25 show the results of simulations, where individual effects can be studied. The quadratic difference between the resolution curves with the effect under study switched on and the resolution curve without background rate (see Figures 6.1 and 6.3) is plotted. Based on these results the following comments can be made:

- The contribution of the field fluctuations is rather small for the linear gas (see Figure 6.24). Since the drift velocity is only weakly depending on E/p (see Figure 3.3), variations of the drift field translate only into small variations of the drift time. For the non-linear gas mixture (see Figure 6.25) this contribution dominates.

- The baseline shift (9 p.i.e) dominates the resolution deterioration of the linear gas. It shifts the threshold to higher electrons (25 p.i.e $\rightarrow$ 34 p.i.e). The contribution of the gain drop ($G/G_0 = 0.88$) is smaller over the whole drift distance since the effective threshold shifts only to $G_0/G \cdot 25$ p.i.e $= 28.4$ p.i.e. With a linear gas the pulse height increases with the radius[4] and hence the leading edge becomes steeper. Therefore raising the threshold affects the resolution less at bigger radii, hence both effects decrease with bigger drift distance r. In the non-linear gas mixture the drift velocity decreases with bigger radii (see Figure 3.4), hence a jitter in the threshold-crossing times translates into a smaller resolution deterioration at bigger drift distances (see contribution of the gain drop in Figure 6.25).

- The baseline fluctuations in Figure 6.24 deteriorate the resolution slightly (see Figure 6.19) since the threshold was kept at the 25^{th} p.i.e ($5\times\sigma_{\text{noise}}$). Raising the threshold to $5 \times \sigma_{\text{noise+fluct}}$ would result in a resolution deterioration comparable to the contribution of the gain drop.

- The difference between "all effects on" and the quadratic sum of all effects in Figure 6.24 shows that there is a correlation between individual contributions. The quadratic sum underestimates the resolution deterioration because a baseline shift amplifies the effect of the gain drop: The baseline shift moves the threshold from the 25^{th} p.i.e to the 34^{th} p.i.e. Multiplying this with G_0/G yields a threshold of 39 p.i.e which is higher than we obtain by summing up the two individual effects[5].

The individual effects that contribute to a high-rate resolution-deterioration were studied in the simulation. The resolution deterioration for the non-linear baseline gas Ar/CO_2 93/7 is dominated by the field fluctuations. For linear gas mixtures this effect is negligible.

[4]In a linear gas the time difference between individual clusters of ionisation electrons arriving at the wire becomes smaller with greater distances between the track and the wire, consequently the pulse heights increase.

[5]In this threshold region the resolution degrades linearly with higher thresholds.

Chapter 7

Systematic Errors to the Space-Time Relationship

7.1 Introduction

The drift velocity v_{D} is a function of $\frac{E}{\rho}$. Hence environmental changes which influence either the electric field E or the gas density ρ affect the drift velocity in a tube and consequently the rt-relation. However, this effect is negligible for linear gas mixtures (e.g. $Ar/N_2/CH_4$ 91/4/5) because their drift velocity depends only weakly on the ratio of $\frac{E}{\rho}$. For non-linear gas mixtures (e.g. the baseline gas Ar/CO_2 93/7) these effects become more important. This chapter describes in detail all different effects contributing to systematic errors to the rt-relation (see also [ALE:98c]).

Variations of the rt-relation during auto-calibration will show up as a single-tube resolution-deterioration and produce perhaps non-Gaussian tails in the residual distribution. Changes in the environmental parameters after auto-calibration will distort the rt-relation systematically resulting in a wrong prediction of the radius r at a given drift time t, or in other words, provoking a systematic error to the single-tube track-position measurement.

This chapter will describe all effects causing such systematic errors to the rt-relation under realistic LHC conditions, estimate its influences on the reconstructed muon-momentum resolution and finally introduce possible first-order corrections to systematic effects.

Different effects will cause deviations from the original rt-relation $r_0(t)$, resulting in

$$r(t) = r_0(t) + \delta r(t) \ . \tag{7.1}$$

The deviation $\delta r(t)$ and hence $r(t)$ will be functions of the background rate, the gas gain, the gas density, the gas composition, the non-concentricity of the anode wire and the magnetic field. In addition we expect a rather small contribution from the auto-calibration itself. Thus we will decompose $\delta r(t)$ into

$$\delta r(t) = \delta r_{\mathrm{F}}(t) + \delta r_{\mathrm{G}}(t) + \delta r_{\mathrm{D}}(t) + \delta r_{\mathrm{gas\,comp}}(t) + \delta r_{\mathrm{C}}(t) + \delta r_{\mathrm{M}}(t) + \delta r_{\mathrm{autocal}}(t) \ , \tag{7.2}$$

where $\delta r_{\mathrm{F}}(t)$ is the error due to high-rate induced changes of the drift field (space-charge effect), $\delta r_{\mathrm{G}}(t)$ the contribution of the gain drop (space-charge effect and temperature effect), $\delta r_{\mathrm{D}}(t)$ the gas-density effect (e.g. due to temperature changes), $\delta r_{\mathrm{gas\,comp}}(t)$ the expected effect as a consequence of variations in the gas composition, $\delta r_{\mathrm{C}}(t)$ the error due to a non-concentricity of the anode wire, $\delta r_{\mathrm{M}}(t)$ the systematics due to differences in the magnetic field and $\delta r_{\mathrm{autocal}}(t)$ the systematic error of the rt-relation obtained by auto-calibration.

In the following we will quantify the systematic error to the rt-relation with the root mean square of the difference $\delta r^{\mathrm{r.m.s}}$ between the original and the distorted rt-relation (b is the inner tube radius):

$$\delta r^{\mathrm{r.m.s}} = \sqrt{\frac{1}{b}\int_0^b \delta r(r)^2 \, \mathrm{d}r} \ . \tag{7.3}$$

7.2 Sources of Systematic Errors to the Space-Time Relationship

This section describes briefly the environment in which the ATLAS Muon Spectrometer is expected to work (for more details see Chapter 2). Varying background rate, gas density or gas composition cause systematic errors to the rt-relation. Furthermore, systematic errors of the rt-relation due to auto-calibration, magnetic-field differences and non-concentricity of the wire are considered. All the measurements and simulations are done for 3 bar gas pressure, a gas gain of 2×10^4, a wire radius $a = 25\,\mu$m and an inner tube radius of $b = 14.6$ mm.

7.2.1 Rate Environment

Figure 7.1 shows the background environment of the ATLAS Muon Spectrometer. The impact of the background rate on the single-tube spatial-resolution was already discussed in detail in Section 6.2. A more detailed description of the ATLAS radiation background is given in Chapter 2.

The background rates will not be constant. This effects the rt-relation in two different ways: Because of ions drifting back to the cathode space charge in the drift region builds up and causes a drift-field change and a gain drop.

- **Gain Drop:**
  Since the electric field on the wire becomes smaller in the presence of space charge, the gain drops. Measurements and simulations of the gain drop are described in Section 6.2.2. We expect a gain drop of $G/G_0 \approx 0.88$ at a background rate of 1500 Hz/cm and $G_0 = 2 \times 10^4$. Figure 7.2 illustrates the reason for the systematic error. The average signal maximum for muons is $h \approx 150$ p.i.e. Assuming a linear signal rising edge yields a shift of the threshold-crossing time Δt_{thr} of ~ 0.4 ns (peaking time $t_{\mathrm{p}} = 15$ ns, 20 p.i.e threshold at a gain drop of $G/G_0 = 0.88$). With a drift velocity

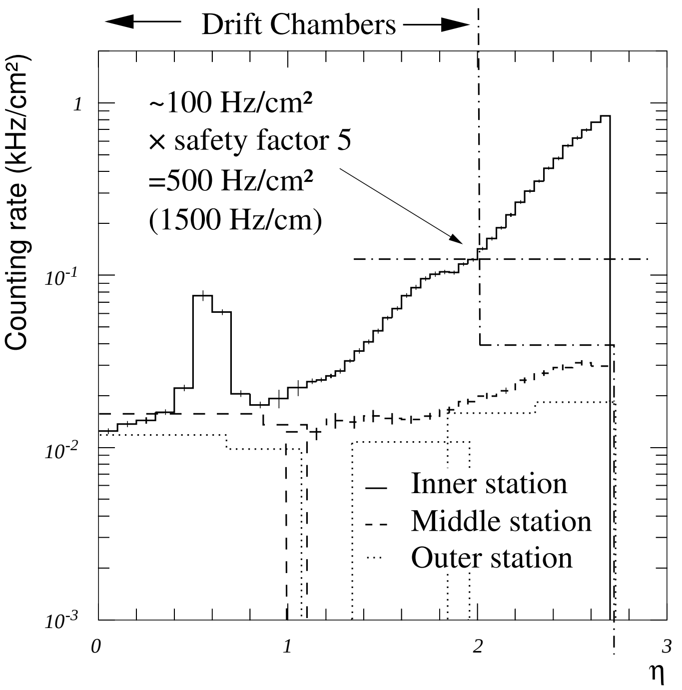

Figure 7.1: *Pseudo-rapidity dependence of the total counting rate in the three precision-chamber stations at nominal luminosity* [ATM:97].

$\sim 30\,\mu$m/ns we get an average systematic error of the predicted drift radius r of $\delta r_{\mathrm{G}}^{\mathrm{r.m.s}} \approx 12\,\mu$m. This value is almost independent of the drift gas. Thus the systematic error to the rt-relation due to gain drop is a very small effect and can be neglected even for bigger gain drops[1]. Another effect which can become important for auto-calibration is the shift of t_0 to later times[2] by about 1 ns.

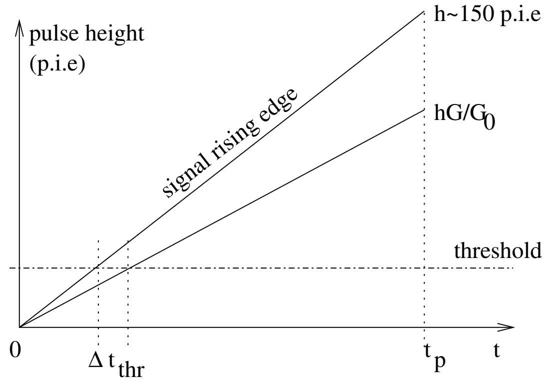

Figure 7.2: *At a given gain drop G/G_0 the threshold-crossing time shifts to later times, consequently the drift radius is overestimated if the rt-relation without gain drop is used.*

[1]The effect scales with $\left(\frac{G_0}{G} - 1\right)$.
[2]Note, that for a baseline shift of ~ 9 p.i.e, t_0 will be further shifted to later times by about 2 ns.

- **Drift-Field Change:**
  The ions which are drifting back from the wire to the cathode surface produce a charge density that is changing the drift field (see Section 6.2.2, Figures 6.21 and 6.22). For non-linear gas mixtures like Ar/CO_2 this is the dominating systematic error to the rt-relation. Applying Equation (7.4) the effect can be quantified and shows an error of $\delta r_{\mathrm{F}}^{\mathrm{r.m.s}} = 120\,\mu$m for a rate difference of 1500 Hz/cm with Ar/CO_2 93/7 ($Ar/N_2/CH_4$ 91/4/5 gives only 18 μm). Figure 7.10 (a) shows that the systematic error to the rt-relation induced by high-rate drift-field changes is not linear with r, nevertheless the root mean square as described in Equation (7.3) represents a very good figure of merit for the impact on the reconstructed muon-momentum resolution. The drift-field change reduces the maximum drift time by about 20 ns (Ar/CO_2 93/7).

In Appendix A.1.1 the derivation for a correction of the systematic error due to a drift-field change is presented. The product of the background rate N_{c}, the gas gain G and the charge deposit Q can be extracted from the monitored chamber current ($I_{\mathrm{ch}} \propto N_{\mathrm{c}}GQ$):

$$\delta r_{\mathrm{F}}(t) = \frac{N_{\mathrm{c}}GQb^2 \ln\frac{b}{a}}{8\pi\varepsilon_0\mu V_0^2}\left[tr_0'(t) - r_0(t) + \frac{6\ln\frac{b}{a}}{b^2}r_0'(t)\int\limits_0^t \left(\frac{r_0'(t')}{r_0'(t)} - 1\right) r_0(t')^2\,\mathrm{d}t'\right] , \quad (7.4)$$

where μ is the ion mobility, V_0 the wire potential and $r_0'(t) = \frac{\partial r_0(t)}{\partial t}$ the first derivative of $r_0(t)$ (see Appendix A.1.1 for a more detailed description). Another possibility to reduce this big systematic error would be to perform auto-calibration several times a day since the main rate variation will be due to the fill-up cycle of the LHC which causes a relatively slow rate decrease.

Figure 7.3 shows the measurement, the simulation and the calculation of the systematic error $\delta r_{\mathrm{F}}(t)$. The correction reduces the systematic error $\delta r_{\mathrm{F}}^{\mathrm{r.m.s}}$ from 120 μm to $< 30\,\mu$m. The calculation overestimates the rate effect for big radii because for the derivation of Equation (7.4) a first-order approximation of the drift-field change was used (see Appendix A.1.1). In Figure 7.3 also a small gain-drop correction was applied.

Since the background rate will not be constant, we have to consider the time variations of the rt-relation due to time-dependent space-charge effects. The gain drop will provoke a negligible systematic error of $\sim 12\,\mu$m. The drift-field change will cause a big systematic error $\delta r_{\mathrm{F}}^{\mathrm{r.m.s}} = 120\,\mu$m for the non-linear baseline gas at a rate difference of 1500 Hz/cm. A correction based on the monitored chamber current can reduce this error to $< 30\,\mu$m.

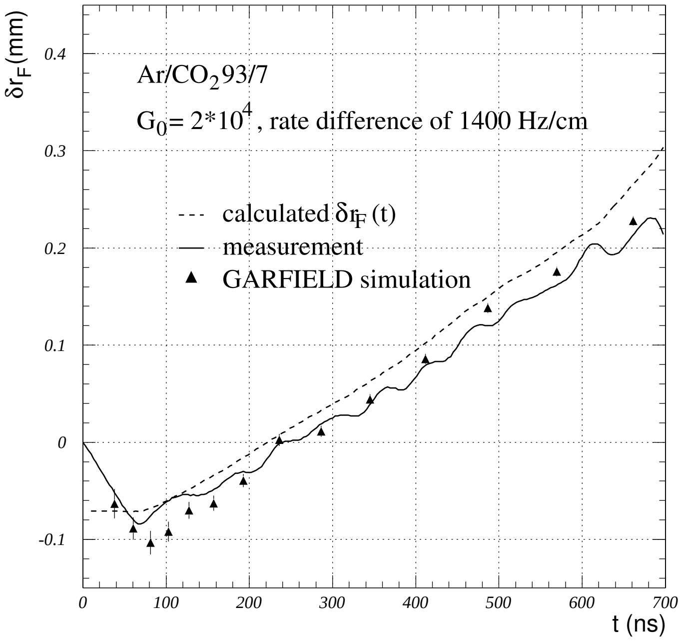

Figure 7.3: *The systematic error $\delta r_{\mathrm{F}}(t)$ to the rt-relation due to rate variations $\delta r_{\mathrm{F}}(t)$ as a function of the drift time t. The plot compares measurements with GARFIELD simulations and the calculation of $\delta r_{\mathrm{F}}(t)$ according to Equation (7.4).*

7.2.2 Temperature Effects

Various heat sources and sinks in the Muon Spectrometer will result in temperature gradients. Temperature differences in the Muon Spectrometer are estimated to be at the level of 3 K (see [ATM:97]).

The diurnal temperature variations in the cavern will be significantly smaller at the level of $\Delta T = \pm 1\,\mathrm{K}$.

Assuming constant pressure the following contributions have to be considered:

- **Gas-Gain Stability:**
  Temperature related density variations induce gain variations. According to Diethorn's formula [DIE:56] ($\frac{\rho(T_0)}{\rho(T)} = \frac{T}{T_0}$, $T = T_0 + \Delta T$)

$$G(T) = \left[\frac{E(a)\rho(T_0)}{E_{\min}(\rho(T_0))\rho(T)}\right]^{\frac{aE(a)}{\Delta V}\ln 2} \quad \rightarrow \quad \frac{G(T)}{G(T_0)} = \left[\frac{T}{T_0}\right]^{\frac{V_0 \ln 2}{\Delta V \ln \frac{b}{a}}} , \qquad (7.5)$$

  where $E(a)$ is the electric field on the wire surface and $E_{\min}$ and ΔV are the Diethorn parameters (see Table 5.1 for Ar/CO_2 mixtures), an isobar temperature change of $\Delta T = -5\,\mathrm{K}$ translates into a gain drop of $G(T)/G(T_0) = 0.9$. The impact of a gain drop on the spatial resolution has already been discussed in Section 6.2.2. The systematic error to the rt-relation caused by this effect is negligible (see Section 7.2.1).

- **Stability of the Drift Velocity:**
  The drift velocity v_{D} is a function of $\frac{E}{\rho}$. Thus a change of the gas density will influence the drift time t at a given drift distance r. This systematic error to the rt-relation can be calculated (see Equation (7.6) and the derivation in Appendix A.1.2). For $\mathrm{Ar/CO_2}$ 93/7 an isobar temperature change of $\Delta T = 2\,\mathrm{K}$ results in an error of $\delta r_{\mathrm{D}}^{\mathrm{r.m.s}} = 27\,\mu\mathrm{m}$ (for $\mathrm{Ar/N_2/CH_4}$ 91/4/5 $\delta r_{\mathrm{D}}^{\mathrm{r.m.s}} = 4\,\mu\mathrm{m}$).

In the ATLAS gas distribution the gas density will be controlled by keeping the ratio of $\frac{\text{pressure}}{\text{temperature}} \propto \rho$ constant (see also [DEI:97]). However, the gas density will perform small variations since the pressure equalises in the gas volume. However, the control of the gas density in the gas distribution will further reduce temperature effects. We estimate the residual variations to be at the level of $|1 - \rho/\rho_0| < 0.4\,\%$ (see Appendix A.1.2), which cause a systematic error of $\delta r_{\mathrm{D}}^{\mathrm{r.m.s}} = 15\,\mu\mathrm{m}$ ($\mathrm{Ar/CO_2}$ 93/7).

In Appendix A.1.2 the impact of a gas-density change on the rt-relation – e.g. as a consequence of temperature variations – is described in an analytical model. This model can predict the systematic error with high accuracy and hence makes a correction possible:

$$\delta r_{\mathrm{D}}(t) = \left(\frac{\rho_0}{\rho} - 1\right)\left(r_0(t) - t \cdot r_0'(t)\right) . \tag{7.6}$$

Figure 7.4 compares GARFIELD simulations and calculations of the systematic error due to large gas-density variations and shows excellent agreement.

Applying the density correction presented in Equation (7.6) we can reduce the systematic error $\delta r_{\mathrm{D}}^{\mathrm{r.m.s}}$ to smaller than $10\,\mu\mathrm{m}$ provided the temperature of the gas is known with an accuracy of 0.2 % (0.6 K). Whether the temperature sensors on the chambers can provide this information has to be tested.

In the ATLAS gas distribution the gas density will be controlled. Therefore temperature variations will cause only small systematic errors to the rt-relation. For the baseline gas we expect a systematic error of $\delta r_{\mathrm{D}}^{\mathrm{r.m.s}} \approx 15\,\mu\mathrm{m}$ which can be further reduced by applying corrections based on the measurements of the temperature sensors on the chambers.

7.2.3 Gas Composition

The drift properties of $\mathrm{Ar/CO_2}$ mixtures depend crucially on the exact $\mathrm{CO_2}$ content. Table 6.1 points out the vast differences of the maximum drift time $t_{\max}$ for a change of the $\mathrm{CO_2}$ content of only one percentage point. It is not the absolute value of the gas composition, but the stability in time, that will be crucial for the performance of our spectrometer. Another important aspect is the stability of the water content.

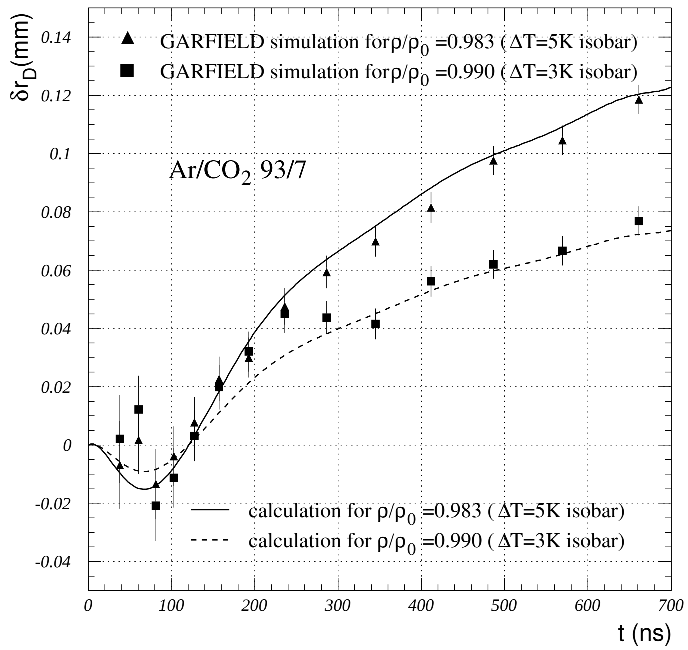

Figure 7.4: *The systematic error to the rt-relation $\delta r_{\mathrm{D}}(t)$ due to density variation as a function of the drift time t. The plot compares GARFIELD simulations with the calculation of $\delta r_{\mathrm{D}}(t)$ as described above and in Appendix A.1.2.*

Figure 7.5 demonstrates the change of the drift properties in terms of a distortion of the rt-relation $\delta r_{\text{gas comp}}$. In order to restrict $\delta r^{\text{r.m.s}}_{\text{gas comp}}$ to a maximum of $40\,\mu$m, the absolute composition variation has to stay below 0.1 % absolute.

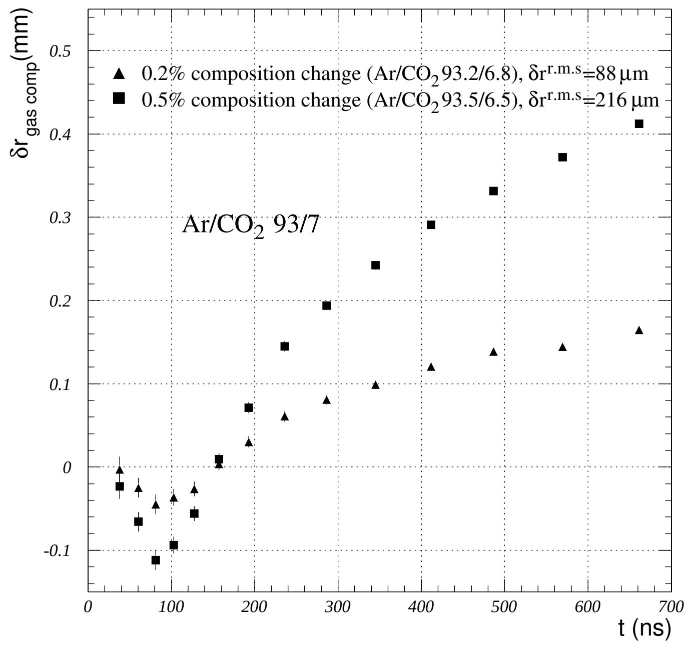

Figure 7.5: *Systematic error to the rt-relation due to changes of the gas composition. GARFIELD simulation, calculation of the gas properties with MAGBOLTZ.*

Because of the very small flow rate (1 volume exchange per 10 h) such variations in the gas composition will distribute very slowly over the whole Muon Spectrometer. Thus even with exact monitoring after the mixer it is very difficult to know the actual gas composition in the chambers. A correction for this effect is therefore practically not possible.

The MDT system may be operated with a small admixture of water vapour to the drift gas. Its value would be determined with regard to a maximum stability of the drift properties[3]. Figure 7.6 shows GARFIELD simulations of the systematic error due to variations of the water content. The nominal water content is 1000 ppm. As described in [KIR:97] the impact of water on the rt-relation is usually not very well predicted by GARFIELD. Nevertheless Figure 7.6 gives us an estimate of the magnitude of the effect. If we estimate the stability of the water content to be 3 % the systematic error will be smaller than 10 μm. This value has to be confirmed by measurements.

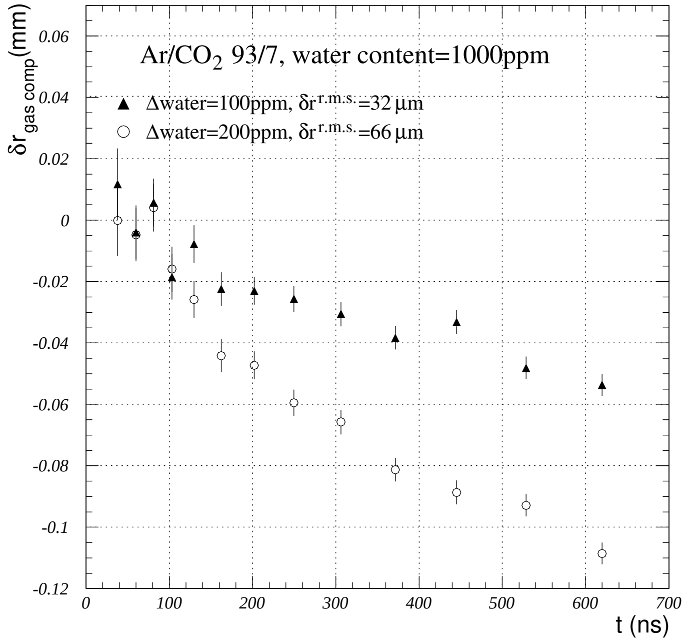

Figure 7.6: *Systematic error to the rt-relation due to changes of the water content. GARFIELD simulation, calculation of the gas properties with MAGBOLTZ.*

In order to keep the systematic error due to gas-composition variations low ($\delta r^{\mathrm{r.m.s}}_{\mathrm{gas\ comp}} < 40\,\mu\mathrm{m}$), the gas-composition variation has to stay below 0.1 % absolute (for the baseline gas). With an assumed stability of the water content of better than 3 % the resulting systematic error will be only about 10 μm.

[3]Usually the maximum drift time shows a minimum at a few thousand ppm depending on the drift gas. There the highest stability of the drift properties is guaranteed (see [KIR:97]). This optimal water content has to be determined by measurements.

7.2.4 Concentricity of the Anode Wire

Temperature differences between MDT multilayers deform the chamber. The in-plane alignment will measure the fundamental mode of such deformations, but cannot prevent loss of concentricity of the anode wires relative to the tubes, which is required not to exceed $100\,\mu$m r.m.s [ATM:97][4]. Measurements on MDT prototypes, confirmed by finite-element calculations, show that gradients of $\Delta T = 3\,$K are tolerable for chambers with tube lengths below 3 m [DAL:97]. Such a non-concentricity of the wire translates into an rt-relation with two different branches, one for each side of the wire. Let be s the distance between the tube axis and the wire and φ the polar angle, then the first-order approximation (all terms with $\mathcal{O}[(\mathrm{s/b})^2]$ neglected) of the new drift field $|\vec{E}(r,\varphi)|$ is

$$|\vec{E}(r,\varphi)| \approx \frac{V_0}{r \ln \frac{b}{a}} \left(1 + \frac{rs}{b^2} \cos\varphi\right) . \tag{7.7}$$

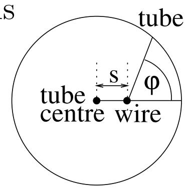

$\varphi = 0$ is fixed in the direction of the nearest distance between the non-concentric wire and the tube wall. Using Equation (7.7) we can calculate the systematic error to the rt-relation δr_{C} as a function of s and φ – the derivation is shown in Appendix A.1.3 – ($r_0(t)$ is the rt-relation for $s = 0$):

$$\delta r_{\mathrm{C}}(t) = 2\frac{s}{b^2} \cos(\varphi) r_0'(t) \int\limits_0^t \left(\frac{r_0'(t')}{r_0'(t)} - 1\right) r_0(t')\,\mathrm{d}t' . \tag{7.8}$$

Figure 7.7 shows a measurement with a wire being $500\,\mu$m out of centre and a calculation of $\delta r_{\mathrm{C}}(t)$. For $s = 100\,\mu$m the r.m.s of the difference between one branch and the rt-relation for $s = 0$ is in the order of $15\,\mu$m for mixtures like Ar/CO_2. For linear gases such as $Ar/N_2/CH_4$ 91/4/5 the effect is negligible ($\delta r_{\mathrm{C}}^{\mathrm{r.m.s}} = 2\,\mu$m). Auto-calibration would deliver the mean between the two branches as rt-relation, the residual distribution will show non-Gaussian tails. However, the reconstructed muon-momentum resolution stays almost unchanged (see Section 7.4) for an effect of this magnitude. Furthermore, the effect will be even smaller in ATLAS because due to geometrical considerations the shortest line from the wire to the muon track will be most likely at $\varphi = \pm\frac{\pi}{2}$.

The distance between the tube axis and the wire is required not to exceed $100\,\mu$m r.m.s, averaged over the whole tube length. For such a non-concentricity we expect a systematic error of $\delta r_{\mathrm{C}}^{\mathrm{r.m.s}} \approx 15\,\mu$m. If the exact position of the wire is known the distortion of the rt-relation can be predicted.

[4] I.e. the distance between the anode wire and the tube axis is not allowed to exceed $100\,\mu$m r.m.s, averaged over the whole tube length. Assuming a parabolic deviation from the tube axis (perfect concentricity at the tube ends) the maximum distance from the tube axis (in the middle of the tube) can be $\sqrt{15/8} \cdot 100\,\mu\mathrm{m} \approx 137\,\mu$m still yielding $100\,\mu$m r.m.s. Note, that engineers define concentricity as the whole window of possible wire positions, according to this definition our tubes will have a concentricity of $\sim 274\,\mu$m.

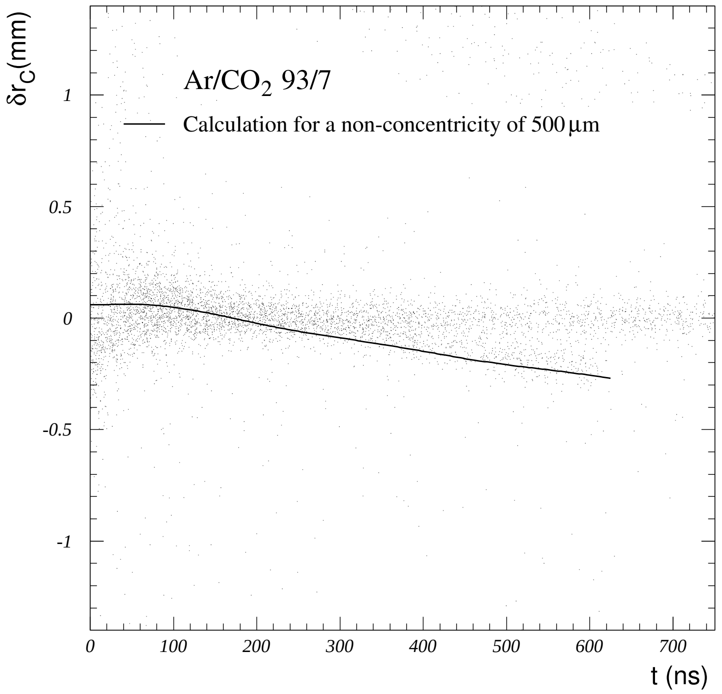

Figure 7.7: *Two branches of the rt-relation at a non-concentricity of* $500\,\mu$m. *The calculation of* $\delta r_{\mathrm{C}}(t)$ *according to Equation (7.8) fits very well to the measurement (offset at* $t = 0$ *due to wrong* t_0*). The two branches are at* $\varphi = 0$ *and* $\varphi = \pi$*. The plot shows the residuals of single events (i.e. the position obtained with the branch of the rt-relation at* $\varphi = \pi$ *minus the position predicted by ODYSSEUS).*

7.2.5 Differences of the Magnetic Field

The rt-relation depends on the magnetic field[5] B. In Section 5.8 the impact of a magnetic field on the electron drift is described. Since the magnetic field will vary throughout the spectrometer, auto-calibration zones are restricted in its size. However, we have to expect differences in the magnetic field of $\Delta B \approx 100\,\mathrm{G}$ ($\Delta B/B \approx 2\,\%$) within one auto-calibration zone. Hence we will obtain an average rt-relation within one zone, which will differ slightly from the local rt-relations.

Figure 7.8 presents GARFIELD simulations of the systematic error to the rt-relation due to differences of the magnetic field in one auto-calibration zone. It shows a systematic error $\delta r_{\mathrm{M}}^{\mathrm{r.m.s}}$ of $8\,\mu$m for differences in the magnetic field of $2\,\%$. The systematic error due to differences of the magnetic field in one auto-calibration zone is therefore a very small effect[6].

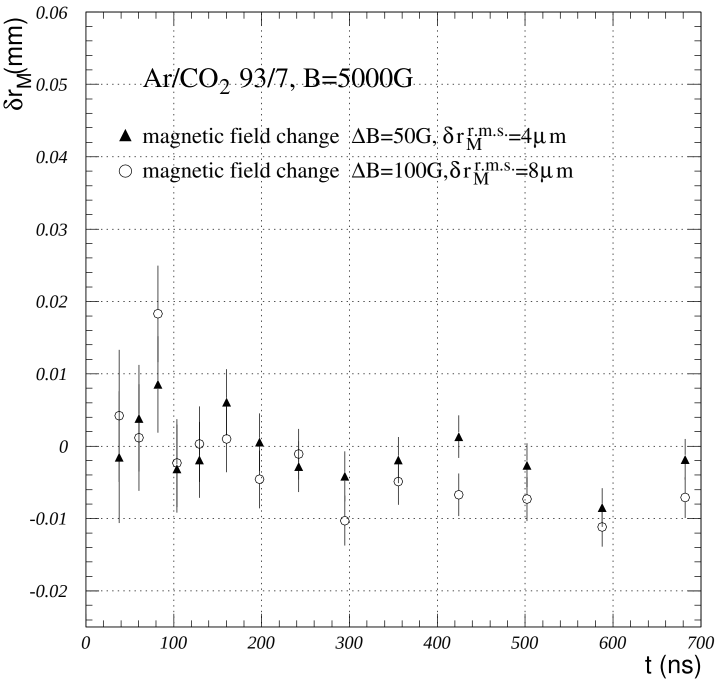

Figure 7.8: *Systematic Error δr_{M} due to differences in the magnetic field ($B = 0.5\,\mathrm{T}$ parallel to the wire, $\Delta B = 50\,\mathrm{G}$ and $100\,\mathrm{G}$, $G = 2\times10^4$, $p = 3\,\mathrm{bar}$).*

The systematic error caused by differences in the magnetic field within one auto-calibration zone will be small. Simulations yielded a $\boldsymbol{\delta r_{\mathrm{M}}^{\mathrm{r.m.s}}}$ of only $\mathbf{8\,\mu}$m for differences in the magnetic field of 2 %.

[5]We consider only the influence of magnetic fields parallel to the wire (wire $\parallel z$) $\vec{B} = B_z\vec{e_z}$ as it will be to a first approximation in the ATLAS Muon Spectrometer.

[6]For larger Lorentz angles (see Section 5.8) than the one of Ar/CO_2 93/7 the effect will increase slightly.

7.2.6 Systematics of Auto-Calibration

The ATLAS Muon Spectrometer will assume the same space-time relationship for certain areas of limited size. Within such areas the rt-relation will be obtained by auto-calibration. The size of auto-calibration zones will be determined by the necessary angular spread of the muon tracks ($\alpha^{\mathrm{r.m.s}}_{\mathrm{tracks}} \approx 2\,^\circ$), statistical considerations and the non-uniformity of the magnetic field.

The auto-calibration method was developed and tested with test-beam measurements [VIE:96, SAM:97, CRE:97] and typically yields the rt-relation with an accuracy of $\delta^{\mathrm{r.m.s}}_{\mathrm{autocal}} < 20\,\mu$m.

Compared to other sources of systematic errors to the rt-relation $\delta^{\mathrm{r.m.s}}_{\mathrm{autocal}}$ is rather small, but it depends strongly on the angular spread of the muon tracks used.

Figure 7.9 shows measurements of the dependence of the systematic error $\delta^{\mathrm{r.m.s}}_{\mathrm{autocal}}$ on the angular spread of the muon tracks $\alpha^{\mathrm{r.m.s}}_{\mathrm{tracks}}$ (measurements with the Calypso MDT chamber [CRE:97]). It points out that for an angular spread of $\alpha^{\mathrm{r.m.s}}_{\mathrm{tracks}} > 1.5\,^\circ$ the systematic error due to auto-calibration $\delta^{\mathrm{r.m.s}}_{\mathrm{autocal}}$ is smaller than $20\,\mu$m.

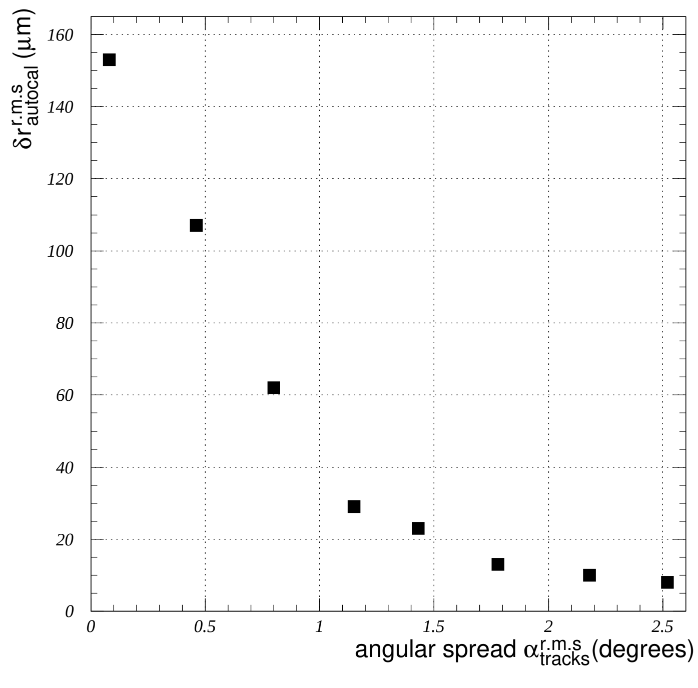

Figure 7.9: *The systematic error to the rt-relation due to auto-calibration $\delta^{\mathrm{r.m.s}}_{\mathrm{autocal}}$ as a function of the angular spread of the muon tracks $\alpha^{\mathrm{r.m.s}}_{\mathrm{tracks}}$ (measurements from the H8 test beam* [CRE:97]*).*

Test-beam studies showed that an angular spread of muon tracks of $\alpha^{\mathrm{r.m.s}}_{\mathrm{tracks}} \approx 2\,^\circ$ is necessary for auto-calibration. Then the systematic error will be smaller than $20\,\mu$m.

7.3 Systematic Errors with Linear and Non-Linear Drift Gases

Figure 7.10 summarises the stability of the rt-relation for non-linear drift gases like Ar/CO_2 mixtures and linear gases such as $Ar/N_2/CH_4$ 91/4/5. Only the systematic errors due to a gain drop and due to auto-calibration are gas-independent. The plots are calculations performed according to the way introduced in Appendix A.1. The magnitude of systematic errors is a direct measure for the linearity of a drift gas (the values for $\delta r^{\mathrm{r.m.s}}$ are listed in the plots and in Table 7.1 for many different drift gases).

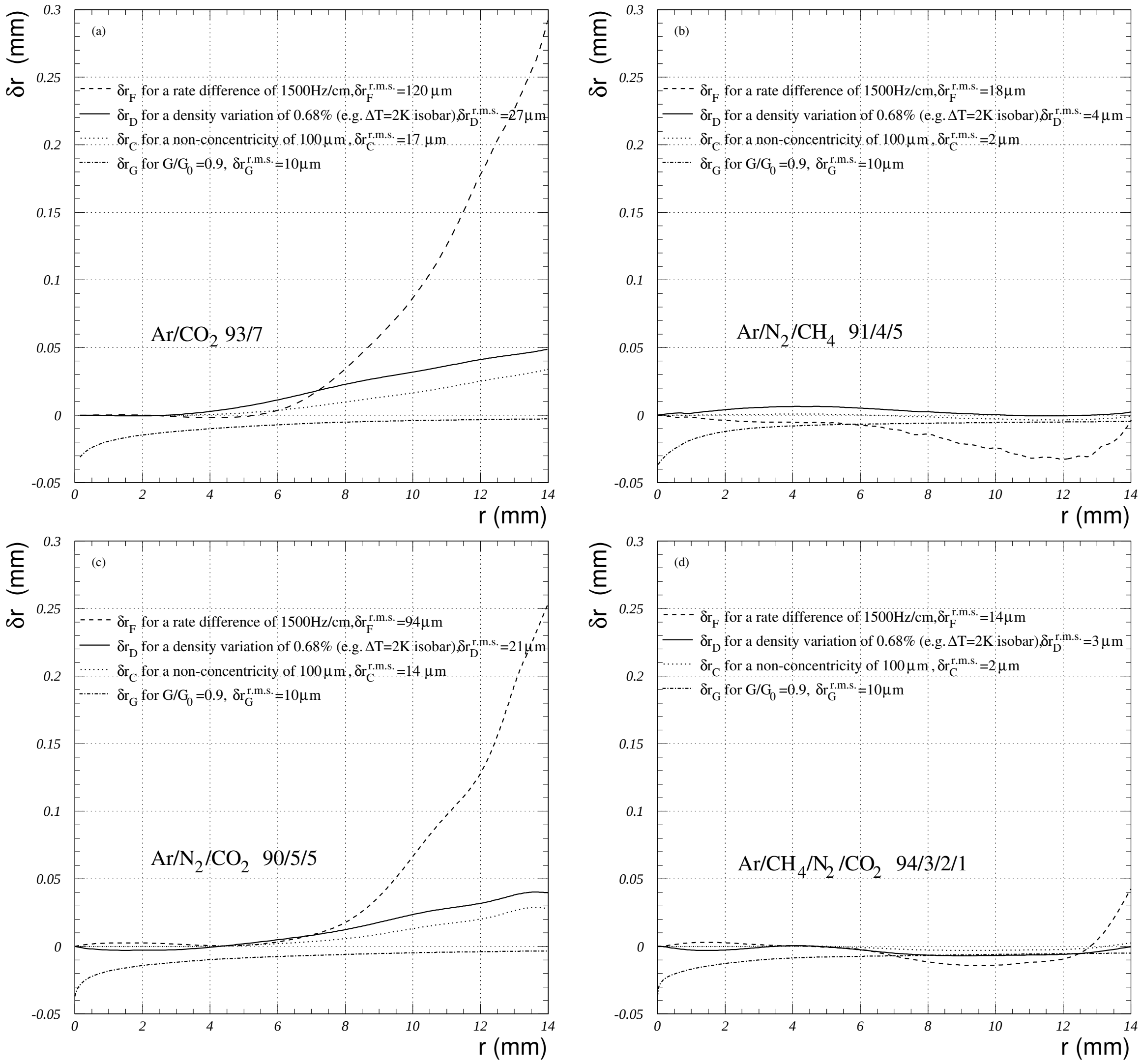

Figure 7.10: *Systematic errors to the rt-relations $\delta r(t) = r(t) - r_0(t)$ due to changes of the environmental parameters. The values for $\delta r^{\mathrm{r.m.s}}$ are listed in the plots.*

As expected we find significant systematic errors to the rt-relation for non-linear gas mixtures, which will therefore need a correction.

gas mixture	$\delta r_{\mathrm{F}}^{\mathrm{r.m.s}}$ (μm) ΔRate = = 1500 Hz/cm	$\delta r_{\mathrm{D}}^{\mathrm{r.m.s}}$ (μm) $\rho/\rho_0 = 0.993$ ($\Delta T = 2$ K isobar)	$\delta r_{\mathrm{C}}^{\mathrm{r.m.s}}$ (μm) $s = 100\,\mu$m	$\delta r_{\mathrm{G}}^{\mathrm{r.m.s}}$ (μm) $G/G_0 = 0.9$	$\delta r_{\mathrm{autocal}}^{\mathrm{r.m.s}}$ (μm)
$Ar/N_2/CH_4$ 91/4/5	18	4	2	10	< 20
$Ar/N_2/CO_2$ 90/5/5	94	21	14	10	< 20
$Ar/CH_4/N_2/CO_2$ 94/3/2/1	14	3	2	10	< 20
Ar/CO_2 90/10	123	28	18	10	< 20
Ar/CO_2 92/8	113	28	16	10	< 20
Ar/CO_2 93/7	120	27	17	10	< 20
Ar/CO_2 94/6	123	25	16	10	< 20

Table 7.1: *Values for the biggest expected errors $\delta r^{\mathrm{r.m.s}}$ to the rt-relation. The calculations have been done according to the method described in Appendix A.1. The systematic errors due to variations of the gas composition and due to magnetic field differences have only been simulated for* Ar/CO_2 93/7 *and are therefore not included in the table (see Sections 7.2.3 and 7.2.5).*

The magnitudes of systematic errors to the track-position measurement in one tube are a direct measure for the linearity of a drift gas. Whereas in linear drift gases all the effects stay well below 20 μm, variations of the environmental parameters such as the background rate can provoke huge distortions of the rt-relations of non-linear drift gases like Ar/CO_2 93/7. For the biggest effects corrections are possible, but they imply a loss of system robustness.

7.4 Impact of Systematic Errors to the Space-Time Relationship on the Reconstructed Muon-Momentum Resolution

In Section 7.2 the systematic errors to the track-position measurement in one tube have been discussed in detail. Such errors evoke wrongly reconstructed tracks in a whole chamber. Furthermore, the pattern-recognition efficiency suffers from these effects. Here, we want to study their impact on the reconstructed muon-momentum resolution.

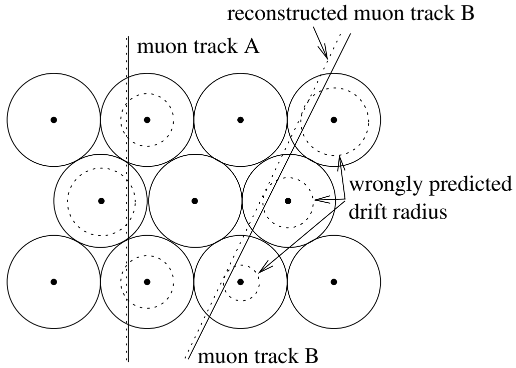

Figure 7.11: *The sketch shows the impact of systematic errors to the rt-relation on a reconstructed muon track in one multilayer. Muon track* A *is reconstructed almost correctly despite the systematic error (but decreased pattern-recognition efficiency) whereas the reconstructed muon track* B *shows a big deviation from the original position.*

Figure 7.11 illustrates that the error on the reconstructed track position in one multilayer depends strongly on the angle and the position of the muon track. Therefore a correct simulation of the impact on the reconstructed muon-momentum resolution has to involve the geometry of the whole spectrometer and the magnetic field. Such simulations have been performed with DICE/ATRECON. DICE [ART:95] is a program based on GEANT calculating the output of all detector systems in ATLAS for real physics events, using the exact geometry of the detector. ATRECON is a program which reconstructs the momenta and energies of the particles by using the output of DICE.

In the simulations described here a perfect calibration of the magnetic field and a perfect chamber alignment was assumed.

Figures 7.12 and 7.13 show the results of the simulations. Only muons with a transverse momentum of $p_{\mathrm{T}} = 1\,\mathrm{TeV/c}$ were considered since errors in the position measurement have its biggest impact on the reconstruction of muon tracks with high momenta. For small muon momenta the resolution is dominated by multiple scattering (see Figure 2.3).

Figure 7.12 shows the contribution of systematic errors to the reconstructed muon momentum (quadratic difference to the value without systematic error). As expected, a linear increase of the deterioration with $\delta r^{\mathrm{r.m.s}}$ can be seen. In order to obtain an estimate of the effect having a systematic error $\delta r^{\mathrm{r.m.s}}$ only in the inner station of the spectrometer, the contribution was scaled with $\frac{1}{\sqrt{3}}$ (e.g. the rate effect δr_{F} will only appear in the inner station).

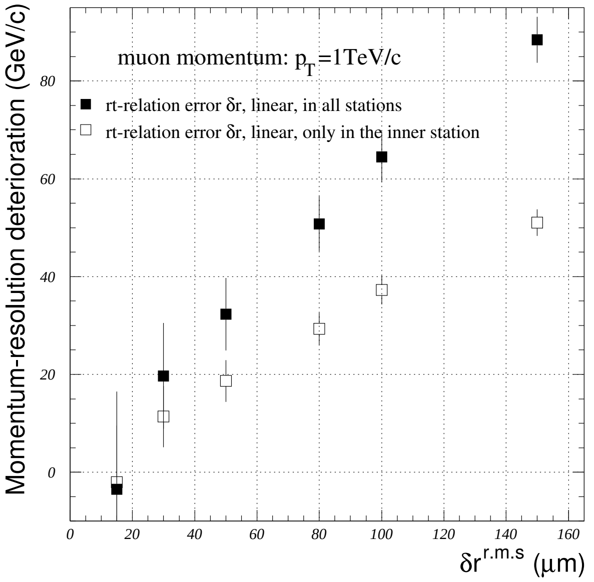

Figure 7.12: *DICE* [ART:95] *simulations of the momentum-resolution deterioration (quadratic difference) versus $\delta r^{\mathrm{r.m.s}}$ for muons with $p_{\mathrm{T}} = 1\,\mathrm{TeV/c}$. The full squares show the deterioration for a distorted rt-relation in all chambers. The open squares simulate a systematic error only in the inner station.*

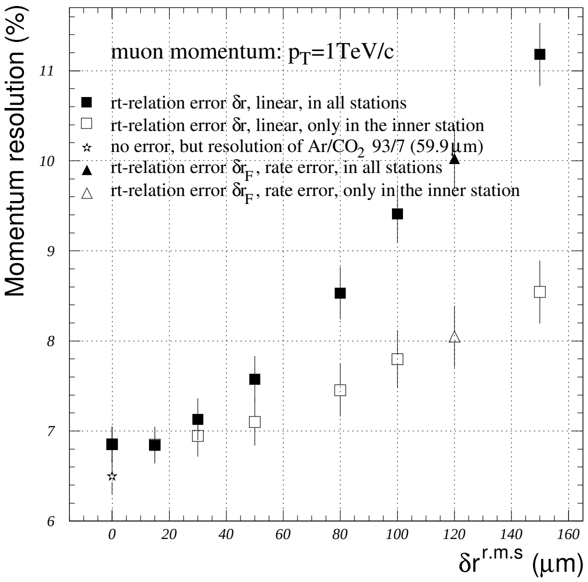

Figure 7.13: *DICE* [ART:95] *simulations of the reconstructed muon-momentum resolution for muons with $p_{\mathrm{T}} = 1\,\mathrm{TeV/c}$ in %. The squares are simulations with a linear distortion ($\delta r(r) = \frac{\delta r^{\mathrm{r.m.s}}\sqrt{3}}{b} \cdot r$), the triangles show a simulation with a real distortion δr_{F} as shown in Figure 7.10 (a).*

Figure 7.13 presents the relation between the reconstructed muon momentum and the systematic error $\delta r^{\mathrm{r.m.s}}$. It indicates that up to a systematic error of $\delta r^{\mathrm{r.m.s}} \leq 50\,\mu\mathrm{m}$ in all tubes of the detector the reconstructed momentum resolution stays almost unchanged ($\Delta p_{\mathrm{T}}/p_{\mathrm{T}} = 7$–$7.5\,\%$). For bigger systematic errors the resolution degrades quickly. Considering a systematic error only in the inner muon station (e.g. systematic error due to rate effects) the deterioration of the resolution is less (white squares in the plot). The squares have been calculated using a linear distortion of the rt-relation ($\delta r(r) = \frac{\delta r^{\mathrm{r.m.s}}\sqrt{3}}{b} \cdot r$), whereas for the triangles a real systematic error $\delta r_{\mathrm{F}}(r)$ like in Figure 7.10 (a) was applied. Note, that independent of the shape of the distortion $\delta r(r)$, the $\delta r^{\mathrm{r.m.s}}$ represents a very good figure of merit for the impact on the reconstructed muon-momentum resolution.

Since we expect much larger systematic errors $\delta r^{\mathrm{r.m.s}}$ than $50\,\mu\mathrm{m}$ for non-linear gas mixtures like Ar/CO_2, corrections will be necessary. They have been introduced already in Section 7.2, the full derivations can be found in Appendix A.1.

Systematic errors that are bigger than $\delta r^{\mathrm{r.m.s}} \approx 50\,\mu\mathrm{m}$ will deteriorate the reconstructed muon-momentum resolution significantly. For the non-linear baseline gas this means that for changes in environmental parameters corrections have to be applied based on the slow-control data.

7.5 Conclusion: Ar/CO_2 93/7, a Viable Solution

The last three chapters dealt with the operating point and systematic errors of the baseline gas Ar/CO_2 93/7. Furthermore, different drift gases have been compared in terms of resolution, and stability of the rt-relation.

Measurements confirmed with GARFIELD simulations show that a resolution of $\sim 60\,\mu$m without background ($\sim 56\,\mu$m with time-slewing correction) and $\sim 87\,\mu$m with a background rate of 1400 Hz/cm ($\sim 82\,\mu$m with time-slewing correction) can be achieved for the baseline gas Ar/CO_2 93/7 at a gas gain of $G_0 = 2 \times 10^4$. For higher gas gains the resolution without time-slewing correction improves slightly with no background. But higher gain hardly improves the resolution with correction and rate effects become worse.

The afterpulsing rate was measured and was found to be 3 % (Ar/CO_2 93/7, $G = 2 \times 10^4$). Afterpulses themselves do not cause big problems (very small pulses) but are a sign of incomplete quenching properties of the considered drift gas.

Simulations yielded an occupancy of 16 % for the baseline gas at 300 kHz. For bipolar shaping with a fixed dead time of 700 ns this corresponds to an inefficiency of 25 %.

baseline gas	Ar/CO_2 93/7
gas pressure p	3 bar
gas gain G_0	2×10^4
operating voltage	3080 V
peaking time t_p	10–15 ns
noise σ_{noise}	< 4 p.i.e
threshold	$5 \times$ noise (~ 20 p.i.e)
afterpulsing rate	3 %
maximum drift time	
no B-field $t_{max}^{0\,T}$	~ 700 ns
B-field of 0.5 T $t_{max}^{0.5\,T}$	~ 720 ns
Lorentz angle $\langle\Psi\rangle$	9.3 °
resolution IQA $\bar{\sigma}$	
no rate	60 μm
rate of 1400 Hz/cm	87 μm
$\bar{\sigma}$ **time-slew. corrected**	
no rate	56 μm
rate of 1400 Hz/cm	82 μm
maximum occupancy	
rate = 300 kHz/tube	~ 16 %

Table 7.2: *Summary: Working point of the MDTs for the baseline gas.*

effect	$\delta r^{r.m.s}$ (μm)
background rate	
Δrate = 1500 Hz/cm	120
with correction	< 30
gas density	
$\rho/\rho_0 = 0.993$	27
with correction	< 10
gas composition	
Δcomposition = 0.1 %	44
non-concentricity	
$s = 100\,\mu$m	17
gain drop	
$G/G_0 = 0.9$	10
B-field difference	
$\Delta B = 100$ G	8
auto-calibration	< 20
total (quadratic sum)	
without correction	< 135
with correction	< 65

Table 7.3: *Summary: Systematic errors for the baseline gas.*

Table 7.2 summarises the working point for our MDT system, in Table 7.3 the systematic errors to the rt-relation (1-σ values) are listed. Adding all systematic errors (quadratic sum) results in $\delta r_{total}^{r.m.s} < 135\,\mu$m without corrections and in $\delta r_{total}^{r.m.s} < 65\,\mu$m respectively, if the corrections are applied. The systematic error after corrections is dominated by the systematic error due to variations of the gas composition.

The different contributions to a systematic error to the rt-relation were discussed in detail in this chapter. The biggest effect is the background rate variation which will introduce a systematic error to the rt-relation of $\delta r_{\mathrm{F}}^{\mathrm{r.m.s}} = 120\,\mu\mathrm{m}$ ($\Delta\mathrm{Rate} = 1500\,\mathrm{Hz/cm}$ for the baseline mixture). Simulations of the impact of such systematic errors on the reconstructed muon momentum have been performed. They show that up to a systematic error of $\delta r^{\mathrm{r.m.s}} \leq 50\,\mu\mathrm{m}$ the reconstructed momentum resolution stays almost unaffected ($\Delta p_{\mathrm{T}}/p_{\mathrm{T}} \approx 7$–$7.5\,\%$ for a $p_{\mathrm{T}} = 1\,\mathrm{TeV}/c$, perfect chamber alignment and magnetic field calibration assumed). For bigger systematic errors ($\delta r^{\mathrm{r.m.s}} > 50\,\mu\mathrm{m}$) a rapid resolution deterioration was observed (see Figure 7.13).

Two of the biggest systematic errors (i.e. the systematic error due to rate variations and due to density variations) can be predicted by analytical models. Corrections are introduced, which can reduce the systematic error to a large extent (e.g. $\delta r_{\mathrm{F}}^{\mathrm{r.m.s}} = 120\,\mu\mathrm{m}$ reduces to $\delta r_{\mathrm{F}}^{\mathrm{r.m.s}} < 30\,\mu\mathrm{m}$ after correction). Measurements and GARFIELD simulations show very good agreement for a lot of the considered effects. The analytical model developed for corrections predicts the changes of the rt-relation with high accuracy.

In summary, $\mathrm{Ar/CO_2}$ has an excellent operational lifetime, whereas linear gases with hydrocarbons tend to age rapidly. However, the non-linearity of $\mathrm{Ar/CO_2}$ requires the careful control of and corrections for changes of the environmental conditions. The various effects have been measured and simulated. The studies demonstrate how to operate the Muon Spectrometer at the $80\,\mu\mathrm{m}$ resolution level in the LHC environment.

Chapter 8

Systematic Errors to the Muon-Momentum Measurement

8.1 The Absolute Mass Scale of the Muon Spectrometer

The momentum resolution and the absolute momentum scale of the Muon-System measurements depend on the alignment of the precision chambers, the knowledge of the magnetic field and the knowledge of the muon energy loss in the calorimeters. These three contributions influence the absolute value of the measured momentum $\bar{p}_j$, which can be expressed in the following way (the index i stands for one segment of the detector):

$$\bar{p}_j = \frac{K_i \frac{1}{\alpha_i} B_i}{s_j + \delta x_i} - \frac{1}{\alpha_i} \Delta p_i(p_j) \;, \tag{8.1}$$

where α_i is a magnetic-field scale-factor, s_j is the true sagitta, δx_i represents the tower misalignment and $\Delta p_i(p_j)$ is the energy loss as a function of the momentum p_j. The factor K_i translates the measured sagitta into a momentum and will be calculated according to the magnetic-field maps[1].

Since the track curvature measurement in the Muon System is obtained from only three vectors, the measurements themselves provide little redundancy, and an in situ recalibration of the Muon System with reconstructed tracks will require some knowledge of the incoming track curvature. Additional information can be provided by three methods:

- Special runs without magnetic field, which provide straight muon tracks for calibrating the alignment system, assuming they do not introduce additional uncertainties.

[1]For the very simple case of a homogeneous magnetic field B (in T), K_i becomes $\sim c \cdot l_i^2/(8 \cdot 10^9)\,\mathrm{GeV}/c \cdot \mathrm{m/T}$ (l_i is the length of the trajectory). The azimuthal component of the magnetic field in the Muon Spectrometer is shown in Figures 8.7 and 8.8.

- A comparison with the momentum measured in the Inner Detector. The large statistics of $\mathrm{W} \to \mu\nu$ and $\mathrm{Z} \to \mu^+\mu^-$ decays will allow a very precise cross calibration of the Muon System with the Inner Detector.

- The use of $\mathrm{Z} \to \mu^+\mu^-$ decays, for which the precisely known Z mass M_{Z} provides strong constraints on the unknown parameters which may affect the measurements of the muon momenta. Section 8.2 demonstrates how the calibration of the magnetic field and the energy loss in the calorimeters can be considerably improved by making use of $\mathrm{Z} \to \mu^+\mu^-$ decays.

8.1.1 Alignment of the Precision Chambers

The alignment of the precision chambers is required to be sufficiently accurate, such that the alignment contribution to the final measurement error ($30\,\mu$m sagitta accuracy) remains well below the chamber measurement error ($50\,\mu$m sagitta accuracy). The alignment system is based on optical straightness monitors (see [ATM:97]). The dominant uncertainty arises from the positioning of the optical sensors on the precision chambers or on carbon-fibre bars, the precision of which has to be better than $20\,\mu$m.

At the start of the experiment and after each major shutdown it is planned to use straight muon tracks (data taken with the toroidal magnetic field off) to check the alignment system and to provide effective corrections which should account for errors in the positioning of the alignment sensors. Given that the sensor position on the chambers will be very stable – and over all independent from switching the magnetic field on or off – these corrections should be applicable to data taken with the normal B-field. In order to keep any systematic effect on the sagitta corrections for the whole system below $2\,\mu$m, the residual field from the magnetised iron has to be controlled to $< 20\,\%$ during the field-off runs.

Preliminary simulation studies [NIS:92] have shown that this correction procedure can be implemented easily for the barrel part of the Muon System and that at low luminosity enough statistics are collected in less than one hour to achieve a precision of $30\,\mu$m on the sagitta corrections.

8.1.2 Magnetic Field

In order to measure the field under experimental conditions, with all detector components in place and the presence of magnetic material[2] the Muon System will be equipped with about 1500 Hall probes (see [ATM:97]). The readings will be compared with 3D calculations and used for reconstructing the position and the shape of the toroid conductors with respect to the chambers. Preliminary simulation studies using a simplified coil-deformation model have shown that the magnetic field can be determined to a relative accuracy of $0.2\,\%$. However, there are sources of systematic errors in this method due to magnetic material,

[2] These are mainly the Tile Calorimeter and the iron girder serving as return yoke for the solenoid flux.

which changes the B-field. Hence a calibration, as introduced in Section 8.2, will serve as an important cross check or even as "detector of hidden magnetic material".

8.1.3 Energy Loss

The energy loss of muons may be measured in the calorimeters. However, the energy loss in the passive elements of the calorimeter, in the magnetic-field return yoke outside the calorimeters and energy loss due to material in the Muon-Spectrometer volume will not be measured directly. This information will be obtained by the energy-loss calibration using $Z \rightarrow \mu^+\mu^-$ events (see Section 8.2). In this way correction factors with which the calorimeter measurement can be corrected are obtained.

Another possibility of calibrating the energy loss is the cross check between the (calibrated) Inner-Detector momentum-measurement and the momentum measurement in the Muon Spectrometer, provided its alignment and magnetic field is calibrated.

There are three sources of systematic errors to the muon-momentum measurement: the alignment of the precision chambers, the knowledge of the toroidal magnetic field and the knowledge of the energy loss in the calorimeters. The alignment will be calibrated using straight tracks (field off), the magnetic field monitored by Hall probes, and the known momentum of muons from the $Z \rightarrow \mu^+\mu^-$ decay will be used to calibrate the magnetic field and the energy loss. The comparison with the calibrated Inner-Detector measurement will provide further cross-check.

8.2 Absolute Mass-Scale Calibration at the 10^{-3} Level

8.2.1 Introduction

Calibration is an essential task in large systems like the ATLAS Muon Spectrometer, which is designed to achieve high precision in tracking measurements. In particular at the LHC, a precise determination of the absolute muon-momentum scale will be necessary to exploit a wide physics potential and to achieve very accurate measurements.

Physics resonances such as $Z \rightarrow \mu^+\mu^-$ will allow to cover momentum ranges up to several hundred GeV, produced with high rates at LHC ($\sim 20\,\mathrm{Hz}$ at high luminosity).

The absolute calibration of the Muon Spectrometer depends on the alignment of the precision chambers, the accuracy of the magnetic-field measurement and the exact calibration of the muon energy loss measured in the calorimeters (see Section 8.1).

In this study the alignment of the precision chambers was assumed to be perfect.

It is shown that with a sample of 10,000 events and with the track information from the Muon System alone it is possible to calibrate the energy loss with high accuracy (45 MeV at small pseudo-rapidities, for 50 GeV muons) and to obtain at the same time information about the absolute scale of the magnetic field.

The physics requirements for the accuracy of the absolute mass-scale calibration can be translated into the following numbers:

- the energy loss has to be calibrated with an accuracy of $\sigma_{\Delta E} < 30\,\mathrm{MeV}$;
- the magnetic field has to be known with $\sigma_B/B < 5 \cdot 10^{-4}$ and
- the alignment error must not cause a sagitta error bigger than $\sigma_{\mathrm{sag}} = 30\,\mu\mathrm{m}$.

8.2.2 Calibration Method

The $\mathbf{Z \longrightarrow \mu^+\mu^-}$ Decay

The known mass of Z ($M_{\mathrm{Z}} = 91.187 \pm 0.007\,\mathrm{GeV}/c^2$ [PAR:98][3], full width $\Gamma_{\mathrm{Z}} = 2.490 \pm 0.007\,\mathrm{GeV}/c^2$ [PAR:98]) gives information about the momenta of the two muons and hence the curvature of their tracks. This information can be used to calibrate the energy loss of muons in the calorimeters and to gain information about the magnetic field (see also [ALE:99a]).

From the conservation of the relativistic momenta $p^\nu_{\mathrm{Z}} = p^\nu_{\mu^+} + p^\nu_{\mu^-}$ $(\nu = 0\ldots 3)$ we obtain the following equation ($\vec{p}_1$ and $\vec{p}_2$ are the momenta of the two muons, p_1 and p_2 its absolute values):

$$\begin{pmatrix} \sqrt{M_{\mathrm{Z}}^2c^2 + p_{\mathrm{Z}}^2} \\ p_{\mathrm{Z}}\cos\varphi_{\mathrm{Z}}\sin\theta_{\mathrm{Z}} \\ p_{\mathrm{Z}}\sin\varphi_{\mathrm{Z}}\sin\theta_{\mathrm{Z}} \\ p_{\mathrm{Z}}\cos\theta_{\mathrm{Z}} \end{pmatrix} = \begin{pmatrix} \sqrt{m_\mu^2c^2 + p_1^2} \\ p_1\cos\varphi_1\sin\theta_1 \\ p_1\sin\varphi_1\sin\theta_1 \\ p_1\cos\theta_1 \end{pmatrix} + \begin{pmatrix} \sqrt{m_\mu^2c^2 + p_2^2} \\ p_2\cos\varphi_2\sin\theta_2 \\ p_2\sin\varphi_2\sin\theta_2 \\ p_2\cos\theta_2 \end{pmatrix}, \tag{8.2}$$

where φ_i and θ_i $(i = 1, 2)$ are the angles of the muon tracks at the vertex[4]. Neglecting the muon mass m_μ we get two equations, one from the energy component and one from the three momentum components:

$$\begin{aligned} M_{\mathrm{Z}}^2c^2 + p_{\mathrm{Z}}^2 &= p_1^2 + p_2^2 + 2p_1p_2\,, \\ p_{\mathrm{Z}}^2 &= p_1^2 + p_2^2 + 2p_1p_2[\cos\theta_1\cos\theta_2 + \cos(\varphi_1-\varphi_2)\sin\theta_1\sin\theta_2]\,. \end{aligned} \tag{8.3}$$

Eliminating p_{Z} leads to

$$M_{\mathrm{Z}}^2c^2 = 2p_1p_2[1 - \cos\theta_1\cos\theta_2 - \cos(\varphi_1-\varphi_2)\sin\theta_1\sin\theta_2] = 2p_1p_2\cdot\mathcal{F}(\varphi_1,\theta_1,\varphi_2,\theta_2)\,. \tag{8.4}$$

[3] This value of M_{Z} was also used for the event generation with PYTHIA.

[4] Those angles are found by tracking back the reconstructed muon track from the Muon System through the calorimeters and the solenoid to the vertex.

Taking into account the muon mass m_μ the leading 1 in the square brackets of Equation (8.4) has to be replaced by

$$1 \rightarrow \frac{m_\mu^2 c^2}{p_1 p_2} + \sqrt{1 + \frac{m_\mu^2 c^2}{p_1^2}} \sqrt{1 + \frac{m_\mu^2 c^2}{p_2^2}} = 1 + \delta(p_1, p_2) \; . \tag{8.5}$$

The small correction $\delta(p_1, p_2)$ in Equation (8.5) has a mean value of $\langle\delta\rangle = 7.6 \cdot 10^{-6}$ and an r.m.s of $5.4 \cdot 10^{-6}$.

For the calibration described below, the muon mass ($m_\mu = 105.658\,\mathrm{MeV}/c^2$ [PAR:98]) was taken into account according to Equation (8.5) ($\mathcal{F}(\varphi_1, \theta_1, \varphi_2, \theta_2) \rightarrow \mathcal{F}(\varphi_1, \theta_1, \varphi_2, \theta_2) + \delta(p_1, p_2)$) but the weak dependence of $\delta(p_1, p_2)$ on the energy loss and the magnetic-field scale-factors was neglected.

The Energy Loss

The energy loss of muons in material is a function of the muon energy (or the muon momentum, respectively). This function was simulated for different materials in [LOH:85]. Figure 8.1 shows the energy loss in iron $\varepsilon(p)$ normalised to 50 GeV muons. Figure 8.2

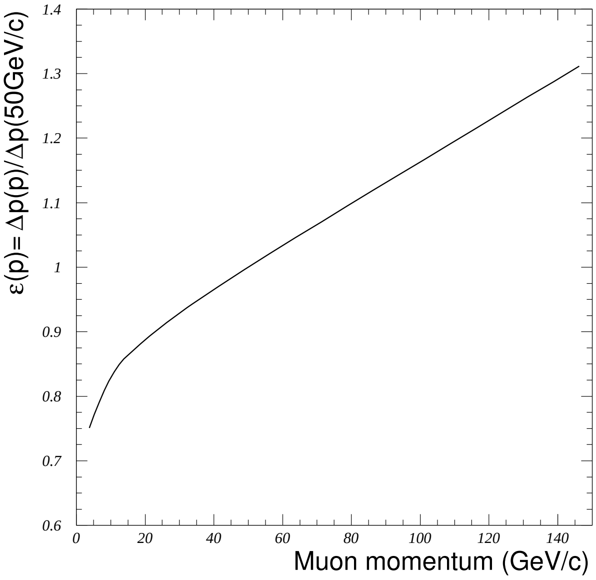

Figure 8.1: *The plot shows the normalised energy loss $\varepsilon(p)$ of muons (1 is the energy loss of muons with 50 GeV) in iron* [LOH:85].

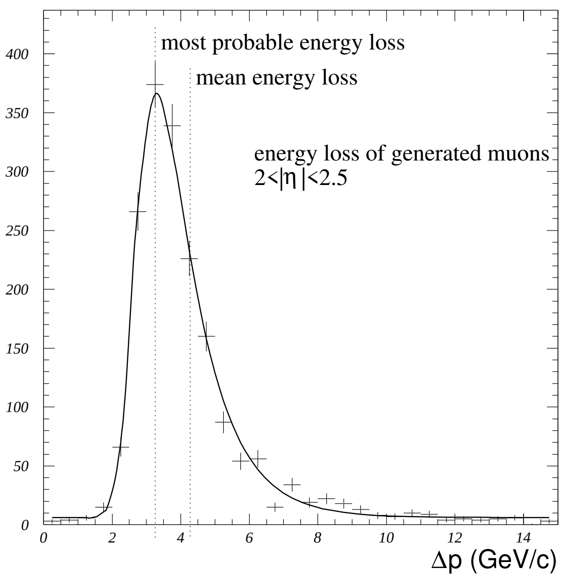

Figure 8.2: *The plot shows the energy-loss distribution in the calorimeter (DICE* [ART:95] *simulation).*

shows a DICE-simulation of the energy-loss distribution which corresponds very well to the measured distribution shown in [HEN:95]. The energy loss in DICE is simulated based on GEANT by taking into account the exact geometry of the calorimeters and all the additional material in the detector volume. For the energy-loss calibration only the mean energy loss was taken into account since a calibration algorithm which is taking into account the whole energy-loss distribution (Landau distribution) has more parameters. In order to obtain a mean energy loss a cut-off at $\Delta p = 15\,\mathrm{GeV}/c$ was applied. For calibrating the measured energy loss in the calorimeters the mean energy loss is adequate.

In the following we will split the energy loss of a muon into the momentum-dependent and the angle-dependent part:

$$\Delta p(p, \theta) = \varepsilon(p) \cdot \Delta p(\theta) \;, \tag{8.6}$$

with $\Delta p(\theta)$ being the mean energy loss of a muon with an energy of 50 GeV at an angle θ. In this study the small φ-dependence of the energy loss was neglected. However, the calibration algorithm described below would not have to be changed introducing a φ-dependence of the energy loss.

Scale Factors of the Magnetic Field

The toroidal magnetic field of the Muon Spectrometer will be measured using about 1500 Hall probes which determine the field components locally. The number of probes and their location will be optimised according to field inhomogeneities and costs. By performing a χ^2 minimisation the exact position of the coils can be retrieved. Using this information the magnetic field map is calculated [ATM:97].

This method will provide us with a detailed description of the toroidal magnetic field. However, there will be no way to exclude systematic errors due to neglected magnetic material or insufficient knowledge of its exact position. Such systematic errors will shift the absolute mass scale of the Muon Spectrometer. By reconstructing events with known curvature such as $\mathrm{Z} \rightarrow \mu^+\mu^-$, one can find scale factors of the magnetic field. In this study we were mainly limited by statistics which will not be the case during ATLAS operation since we expect a rate of $\sim 20\,\mathrm{Hz}$ for $\mathrm{Z} \rightarrow \mu^+\mu^-$ [NIS:92] (for low luminosity still $\sim 1.5\,\mathrm{Hz}$).

Note, that such magnetic-field scale-factors will deteriorate the accuracy of the magnetic field maps locally but adjust the means of the field integrals ($\int B\mathrm{d}l$ along the muon tracks) to the correct values.

To check the calibration algorithm for magnetic-field scale-factors by means of simulation, the magnetic field was scaled with $1/\alpha(\varphi, \theta)$ during the track reconstruction with MUONBOX. Doing so we obtained systematically "wrongly" reconstructed values $\bar{p}_{(\varphi,\theta)} = p^{\mathrm{Muon\ System}}/\alpha(\varphi, \theta)$ for the muon momenta. Applying the calibration algorithm described below the factor $\alpha(\varphi, \theta)$ could be retrieved with high accuracy.

The Calibration Algorithm

Allowing scale factors of the magnetic field $\alpha(\varphi,\theta)$ and an energy loss $\varepsilon(p)\Delta p(\theta)$ the momentum p is

$$p = \alpha(\varphi,\theta)\bar{p} + \varepsilon(p)\Delta p(\theta) \;, \tag{8.7}$$

and Equation (8.4) becomes

$$M_Z^2c^2 = 2\cdot[\alpha(\varphi_1,\theta_1)\bar{p}_1 + \varepsilon(p_1)\Delta p(\theta_1)]\cdot[\alpha(\varphi_2,\theta_2)\bar{p}_2 + \varepsilon(p_2)\Delta p(\theta_2)]\cdot\mathcal{F}(\varphi_1,\theta_1,\varphi_2,\theta_2) \;, \tag{8.8}$$

where $\bar{p}_1$ and $\bar{p}_2$ are the measured momenta in the Muon System. The quantities p_1 and p_2 which appear as arguments of the function ε are approximated with $p_{1,2} = \alpha(\varphi_{1,2},\theta_{1,2})\bar{p}_{1,2} + \langle\Delta p\rangle$, where $\langle\Delta p\rangle$ is the mean energy loss in the calorimeter.

In the following we describe the functions $\alpha(\varphi,\theta)$ and $\Delta p(\theta)$ with discrete points α_i $(i = 1\ldots n)$ and Δp_j $(j = 1\ldots m)$ which represent the mean values of the functions in a certain area of φ or θ, respectively.

The problem of determining the parameters α_i and Δp_j can be reduced to maximising the probability (N events; I stands for all the additional information we have, such as Equation (8.8); $\{\bar{p}_1,\bar{p}_2\}_k$ is the k^{th} measured pair of muon momenta $\bar{p}_1$ and $\bar{p}_2$) [SIV:97]

$$\mathcal{P} = \prod_{k=1}^{N} \mathrm{prob}(\alpha_i,\Delta p_j|\{\bar{p}_1,\bar{p}_2\}_k, I) \;, \tag{8.9}$$

which is the same as maximising its logarithm:

$$\mathcal{L}(\alpha_i,\Delta p_j) = \ln\mathcal{P} = \sum_{k=1}^{N} \ln\left(\mathrm{prob}(\alpha_i,\Delta p_j|\{\bar{p}_1,\bar{p}_2\}_k, I)\right) \;. \tag{8.10}$$

Due to the natural width Γ_Z we have to introduce the mass parameter $(\tilde{m}_Z)_k$ being the Z-mass for event k. Hence we have to substitute M_Z by the mass parameter $(\tilde{m}_Z)_k$ in Equation (8.8). Using Bayes' theorem we get:

$$\begin{aligned}\mathrm{prob}(\alpha_i,\Delta p_j,(\tilde{m}_Z)_k|\{\bar{p}_1,\bar{p}_2\}_k, I) \;\propto\;& \mathrm{prob}(\{\bar{p}_1,\bar{p}_2\}_k|\alpha_i,\Delta p_j,(\tilde{m}_Z)_k, I)\cdot \\ & \mathrm{prob}(\alpha_i|I)\cdot\mathrm{prob}(\Delta p_j|I)\cdot\mathrm{prob}((\tilde{m}_Z)_k|I) \;,\end{aligned} \tag{8.11}$$

where we should put in all our information we have about the α_i and Δp_j into

$$\mathrm{prob}(\alpha_i|I) = \begin{cases} 0 & : \alpha_i < 0 \\ \text{const.} & : \alpha_i \geq 0 \end{cases} \;, \qquad \mathrm{prob}(\Delta p_j|I) = \begin{cases} 0 & : \Delta p_j < 0 \\ \text{const.} & : \Delta p_j \geq 0 \end{cases} \;. \tag{8.12}$$

The probability $\mathrm{prob}((\tilde{m}_Z)_k|I)$ can be approximated with a Breit-Wigner distribution:

$$\mathrm{prob}((\tilde{m}_Z)_k|I) \approx \frac{1}{2\pi}\,\frac{\Gamma_Z}{\Gamma_Z^2/4 + ((\tilde{m}_Z)_k - M_Z)^2} \;. \tag{8.13}$$

For the remaining term in Equation (8.11) we have to put in our knowledge of the physics of the Z decay. To calculate the probability of a measured pair $\{\bar{p}_1,\bar{p}_2\}_k$ at given values of

α_i, Δp_j and $(\tilde{m}_\mathrm{Z})_k$ we look how probable it is that Equation (8.8) is not totally satisfied due to errors[5] on the measured quantities $\bar{p}_1$, $\bar{p}_2$ and $\mathcal{F}(\varphi_1, \theta_1, \varphi_2, \theta_2)$:

$$\begin{aligned} f(\{\bar{p}_1, \bar{p}_2\}_k, \mathcal{F}, \alpha_i, \Delta p_j) &\equiv 2 \cdot (\alpha_{i_1}\bar{p}_1 + \varepsilon(p_1)\Delta p_{j_1}) \cdot (\alpha_{i_2}\bar{p}_2 + \varepsilon(p_2)\Delta p_{j_2}) \cdot \mathcal{F} \;, \\ \sigma_f(\{\bar{p}_1, \bar{p}_2\}_k, \mathcal{F}, \alpha_i, \Delta p_j) &= \sqrt{\left(\frac{\partial f}{\partial \bar{p}_1}\right)^2 \sigma_{\bar{p}_1}^2 + \left(\frac{\partial f}{\partial \bar{p}_2}\right)^2 \sigma_{\bar{p}_1}^2 + \left(\frac{\partial f}{\partial \mathcal{F}}\right)^2 \sigma_{\mathcal{F}}^2} \;, \end{aligned} \tag{8.14}$$

where $\sigma_\mathcal{F}$ has to be calculated from the errors σ_{φ_1}, σ_{φ_2}, σ_{θ_1} and σ_{θ_2}. Those and $\sigma_{\bar{p}_1}$ and $\sigma_{\bar{p}_2}$ are obtained from the error matrix of the track fit. Hence we can write down a Gaussian approximation for

$$\begin{aligned} \mathrm{prob}(\{\bar{p}_1, \bar{p}_2\}_k | \alpha_i, \Delta p_j, (\tilde{m}_\mathrm{Z})_k, I) \;\approx\; & \frac{1}{\sqrt{2\pi}\sigma_f(\{\bar{p}_1, \bar{p}_2\}_k, \mathcal{F}, \alpha_i, \Delta p_j)} \cdot \\ & \exp\left(-\frac{((\tilde{m}_\mathrm{Z})_k^2 c^2 - f(\{\bar{p}_1, \bar{p}_2\}_k, \mathcal{F}, \alpha_i, \Delta p_j))^2}{2\sigma_f(\{\bar{p}_1, \bar{p}_2\}_k, \mathcal{F}, \alpha_i, \Delta p_j)^2}\right) \;. \end{aligned} \tag{8.15}$$

Taking advantage of marginalisation and using Equations (8.11) we obtain

$$\begin{aligned} \mathrm{prob}(\alpha_i, \Delta p_j | \{\bar{p}_1, \bar{p}_2\}_k, I) &= \int_{-\infty}^{\infty} \mathrm{prob}(\alpha_i, \Delta p_j, (\tilde{m}_\mathrm{Z})_k | \{\bar{p}_1, \bar{p}_2\}_k, I) \; \mathrm{d}(\tilde{m}_\mathrm{Z})_k \\ &\propto \mathrm{prob}(\alpha_i | I) \cdot \mathrm{prob}(\Delta p_j | I) \cdot \\ &\quad \int_{-\infty}^{\infty} \mathrm{prob}(\{\bar{p}_1, \bar{p}_2\}_k | \alpha_i, \Delta p_j, (\tilde{m}_\mathrm{Z})_k, I) \cdot \mathrm{prob}((\tilde{m}_\mathrm{Z})_k | I) \; \mathrm{d}(\tilde{m}_\mathrm{Z})_k \;, \end{aligned} \tag{8.16}$$

which can be calculated for each event k using Equations (8.12), (8.13) and (8.15). The integral in Equation (8.16) has to be calculated numerically. Now we are prepared to calculate the log-likelihood $\mathcal{L}(\alpha_i, \Delta p_j)$ for each set of α_i and Δp_j.

For better readability let us define the vector $\vec{X}$:

$$\vec{X} = \begin{pmatrix} \Delta p_1 \\ \vdots \\ \Delta p_m \\ \alpha_1 \\ \vdots \\ \alpha_n \end{pmatrix} \;, \tag{8.17}$$

for m different values for the energy loss and n scale factors of the magnetic field. In order to find the maximum of the log-likelihood $\mathcal{L}(\vec{X})$ we can take advantage of the Newton-Raphson algorithm [SIV:97]. This algorithm is often used to find the roots of a function.

[5] We assume Gaussian errors on the measured quantities.

Here we are trying to solve the equation $\nabla\mathcal{L}(\vec{X}) = 0$. The algorithm can be summarised with the recursion relationship

$$\vec{X}_{k+1} = \vec{X}_k - [\nabla\nabla\mathcal{L}(\vec{X}_k)]^{-1}\nabla\mathcal{L}(\vec{X}_k) \;, \tag{8.18}$$

where $\vec{X}_k$ is our estimate of the solution after $k-1$ iterations. If the corrections made in one step are too big one has the possibility to subtract a small number $c > 0$ from the diagonal elements of the symmetric matrix $\nabla\nabla\mathcal{L}$. This lowers the amplitude of the correction made in one step but has no effect on its orientation. Thus the algorithm becomes more stable. Usually it converges after a few iterations (< 20). Since the function $\mathcal{L}(\vec{X})$ was calculated numerically, the terms

$$\nabla\nabla\mathcal{L} = \begin{pmatrix} \frac{\partial\partial\mathcal{L}}{\partial\Delta p_1\partial\Delta p_1} & \cdots & \frac{\partial\partial\mathcal{L}}{\partial\Delta p_1\partial\Delta p_m} & \frac{\partial\partial\mathcal{L}}{\partial\Delta p_1\partial\alpha_1} & \cdots & \frac{\partial\partial\mathcal{L}}{\partial\Delta p_1\partial\alpha_n} \\ \vdots & \ddots & \vdots & \vdots & \ddots & \vdots \\ \frac{\partial\partial\mathcal{L}}{\partial\Delta p_m\partial\Delta p_1} & \cdots & \frac{\partial\partial\mathcal{L}}{\partial\Delta p_m\partial\Delta p_m} & \frac{\partial\partial\mathcal{L}}{\partial\Delta p_m\partial\alpha_1} & \cdots & \frac{\partial\partial\mathcal{L}}{\partial\Delta p_m\partial\alpha_n} \\ \frac{\partial\partial\mathcal{L}}{\partial\alpha_1\partial\Delta p_1} & \cdots & \frac{\partial\partial\mathcal{L}}{\partial\alpha_1\partial\Delta p_m} & \frac{\partial\partial\mathcal{L}}{\partial\alpha_1\partial\alpha_1} & \cdots & \frac{\partial\partial\mathcal{L}}{\partial\alpha_1\partial\alpha_n} \\ \vdots & \ddots & \vdots & \vdots & \ddots & \vdots \\ \frac{\partial\partial\mathcal{L}}{\partial\alpha_n\partial\Delta p_1} & \cdots & \frac{\partial\partial\mathcal{L}}{\partial\alpha_n\partial\Delta p_m} & \frac{\partial\partial\mathcal{L}}{\partial\alpha_n\partial\alpha_1} & \cdots & \frac{\partial\partial\mathcal{L}}{\partial\alpha_n\partial\alpha_n} \end{pmatrix} , \qquad \nabla\mathcal{L} = \begin{pmatrix} \frac{\partial\mathcal{L}}{\partial\Delta p_1} \\ \vdots \\ \frac{\partial\mathcal{L}}{\partial\Delta p_m} \\ \frac{\partial\mathcal{L}}{\partial\alpha_1} \\ \vdots \\ \frac{\partial\mathcal{L}}{\partial\alpha_n} \end{pmatrix} \tag{8.19}$$

were approximated by finite-differences

$$\frac{\partial\mathcal{L}(\vec{X})}{\partial X_k} \approx \frac{\mathcal{L}(X_k+\delta, X_{\neq k}) - \mathcal{L}(\vec{X})}{\delta} \;. \tag{8.20}$$

Finally we want to know the corresponding error matrix for the vector $\vec{X}$ ($i,j = 1\ldots n{+}m$):

$$[\sigma^2]_{ij} = -[(\nabla\nabla\mathcal{L}(\vec{X}))^{-1}]_{ij} \;. \tag{8.21}$$

Approximated Analytical Form for $\mathcal{L}(\vec{X})$

In Appendix A.2 a derivation of an analytical approximation of $\mathcal{L}(\vec{X})$ is introduced. Such an analytical form will speed up the Newton-Raphson algorithm maximising the log-likelihood.

Here, the log-likelihood $\mathcal{L}(\vec{X})$ was calculated numerically.

A calibration algorithm was developed that allows to calibrate the energy loss in the calorimeters together with magnetic-field scale-factors. The energy loss and the magnetic-field scale-factors can be calibrated as a function of φ and η.

8.2.3 Results

Calibration of Energy Loss and Scale Factors

A sample of 10,000 events was processed through DICE [ART:95] and ATRECON. During the event reconstruction in the Muon System with MUONBOX the magnetic field was changed by different scale factors α_i for different regions ($\vec{B} \to \vec{B}/\alpha$). Applying the method described before, it was possible to retrieve these scale factors with high accuracy and to calibrate the mean energy loss as a function of θ or the pseudo-rapidity $\eta = -\ln(\tan\frac{\theta}{2})$, respectively.

The Newton-Raphson algorithm (see Equation (8.18)) is rather independent from the chosen starting values. For our analysis reasonable starting values were generated by taking the generated values and smearing them by 10 %.

A crucial point is the selection of good tracks for the calibration. Since the energy loss obeys a Landau distribution there are several events which have a huge energy loss and therefore a very large negative log-likelihood $\mathcal{L}$. We applied a cut-off for events with $\mathcal{L}(\vec{X}_0) < -14$. This value was found empirically by minimising the number of iterations necessary to converge.

For symmetry reasons the energy loss was calculated as a function of $|\eta|$.

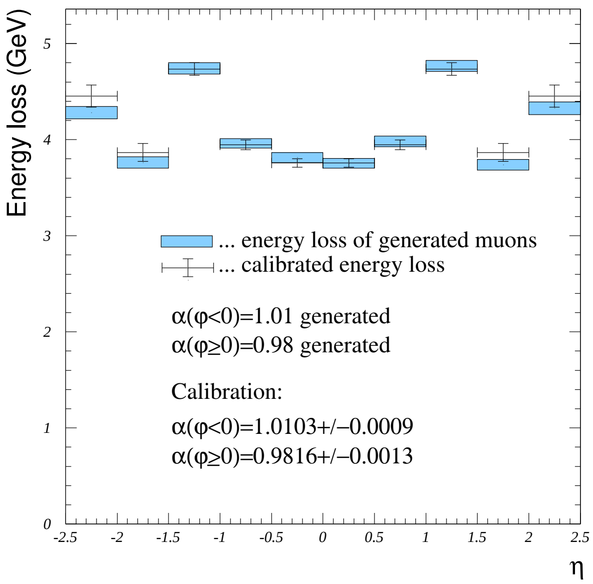

Figure 8.3: *Calibrated energy loss as a function of η for 50 GeV muons. The variations of the energy loss as a function of η reflect the changing amounts of absorber in the calorimeter. The magnetic-field scale-factor α is a function of φ.*

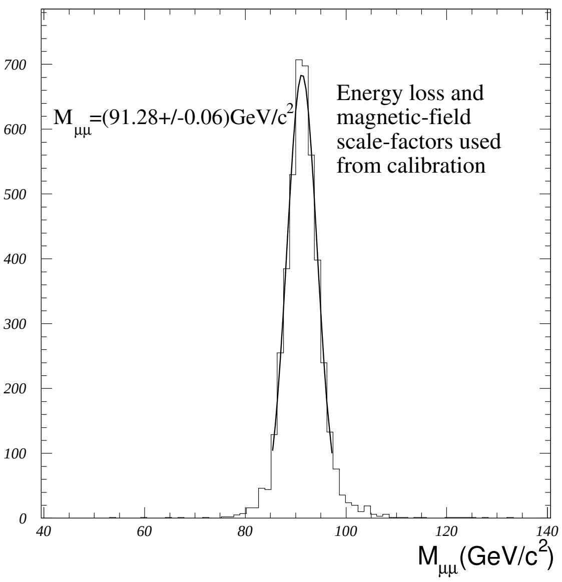

Figure 8.4: *$M_{\mu\mu}$ using the calibration from Figure 8.3. The magnetic-field scale-factor α is a function of φ.*

Figure 8.3 shows the energy loss (for 50 GeV muons) as a function of η. The calibrated

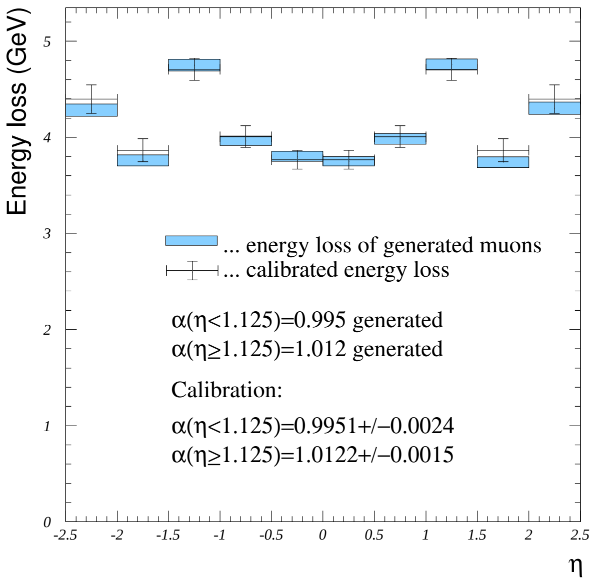

Figure 8.5: *Calibrated energy loss as a function of η for 50 GeV muons. The variations of the energy loss as a function of η reflect the changing amounts of absorber in the calorimeter. The magnetic-field scale-factor α is a function of η.*

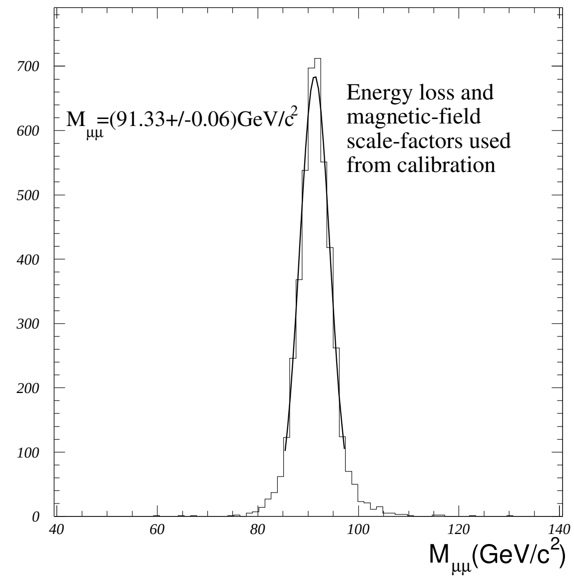

Figure 8.6: *$M_{\mu\mu}$ using the calibration from Figure 8.5. The magnetic-field scale-factor α is a function of η.*

energy loss is compared with the generated energy loss, they are in excellent agreement. The accuracy is 45 MeV for small $|\eta|$ (barrel region) and about 100 MeV for $|\eta| \approx 2$. This accuracy can be further improved by processing more events. Two magnetic-field scale-factors ($\alpha_1 = \alpha(\varphi < 0)$ and $\alpha_2 = \alpha(\varphi \geq 0)$) were calibrated at the same time. They could be retrieved with an accuracy of $\sim 1 \cdot 10^{-3}$. To obtain the desired accuracy of 30 MeV for the energy loss and $5 \cdot 10^{-4}$ for the magnetic-field scale-factors the number of events per channel (here $n \times m = 2 \times 5 = 10$ channels) has to be increased by approximately a factor six.

In Figure 8.5 the magnetic-field scale-factor α was a function of η ($\alpha_1 = \alpha(\eta < 1.125)$ and $\alpha_2 = \alpha(\eta \geq 1.125)$). Compared to Figure 8.3 the accuracy of the calibrated energy loss is slightly deteriorated. This is due to the fact that now the energy loss as well as α are functions of η and therefore stronger correlated in the likelihood function.

Figures 8.4 and 8.6 show the reconstructed mass $M_{\mu\mu}$ using the results of the calibration. One can notice that the reconstructed mass $M_{\mu\mu}$, which of course should correspond with M_{Z}, is slightly too high which is due to the fact that the mean energy loss was used, but the most probable energy loss is smaller. However, this calibration is meant to calibrate the energy loss being measured in the calorimeters and not to provide the full information about the energy loss of muons entering the spectrometer.

Retrieving Information about the Iron Contribution to the Magnetic Field

The magnetic field in the Muon Spectrometer is composed by the Biot-Savart contribution coming from the coils and a superimposed iron contribution from the magnetic material in the spectrometer volume (see Figures 8.7 and 8.8). The iron contribution is calculated by means of finite elements (TOSCA). However, the exact information about the position of magnetic material (especially the calorimeter volume and the surrounding solenoid return yoke) is essential to gain the required accuracy of the magnetic field maps.

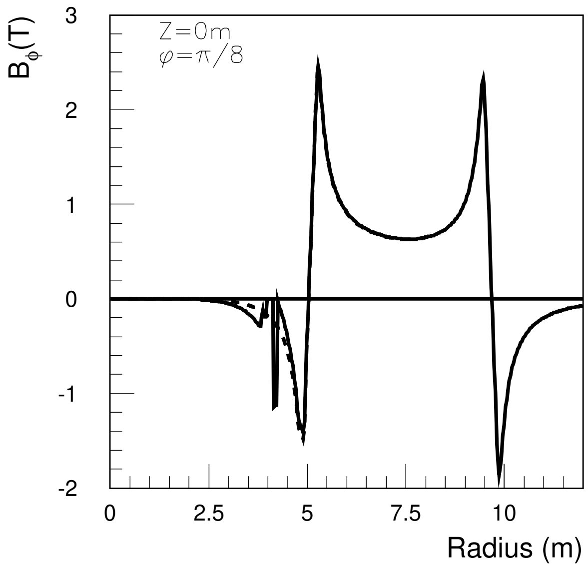

Figure 8.7: *Radial dependence of the azimuthal component of the magnetic field at $\eta = 0$ and $\varphi = 22.5\,°$. The full line is the full field, including the iron contribution, the dashed line is the Biot-Savart contribution* [ATM:97].

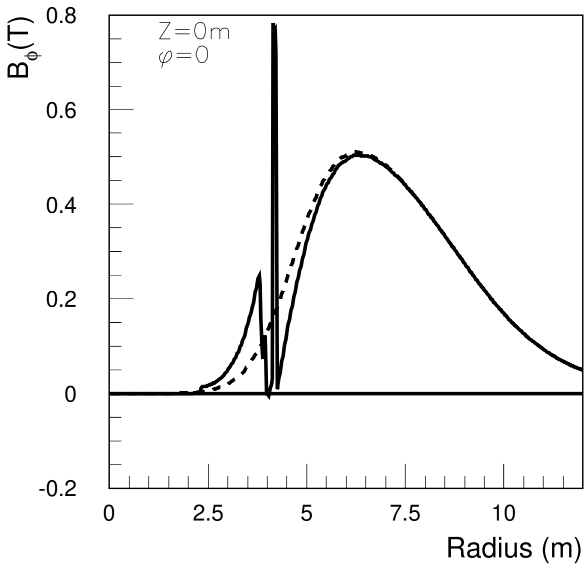

Figure 8.8: *Radial dependence of the azimuthal component of the magnetic field at $\eta = 0$ and $\varphi = 0\,°$. The full line is the full field, including the iron contribution, the dashed line is the Biot-Savart contribution* [ATM:97].

In order to find out what we could learn about the position of the iron contribution in our detector from reconstructing $\mathrm{Z} \to \mu^+\mu^-$ events, the B-field integrals along the muon tracks ($\int B\mathrm{d}l$) were calculated for different shifts of the iron contribution. These integrals were taken as an estimate for the behaviour of the sagitta. Figure 8.9 and 8.10 show the quotient $\int B_{\mathrm{shift}}\mathrm{d}l / \int B_{\mathrm{noshift}}\mathrm{d}l$ as a function of φ. It can be seen that the direction of the shift in the x-y plane can be retrieved (fit parameter P1, accuracy $\sigma_{\mathrm{P1}} \approx 0.2$) provided the magnetic-field scale-factors α_i as a function of φ are known. The parameter P2 of the fitted function $(\mathrm{P3} + \mathrm{P2}\cos(\varphi - \mathrm{P1}))$ yields information about the length of the shift out of the centre.

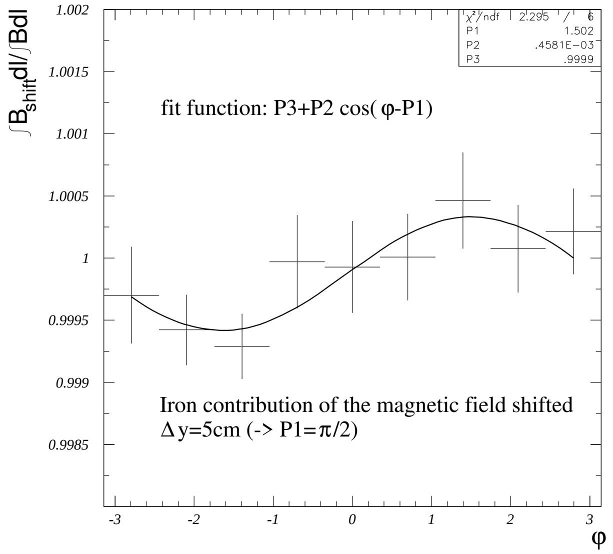

Figure 8.9: *Variation of the field integral along the muon track ($\int B_{\mathrm{shift}}\mathrm{d}l/\int B_{\mathrm{noshift}}\mathrm{d}l$) as a function of φ for a shift of the iron contribution of $(\Delta x, \Delta y, \Delta z) = (0, 5\,\mathrm{cm}, 0)$.*

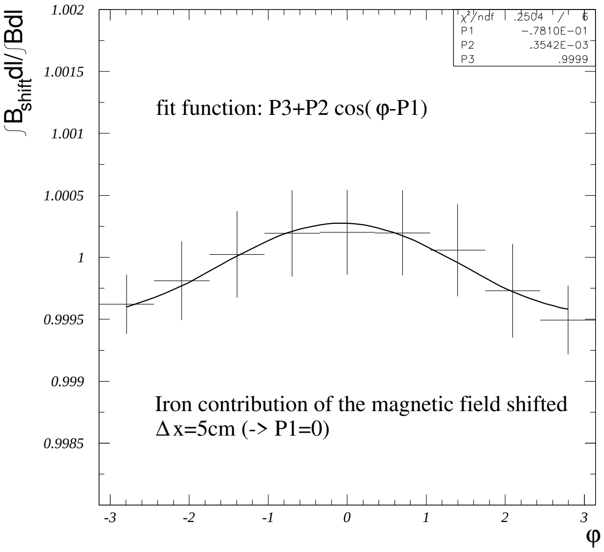

Figure 8.10: *Variation of the field integral along the muon track ($\int B_{\mathrm{shift}}\mathrm{d}l/\int B_{\mathrm{noshift}}\mathrm{d}l$) as a function of φ for a shift of the iron contribution of $(\Delta x, \Delta y, \Delta z) = (5\,\mathrm{cm}, 0, 0)$.*

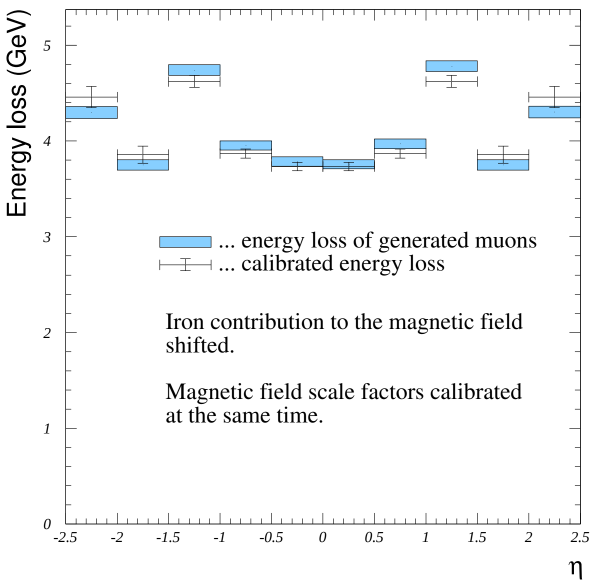

Figure 8.11: *Calibrated energy loss as a function of η for $50\,\mathrm{GeV}$ muons. The energy loss was calibrated at the same time as the magnetic-field scale-factors shown in Figure 8.12.*

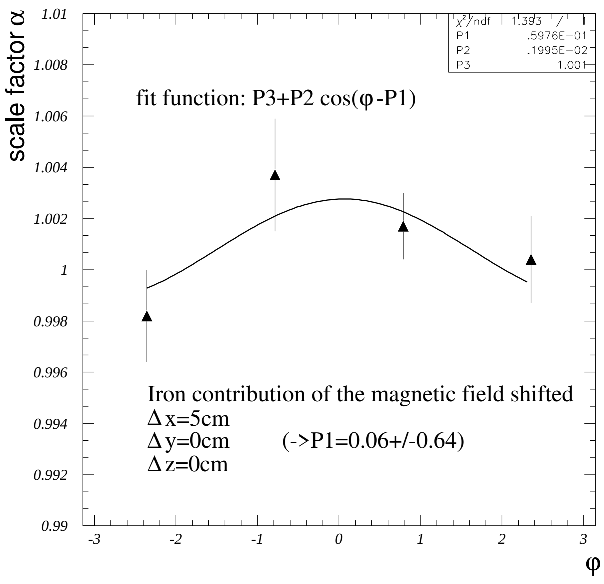

Figure 8.12: *Calibrated magnetic-field scale-factor α as a function of φ for a shift of the iron contribution of $(\Delta x, \Delta y, \Delta z) = (5\,\mathrm{cm}, 0, 0)$.*

This concept was tested in the simulation: During reconstruction with MUONBOX the iron contribution to the magnetic field was shifted out of the centre of the detector (shift in the x-y plane, z position unchanged). The magnetic field for each muon was hence calculated by the Biot-Savart contribution (unshifted) plus the shifted iron contribution. By means of calibrating several scale factors α_i (here $i = 1 \ldots 4$) as a function of φ, the direction of the shift could be retrieved. Since we were limited to 10,000 events, the accuracy was found to be rather poor. However, Figure 8.12 shows the results for a shift of the iron contribution of $(\Delta x, \Delta y, \Delta z) = (5\,\mathrm{cm}, 0, 0) \rightarrow \varphi = 0$. The direction of the shift could be retrieved $\varphi = 0.06 \pm 0.64$. The length of the shift out of the centre (fit parameter P2) was obtained with a statistical error of 65 %. To achieve an accuracy of 1 mm, we would need a factor 1000 bigger sample. At the same time the energy loss was calibrated and is shown in Figure 8.11.

However, it has been shown that the problem of gaining information about the magnetic material in the spectrometer volume can be reduced to retrieving magnetic-field scale-factors from $\mathrm{Z} \rightarrow \mu^+\mu^-$.

It has been shown that with a sample of only 10,000 events the energy loss in the barrel region could be evaluated with an accuracy of 45 MeV. Scale factors of the magnetic field have been found with an accuracy of $\sim 1 \cdot 10^{-3}$. The energy loss and the scale factors were calibrated at the same time. The accuracy is limited by statistics and can therefore be further improved. The problem of gaining information about the iron contribution to the magnetic field has been reduced to retrieving scale factors of the magnetic field. The direction of a shift of the iron contribution in the x-y plane was found with rather poor accuracy, since we were limited strongly by statistics.

Chapter 9

Conclusion

We have analysed the properties of a new baseline gas Ar/CO_2 93/7 and demonstrated that it is the viable solution for the ATLAS MDT system. This gas was studied because it had been shown to have the required operational lifetime needed for the ATLAS experiment. However, to reach its full potential a careful study and understanding of a large number of systematic effects was needed. In this thesis we have evaluated contributions to the spatial resolution, the single-tube track-position measurement and system effects associated with the absolute momentum scale.

The characteristics of the baseline gas and the working parameters of the MDTs are summarised in Table 9.1. Measurements, confirmed by GARFIELD simulations, give a spatial resolution of $\sim 60\,\mu$m without background ($\sim 56\,\mu$m with time-slewing correction) and $\sim 87\,\mu$m with a background rate of 1400 Hz/cm ($\sim 82\,\mu$m with time-slewing correction) at 3 bar and a gas gain of $G_0 = 2 \times 10^4$. This is compatible with the required resolution of $\bar{\sigma} < 80\,\mu$m even at the highest background rates. The different contributions to a resolution deterioration have been investigated extensively and are well understood. Due to the new drift gas the front-end electronics had to be redesigned to give only one hit per signal. Bipolar shaping with a fixed dead time of 700 ns was found to be the most robust and practical solution.

A full analysis of systematic errors affecting the track-position measurement in one tube has been performed under realistic LHC conditions. In Table 9.2 these systematic errors (1-σ values) are summarised. Adding all systematic errors (quadratic sum) results in $\delta r_{\mathrm{total}}^{\mathrm{r.m.s}} < 135\,\mu$m without corrections and in $\delta r_{\mathrm{total}}^{\mathrm{r.m.s}} < 65\,\mu$m respectively, if the corrections are applied. For such a systematic error the momentum resolution will deteriorate less than 1 % absolute for muons with a transverse momentum of $p_{\mathrm{T}} = 1\,\mathrm{TeV}/c$ (simulations for the whole Muon System performed with DICE/ATRECON).

Finally, all sources of systematic errors to the muon-momentum measurement have been investigated. The momentum resolution and the absolute momentum scale of the Muon-System measurements depend on the alignment of the precision chambers, the knowledge of the magnetic field and the knowledge of the energy loss in the calorimeters. Results obtained with a sample of 10,000 Z $\rightarrow \mu^+\mu^-$ events proved that the energy loss and the magnetic field can be calibrated with high accuracy (see Table 9.3). Calibration at the level

baseline gas	Ar/CO_2 93/7
gas pressure p	3 bar
gas gain G_0	2×10^4
operating voltage	3080 V
peaking time t_p	10–15 ns
noise σ_{noise}	< 4 p.i.e
threshold	5 × noise (~ 20 p.i.e)
afterpulsing rate	3 %
maximum drift time	
no B-field $t_{max}^{0\,T}$	~ 700 ns
B-field of 0.5 T $t_{max}^{0.5\,T}$	~ 720 ns
Lorentz angle $\langle\Psi\rangle$	9.3°
resolution IQA $\bar{\sigma}$	
no rate	60 μm
rate of 1400 Hz/cm	87 μm
$\bar{\sigma}$ **time-slew. corrected**	
no rate	56 μm
rate of 1400 Hz/cm	82 μm
maximum occupancy	
rate = 300 kHz/tube	~ 16 %

Table 9.1: *Summary: Working point of the MDTs for the baseline gas.*

effect	$\delta r^{r.m.s}$ (μm)
background rate	
Δrate = 1500 Hz/cm	120
with correction	< 30
gas density	
$\rho/\rho_0 = 0.993$	27
with correction	< 10
gas composition	
Δcomposition = 0.1 %	44
non-concentricity	
$s = 100\,\mu$m	17
gain drop	
$G/G_0 = 0.9$	10
B-field difference	
$\Delta B = 100$ G	8
auto-calibration	< 20
total (quadratic sum)	
without correction	< 135
with correction	< 65

Table 9.2: *Summary: Systematic errors for the baseline gas.*

	Accuracy of the		
	calibration of the energy loss	knowledge of the magnetic field	sagitta measurement alignment error
	$\sigma_{\Delta E}$	σ_B/B	σ_{sag}
requirements	30 MeV	$5 \cdot 10^{-4}$	30 μm
results with 10,000 events	45 MeV*	$1 \cdot 10^{-3}$	—

Table 9.3: *Summary: Systematic errors to the momentum measurement; requirements and results of a calibration of the absolute mass scale using* 10,000 Z $\rightarrow \mu^+\mu^-$ *events. The value marked with* * *was obtained for small* $|\eta|$.

of $\sigma_B/B = 5 \cdot 10^{-4}$ and $\sigma_{\Delta E} = 30$ MeV appears feasible, provided that six times greater statistics per channel are available.

In summary, this work showed that the ATLAS Muon System will satisfy the following requirements: the new baseline gas Ar/CO_2 93/7 guarantees operation for over ten years at high luminosity. A full analysis of systematic effects on spatial resolution, track-position and momentum measurement shows that this spectrometer can be operated at $\Delta p_T/p_T \approx 10\,\%$ at $p_T = 1\,\text{TeV}/c$. This performance will allow ATLAS to explore the full physics potential of the LHC.

Appendix A

A.1 First-Order Corrections to Variations of the Space-Time Relationship

This chapter describes first-order corrections to the rt-relation if the parameters, causing a systematic error, are known. This will be the case for the gas density change, which can be calculated from the temperature measurements, and the background rate, which can be extracted from the current measurement. Since the rt-relation $r_0(t)$ will be obtained locally by auto-calibration [VIE:96, CRE:97], the function $r_0(t)$ yields the exact information about the drift properties at the time of auto-calibration. Hence, by monitoring the changes of environmental parameters with respect to their values at that time, it will be possible to apply corrections for various effects.

In the following, corrections to the rt-relation $r_0(t)$ at a gas density ρ_0 without background rate ($N_\mathrm{c} = 0$) will be introduced. Thus the rt-relation becomes a function of $\frac{\rho}{\rho_0}$ and $N_\mathrm{c} \cdot G$ where N_c is the background rate per unit length and G the gas gain:

$$\begin{aligned} r(t, \frac{\rho}{\rho_0}, N_\mathrm{c} \cdot G) &= r_0(t) + \delta r_\mathrm{D}(t, \frac{\rho}{\rho_0}) + \delta r_\mathrm{F}(t, N_\mathrm{c} \cdot G) = \\ &= r_0(t) + \left(\frac{\rho_0}{\rho} - 1 \right) \mathcal{D}_\mathrm{corr}(t) + \nu(N_\mathrm{c} \cdot G) \mathcal{F}_\mathrm{corr}(t) \ . \end{aligned} \tag{1}$$

The dimensionless parameter ν which contains the background rate N_c, the gas gain G and the average charge deposit Q and the two $r_0(t)$-dependent functions $\mathcal{D}_\mathrm{corr}(t)$ and $\mathcal{F}_\mathrm{corr}(t)$ will be discussed later. At the end of this section a non-concentricity correction δr_C as a function of the deviation s of the wire out of the tube centre is presented. It will be very difficult to estimate the parameter s; maybe a prediction by means of the in-plane alignment-system measurements is possible. For non-concentricities below $100\,\mu$m r.m.s δr_C is rather small (see Section 7.2.4) and therefore a correction of $r_0(t)$ is not necessary.

Because of

$$r(t) = \int_0^t v(t')\,\mathrm{d}t' \quad \rightarrow \quad r_0(t) + \delta r(t) = \int_0^t v_0(t')\,\mathrm{d}t' + \int_0^t \delta v(t')\,\mathrm{d}t' \ , \tag{2}$$

we obtain

$$\delta r(t) = \int_0^t \delta v(t')\,\mathrm{d}t' = \int_0^t (\overbrace{v_0'(t')}^{r_0''(t')}\,\Delta t(t') + \mathcal{O}[\Delta t(t')^2])\,\mathrm{d}t' \;, \tag{3}$$

where $\Delta t(t')$ is defined by

$$\mathcal{E}_0(r_0(t' + \Delta t(t'))) \equiv \mathcal{E}_{\text{new}}(r(t')) \;. \tag{4}$$

In Equation (4) $\mathcal{E}_0(r)$ stands for $\frac{E_0(r)}{\rho_0}$, where $E_0(r)$ is the drift field without background rate and ρ_0 the gas density when $r_0(t)$ was auto-calibrated. $\mathcal{E}_{\text{new}}(r)$ is the new drift field divided by the new gas density $\frac{E_{\text{new}}(r)}{\rho}$. The drift velocity $v(t)$ is a function of $\frac{E}{\rho}$ and therefore of $\mathcal{E}$, therefore $v_0'(t')\Delta t(t')$ represents the first-order correction of the drift velocity (see Figure 1).

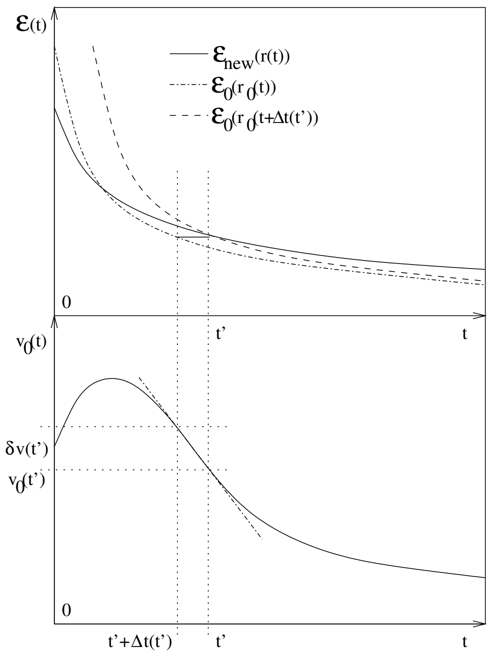

Figure 1: *Sketch illustrating Equation (3) and (4). $v_0'(t')\Delta t(t')$ is the necessary correction to the drift velocity ($\delta v(t')$) for the time t'.*

In the following, we want to separate the two effects, thus either the drift field changes ($E_0 \to E_{\text{new}}$ and $r(t) = r_0(t) + \delta r_{\text{F}}(t)$) or the gas density changes ($\rho_0 \to \rho$ and $r(t) = r_0(t) + \delta r_{\text{D}}(t)$). Taylor expansion of the left side of Equation (4) yields (terms with $\mathcal{O}[\Delta t(t')^2]$ or higher are neglected):

$$\begin{aligned} \mathcal{E}_0(r_0(t')) + \frac{\partial \mathcal{E}_0(r_0(t'))}{\partial t'}\Delta t(t') &= \mathcal{E}_{\text{new}}(r(t')) \;, \\ -\frac{V_0 r_0'(t')}{\rho_0 r_0(t')^2 \ln\frac{b}{a}}\Delta t(t') &= \mathcal{E}_{\text{new}}(r(t')) - \mathcal{E}_0(r_0(t')) \;, \end{aligned} \tag{5}$$

where $\mathcal{E}_0(r) = \frac{V_0}{\rho_0 r \ln\frac{b}{a}}$ was used (a is the wire radius and b is the inner tube radius, here $a = 25\,\mu$m and $b = 1.46\,$cm). In the following, the calculation of $\mathcal{E}_{\text{new}}(r(t')) - \mathcal{E}_0(r_0(t'))$ for the different effects will be discussed.

A.1.1 Gas-Density Correction $\delta r_{\mathrm{D}}(t)$

The gas density will be controlled in the gas distribution. Still, different gas temperatures in the gas volume will cause density variations. These density variations will be rather difficult to predict but in principle we can calculate the gas density ρ in a chamber part by using the monitored temperature T on the chamber, the gas density ρ_{rack} and the temperature T_{rack} in the gas distribution and take advantage of the fact, that the pressure will equalise in the gas volume (the gravitational pressure drop[1] is $\xi = 0.53\,\text{mbar/m}$).

We can consider our drift gas to obey the ideal gas equation:

$$\rho \cdot R \cdot T = p \quad \longrightarrow \quad \rho = \frac{\rho_{\text{rack}} R T_{\text{rack}} - \Delta h \xi}{RT} \,, \tag{6}$$

where ρ is the gas density in the considered chamber, R the gas constant (e.g. $R_{\text{Ar}} = 208\,\text{J}\,\text{kg}^{-1}\text{K}^{-1}$, $R_{\text{CO}_2} = 188\,\text{J}\,\text{kg}^{-1}\text{K}^{-1}$), T the gas temperature in the chamber, Δh the altitude difference between the considered chamber and the gas distribution and p the gas pressure. Equation (6) yields for $\Delta h = 5\,\text{m}$ and a difference between the temperature variation in the chamber (ΔT) and the temperature variation in the gas distribution[2] (ΔT_{rack}) of $\Delta T - \Delta T_{\text{rack}} = 1\,\text{K}$ a density decrease of $\rho/\rho_0 = 0.9957$.

As described in Section 7.2.2 the gas density ρ_{rack} will be kept constant.

With Equation (6) we obtain by applying Taylor expansion ($r(t) = r_0(t) + \delta r_{\mathrm{D}}(t)$, $\delta r_{\mathrm{D}}(t) \ll r_0(t) \quad \forall\, t$):

$$\begin{aligned} \mathcal{E}_{\text{new}}(r(t)) - \mathcal{E}_0(r_0(t)) &= \frac{\rho_0}{\rho} \frac{V_0}{\rho_0 r_0(t) \ln \frac{b}{a}} \left(1 - \frac{\delta r_{\mathrm{D}}(t)}{r_0(t)}\right) - \frac{V_0}{\rho_0 r_0(t) \ln \frac{b}{a}} = \\ &= \frac{V_0}{\rho_0 r_0(t) \ln \frac{b}{a}} \left(\frac{\rho_0}{\rho} - 1 - \frac{\rho_0}{\rho} \frac{\delta r_{\mathrm{D}}(t)}{r_0(t)}\right) \,. \end{aligned} \tag{7}$$

Using Equations (5) and (3) we get:

$$\delta r_{\mathrm{D}}(t) = \int_0^t \frac{r_0''(t')}{r_0'(t')} \left[\left(1 - \frac{\rho_0}{\rho}\right) r_0(t') + \frac{\rho_0}{\rho} \delta r_{\mathrm{D}}(t')\right] \mathrm{d}t' \,. \tag{8}$$

Differentiation on both sides yields a differential equation with the solution

$$\delta r_{\mathrm{D}}(t) = -\left(\frac{\rho_0}{\rho} - 1\right) r_0'(t)^{\frac{\rho_0}{\rho}} \int_0^t \frac{r_0''(t')}{r_0'(t')^{\left(1 + \frac{\rho_0}{\rho}\right)}} r_0(t')\, \mathrm{d}t' \,. \tag{9}$$

For real rt-relations ($r_0'(t)$ varies less than a factor 5 over the whole drift time t) and density changes less then $1\,\%$ ($|\frac{\rho_0}{\rho} - 1| < 0.01$, this corresponds to an isobar temperature change of

[1] Only chambers in approximately the same altitude will be connected to reduce pressure differences induced by gravitation.

[2] Both (ΔT and ΔT_{rack}) with respect to the temperature during auto-calibration.

$|\Delta T| < 3\,\mathrm{K}$) we can regard $r_0'(t)^{-\left(\frac{\rho_0}{\rho}-1\right)}$ as constant, take it out of the integral and cancel it down (error less than 2 %):

$$\delta r_{\mathrm{D}}(t) = -\left(\frac{\rho_0}{\rho} - 1\right) r_0'(t) \int_0^t \frac{r_0''(t')}{r_0'(t')^2} r_0(t')\,\mathrm{d}t' \,. \tag{10}$$

The remaining integral can be solved:

$$\boxed{\delta r_{\mathrm{D}}(t) = \left(\frac{\rho_0}{\rho} - 1\right)(r_0(t) - t \cdot r_0'(t)) = \left(\frac{\rho_0}{\rho} - 1\right)\mathcal{D}_{\mathrm{corr}}(t) \,.} \tag{11}$$

The obtained correction was compared with GARFIELD[3] simulations, they are in excellent agreement (see Figure 7.4).

A.1.2 Rate Correction $\delta r_{\mathrm{F}}(t)$

As described in Section 7.2.1 the ATLAS Muon System will have to cope with rate differences of up to 1500 Hz/cm. Section 7.4 shows the big impact of systematic errors to the rt-relation on the reconstructed muon-momentum resolution.

The rate correction $\delta r_{\mathrm{F}}(t)$ is a function of the product $N_{\mathrm{c}} \cdot G$, where N_{c} is the background count rate per unit length along the wire and G the effective gas gain including the gain drop. Furthermore the average charge deposit per background event Q has to be known[4]. The value of the product $N_{\mathrm{c}} \cdot G \cdot Q$ can be derived from the current I_{ch} in the operating chamber. This current I_{ch} will be monitored.

$$N_{\mathrm{c}} \cdot G \cdot Q = \frac{I_{\mathrm{ch}}}{\mathcal{L}_{\mathrm{ch}}} \,, \tag{12}$$

where $\mathcal{L}_{\mathrm{ch}}$ is the total tube length of the considered chamber. In Equation (12) a homogeneous irradiation of the chamber was assumed.

In Section 6.2.2 a first-order approximation of the field change as a consequence of space charge was introduced (see Equation (6.19)). Using the dimensionless parameter ν

$$\nu \equiv \frac{N_{\mathrm{c}} G Q b^2 \ln\frac{b}{a}}{8\pi\varepsilon_0 \mu V_0^2} = \frac{I_{\mathrm{ch}} b^2 \ln\frac{b}{a}}{8\pi\varepsilon_0 \mu \mathcal{L}_{\mathrm{ch}} V_0^2} \,, \tag{13}$$

where μ is the ion mobility (e.g. $\mu_{\mathrm{Ar^+\,in\,Ar}}(1\,\mathrm{bar}) = 1.535\,\mathrm{cm^2V^{-1}s^{-1}}$ [MCD:73]) and a and b the wire and tube radius, we get:

$$\mathcal{E}_{\mathrm{new}}(r(t)) = \frac{V_0}{\rho_0 r(t) \ln\frac{b}{a}}(1 - \nu) + \frac{2\nu V_0}{\rho_0 b^2}\, r(t) \,. \tag{14}$$

[3] GARFIELD [VEE:98] is interfaced to MAGBOLTZ [BIA:98] which calculates the drift properties of gas mixtures at given temperatures.

[4] Measurements complemented by simulations determined the average energy deposit of a background photon to be $\sim 36\,\mathrm{keV}$ at a magnetic field of 0.6 T [BOY:97].

Applying Taylor expansion ($r(t) = r_0(t) + \delta r_\mathrm{F}(t)$, $\delta r_\mathrm{F}(t) \ll r_0(t) \quad \forall\, t$) and using Equation (5) we obtain

$$\Delta t(t) = \frac{1}{r_0'(t)} \left[\nu r_0(t) - \frac{2\nu \ln\frac{b}{a}}{b^2} r_0(t)^3 + \delta r_\mathrm{F}(t) \left(1 - \nu - \frac{2\nu \ln\frac{b}{a}}{b^2} r_0(t)^2 \right) \right] . \tag{15}$$

Inserting in Equation (3) and differentiating on both sides yields a differential equation

$$\delta r_\mathrm{F}(t) \frac{r_0''(t)}{r_0'(t)} \left(1 - \nu - \frac{2\nu \ln\frac{b}{a}}{b^2} r_0(t)^2 \right) - \frac{\partial \delta r_\mathrm{F}(t)}{\partial t} = \frac{r_0''(t)}{r_0'(t)} \left(\frac{2\nu \ln\frac{b}{a}}{b^2} r_0(t)^3 - \nu r_0(t) \right) , \tag{16}$$

with the solution

$$\delta r_\mathrm{F}(t) = \nu r_0'(t)^{(1-\nu)} e^{-g(t)} \int_0^t e^{g(t')} \frac{r_0''(t')}{r_0'(t')^{(2-\nu)}} \left(r_0(t') - \frac{2 \ln\frac{b}{a}}{b^2} r_0(t')^3 \right) \mathrm{d}t' . \tag{17}$$

The function $g(t)$ in Equation (17) is defined as

$$g(t) \equiv \frac{2\nu \ln\frac{b}{a}}{b^2} \int_0^t \frac{r_0''(t')}{r_0'(t')} r_0(t')^2 \,\mathrm{d}t' , \tag{18}$$

and has values for mixtures like Ar/CO_2 between $g(0) \approx 10^{-4}$ and $g(t_\mathrm{max}) \approx 6 \cdot 10^{-2}$, and even smaller values for less non-linear gas mixtures. Hence the exponential function in the integral can be regarded as constant, written out of the integral and cancelled down (error less than 6 %). The same applies for the $r_0'(t)^{-\nu}$-terms (even for the highest considered background rates ν is smaller than 10^{-2} and $r_0'(t)$ usually varies less than a factor 5 over the whole drift time $t \rightarrow$ error less than 2 %). Simplifying the integrals leads to

$$\boxed{\delta r_\mathrm{F}(t) = \nu \left[t r_0'(t) - r_0(t) + \frac{6 \ln\frac{b}{a}}{b^2} r_0'(t) \int_0^t \left(\frac{r_0'(t')}{r_0'(t)} - 1 \right) r_0(t')^2 \,\mathrm{d}t' \right] = \nu \mathcal{F}_\mathrm{corr}(t) .} \tag{19}$$

Figure 7.3 compares measurements with GARFIELD simulations and the calculation of $\delta r_\mathrm{F}(t)$ according to Equation (19) and shows a good agreement. The correction reduces $\delta r_\mathrm{F}^\mathrm{r.m.s.}$ from 120 μm to $< 30\,\mu$m. Note, that Equation (19) overestimates the rate effect at high rates (see Figure 7.3) since a first-order approximation for the field change was used in Equation (14).

A.1.3 Non-Concentricity Correction $\delta r_\mathrm{C}(t)$

In this section we want to derive Equation (7.8). As a starting point we want to use Equation (7.7), which was obtained by calculating the electric field for a small deviation s of the wire out of the tube centre by means of mirror charges[5]: The line charge on the wire was found to be

$$\gamma = \frac{2\pi\varepsilon_0 V_0}{\ln\frac{b^2-s^2}{ab}} = \frac{2\pi\varepsilon_0 V_0}{\ln\frac{b}{a}} \cdot \left[1 + \frac{s^2}{b^2\ln\frac{b}{a}} + \mathcal{O}[(s/b)^4]\right] . \tag{20}$$

Writing down the whole expression for the electric field in a plane perpendicular to the wire

$$\vec{E}(x,y) = \frac{V_0}{\ln\frac{b^2-s^2}{ab}} \cdot \left[\frac{\begin{pmatrix} x-s \\ y \end{pmatrix}}{(x-s)^2+y^2} - \frac{\begin{pmatrix} x-\frac{b^2}{s} \\ y \end{pmatrix}}{(x-\frac{b^2}{s})^2+y^2}\right] , \tag{21}$$

transforming it into polar coordinates ($x = r\cos\varphi + s$ and $y = r\sin\varphi$) and performing a Taylor expansion for $s \ll b$ leads to

$$|\vec{E}(r,\varphi)| = \frac{V_0}{r\ln\frac{b}{a}}\left(1 + \frac{rs}{b^2}\cos\varphi + \mathcal{O}[(s/b)^2]\right) , \tag{22}$$

which is identical with Equation (7.7). Following the way which was used for the other corrections we start with

$$\mathcal{E}_\mathrm{new}(r(t)) - \mathcal{E}_0(r_0(t)) = \frac{V_0}{\rho_0\ln\frac{b}{a}}\left(\frac{s}{b^2}\cos\varphi - \frac{\delta r_\mathrm{C}}{r_0(t)^2}\right) , \tag{23}$$

where Taylor expansion was used ($r(t) = r_0(t) + \delta r_\mathrm{C}(t)$, $\delta r_\mathrm{C}(t) \ll r_0(t) \ \forall\, t \rightarrow \frac{1}{r_0(t)+\delta r_\mathrm{C}(t)} = \frac{1}{r_0(t)} - \frac{\delta r_\mathrm{C}(t)}{r_0(t)^2} + \mathcal{O}[\delta r_\mathrm{C}(t)^2]$). Using Equation (3) and differentiating on both sides yields a differential equation

$$\frac{\partial\delta r_\mathrm{C}(t)}{\partial t} - \frac{r_0''(t)}{r_0'(t)}\delta r_\mathrm{C}(t) = -\frac{r_0''(t)}{r_0'(t)} \cdot \frac{s r_0(t)^2}{b^2}\cos\varphi , \tag{24}$$

with the solution already shown in Equation (7.8)

$$\boxed{\delta r_\mathrm{C}(t) = -\frac{s}{b^2}\cos(\varphi) r_0'(t)\int_0^t \frac{r_0''(t')}{r_0'(t')^2} r_0(t')^2\,\mathrm{d}t' = 2\frac{s}{b^2}\cos(\varphi) r_0'(t)\int_0^t \left(\frac{r_0'(t')}{r_0'(t)} - 1\right) r_0(t')\,\mathrm{d}t' .} \tag{25}$$

Figure 7.7 compares the measurement of the two branches of the rt-relation for $\varphi = 0$ and $\varphi = \pi$ with the prediction of the effect using Equation (25) and shows very good agreement.

[5]The field of a line charge γ at the distance s from the tube centre can be calculated inside the tube by assuming a mirror line charge $\tilde{\gamma} = -\gamma$ at the distance $\frac{b^2}{s}$ from the tube centre, which lies outside the tube.

A.2 Approximated Analytical Form for $\mathcal{L}(\vec{X})$

In order to obtain an analytical form of $\mathcal{L}(\vec{X})$ (see Section 8.2.2), we have to concentrate on modifying the distributions given in Equations (8.13) and (8.15) to be able to solve the integral in Equation (8.16). We will start by approximating the Breit-Wigner distribution with a Gaussian distribution. Consequently Equation (8.13) becomes

$$\mathrm{prob}((\tilde{m}_\mathrm{Z})_k|I) \approx \frac{2}{\sqrt{2\pi}\Gamma_\mathrm{Z}} \cdot \exp\left(-\frac{((\tilde{m}_\mathrm{Z})_k c - M_\mathrm{Z}c)^2}{2(\Gamma_\mathrm{Z}c/2)^2}\right) . \tag{26}$$

To be able to convolute the two distributions in Equation (8.16) we have to approximate $\mathrm{prob}(\{\bar{p}_1, \bar{p}_2\}_k|\alpha_i, \Delta p_j, (\tilde{m}_\mathrm{Z})_k, I)$ with

$$\begin{aligned}\mathrm{prob}(\{\bar{p}_1, \bar{p}_2\}_k|\alpha_i, \Delta p_j, (\tilde{m}_\mathrm{Z})_k, I) \;\approx\; & \frac{2\sqrt{f(\{\bar{p}_1, \bar{p}_2\}_k, \mathcal{F}, \alpha_i, \Delta p_j)}}{\sqrt{2\pi}\sigma_f(\{\bar{p}_1, \bar{p}_2\}_k, \mathcal{F}, \alpha_i, \Delta p_j)} \cdot \\ & \exp\left(-\frac{\left((\tilde{m}_\mathrm{Z})_k c - \sqrt{f(\{\bar{p}_1, \bar{p}_2\}_k, \mathcal{F}, \alpha_i, \Delta p_j)}\right)^2}{2\frac{\sigma_f(\{\bar{p}_1, \bar{p}_2\}_k, \mathcal{F}, \alpha_i, \Delta p_j)^2}{4\cdot f(\{\bar{p}_1, \bar{p}_2\}_k, \mathcal{F}, \alpha_i, \Delta p_j)}}\right) .\end{aligned} \tag{27}$$

Now the integral in Equation (8.16) can be calculated analytically (convolution of two Gaussian distributions):

$$\begin{aligned}\sigma_k^\mathrm{tot}(\{\bar{p}_1, \bar{p}_2\}_k, \mathcal{F}, \alpha_i, \Delta p_j) \;=\; & \frac{1}{2} \cdot \sqrt{\Gamma_\mathrm{Z}^2 c^2 + \frac{\sigma_f(\{\bar{p}_1, \bar{p}_2\}_k, \mathcal{F}, \alpha_i, \Delta p_j)^2}{f(\{\bar{p}_1, \bar{p}_2\}_k, \mathcal{F}, \alpha_i, \Delta p_j)}} , \\ \mathrm{prob}(\alpha_i, \Delta p_j|\{\bar{p}_1, \bar{p}_2\}_k, I) \;\propto\; & \mathrm{prob}(\alpha_i|I) \cdot \mathrm{prob}(\Delta p_j|I) \cdot \frac{1}{\sqrt{2\pi}\sigma_k^\mathrm{tot}(\{\bar{p}_1, \bar{p}_2\}_k, \mathcal{F}, \alpha_i, \Delta p_j)} \cdot \\ & \exp\left(-\frac{\left(M_\mathrm{Z}c - \sqrt{f(\{\bar{p}_1, \bar{p}_2\}_k, \mathcal{F}, \alpha_i, \Delta p_j)}\right)^2}{2 \cdot \sigma_k^\mathrm{tot}(\{\bar{p}_1, \bar{p}_2\}_k, \mathcal{F}, \alpha_i, \Delta p_j)^2}\right) .\end{aligned} \tag{28}$$

Inserting this expression into Equation (8.10) yields an analytical expression for $\mathcal{L}(\vec{X})$. It might be more convenient to use such an analytical expression to maximise the log-likelihood $\mathcal{L}(\vec{X})$.

Appendix B

Glossary

ADC	**A**nalog to **D**igital **C**onverter;
ALEPH	Particle-physics experiment installed at LEP;
ALICE	**A** **L**arge **I**on **C**ollider **E**xperiment,
	particle-physics experiment planned for LHC;
ATLAS	**A** **T**oroidal **L**HC **A**pparatu**S**,
	particle-physics experiment planned for LHC;
ATRECON	**AT**LAS **RECON**struction, program to reconstruct ATLAS events;
BI	**B**arrel **I**nner station;
BM	**B**arrel **M**iddle station;
BO	**B**arrel **O**uter station;
BOS	MDT chamber: **B**arrel **O**uter **S**mall;
CERN	**C**entre **E**uropéen pour la **R**echerche **N**ucléaire;
	The European Laboratory for Particle Physics;
CMS	**C**ompact **M**uon **S**olenoid,
	particle-physics experiment planned for LHC;
CSC	**C**athode **S**trip **C**hamber;
DAQ	**D**ata **A**c**Q**uisition;
DELPHI	**D**etector for **EL**ectron, **P**hoton and **H**adron **I**dentification,
	Particle-physics experiment installed at LEP;
DICE	**D**etector **I**ntegration for a **C**ollider **E**xperiment,
	ATLAS simulation program based on GEANT;
EI	**E**nd-cap **I**nner station;
EM	**E**nd-cap **M**iddle station;
EMS	MDT chamber: **E**nd-cap **M**iddle **S**mall;
ENC	**E**quivalent **N**oise **C**harge;
EO	**E**nd-cap **O**uter station;
FADC	**F**lash **A**nalog to **D**igital **C**onverter;
GARFIELD	Drift chamber simulation program;

GEANT	Program to simulate detector characteristics and performance;
GIF	**G**amma **I**rradiation **F**acility;
Hedgehog board	MDT front-end electronics board, adapted to the multilayer pin layout;
HEED	Program to compute energy loss of fast particles in gases;
HV	**H**igh **V**oltage;
H8	SPS beam line in the north area at CERN, test beam for chamber tests;
IQA	Number to characterise the resolution: **I**nverse **Q**uadratic **A**verage;
LAr	**L**iquid **Ar**gon;
LEP	**L**arge **E**lectron **P**ositron Collider;
LEP2	Upgrade of the **L**arge **E**lectron **P**ositron Collider;
LHC	**L**arge **H**adron **C**ollider;
LHCb	**L**arge **H**adron **C**ollider **B** Physics Experiment;
LVL1/2/3	**L**e**V**e**L** 1/2/3;
L3	**L**EP **3**, Particle-physics experiment installed at LEP;
MAGBOLTZ	Program to compute gas transport parameters;
MDT	**M**onitored **D**rift **T**ube;
MSSM	**M**inimal **S**uper-symmetric Extension of the **S**tandard **M**odel;
MUONBOX	Program to simulate the detector response in the Muon System;
ODYSSEUS	Silicon telescope used in the test beam;
OPAL	**O**mni-**P**urpose **A**pparatus for **L**EP, Particle-physics experiment installed at LEP;
p.i.e	Measure for the pulse height: **p**rimary **i**onisation **e**lectron;
PS	**P**roton **S**ynchrotron;
PYTHIA	Program used to simulate the LHC event generation;
QCD	**Q**uantum **C**hromo **D**ynamics;
QED	**Q**uantum **E**lectro **D**ynamics;
RASNIK	Three-point alignment monitors: **R**ed **A**lignment **S**ystem of **NIK**HEF;
RPC	**R**esistive **P**late **C**hamber;
SCT	**S**emi **C**onductor **T**racker;
SM	**S**tandard **M**odel;
SPS	**S**uper **P**roton **S**ynchrotron;
SUSY	**SU**per **SY**mmetry;
TDC	**T**ime to **D**igital **C**onverter;
TDR	**T**echnical **D**esign **R**eport;
TGC	**T**hin **G**ap **C**hamber;
TOSCA	Finite element program for the calculation of magnetic fields;
TRT	**T**ransition **R**adiation **T**racker;
X5	SPS beam line in the west area at CERN, test beam for chamber tests.

Bibliography

[ALE:98a] M. Aleksa, N.P. Hessey, W. Riegler: *MDT Noise Measurements in the X5 and H8 Test Beam*, ATLAS MUON-NO-98-254, CERN (1998).

[ALE:98b] M. Aleksa, M. Deile, N.P. Hessey, W. Riegler: *MDT Performance in a High Rate Background Environment*, ATLAS MUON-NO-98-258, CERN (1998).

[ALE:98c] M. Aleksa, W. Riegler: *Non-Linear MDT Drift Gases like* Ar/CO_2, ATLAS MUON-NO-98-268, CERN (1998).

[ALE:99a] M. Aleksa: *Absolute Mass Scale Calibration Using* $Z \to \mu^+\mu^-$, ATLAS MUON-NO-99-01, CERN (1999).

[ALE:99b] M. Aleksa, W. Riegler: *Bipolar versus Unipolar Shaping of MDT Signals*, ATLAS MUON-NO-99-03, CERN (1999).

[ALE:99c] M. Aleksa et al.: *Rate Effects in High-Resolution Drift Chambers*, CERN-EP/99-101 (1999).

[ALI:95] ALICE Collaboration: *ALICE Technical Proposal*, CERN/LHCC 95-71 (1995).

[ALK:70] G. D. Alkhazov: *Statistics of electron avalanches and ultimate resolution of proportional counters*, Nucl. Intrum. Methods **89** (1970) 155.

[ART:95] A. Artamonov et al.: *DICE-95*, ATLAS SOFT-95-014, CERN (1995).

[ATC:96] ATLAS Calorimeter Collaboration: *ATLAS Calorimeter Technical Design Reports*, CERN/LHCC 96-40, 96-41, 96-42 (1996).

[ATI:97] ATLAS Inner Detector Collaboration: *ATLAS Inner Detector Technical Design Report*, CERN/LHCC 97-16 and 97-17 (1997).

[ATL:94] ATLAS Collaboration: *ATLAS Technical Proposal*, CERN/LHCC 94-38 (1994).

[ATL:99] ATLAS Collaboration: *ATLAS Detector and Physics Performance Technical Design Report*, CERN/LHCC 99-15 (1999).

[ATM:95] The ATLAS Muon Detector Physics Group: *Criteria for the Choice of the MDT Operating Point*, ATLAS MUON-NO-95-98, CERN (1995).

[ATM:97] ATLAS Muon Collaboration: *Technical Design Report*, CERN/LHCC 97-22, June 1997, available on the WWW-page:
`http://atlasinfo.cern.ch/Atlas/GROUPS/MUON/TDR/Web/TDR.html`

[BAL:93] V.E. Balakin et al.: *Measurements of Seismic Vibrations in the CERN TT2A Tunnel for Linear Collider Studies*, CERN-SL/93-30, CERN (1993).

[BAR:94] S.A. Baranov, I.R. Boyko, G.A. Chelkov, M.A. Ignatenko: *Gamma Sensitivity of Pressurised Drift Tubes*, ATLAS MUON-NO-94-36, CERN (1994).

[BAT:94] G. Battistoni et al.: *Background Calculations for the ATLAS Detector and Hall*, ATLAS GEN-NO-94-10, CERN (1994).

[BIA:98] S. Biagi: *MAGBOLTZ: program to compute gas transport parameters*, Version 1.10, CERN.

[BLU:93] W.Blum, L. Rolandi: *Particle Detection with Drift Chambers*, Springer Verlag, Berlin-Heidelberg-New York (1993).

[BNL:73] *Common base preamplifier IO354-2 and shaping amplifier IO532-01*, Instrumentation Division, Brookhaven National Laboratory, Upton, New York (1973).

[BOY:95] I.R. Boyko et al.: *Investigation of the Ratio between the Streamer and Proportional Signals in Drift Tubes*, ATLAS MUON-NO-95-88, CERN (1995).

[BOY:97] I.R. Boyko et al.: *MDT Gamma Response*, ATLAS MUON-NO-97-194, CERN (1997).

[CMS:94] CMS Collaboration: *CMS Technical Proposal*, CERN/LHCC 94-43 (1994).

[CMS:97] GIF Webpage of the CMS collaboration:
`http://www1.pv.infn.it/vitulo/testbeam/simulation.html`

[CRE:97] P. Creti et al.: *Test-beam results from the Calypso MDT chamber*, ATLAS MUON-NO-97-196, CERN (1997).

[DAL:97] C.W. Daly et al.: ATLAS MUON-NO-97-144, CERN (1997).

[DEI:96a] M. Deile et al.: *Test Beam Studies of the Gas Mixtures ... for Drift Tubes*, ATLAS MUON-NO-96-122, CERN (1996).

[DEI:96b] M. Deile: *Optimierung der Operationsparameter von Hochdruckdriftrohren für ATLAS*, diploma thesis, LMU Munich (1996).

[DEI:97] M. Deile, N.P. Hessey: *Density Control of MDT Gas*, ATLAS MUON-NO-97-203, CERN (1997).

[DEI:98] M. Deile, N. Hessey, A. Staude: *MDT Track Fitting with the Maximum Likelihood Method*, ATLAS MUON-NO-98-240, CERN (1998).

[DEI:99] M. Deile, J. Dubbert, N.P. Hessey, A. Staude: *ODYSSEUS - a Silicon Telescope for Test Beam Experiments*, ATLAS COM-MUON-99-015, CERN (1999).

[DEL:99] DELPHI Collaboration: *Search for Neutral Higgs Bosons in* $\mathrm{e}^+\mathrm{e}^-$ *Collisions at* $\sqrt{s} = 188.7\,\mathrm{GeV}$, submitted to HEP'99 Conference, Tampere (July 1999).

[DIE:56] W. Diethorn: *A methane proportional counter system for natural radiocarbon measurements*, USAEC Report NY06628 (1956).

[EER:92] P. Eerola: *Measurement of CP-violation in B-decays with the ATLAS experiment*, ATLAS PHYS-NO-92-09, CERN (1992).

[FER:95] A. Ferrari, P. Sala: *Background Rates in the Muon System: Recent Results and the Effect of the Tungsten Plug*, ATLAS MUON-NO-95-90, CERN (1995).

[FER:97] A. Ferrari, P. Sala: *Shielding Modifications and their Influence on the Background Values*, ATLAS MUON-NO-97-162, CERN (1997).

[GSC:97] E. Gschwendtner et al.: *Analysis of the X-tomograph scan data for MDT chamber prototypes*, ATLAS MUON-NO-175, CERN (1997).

[HAZ:97] E. Hazen et al.: *An Integrated Multi-Channel Readout for ATLAS MDTs*, `http://ohm.bu.edu/bmc/lerb2/paper_html/paper_html.html`.

[HEN:95] A. Henriques et al.: *The Muon Energy Losses in the Tile Calorimeter*, ATLAS TILE-CAL-NO-95-68, CERN (1995).

[HES:98] N.P. Hessey: *The precision drift chambers for the ATLAS Muon Spectrometer*, Nucl. Intrum. Methods **A419** (1998) 326-330

[JAR:90] G. Jarlskog and D. Rein (editors): *Proceedings of the Large Hadron Collider Workshop*, CERN/90-10 (1990).

[KIR:97] S. Kircher et al.: *Influence of aqueous vapour on the drift properties of MDT gases*, ATLAS MUON-NO-97-214, CERN (1997).

[LAN:57] Landolt-Boernstein: vol. 4/3, *Eigenschaften des Plasmas*, no 44315, 6th edn, Springer, Berlin-Heidelberg (1957).

[LHC:98] LHCb Collaboration: *LHCb Technical Proposal*, CERN/LHCC 98-4 (1998).

[LOH:85] W. Lohmann et al.: *Energy Loss of Muons in the Energy Range 1-10000* GeV, CERN Yellow Report 85-03 (1985).

[MAC:82] C.M. Ma et al., MIT Technical Report 129 (1982).

[MCD:73] E.W. McDaniel and E.A. Mason: *The Mobility and Diffusion of Ions in Gases*, Wiley, New York (1973).

[NIC:74] P.W. Nicholson: *Nuclear Electronics*, John Wiley and Sons (1974).

[NIS:92] A. Nisati: *Alignment of Muon Chambers with* $\mathrm{Z}\rightarrow \mu^+\mu^-$ *Events*, ATLAS MUON-NO-92-09, CERN (1992).

[PAR:98] The European Physical Journal C: *Review of Particle Physics*, (1998).

[RAM:39] S. Ramo: *Currents induced in electron motion*, PROC. IRE **27**, (1939) 584.

[RIE:97a] W. Riegler: *MDT Efficiency, Double Track Separation*, ATLAS MUON-NO-97-173, CERN (1997).

[RIE:97b] W. Riegler: *Limits to Drift Chamber Resolution*, PhD Thesis, CERN (1997).

[RIE:99] W. Riegler, M. Aleksa et al.: *Resolution Limits of Drift Tubes*, CERN-EP/99-99 (1999).

[SAM:97] T. Sammer: *Autokalibration von Driftrohrkammern für das ATLAS-Myonspektrometer*, diploma thesis, LMU Munich (1997).

[SIV:97] D.S. Sivia: *Data Analysis, A Bayesian Tutorial*, Oxford Science Publications (1997).

[SMI:95] I. Smirnov: *HEED: program to compute energy loss of fast particles in gases*, Version 1.01, CERN.

[SPE:97] M. Spegel: *On the Lifetime of Proportional Counters*, PhD thesis, CERN (1997).

[SUS:79] L. Susskind: Phys. Rev. **D20** (1979) 2619.

[VEE:98] R. Veenhof: *GARFIELD: Simulation of gaseous detectors*, Version 6.27, CERN, write-up: `http://wwwinfo.cern.ch/writeup/garfield`

[VIE:96] G. Viehhauser: *Detector Physics of the ATLAS precision muon chambers*, PhD thesis, CERN (1996).

[WEI:79] S. Weinberg: Phys. Rev. **D19** (1979) 1277.

Curriculum Vitae

9 July 1972	Born in Vienna
09/78 – 06/82	Primary School in Vienna
09/82 – 06/90	High School ("Bundesrealgymnasium Wien XIX") All certificates with distinction
10/90 – 05/91	Military service at the Austrian Army (studying meteorology, working in an airport weather station), in my spare time learned basic Italian in a course at the "Universität Wien"
10/91 – 10/96	Study of Physics at the "Technische Universität Wien" Diploma thesis on *Investigations of High-Temperature Superconductors Using a Transmission Electron Microscope*, finishing with a Diploma in shortest time possible (10 semesters), second part of Diploma with distinction Yearly scholarship for exceptional success at the university (for the best 40 out of 8000 students) from 1993 to 1999
Sept. 93 – 96	Yearly internship positions at SIEMENS Program and System Development in Vienna
10/93 – 06/95	Parallel studies at the "Wirtschaftsuniversität Wien" for gaining basic knowledge in the field of economics
10/94 – 06/95	Learned basic Spanish in a course at the "Wirtschaftsuniversität Wien"
03/97 – 09/99	Selected for the Austrian Doctoral Student Program at CERN (Geneva): Doctoral thesis within the ATLAS Muon Collaboration about the *Performance of the ATLAS Muon Spectrometer*
04/97 – 03/99	Learned French in courses at CERN (Geneva)

List of Publications

1. M. Aleksa: *Transmissionselektronenmikroskopische Untersuchung von neutroneninduzierten Defekten in* $Bi_2Sr_2CaCu_2O_{8+\delta}$, diploma thesis (1996)

2. M. Aleksa, P. Pongratz, O. Eibl, F.M. Sauerzopf, H.W. Weber, T.W. Li, P.H. Kes: *TEM observation of neutron-induced collision cascades in* $\mathrm{Bi}-2212$ *single crystals*, Physica C **297** (1998)

3. N. Hessey on behalf of the ATLAS Muon Collaboration: *The Precision Drift Chambers for the ATLAS Muon Spectrometer*, Nucl. Instrum. Methods **A419** (1998)

4. M. Aleksa, N.P. Hessey, W. Riegler: *MDT Noise Measurements in the X5 and H8 Test Beams*, ATLAS MUON-NO-98-254, CERN (1998)

5. M. Aleksa, M. Deile, N.P. Hessey, W. Riegler: *MDT Performance in a High Rate Background Environment*, ATLAS MUON-NO-98-258, CERN (1998)

6. M. Aleksa, W. Riegler: *Non-Linear MDT Drift Gases like* Ar/CO_2, ATLAS MUON-NO-98-268, CERN (1998)

7. W. Riegler, M. Aleksa: *Bipolar versus Unipolar Shaping of MDT Signals*, ATLAS MUON-NO-99-003, CERN (1999)

8. W. Riegler, M. Aleksa, M. Deile, J. Dubbert, C. Fabjan, C. Gruhn, N.P. Hessey, T. Sammer: *Resolution Limits of Drift Tubes*, CERN-EP/99-99, submitted to Nucl. Instrum. Methods (1999)

9. W. Riegler, M. Aleksa, M. Deile, J. Dubbert, C. Fabjan, C. Gruhn, N.P. Hessey, T. Sammer: *Front-End Electronics for Drift Tubes in a High-Rate Environment*, CERN-EP/99-100, submitted to Nucl. Instrum. Methods (1999)

10. M. Aleksa: *Absolute Mass Scale Calibration Using* $\mathrm{Z} \rightarrow \mu^+\mu^-$, ATLAS MUON-NO-99-001, CERN (1999)

11. M. Aleksa, M. Deile, J. Dubbert, C. Fabjan, C. Gruhn, N.P. Hessey, W. Riegler, T. Sammer: *MDT Performance in a High Rate Background Environment*, CERN-EP/99-101, submitted to Nucl. Instrum. Methods (1999)

I only quoted those publications to which I made a major contribution.

Lebenslauf

9. Juli 1972	Geboren in Wien
09/78 – 06/82	Volksschule in Wien
09/82 – 06/90	Bundesrealgymnasium Wien XIX Abschluß: Matura, alle Zeugnisse mit Auszeichnung
10/90 – 05/91	Grundwehrdienst beim Österreichischen Bundesheer (meteorologische Ausbildung, Arbeit in der Wetterstation eines Militärflugplatzes), in meiner Freizeit Italienischkurs an der Universität Wien
10/91 – 10/96	Studium der Technischen Physik an der TU Wien Diplomarbeit über *Transmissionselektronenmikroskopische Untersuchungen von Hochtemperatursupraleitern* Abschluß: Diplom in Mindestzeit (10 Semester), 2. Studienabschnitt mit ausgezeichnetem Erfolg Jährliches Leistungsstipendium für hervorragenden Studienerfolg (für die besten 40 von 8000 Studenten), von 1993 bis 1999
Sept. 93 – 96	Jährliche einmonatige Ferialarbeit bei SIEMENS Programm- und Systementwicklung in Wien
10/93 – 06/95	Absolvierung von Vorlesungen auf der WU Wien zur Erlangung von Basiskenntnissen im Bereich der Wirtschaft
10/94 – 06/95	Spanischkurs an der WU Wien
03/97 – 09/99	Ausgewählt für das ,,Austrian Doctoral Student Program“ am CERN (Genf): Doktorarbeit in der ATLAS Muon Kollaboration über *Die Messgenauigkeit des ATLAS Myonspektrometers* (verfasst in englischer Sprache)
04/97 – 03/99	Französischkurse am CERN (Genf)